

Mechanistic Study of Under Deposit Corrosion of Mild Steel in Aqueous Carbon Dioxide
Solution

A dissertation presented to
the faculty of
the Russ College of Engineering and Technology of Ohio University

In partial fulfillment
of the requirements for the degree
Doctor of Philosophy

Jin Huang

December 2013

© 2013 Jin Huang. All Rights Reserved.

This dissertation titled

Mechanistic Study of Under Deposit Corrosion of Mild Steel in Aqueous Carbon Dioxide

Solution

by

JIN HUANG

has been approved for

the Department of Chemical and Biomolecular Engineering

and the Russ College of Engineering and Technology by

Srdjan Nešić

Professor of Chemical and Biomolecular Engineering

Dennis Irwin

Dean, Russ College of Engineering and Technology

ABSTRACT

HUANG, JIN, Ph.D., December 2013, Chemical Engineering

Mechanistic Study of Under Deposit Corrosion of Mild Steel in Aqueous Carbon Dioxide Solution (234 pp.)

Director of Dissertation: Srdjan Nešić

Silica sand is produced from geological formations that contain hydrocarbons and has the potential to be transported with extracted oil and gas along pipeline transmission systems. Consequently, the presence of sand is a significant challenge to production in the oil and gas industry. A particular threat is so called under deposit corrosion, which refers to accelerated corrosion processes that develop underneath the deposit. Such accelerated corrosion processes may cause leakage of pipelines or result in catastrophic failure without control and prevention. Therefore, it is important to understand the mechanisms of under deposit corrosion. In this dissertation, possible mechanisms of CO₂ corrosion of mild steel under sand deposits are proposed and evaluated. Both uniform corrosion processes and localized corrosion were studied.

Electrochemical experiments were conducted with and without corrosion inhibitor to examine the effect of silica sand deposits on CO₂ corrosion of mild steel. A simple and reliable method for testing of localized under deposit corrosion was developed and verified. It was established that in a solution free of corrosion inhibitor, both anodic and cathodic reactions are retarded by the sand deposit. The presence of the sand also caused a water chemistry difference between deposit covered areas and adjacent uncovered

surface regions. This water chemistry difference resulted in a higher solution pH on the steel surface and promoted iron carbonate formation, which acted as a further mass transfer barrier for diffusion. A mechanistic electrochemical model was developed which was able to capture the characteristic features of the effect of sand deposits and was capable of predicting the under deposit corrosion rate.

In the study of under deposit corrosion in inhibited environments, three uniform corrosion inhibitors were tested. The effects of environmental factors such as pH and temperature in conjunction with deposit particle size and porosity on inhibition were evaluated. The effect of sand deposit on inhibition mechanisms of different types of corrosion inhibitors were proposed and examined. It was found that general depletion of surfactant inhibitor (imidazoline type) by adsorption on the silica sand surface was not the critical factor that causes inhibition failure in under deposit CO₂ corrosion. Slow diffusion of inhibitor through the porous sand deposit layer was also not the limiting factor in cases where inhibition failed. Localized corrosion in the form of pitting was identified in under deposit corrosion and related to the inability of the inhibitor to protect the steel surface in the crevices immediately underneath individual sand particles. These pits rapidly propagated due to galvanic effects, eventually merging and causing a high rate of attack underneath sand deposits.

DEDICATION

To

My parents, Cuilan Liu and Legen Huang

For their

Love, faith and sacrifice

ACKNOWLEDGEMENTS

First and foremost, I would like to express my sincere gratitude to my advisor Dr. Srdjan Nešić. Without his support, guidance and challenge, this dissertation could not have been completed. Not only was Dr. Nešić an expert supervisor in my academic work, but also has he been the most patient and brilliant mentor in my life. Under his supervision and encouragement, my professional skills have been greatly developed and my confidence has been largely enhanced. From his word and deed, I learned wisdom. Having Dr. Nešić as my advisor, I couldn't have been luckier.

My deepest affection goes to my industry mentors and friends Dr. Yang Yang and Dr. Xuanping Tang, who have given me tremendous guidance, help and support since the first day I arrived in the United States. I am very thankful for their love and friendship.

I would like to thank Dr. Bruce Brown. As my project leader, he helped me and supported me for the whole project on a daily basis. Whenever I needed help for my research or just felt like complaining about my problems, he was always the one I could turn to.

I am grateful to Dr. Sonja Richter, Dr. David Young, Dr. Xiu Jiang, Dr. Dingrong Qu, Dr. Yoon-Seok Choi, Dr. Fernando Farelas, Dr. Brian Kinsella and Dr. Bert Pots for their advices on my research and career. I have benefited a lot from my discussion with them. I am also very thankful to the faculty members Dr. Valerie Young, Dr. Daniel Gulino and Mr. Thomas Riggs for their help on keeping me on track in my academic progress.

My appreciations are extended to Dr. Michael Prudich, Dr. Kevin Crist, Dr. Howard D. Dewald and Dr. Michael P. Jensen for giving me valuable comments and suggestions on my dissertation and serving as my committee members.

I would also like to thank Mr. Albert Schubert, Mr. Cody Shafer, Mr. Steve Upton, Mr. Phil Bullington, Mr. Alexis Barxias and Mr. Danny Cain for their assistance in the technical work. I am very thankful to all the fellow students, post-docs, staff and visiting scholars for creating such a joyful and wonderful environment at the institute. My PhD life would not be so colorful without their company. Special thanks to Ms. Edie Chalfant and Ms. Rebecca Gill for their invaluable help to improve my English and understanding of American culture.

I would like to acknowledge the CC JIP sponsor companies for their financial support and technical advices on my research.

Last but not least, I am highly indebted to my parents, Cuilan Liu and Legen Huang, who always put their faith in me and encourage me to pursue my dreams and who sacrifice so I can be the person I am today. I would also like to thank Mr. Peng Lin for his devoted love and care over the past years.

TABLE OF CONTENTS

	Page
Abstract	3
Dedication	5
Acknowledgements	6
List of Tables	11
List of Figures	12
Chapter 1. Introduction	27
Chapter 2. Literature Review	30
2.1 Carbon Dioxide Corrosion	30
2.1.1 Carbon Dioxide Corrosion Mechanisms	30
2.1.2 Key Factors Affecting Aqueous CO ₂ Corrosion of Mild Steel	32
2.2 Corrosion Inhibitors	34
2.3 Under Deposit Corrosion	36
2.3.1 Deposits	38
2.3.2 Under Deposit Corrosion Testing Methods	39
2.3.3 Under Deposit Corrosion Mechanisms	41
Chapter 3. Objectives and Scope	46
Chapter 4. Under Deposit CO ₂ Corrosion of Mild Steel in Environment without Corrosion Inhibitors	48
4.1 Introduction	48
4.2 Experimental Methods	48
4.2.1 Experimental Setup	48
4.2.2 Working Electrode Design	51
4.2.3 Deposit Properties	53
4.2.4 Experimental Procedure	56
4.2.5 Test Matrix	57
4.3 Results and Discussion	61
4.3.1 Effect of Deposit Porosity	61
4.3.2 Effect of Deposit Depth	69
4.3.3 Effect of Temperature	73

4.3.4 Influence of Solution pH.....	76
4.3.5 Longer Experiment Duration	83
4.4 Electrochemical Modeling.....	91
4.4.1 Summary of Experimental Observations	91
4.4.2 Corrosion Rate Prediction.....	92
4.4.3 Model Verification.....	96
4.5 Summary	103
Chapter 5. Inhibition of CO ₂ Corrosion of Mild Steel under Silica Sand Deposits .	104
5.1 Introduction.....	104
5.2 Experimental Method.....	104
5.2.1 Experimental Setup.....	104
5.2.2 Deposit	105
5.3 Inhibitor.....	107
5.2.4 Experimental Procedure.....	109
5.4 Results and Discussion	111
5.4.1 K1 (Imidazoline) Performance Under Sand Deposit.....	111
5.4.2 K2 (Ammonium Chloride) Performance	114
5.4.3 K3 (Thiosulfate) Performance	117
5.4.4 K4 Performance	119
5.4.5 Al ₂ O ₃ Deposit.....	122
5.4.6 Inhibition Failure Mechanisms for Surfactant Corrosion Inhibitors on Silica Sand.....	126
5.4.7 Localized Corrosion.....	135
5.5 Summary	145
Chapter 6. Localized Corrosion of Mild Steel under Silica Sand Deposit in Inhibited Environments	148
6.1 Introduction.....	148
6.2 Experimental Method.....	149
6.2.1 Experiment Setup and Procedure.....	149
6.2.2 Deposit and Inhibitor	151
6.3 Results and Discussion	153

6.3.1 Establishment of a Galvanic Cell between Silica Sand Covered Electrode and Exposed Electrode	153
6.3.2 Location and Propagation of Localized Under Deposit Corrosion.....	164
6.4 Proposed Mechanisms of Localized Corrosion in Under Deposit Corrosion of Mild Steel.....	212
6.5 Summary	217
Chapter 7. Conclusions and Recommendations for Future Work	219
7.1 Conclusions.....	219
7.2 Recommendations for Future Work	220
References.....	222

LIST OF TABLES

	Pages
Table 4.1 Chemical composition of X65 mild steel (mass % balance is Fe).....	51
Table 4.2 Physical properties of solids used for under deposit corrosion experiments....	54
Table 4.3 Test conditions.....	58
Table 4.4 Test matrix for the experiments looking into the effect of deposit porosity....	58
Table 4.5 Test matrix for the experiments looking into the effect of deposit depth.....	59
Table 4.6 Test matrix for the experiments looking into the effect of temperature.	59
Table 4.7 Test matrix for the experiments looking into the effect of solution pH.	60
Table 5.1 Inhibitors used for present work.	108
Table 5.2 Experiment conditions.	111
Table 5.3 Summary of cases where pits were found.	145
Table 6.1 Experimental conditions.	150
Table 6.2 Inhibitors used in present work.....	153
Table 6.3 Chemical composition of C1018 mild steel (mass % balance is Fe).....	154

LIST OF FIGURES

	Page
Figure 4.1 Standard three-electrode glass cell setup.....	50
Figure 4.2 View of an API 5L X65 mild steel experiment specimen.....	51
Figure 4.3 API 5L X65 mild steel specimen holder: (A) base, with three gold contacts to connect the steel specimen and wire for electrochemical measurement; (B) steel sample holder, where steel specimen is installed; (C) sand holder, which can be filled up to hold a 2 mm thick sand deposit.....	53
Figure 4.4 SEM images of inorganic silica sand particles and SiO ₂ powder	55
Figure 4.5 LPR corrosion rate and corrosion potential over time at test conditions T = 25°C, 1 wt% NaCl soultion, pH = 5.0, 2 mm deposit.....	63
Figure 4.6 EIS Nyquist plots and Bode plots at test conditions 25°C, 1 wt% NaCl solution, pH = 5.0, 2 mm deposit, 20 hours exposure.	64
Figure 4.7 Potentiodynamic sweeps at test conditions 25°C, 1 wt% NaCl solution, pH = 5.0, 2 mm deposit, in the 24 th hour of exposure.....	67
Figure 4.8 SEM images of the steel surface exposed for 24 hours at conditions 25°C, 1 wt% NaCl solution, pH = 5.0, with 2 mm deposit.....	68
Figure 4.9 LPR corrosion rate and corrosion potential over time under sand deposit at test conditions T = 25°C, 1 wt% NaCl soultion, pH = 5.0, 2 mm deposit.	70
Figure 4.10 EIS Nyquist plots at test conditions 25°C, 1 wt% NaCl solution, pH = 5.0, 20 hours exposure, under sand deposit.	71

Figure 4.11 Potentiodynamic sweeps at test conditions 25°C, 1 wt% NaCl solution, pH 5.0, in the 24 th hours exposure, under sand deposit.	72
Figure 4.12 LPR corrosion rate and corrosion potential over time at test conditions 1 wt% NaCl soultion, pH = 5.0, under 5 mm SiO ₂ powder deposit at different temperatures. ...	74
Figure 4.13 SEM images of the steel surface exposed for 24 hours at conditions 1 wt% NaCl solution, pH 5.0, with 5 mm SiO ₂ deposit.....	75
Figure 4.14 LPR corrosion rate and corrosion potential over time at test conditions T = 25°C, 1 wt% NaCl soultion, with 10 mm sand deposit at different bulk solution pH.....	77
Figure 4.15 Surface pH probe design (Han, 2009).	79
Figure 4.16 SEM image of compressed mesh used for in the surface pH probe. (Han, 2009)	79
Figure 4.17 Surface pH measured at different temperature at conditions 1 wt% NaCl solution, pH 5.0, with 5 mm SiO ₂ powder deposit, 24 hours exposure.....	81
Figure 4.18 Surface pH measured at different temperature at conditions 1 wt% NaCl solutions, pH 5.0, with 5 mm sand deposit, 24 hours exposure.....	81
Figure 4.19 Surface pH measured at different temperature at conditions 1 wt% NaCl solution, pH 4.0, with 5 mm sand deposit, 24 hours exposure.	82
Figure 4.20 Surface pH measured at different temperature at conditions 1 wt% NaCl solution, pH 6.0, with 5 mm sand deposit, 24 hours exposure.	82
Figure 4.21 LPR corrosion rate and corrosion potential over time at test conditions T = 80°C, 1 wt% NaCl solution, pH = 4.0, 5 mm sand deposit.	84

Figure 4.22 EIS Nyquist plots at test conditions 80°C, 1 wt% NaCl solution, pH = 4.0, with 5 mm sand deposit, 5 days exposure.....	84
Figure 4.23 SEM images of the steel surface after 5 days exposure under 5mm silica sand deposit at 80°C, bulk solution pH 4.0, 1 wt% NaCl solution.	85
Figure 4.24 SEM image of mild steel after 5 days exposure in 1 wt% NaCl solution, pH 4.0 at 80 °C under 5 mm sand deposit (after surface scale removed)	86
Figure 4.25 An image of infinite focusing microscopy scanning of the steel surface after 5 days exposure in 1 wt% NaCl solution, pH 4.0, at 80°C under 5 mm sand deposit (after surface scale was removed)	87
Figure 4.26 LPR corrosion rate and corrosion potential over time at test conditions 80°C, 1 wt% NaCl, pH 5.0, 5 mm silica sand deposit.	90
Figure 4.27 EIS Nyquist plots at different exposure time at test conditions 80°C, 1 wt% NaCl solution, pH = 5.0, 5 mm silica sand deposit.	90
Figure 4.28 SEM image of steel surface after 10 days exposure at test conditions 80°C, 1 wt% NaCl solution, pH 5.0, 5 mm silica sand deposit.	91
Figure 4.29 Potentiodynamic sweeps of CO ₂ corrosion of bare X65 steel at pH 5, 25°C, 1 wt% NaCl solution, $p_{CO_2} = 0.96$ bar.	97
Figure 4.30 Potentiodynamic sweeps of CO ₂ corrosion of X65 steel under different deposit at bulk solution pH 5, 25 °C, 1 wt% NaCl, $p_{CO_2} = 0.96$ bar, 2 mm deposit.....	98
Figure 4.31 Potentiodynamic sweeps of CO ₂ corrosion of X65 steel under silica sand deposit with different depth at bulk solution pH 5, 25 °C, 1 wt% NaCl, $p_{CO_2} = 0.96$ bar, silica sand deposit porosity 39%/.....	99

Figure 4.32 Potentiodynamic sweeps of CO ₂ corrosion of X65 steel under 10 mm silica sand deposit at different temperature effect at bulk solution pH 5, 1 wt% NaCl, silica sand deposit porosity = 39%.....	100
Figure 4.33 Comparison of predicted experimental measured under deposit corrosion rate; at bulk solution pH 5, 25 °C, 1 wt% NaCl solution, $p_{CO_2} = 0.96$ bar, 2 mm deposit.	101
Figure 4.34 Comparison of predicted experimental measured corrosion rate under different depth of deposit; at bulk solution pH 5, 25 °C, 1 wt% NaCl, $p_{CO_2} = 0.96$ bar, silica sand deposit porosity = 39%. ..	102
Figure 4.35 Comparison of predicted and measured corrosion rate under 10 mm silica sand deposit at different temperature; at bulk solution pH 5, 1 wt% NaCl, silica sand deposit porosity = 39%. ..	102
Figure 5.1 SEM images of silica particles of different sizes.	106
Figure 5.2 LPR corrosion rate and corrosion potential over time at test conditions T = 25°C, 1 wt% NaCl, pH 5.0, 70 ppm K1 added on a bare steel surface.	112
Figure 5.3 LPR corrosion rate over time at test conditions T = 25°C, 1 wt% NaCl, pH 5.0, 2 mm sand deposit presented prior to 70 ppm K1 (imidazoline) addition.....	113
Figure 5.4 EIS Nyquist plots at 24 hours exposure at test conditions 25°C, 1 wt% NaCl, pH 5.0, 2 mm sand deposit presented prior to 70 ppm K1 (imidazoline) addition.....	114
Figure 5.5 LPR corrosion rate over time at test conditions T = 25°C, 1 wt% NaCl, pH 5.0, 220 ppm K2 (ammonium chloride) added on a bare steel surface.	115

Figure 5.6 LPR corrosion rate over time at test conditions T = 25°C, 1 wt% NaCl, pH 5.0, 2 mm sand deposit presented prior to 220 ppm K2 (ammonium chloride) addition.	116
.....	116
Figure 5.7 EIS Nyquist plots at 24 hours exposure at test conditions 25°C, 1 wt% NaCl, pH 5.0, 2 mm sand deposit presented prior to 220 ppm (ammonium chloride) K2 addition.	116
.....	116
Figure 5.8 LPR corrosion rate over time at test conditions T = 25°C, 1 wt% NaCl, pH 5.0, 30 ppm K3 (thiosulfate) added on a bare steel surface.	117
.....	117
Figure 5.9 LPR corrosion rate over time at test conditions T = 25°C, 1 wt% NaCl, pH 5.0, 2 mm sand deposit presented prior to 30 ppm K3 (thiosulfate) addition.	118
.....	118
Figure 5.10 EIS Nyquist plots at 25 hours exposure at test conditions 25°C, 1 wt% NaCl, pH 5.0, 2 mm sand deposit presented prior to 30 ppm K3 (thiosulfate) addition.	119
.....	119
Figure 5.11 LPR corrosion rate over time at test conditions T = 25°C, 1 wt% NaCl, pH 5.0, 430 ppm K4 (imidazoline + thiosulfate) added on a bare steel.	120
.....	120
Figure 5.12 LPR corrosion rate over time at test conditions T = 25°C, 1 wt% NaCl, pH 5.0, 2 mm deposit presented prior to 430 ppm K4 (imidazoline + thiosulfate) addition.	120
.....	120
Figure 5.13 EIS Nyquist plots at 25°C, 1 wt% NaCl, pH = 5.0, 2 mm send deposit presented prior to 430 ppm K4 (imidazoline + thiosulfate) addition.	121
.....	121
Figure 5.14 Comparison of the effect of sand deposit on different inhibitors at test conditions 25°C, 1 wt% NaCl solution, pH 5.0. 2 mm sand deposit present prior to inhibitor addition.	122
.....	122
Figure 5.15 SEM images of Al ₂ O ₃ particle and silica sand particle.	124

Figure 5.16 LPR corrosion rate over time at test conditions T = 25°C, 1 wt% NaCl solution, pH 5.0, 2 mm Al ₂ O ₃ deposit presented prior to 70 ppm K1 (imidazoline) addition.....	125
Figure 5.17 EIS Nyquist plots at 25°C, 1 wt% NaCl, pH = 5.0, 2 mm Al ₂ O ₃ deposit presented prior to 70 ppm K1 (imidazoline) addition.....	125
Figure 5.18 LPR corrosion rate over time at test conditions 25°C, 1 wt% NaCl solution, pH 5.0, under various amount of sand deposit which was present prior to 70 ppm K1 (imidazoline) addition.....	127
Figure 5.19 LPR corrosion rate over time at test conditions 1 wt% NaCl solution, pH 5 and 25°C, under different pre-treated silica sand deposits. Deposit present prior to 70 ppm K1 (imidazoline) addition.....	129
Figure 5.20 Comparison of general LPR corrosion rate under different pre-treated sand deposits at test condition 1 wt% NaCl solution, pH 5 and 25°C.	129
Figure 5.21 LPR corrosion rate over time at conditions 1 wt% NaCl solution, pH 5.0, 25°C at two different sizes of sand particles.....	131
Figure 5.22 LPR corrosion rate at test conditions 1 wt% NaCl solution, pH 5.0, 80°C. 2 mm sand deposit present prior to 70 ppm K1 (imidazoline) addition.	132
Figure 5.23 LPR corrosion rate over time at test conditions 1 wt% NaCl solution, bulk pH 5.0, 25°C, 2 mm sand deposit present prior to 1800 ppm K1 (imidazoline) addition.	133
Figure 5.24 LPR corrosion rate over time at test conditions 25°C, 1 wt% NaCl solution, pH 5, sand deposit present prior to 70 ppm K1 (imidazoline) addition.....	134

Figure 5.25 Comparison of stable corrosion rate after 70 ppm of K1 inhibitor added after different amount of sand deposit, at test conditions: 25°C, pH 5, 1 wt% NaCl solutions.

..... 135

Figure 5.26 SEM of steel surface after 5 days exposure at test conditions 25°C, 1 wt% NaCl solution, pH 5.0, 1 layer sand deposit present prior to 70 ppm K1 (imidazoline) addition, corrosion product removed. 136

Figure 5.27 A image from infinite focusing microscopy scanning of pits on steel surface after 5 days exposure, at test conditions 25°C, 1 wt% NaCl solution, pH 5.0, 1 layer sand deposit present prior to 70 ppm K1 (imidazoline) addition. 137

Figure 5.28 LPR corrosion rate over time at test conditions 25°C, 1 wt% NaCl solution, pH 5.0, steel surface is partially covered by sand particles. 138

Figure 5.29 SEM of steel surface after 144 hours exposure at test conditions 25°C, 1 wt% NaCl solution, pH 5.0, steel surface is partially covered by sand particles, corrosion product removed. 139

Figure 5.30 Infinite focusing microscopy scanning of steel surface after 144 hours exposure at test conditions 25°C, 1 wt% NaCl solution, pH 5.0, steel surface is partially covered by sand particles and corrosion product removed. 140

Figure 5.31 SEM image of the steel surface after 160 hours exposure at test conditions 25°C, 1 wt% NaCl solution, 5.0, 2 mm sand deposit present after 70 ppm K1 addition.

..... 141

Figure 5.32 IFM scanning of the steel surface after 160 hours exposure at conditions 25°C, 1 wt% NaCl solution, pH 5.0, 2 mm sand deposit present after 70 ppm K1 addition.

142

Figure 5.33 LPR corrosion rate over time at test conditions 25°C, 1 wt% NaCl solution, pH 5.0, 2 mm sand deposit present after 70 ppm K1 addition..... 143

Figure 6.1 Deposit used for localized corrosion experiments: silica sand particles (750 µm), silica crystals (5 mm). 152

Figure 6.2 Galvanic-couple working electrode. The surface area ratio of the surrounding ring electrode to the central disc electrode is 60:1..... 155

Figure 6.3 LPR corrosion rate (uncoupled) over time at test conditions 25°C, 1 wt% NaCl, pH 5.0. 2 mm sand deposit present only on the central small electrode S1 prior to 70 ppm K1 addition. 158

Figure 6.4 Corrosion potential vs. Ag/AgCl reference electrode (uncoupled) over time at test conditions 25°C, 1 wt% NaCl, pH 5.0. 2 mm sand deposit present only on the central small electrode S1 prior to 70 ppm K1 addition. 159

Figure 6.5 LPR corrosion potential (uncoupled) difference between the two electrodes over time at test conditions 25°C, 1 wt% NaCl, pH 5.0. 2 mm sand deposit present only on the central small electrode S1 prior to 70 ppm K1 addition. 160

Figure 6.6 Galvanic current between the two electrodes coupled together over time at test conditions 25°C, 1 wt% NaCl, pH 5.0. A 2 mm sand deposit is present only on the central small electrode, S1, prior to 70 ppm K1 addition. 161

Figure 6.7 Galvanic effect on corrosion rate at test conditions 25°C, 1 wt% NaCl, pH 5.0. 2 mm sand deposit present only on the central small electrode S1 prior to 70 ppm K1 addition.	163
Figure 6.8 API 5L X65 mild steel specimen holder: (A) base, with three gold contacts to connect the steel specimen and wire for electrochemical measurement; (B) steel sample holder, where steel specimen is installed; (C) sand holder, fill up to 2 mm sand deposit.	165
Figure 6.9 LPR corrosion rate over time at test conditions 25°C, pH 5, 1 wt% NaCl solution saturated with CO ₂ . About 40 grains of sand particles present prior to 70 ppm K1 addition.	166
Figure 6.10 View of the steel surface showing a lot of pits after 40 days exposure at conditions 25°C, pH 5, 1 wt% NaCl solution saturated with CO ₂	168
Figure 6.11 SEM and EDS images of the steel surface with corrosion product layers after 40 days exposure at conditions 25°C, pH 5, 1 wt% NaCl solution saturated with CO ₂ . 169	169
Figure 6.12 Prolifometer image of one of the pits found on the steel surface after 40 days exposure at conditions 25°C, pH 5, 1 wt% NaCl solution saturated with CO ₂	170
Figure 6.13 Comparison of pitting rate and surface averaged corrosion rate obtained from LPR after 40 days exposure at conditions 25°C, pH 5, 1 wt% NaCl solution saturated with CO ₂	171
Figure 6.14 View of one big crystal sitting on the steel surface at test conditions 25°C, pH 5, 1 wt% NaCl solution saturated with CO ₂	172

Figure 6.15 View of the steel surface after 9 days exposure at test conditions 25°C, pH 5, 1 wt% NaCl solution saturated with CO ₂	173
Figure 6.16 SEM and EDX images of the steel surface with corrosion product layers after 9 days exposure at test conditions 25°C, pH 5, 1 wt% NaCl solution saturated with CO ₂	175
Figure 6.17 Infinite focusing microscopy Image of the steel surface after 9 days exposure and corrosion product layer removed at test conditions: 25°C, pH 5, 1 wt% NaCl solution saturated with CO ₂	176
Figure 6.18 Comparison of the pitting rate and surface averaged corrosion rate obtained from weight loss after 9 days exposure at test conditions 25°C, pH 5, 1 wt% NaCl solution saturated with CO ₂	177
Figure 6.19 View of the experiment sample #1 after 25 days exposure with corrosion product layers and without corrosion product layers at test conditions 25°C, pH 5, 1 wt% NaCl solution saturated with CO ₂	179
Figure 6.20 SEM and EDS images of the experiment sample #1 with corrosion product layers after 25 days exposure at test conditions 25°C, pH 5, 1 wt% NaCl solution saturated with CO ₂	180
Figure 6.21 An infinite focusing microscopy image of one of the pits found on the steel surface after 25 days exposure at test conditions 25°C, pH 5, 1 wt% NaCl solution saturated with CO ₂	181

Figure 6.22 Comparison of pitting rate and surface averaged corrosion rate obtained from weight loss method at test conditions 25°C, pH 5, 1 wt% NaCl solution saturated with CO ₂	181
Figure 6.23 Fe ²⁺ concentration vs. time at test conditions 25°C, pH 5, 1 wt% NaCl solution saturated with CO ₂	182
Figure 6.24 Views of the experiment sample #2 after 34 days exposure with corrosion product layers (left) and without corrosion product layers (right) at test conditions 25°C, pH 5, 1 wt% NaCl solution saturated with CO ₂	183
Figure 6.25. SEM and EDS images Pictures of the experiment sample #2 after 34 days exposure with corrosion product layers at test conditions 25°C, pH 5, 1 wt% NaCl solution saturated with CO ₂	184
Figure 6.26 An infinite focusing microscopy image one of the pits found on the steel sample #2 surface after 34 days exposure at test conditions 25°C, pH 5, 1 wt% NaCl solution saturated with CO ₂	185
Figure 6.27 Comparison of pitting rate and surface averaged corrosion rate obtained from weight loss method after 34 days exposure at test conditions 25°C, pH 5, 1 wt% NaCl solution saturated with CO ₂	185
Figure 6.28 Comparison of the pit depth of sample #1 and #2. Test conditions are as described in 6.23, except that for sample #2 it corroded 9 more days with sand particles removed.....	186
Figure 6.29 Views of the experiment sample #1 after 17 days exposure at test conditions 25°C, pH 5, 1 wt% NaCl solution saturated with CO ₂	188

Figure 6.30 SEM images of the experiment sample #1 with corrosion product layers after 17 days exposure at test conditions 25°C, pH 5, 1 wt% NaCl solution saturated with CO₂.

189

Figure 6.31 Infinite focusing microscopy images of the steel surface after corrosion product layer was removed at test conditions 25°C, pH 5, 1 wt% NaCl solution saturated with CO₂..... 190

Figure 6.32 Comparison of pitting rate and surface averaged corrosion rate obtained from weight loss method at test conditions 25°C, pH 5, 1 wt% NaCl solution saturated with CO₂..... 190

Figure 6.33 Fe²⁺ concentration variation over time at test conditions 25°C, pH 5, 1 wt% NaCl solution saturated with CO₂..... 191

Figure 6.34 Views of the experiment sample #2 after 26 days exposure. For this sample, the first 17 days, it was under exactly the same condition as sample #1 as described in Figure 29, but the last 9 days, the sand particles were removed from the steel surface. 192

Figure 6.35 SEM images of the experiment sample #2 with corrosion product layers at test conditions 25°C, pH 5, 1 wt% NaCl solution saturated with CO₂ 193

Figure 6.36 Profilometer Image of the steel surface of sample #2 after corrosion product layer was removed at test conditions 25°C, pH 5, 1 wt% NaCl solution saturated with CO₂..... 194

Figure 6.37 Comparison of pitting rate and surface averaged corrosion rate obtained from weight loss method at test conditions 25°C, pH 5, 1 wt% NaCl solution saturated with CO₂..... 195

Figure 6.38 Comparison of the pit depth of sample #1 and #2 at test conditions 25°C, pH 5, 1 wt% NaCl solution saturated with CO ₂	196
Figure 6.39 Comparison of pitting rate with bare steel corrosion rate and surface averaged corrosion rate from LPR/WL at test conditions 25°C, pH 5, 1 wt% NaCl solution saturated with CO ₂	197
Figure 6.40 Change of pitting depth after silica sand or silica crystal was removed from the steel surface for experiments conducted at 25°C, pH 5, in a 1 wt% NaCl solution saturated with CO ₂	198
Figure 6.41 View of the experiment specimen after 14 days exposure at test conditions: 25°C, pH 5, 1 wt% NaCl solution saturated with CO ₂	199
Figure 6.42 SEM and EDX images of the experiment sample #1 with corrosion product layers. Test conditions: 25°C, pH 5, 1 wt% NaCl solution saturated with CO ₂	200
Figure 6.43 A infinite focusing microscopy image of the experiment sample #1 without corrosion product layers. Test conditions: 25°C, pH 5, 1 wt% NaCl solution saturated with CO ₂	201
Figure 6.44 View of the experiment specimen after 14 days exposure at test conditions: 25°C, pH 5, 1 wt% NaCl solution saturated with CO ₂	202
Figure 6.45 SEM and EDS images of the experiment sample #2 with corrosion product layers. Test conditions: 25°C, pH 5, 1 wt% NaCl solution saturated with CO ₂	203
Figure 6.46 A infinite focusing microscopy image of the experiment sample #2 without corrosion product layers. Test conditions: 25°C, pH 5, 1 wt% NaCl solution saturated with CO ₂	204

Figure 6.47 Comparison of the maximum corrosion rate from IFM scanning with surface averaged corrosion rate obtained from weight loss method. Test conditions: 25°C, pH 5, 1 wt% NaCl solution saturated with CO ₂	204
Figure 6.48 Comparison of pitting rate in two scenarios. Test conditions are 25°C, pH 5, in 1 wt% NaCl solution saturated with CO ₂	205
Figure 6.49 View of the experiment specimen #1 after 14 days exposure at test condition: 25°C, pH 5, 1 wt% NaCl solution saturated with CO ₂	207
Figure 6.50 SEM images of the experiment sample #1 with corrosion product layers at test condition: 25°C, pH 5, 1 wt% NaCl solution saturated with CO ₂	208
Figure 6.51 A infinite focusing microscopy image of experiment sample #1after 14 days exposure at test condition: 25°C, pH 5, 1 wt% NaCl solution saturated with CO ₂	209
Figure 6.52 View of the experiment specimen #2 after 14 days exposure at test condition: 25°C, pH 5, 1 wt% NaCl solution saturated with CO ₂	210
Figure 6.53 SEM images of the experiment sample #1 with corrosion product layers after 14 days exposure at test condition: 25°C, pH 5, 1 wt% NaCl solution saturated with CO ₂	210
Figure 6.54 A infinite focusing microscopy image of experiment sample #1after 14 days exposure at test condition: 25°C, pH 5, 1 wt% NaCl solution saturated with CO ₂	211
Figure 6.55 Comparison of the pitting rate found in the cases with inhibitor K1 (imidazoline) with the maximum corrosion rate found in the cases with inhibitor K3 (thiosulfate) at same test conditions, i.e., 25°C, pH 5, 1 wt% NaCl solutions saturated with CO ₂	212

Figure 6.56 Description of the appearance of localized corrosion in under deposit corrosion in inhibited environment	213
Figure 6.57 Description of the corrosion process in under deposit corrosion in inhibitor-free environment. (Sketches are not drawn to scale)	214
Figure 6.58 Description of the mechanism of localized corrosion in under deposit corrosion in inhibited environment. (Sketches are not drawn to scale)	215

CHAPTER 1. INTRODUCTION

Corrosion is a process in which a metallic material gradually degrades by interaction with the environment. Acidic gases such as CO₂, H₂S are often produced along with oil, natural gas and water from geological formations. When they are dissolved in water, they can be corrosive and pose a significant threat to the integrity of mild steel for oil and gas production and transportation facilities. Corrosion can result in shut down of production, failure or even lead to catastrophic disaster. In a widely-cited study by the National Association of Corrosion Engineers (NACE) the total direct cost of corrosion in the U.S. was estimated to equal \$276 Billion in 1998, approximately 3.1 % of gross domestic product (Koch, 2002). Recent NACE data indicate that corrosion costs in the U.S. now exceed \$1 trillion dollars (Jackson, 2011).

In the oil and gas industry, water is produced and transported with oil and gas from the reservoir to production facilities. Carbon dioxide dissolves in the produced water, which can lead to significant internal corrosion of mild steel. Different strategies have been developed to withstand corrosion for oil and gas production and transportation lines, such as using corrosion resistance alloys (CRAs) or adding corrosion inhibitors. However, for thousands of miles of pipelines, mild steel is still the most cost effective choice.

CO₂ corrosion of mild steel has been extensively studied in the past few decades (e.g. de Waard, 1975, 1993; Schmitt, 1978(a), 1978(b); Bonis, 1989; Nešić, 1996; Dugstad, 2006). The uniform CO₂ corrosion mechanisms have been well understood and key factors affecting CO₂ corrosion such as pH, temperature and flow have been

evaluated. However, little has been understood regarding localized corrosion which is more likely than uniform corrosion to cause catastrophic failures and consequences (Abduh, 2008).

One of the threats that may cause localized corrosion is due to deposited solids. Under deposit corrosion is therefore defined as accelerated corrosion that develops beneath or around deposits present on a metal surface (Johns, 1995). Different types of solids can be found in oil and gas production, transportation and processing facilities like silica sand, elemental sulfur, hydroscopic salts and clay, asphaltenes, wax as well as corrosion product such as iron carbonate and iron sulfide (de Reus, 2005; Papavinasam, 2007).

Silica sand is a big challenge for operation in the oil and gas industry. It may cause erosion corrosion in upstream operations and damage the facilities (Shadley, 1998). It can clog the pipelines if it settles on the bottom (Shadley, 1996; Papavinasam, 2007). The existence of sand has also been frequently cited as responsible for poor corrosion inhibitor performance (Marsh, 2002). A great deal of research effort has been made to investigate the performance of specific corrosion inhibitors in the presence of solid deposit in aqueous CO₂ environment at different processes or conditions (de Reus, 2002; Durnie, 2005; Pedersen, 2008; Turnbull, 2009; Place, 2009; Huang, 2010). However, in only few cases have the mechanisms of under deposit corrosion been discussed (de Reus, 2002; Pedersen, 2008; Huang, 2010). In most of the inhibitor evaluation work done at under deposit conditions, the inhibitors were formulated with more than one active component, and the characteristics and interactions between components were not clear.

Typically the information about the commercial corrosion inhibitor composition was also not available. In addition to the chemical complexity associated with the composition of various corrosion inhibitors, the composition of solids found in pipelines also varies. To simplify the situation, while targeting the under deposit corrosion process, the very common and inert silica sand was chosen for the under deposit corrosion research presented in this dissertation.

The present project started with work done without corrosion inhibitors in order to get an understanding of the effect of silica sand deposits on the CO₂ corrosion process. The effect of environmental factors including pH, temperature, deposit size, and porosity on under deposit CO₂ corrosion was evaluated. A mechanistic model was developed to predict the corrosion rate under inert solid deposits. Corrosion inhibitors with known chemical composition were then added to the study of under deposit systems. Both uniform corrosion and localized corrosion at various sand deposition and corrosion inhibition conditions were studied.

The work presented in this dissertation was a part of the CO₂ corrosion research program conducted within the Institute for Corrosion and Multiphase Technology at Ohio University and has been archived as part of the internal confidential reports to the Corrosion Center Joint Industry Project (CCJIP) Advisory Board Meetings over the period 2008 – 2012. Portions of the work presented in this dissertation have also been published or will be published at NACE (National Association of Corrosion Engineers) International conferences (Huang, 2010, 2011, 2013 and 2014).

CHAPTER 2. LITERATURE REVIEW

A literature review of the issues as they relate to the main topic of this dissertation has been conducted and will be presented below. It covers three main areas: carbon dioxide corrosion, corrosion inhibitor and under deposit corrosion.

2.1 Carbon Dioxide Corrosion

2.1.1 Carbon Dioxide Corrosion Mechanisms

Internal aqueous carbon dioxide corrosion environment is the most common type encountered in the production and transportation processes in oil and gas industry. It is commonly called “sweet” corrosion, so as to be differentiated from “sour” corrosion which is related to environment containing H₂S which is not discussed in this dissertation. The chemical and electrochemical reactions as well as species transport involved in corrosion processes are highly interdependent. Understanding their interplay has been crucial for the development of mechanistic models for CO₂ corrosion of mild steel.

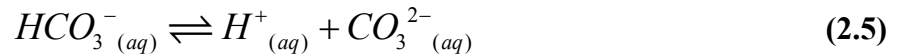
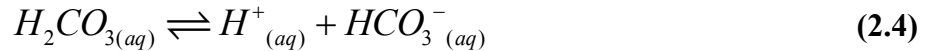
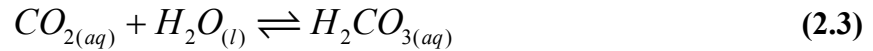
A great deal of research has been made to understand the CO₂ corrosion process in the past few decades (de Waard, 1975, 1993; Bonis, 1989; Nešić, 1996; Dugstad, 2006, Schmitt, 2006). The overall corrosion reaction can be written as:



Three major species, H⁺, H₂CO₃ and HCO₃⁻ can undergo cathodic reduction reactions on the steel surface and balance the oxidative iron dissolution. The corrosion of mild steel in aqueous CO₂ solution without protective corrosion product formation involves several processes: formation of reactant species, transportation of reactants from bulk solution to

the steel surface, electrochemical reactions at the steel surface, and transportation of products from steel surface to bulk solution.

The main chemical processes in CO₂ corrosion include CO₂ gas dissolving in water, forming carbonic acid, as shown in reactions (2.2) – (2.3). Carbonic acid (H₂CO₃) is a weak acid, which dissociates in two steps (reactions (2.4) and (2.5)):

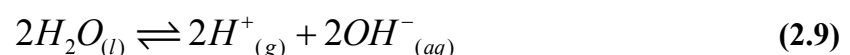


The electrochemical reactions occur on the steel surface and include an anodic reaction and cathodic reactions. Iron is oxidized to form ferrous iron and releases two electrons.



It has been widely agreed that the iron dissolution process occurs in multiple steps and the process involves intermediate species (Bockris, 1961).

For the cathodic part, proton reduction, direct carbonic acid reduction as well as water reduction has commonly been accepted as the main reactions (Nešić, 1996).



In an aqueous CO₂ environment, when the pH of the solution is less than 4, proton reduction (2.7) is dominant. Direct reduction of carbonic acid (Reaction 2.8) becomes significant and plays an important role in determining the corrosion rate when solution pH is in the range of 4 < pH < 6 (Schmitt, 1978(b); Hurlen, 1984; Nešić, 1996). The direct reduction of carbonic acid explains the observation of higher corrosion rates of mild steel in aqueous CO₂ solution than in strong acid solution under the same pH value (Nešić, 1996). Water reduction (reaction 2.9) also needs to be considered for corrosion rate prediction at higher pH and lower concentrations of aqueous CO₂.

2.1.2 Key Factors Affecting Aqueous CO₂ Corrosion of Mild Steel

The mechanisms of CO₂ corrosion of mild steel are determined by the chemical reactions in the bulk solution, electrochemical reactions occurring on the steel surface as well as the transportation of corrosive species involved in all the reactions between the bulk solution and the steel surface. Those reactions and processes all interact with each other and can be affected by many factors.

2.1.1.1 Effect of Water Chemistry

The main species that are involved in water chemistry analysis of an aqueous CO₂ corrosion system include hydrogen ion H⁺, carbonic acid H₂CO₃, bicarbonate ion HCO₃⁻, carbonate ion CO₃²⁻ and ferrous iron Fe²⁺. The change of water chemistry could affect the corrosion process significantly. Concentration of H⁺ in terms of pH has significant direct effects on the corrosion kinetics in CO₂ corrosion. Low pH, i.e., the increased amount of protons “consumes” more electrons leading to higher corrosion rate as can be seen from reaction (2.7), Higher pH of the solution helps the formation of iron carbonate, which

would change the corrosion mechanisms significantly (de Waard, 1975(a); Videm, 1989(a); Nešić, 1996; Schmitt, 2006). The pH of the bulk solution can usually be measured and monitored; however, the electrochemical reactions (2.6 – 2.9) occur at the steel surface, where pH is often not easily measured. It has been shown that when the steel surface is covered by a protective layer, the surface pH is 1 or 2 units higher than the bulk solution pH (Han, 2009; Huang, 2010; Tanupabrungsun, 2012).

The precipitation of iron carbonate according to the reaction written below also has a significant effect on the corrosion process. The tendency of iron carbonate scaling is largely dependent of the water chemistry of the solution and the temperature (Sun, 2006; Nešić, 2007).



2.1.1.2 Effect of partial pressure of CO₂

According to reaction (2.2 –2.4), the higher the partial pressure of CO₂, the faster the carbonic acid formation will be which will result in a higher concentration of H₂CO₃ in the solution. Therefore, more hydrogen from H₂CO₃ reduction can be produced, and a higher corrosion rate is expected.

2.1.1.3 Effect of Temperature

All the chemical, electrochemical reactions as well as transport processes involved in CO₂ corrosion will be accelerated at higher temperature. Higher corrosion rate is expected when the temperature is elevated. However, this is only true when no protective layer is present on the steel surface. When precipitation of ferrous carbonate occurs, corrosion rate does not necessarily increase with increasing temperature anymore

(Tanupabrungsun, 2012). Higher temperature also accelerates ferrous carbonate formation, which will change the corrosion mechanisms and kinetics (Gray, 1990; Tanupabrungsun, 2013).

2.1.1.4 Effect of Flow

As mentioned earlier, the corrosion process is an interplay of chemical and electrochemical reactions as well as transportation of species to and from the metal surface. Flow can enhance mass transport process of the corrosive species to and from the steel surface, where electrochemical reactions are occurring; therefore a higher corrosion rate can be expected. Experimental observations have confirmed that enhanced flow conditions lead to increased corrosion rate when there is no corrosion product layer formed (Schmitt, 1983). However, if a protective corrosion product layer was present, the corrosion rate was found not to be sensitive to flow rate (Nešić, 2003). A great deal of research has been conducted to study if flow could remove or destroy protective corrosion product layers or inhibitor films, no consensus has yet been achieved (Canto, 2011; Yang, 2010). Corrosion process is affected not only by flow rate but more related to flow pattern and oil-water wetting regime in real scenarios (Li, 2009). Flow can be an important factor for erosion-corrosion when the flow rate is high (Shadley, 1998). If flow rate is low, entrained solids may deposit at the bottom of pipelines (Smart, 2009), causing under deposit corrosion problem, which is the topic of this work.

2.2 Corrosion Inhibitors

Although corrosion resistance alloys can be very successful in managing corrosion, mild steel is still the most economically effective material for construction of

pipelines, wells and processing equipment in the oil and gas industry. However, mild steel has poor resistance to corrosion. Therefore, how to control corrosion and mitigate its threat to the integrity of mild steel becomes essential for oil and gas production. One of the most common strategies in oilfield is the use of corrosion inhibitors. According to National Association of Corrosion Engineers (NACE), corrosion inhibitor is “a substance which retards corrosion when added to an environment in small concentrations”. Intensive studies of corrosion inhibitors’ protection mechanisms and their applications to combat corrosion have been conducted for the past twenty years (Hackerman, 1984; Armstrong, 1994; Achour, M, 2008; Paria, 2004). Corrosion inhibitors can be classified into groups of passivating (anodic) or cathodic according to their chemical functionality (Mercer, 1994). Passivating inhibitors retards anodic reaction, i.e., metal oxidation by shifting the corrosion potential to be more positive. Cathodic inhibitors, as indicated by their name, slow down the cathodic reactions. It has been proposed that cathodic inhibitor provide protection to a steel surface by either poisoning the cathodic reaction or by precipitating on the sites where cathodic reactions take place (Thomas, 1994, Atkin, 2003). The most often used corrosion inhibitors are organic inhibitors (Soror, 2003; Paria, 2004). They are surface active chemicals that can be adsorbed on steel surface forming a protective film of adsorbed molecules. Both anodic and cathodic reactions are believed to be retarded by organic inhibitors (Zhang, 2001; Osman, 2003; Popova, 2004; Moretti, 2004). The degree of protection from those inhibitors relies on how much the chemicals can be adsorbed on the steel surface. Organic inhibitors can also be classified as cationic inhibitors or anionic inhibitors depending on the ionic charge of the inhibitor

molecules (Mercer, 1994). Metal surface is usually negatively charged in a solution of pH4-6, and cationic inhibitors such as imidazoline and amines are therefore often used in corrosion inhibitor formulations (Zhang, 2001; Ismail, 2010).

Inhibitors can interact with steels in many ways, especially the commercially used corrosion inhibitors which often are formulated with multiple function groups. Therefore multiple mechanisms instead of single inhibition mechanism should be considered when corrosion inhibitors are evaluated. Ideally, the injected corrosion inhibitor should be able to diffuse through water and reach the steel surface. But this inhibition process can be affected by many factors. The presence of surfaces other than the pipeline metal surface will affect the efficiency of corrosion inhibitor, because the surface active compound may not differentiate between different surfaces and can adsorb on whatever surface they “meet”.

Those unintended target surfaces can be provided by settled sand, corrosion products such as iron carbonate, iron sulfide or barium sulfate, calcium carbonate precipitated during oil and gas production etc. (de Reus, 2002; Horsup, 2007). Diffusion of inhibitors to and from the steel surface is also dependent on flow conditions (Kang, 2008, Miksic, 2009). If flow rate is low, solids can accumulate and deposit at the bottom of pipelines inducing under deposit corrosion (Salama, 2000).

2.3 Under Deposit Corrosion

Under deposit corrosion is defined as localized corrosion that occurs underneath or around deposits present on a steel surface (Johnson 1995, Vera, 2012), and accelerated corrosion can be found under solid deposits on the bottom of horizontal lines (Espan,

2001). Under deposit corrosion has been more frequently cited as being responsible for different failures within the oil and gas industries over the past few years (Morita, 1994; Salama, 2000; de Reus, 2005). National Association of Corrosion Engineers (NACE) has established a technical committee to serve as an information exchange between technologists and corrosion specialists with regard to under deposit corrosion. (Vera, 2012) Other names such as “under-deposit” and “underdeposit” have also been used by different researchers in their publications (Place, 2009; Lepkova, 2010).

Severe corrosion problems such as crevice formation and pitting can be induced by solid deposits in pipelines because they provide a local environment which is chemically and physically different from the areas not covered by a deposit (Cotton, 2001; Li, 2005). Deposition of solids helps prevent corrosive products from being removed by flow and limits corrosion inhibitors from accessing the metal surface. In the oil and gas industry, the deposit composition can be very complicated which leads to a very complex water chemistry underneath those deposits for corrosion analysis. CO₂, H₂S, O₂, and often microbiological influenced corrosion mechanisms can be contributing to cause analyses of failures in the oil and gas industry (Shim, 1988; Sooknah, 2007). Consensus has not yet been established on whether under deposit corrosion is a true “stand-alone” corrosion mechanism (Vera, 2012). In this section, the development of under deposit corrosion study will be reviewed, under deposit corrosion testing methods will be evaluated and proposed mechanisms will be discussed.

2.3.1 Deposits

Deposits encountered in the oil and gas industry can be categorized as inorganic deposits and organic deposits. The most prevalent inorganic deposit is sand in the form of silica, SiO_2 (Abass, 2002). Silica sand is produced from the geological formation and is transported with oil and gas along the pipelines. Most petroleum pipelines have a volumetric concentration of sands ranging from 1% -40% (Zhu, 2010). Inorganic deposits also include corrosion products such as iron carbonate, iron sulfides and iron oxides etc., which arrive from corrosion processes and their effects on corrosion have been intensively investigated (Johnson, 1991; Chokshi, 2005; Crolet, 1998; Foss, 2008). Other scales precipitated from water such as calcium carbonate and barium sulfate are sometimes cited as important factors that interfere with corrosion and threaten the integrity of pipelines (Oddo, 1998).

Typical examples of organic deposits include asphaltene and wax which exist in crude oil in nature. Those organic components of crude oil typically contain oxygen, sulfur and nitrogen heteroatoms. They are surface active and have been identified to be able to inhibit corrosion of mild steel (Kibala, 1999; Yen, 2011).

Biofilm is another example of organic deposits that can be found in petroleum pipelines. Microbiological influenced corrosion threats are usually combined with under deposit corrosion in root cause analysis of failures (Gu, 2009).

Generally, the deposits found in the field are a combination of different organic and inorganic deposits. In this dissertation, only the effect of inorganic solid silica sand

on CO₂ corrosion of mild steel and its role in inducing localized corrosion will be discussed.

2.3.2 Under Deposit Corrosion Testing Methods

A variety of testing methods and techniques have been reported for under deposit corrosion study and evaluation in the past decades. Different aspects of the phenomena in under deposit corrosion have been investigated and assessed.

In the work presented by de Reus, et al. (2005), a protocol to test inhibitor performance under sand deposit using an autoclave setup was developed. A flat specimen was designed to be capped with a raised edge, which can then be filled with solids. The inhibitor performance in areas covered by solid deposits and in exposed areas was studied. The specimen design and assembling enabled electrochemical measurement in the autoclave with a standard 3-finger probe configuration. A “corrosivity toolbox” was also proposed for field verification based on the autoclave testing setup described in this paper.

Pedersen et al. (2008) conducted experiments in a glass cell setup to study the performance of two different types of corrosion inhibitors under sand deposit. A sand covered specimen and one without sand covering was coupled and galvanic corrosion between the coupled specimens was studied using zero resistance ammeter (ZRA). With specially designed specimen holder and lid, the under deposit corrosion experiments can be performed easily in the standard glass cell system, therefore electrochemical techniques can be used to understand the mechanisms of under deposit corrosion.

In the work presented by Turnbull et al. (2009) an approach to evaluate inhibitors under deposit using a multi-electrode array was demonstrated. The multi-electrode array was made of 24 carbon steel electrodes encased in epoxy. During their experiments, the multi-electrode array was mounted in a polyetheretherketone (PEEK) holder where sand deposit can be placed. The multi-electrode array was then galvanically coupled to an external electrode made of the same material and the galvanic corrosion current between the external electrode and each of the electrodes in the array was monitored. The multi electrode array was used in a glass cell system, but could also be easily implemented in autoclaves. The multi-electrode array method developed in this work enables simultaneous assessment of the effect of pre-corrosion on under deposit corrosion, as described by the authors, however, some of the individual electrode in the array showed controversial corrosion behavior which was not discussed by the authors in the paper.

Han (2009) designed an artificial pit to study the propagation of localized corrosion under iron carbonate and sand deposit conditions. The artificial pit was designed where an anode and cathode with a surface area ratio of 1:1000 was separated in the solution while maintaining contact of the substrate metal. The artificial pit method can be powerful in study the propagation of a localized corrosion due to partially damaged corrosion products, such as iron carbonate and iron sulfides. The artificial pit technique also enables direct in situ measurements of the galvanic current developed in a galvanic cell.

In the current research an experimental setup similar to the one proposed by Pedersen et al. (2008) was adopted and developed.

2.3.3 Under Deposit Corrosion Mechanisms

For the past few years, more and more research has been conducted on the under deposit corrosion. However, most of the work done was focused on inhibitor performance evaluation and assessment in conditions when solids settle. Little work has been done to uncover a mechanism to explain the under deposit corrosion process. It has often been postulated that the under deposit corrosion problem is caused by insufficient penetration of corrosion inhibitor to the steel surface, due to parasitic consumption of corrosion inhibitor on the surface of the solid deposits and that the diffusion of the inhibitor is retarded by the solid deposit barriers. The conclusion was often made based on observations from inhibitor performance experiments (Hinds, 2010; Horsup, 2007; Marsh, 2002; Scamehorn, 1982; Tan, 1996). However, what needs to be pointed out is that most of the screening tests for corrosion inhibitor selections were performed using commercial inhibitor formulations which usually contain multiple effective components (such as imidazoline, amine and sulfur compounds). In that case it was not easy to clearly interpret the mechanisms of interaction between those inhibitor formulations and the solids deposits.

Horsup et al. (2007) did a series of experiments to study the adsorption of the alkyl BDMAC (-benzyldimethylammonium chloride) series of corrosion inhibitor on solid deposit using both a syringe technique and a centrifuge method. Their results showed that the corrosion inhibitor had the strongest affinity for both silica sand and iron sulfide, with uptake of 95% and 93% respectively. The authors also indicated that the adsorption potential was dependent upon the nature of the surface and the surface area

available to the inhibitor molecule. The understanding of interactions between the inhibitor's hydrophobic tail groups and their interaction with solid surfaces was also believed to be very important in determining how much of the inhibitor would be lost by unintended adsorption.

Durnie et al. (2005) evaluated the penetration ability of the active components of several corrosion inhibitors instead of formulated products of corrosion inhibitors, which usually contain more than one effective active component. Quaternary amines, imidazoline as well as sulfur containing organic molecule were examined. Adsorption experiments were conducted on each of the active corrosion inhibitor components. It was found that the quaternary amine and sulfur compound penetrate the sand column faster than imidazoline. It was also suggested by the authors that imidazoline and amine shared similar adsorption mechanisms, while the adsorption of sulfur compound on sand was different. Even if the fast penetrating compound (e. g. sulfur containing molecules) showed better corrosion inhibition performance in the corrosion experiments, the authors believed that the ultimate inhibition performance did not depend solely on the penetration rate, but on the extent of adsorption of active components on the metal surface, which was determined by the steady state equilibrium of the active components in the aqueous phase, the hydrocarbon phase, on the solids surface and the metal surface.

In a related work published by the same group of authors (de Reus et al. (2005)), efforts were made to address the mechanism of localized corrosion induced by solid deposit. The possibility of galvanically induced localized corrosion was studied in this work. Galvanic effect was found in an inhibited condition, but only with small amount of

inhibitor (50 ppm). No galvanic effect was observed when the inhibitor dosage was raised to 150 ppm. It was concluded that the galvanically induced localized corrosion, in the form of pitting, was due to a loss of inhibitor from adsorption on the surface of the deposited solids. However, the inhibitors used for the corrosion experiments in this paper were formulated compounds, which contain multiple effective components.

Pedersen et al. (2008) also investigated the risk of galvanic corrosion of API 5L X65 mild steel and performance of imidazoline based corrosion inhibitors under sand deposits. Two different experimental procedures reflecting two scenarios encountered in the field were studied. One was sand deposit prior to inhibitor addition, resembling the case of sand deposition under conditions of insufficient inhibition. In another scenario, inhibitor was added prior to sand deposition representing the case of sand deposition under conditions of adequate inhibition (at least at the bare surface). In their experiments, one specimen, not covered by sand, was galvanically coupled by means of the zero resistance ammeter (ZRA) with another specimen made of the same material but fully covered by sand deposit. In the experiments where sand deposition took place prior to inhibitor addition, the authors found that without coupling to a non-sand covered specimen, the corrosion rate of the sand covered specimen was not affected by the addition of inhibitor. In the experiments where inhibitor was added before sand, severe localized attack was observed, with both imidazoline based inhibitor and alkyl amnio acid based inhibitor, while the worst case was found when alkyl amnio acid inhibitor was added before sand deposition. The authors pointed out that the potential difference between sand covered and un-covered specimen was the driving force for the galvanic

current, however, the measured corrosion potential from their experiments was not discussed in detail in the paper. In another work presented by Gulbrandsen and Pedersen (2007), cetyltrimethylammonium bromide (CTAB) inhibitor was found to be able to change the quartz sand's surface from preferentially water wetting to intermediate wetting, which was believed to be able to affect the corrosion process on the steel surface underneath the sand.

Lepkova et al. (2010) investigated the effect of sand deposit on the surface morphology of 1030 carbon steel using scanning electron microscopy and grazing incidence X-ray diffractometry. The inhibition and localized corrosion mechanisms were discussed from the point of steel surface characteristics. It was found that iron carbonate and iron carbide were both present at the steel surface and serve to protect the steel surface when sand deposit was present. It was suggested by the authors that the galvanic coupling between un-dissolved iron carbide and the steel played an important role in causing accelerated under deposit corrosion. An imidazoline based inhibitor was found to have little effect in protect the steel surface under a sand deposit. However, without corrosion inhibitor, the authors found that the sand deposition caused a negative shift of corrosion potential of the steel surface, which was opposite with the observations from other researchers (Pederson, 2008; Turnbull, 2009; Huang, 2010).

Microbiological influenced corrosion (MIC) is also believed to play an important role associated with under deposit corrosion, typically in the conditions where sulfur containing compounds are present (Sooknah, 2007; Gu, 2009). However, under deposit

corrosion related to MIC will not be covered in this dissertation, therefore, work that has been done on related topics will not be discussed here.

CHAPTER 3. OBJECTIVES AND SCOPE

The presence of a solid deposit is one of the many factors that may result in localized corrosion, which is the biggest concern for ensuring integrity in the oil and gas industry. NACE International's task group (TG) 380 has been working on providing industrial users with tools and means for testing and mitigation to choose from when confronted with an under deposit corrosion issue (Vera, 2012). The goal of this project was to systematically investigate a CO₂ corrosion system under inorganic silica sand deposit so as to understand the under deposit corrosion mechanisms and localized behavior in both uninhibited environments and inhibited environments. The entire research program was divided into three main sections: mechanisms of under deposit CO₂ corrosion in inhibitor-free environments (Chapter 4), inhibitor performance under silica sand deposits (Chapter 5), and localized corrosion under silica sand deposits (Chapter 6).

In Chapter 4, a reliable and reproducible experimental method and procedure developed for under deposit CO₂ corrosion research are demonstrated. The effects of environment factors, including solution pH, temperature, and deposit on under deposit CO₂ corrosion are discussed. A mechanistic model is proposed to predict the CO₂ corrosion process of mild steel under solid deposit in a system free of corrosion inhibitor.

In Chapter 5, the focus is on the effect of solid deposit on inhibitor performance. Corrosion inhibitors with a single active component (imidazoline or thiosulfate) were chosen for the experimental work. Different adsorption mechanisms of the corrosion active compound on solid deposit surface were tested and discussed.

Localized corrosion induced by silica sand deposit was investigated and will be presented in Chapter 6. Experiments were conducted at different deposit configuration and test conditions. Efforts were made to answer the questions of whether or not localized corrosion will occur, when will it happen and how will it propagate. The mechanisms of under deposit CO₂ corrosion were proposed for evaluating and controlling under deposit corrosion and for inhibitor selection and assessment.

CHAPTER 4. UNDER DEPOSIT CO₂ CORROSION OF MILD STEEL IN ENVIRONMENT WITHOUT CORROSION INHIBITORS

4.1 Introduction

Since solid deposits have been reported as an important factor that leads to severe corrosion, it's very important to understand the effect of solid deposit on the corrosion process and the mechanisms in the absence of any complications that arise due to corrosion inhibitors. A series of experiments was conducted with an innovative setup and procedure to study the effect of sold deposits and environmental parameters, such as solution pH, and temperature on CO₂ corrosion of mild steel. The objectives in this part of the work were:

1. To develop a reliable experimental method to investigate the effect of solid deposits on CO₂ corrosion of mild steel.
2. To study the effect of different factors on the under deposit corrosion of mild steel in CO₂ environment.
3. To develop a mechanistic model to predict the corrosion rate of mild steel in CO₂ environment under solid deposits.

4.2 Experimental Methods

4.2.1 *Experimental Setup*

The corrosion experiments presented in this chapter were all conducted in a standard three-electrode glass cell setup as shown in Figure 4.1. The setup included a reference electrode probe, a counter electrode and a working electrode. Reference electrode was filled with a saturated silver/silver chloride electrolyte solution and

connected with an external Luggin capillary. The counter electrode was a concentric ring made from platinum wire and the working electrode was made of a cylindrycal mild steel specimen with an exposed geometric surface area of 8 cm^2 . The working electrode was mounted on a newly designed specimen holder which was electrically connected with a potentiostat to make electrochemical measurements during the experiment. A pH probe was immersed in the test solution to monitor the pH change during the experiment. CO_2 gas was sparged into the solution before each experiment to de-oxygenate the solution, and also during the experiment to maintain a saturated CO_2 corrosion environment. To prevent test solution evaporation at high temperature, a condenser was used.

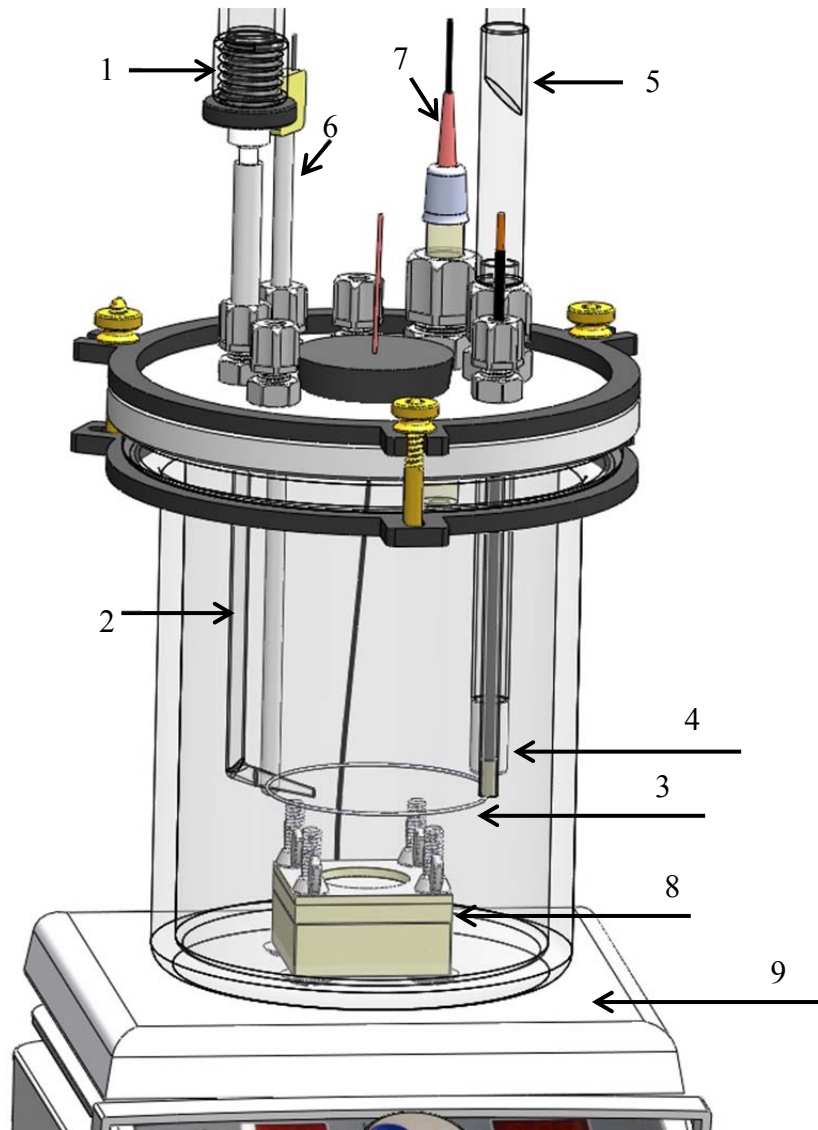


Figure 4.1 Standard three-electrode glass cell setup.

1. Reference electrode; 2. Luggin capillary; 3. Platinum counter electrode; 4. CO₂ gas inlet; 5. Condenser; 6. Thermal probe; 7. pH probe; 8. Specimen holder; 9. Heater.

4.2.2 Working Electrode Design

API 5L X65 pipeline steel was used to make working electrode specimens for all corrosion experiments. The exposed area of the specimen was 8 cm². The chemical composition of this pipeline steel is listed in Table 4.1. The specimens were machined from the parent material into cylindrical discs of 3 mm thick and 3.1 cm diameter, as shown in Figure 4.2.

Table 4.1 Chemical composition of X65 mild steel (mass % balance is Fe)¹.

Al	As	B	C	Ca	Co	Cr	Mn	Mo	Ni	Nb	
0.032	0.008	0.001	0.13	0.002	0.007	0.14	1.16	0.16	0.36	0.017	
P	Pb	S	Sb	Si	Sn		Ta	Ti	V	Zr	Cu
0.009	<0.001	0.009	0.009	0.26	0.007	<0.001	<0.001	0.047	<0.001	0.131	



Figure 4.2 View of an API 5L X65 mild steel experiment specimen.

¹Certified Test Reported by Laboratory Testing INC. 2003.

A plastic specimen holder was designed to limit the wetted area to only the upper face of the specimen and provide an easy way to place a bed of sand on top. The holder consists of three parts: the base, the specimen holder and the deposit holder (see Figure 4.3). Note that the spring-pin connectors for electrical connection in the base and an o-ring around the perimeter of the specimen holder were used to seal against leaks. When mounted in the specimen holder, the specimen's upper surface is flush with the holder. A plastic deposit holder (from 2 to 10 mm high), is then placed on top of the specimen holder and locked into place. Once installed, the deposit is filled with sand to fill all the available volume in the deposit holder.

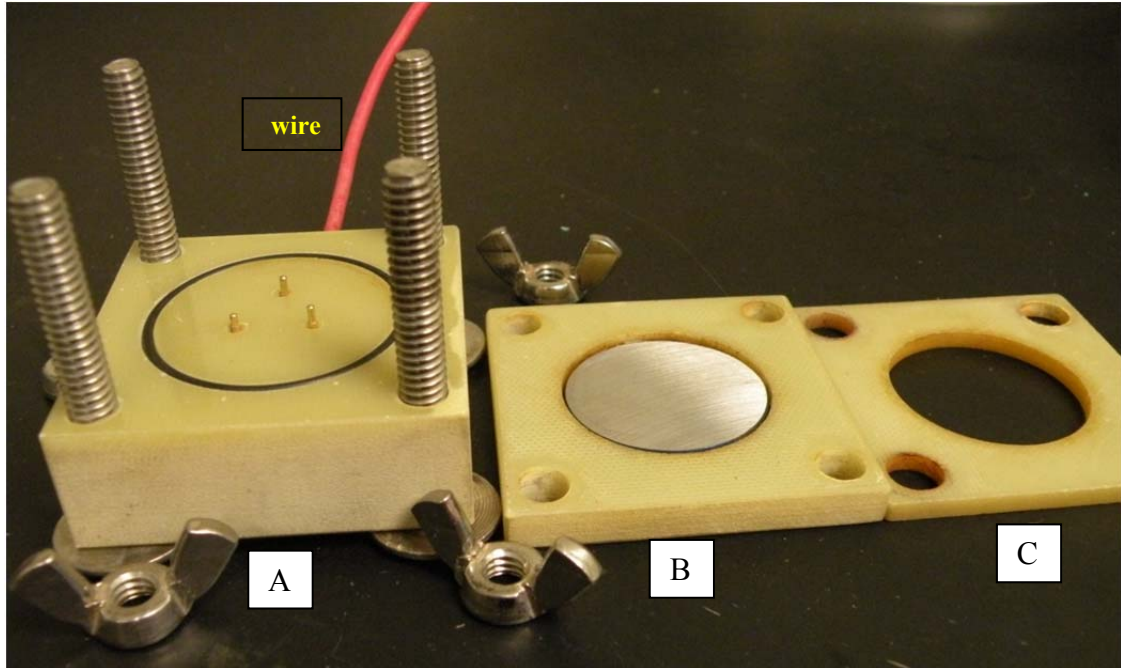


Figure 4.3 API 5L X65 mild steel specimen holder: (A) base, with three gold contacts to connect the steel specimen and wire for electrochemical measurement; (B) steel sample holder, where steel specimen is installed; (C) sand holder, which can be filled up to hold a 2 mm thick sand deposit.

4.2.3 Deposit Properties

Inorganic silica sand particles², and fine silica powder³ were used as solid deposit in the present work. Those deposits are all chemically inert when it comes to corrosion of the experiment specimen made from API 5L X65 steel. Silica sand and silica powder are made from the same parent material, i.e. silica dioxide (SiO_2). The only differences are their grain size and shape, as shown in SEM images in Figure 4.4. The

² CAS-No: 14808-60-7 (S23-3 Ottawa Sand from Fisher Scientific)

³ CAS-No:14808-60-7 (EC No: 238-878-4 from Sigma-Aldrich)

different grain size results in their different physical properties which were measured and listed in Table 4.2.

Table 4.2 Physical properties of solids used for under deposit corrosion experiments.

	Grain size	Bulk density	Porosity
SiO ₂ powder	< 44 µm	0.75 g/cm ³	75%
Silica sand	250 µm	2.5 g/cm ³	39%

Assuming the sand particles are perfect spheres and firmly packed, it can be calculated that there are approximately 4 layers of grains are contained in each millimeter of a sand deposit layer. Unless specified otherwise, deposits were cleaned with DI water and stored in a test solution saturated by CO₂ prior to experiment. A pipette was used to transfer the deposit material onto the corroding specimen for each experiment.

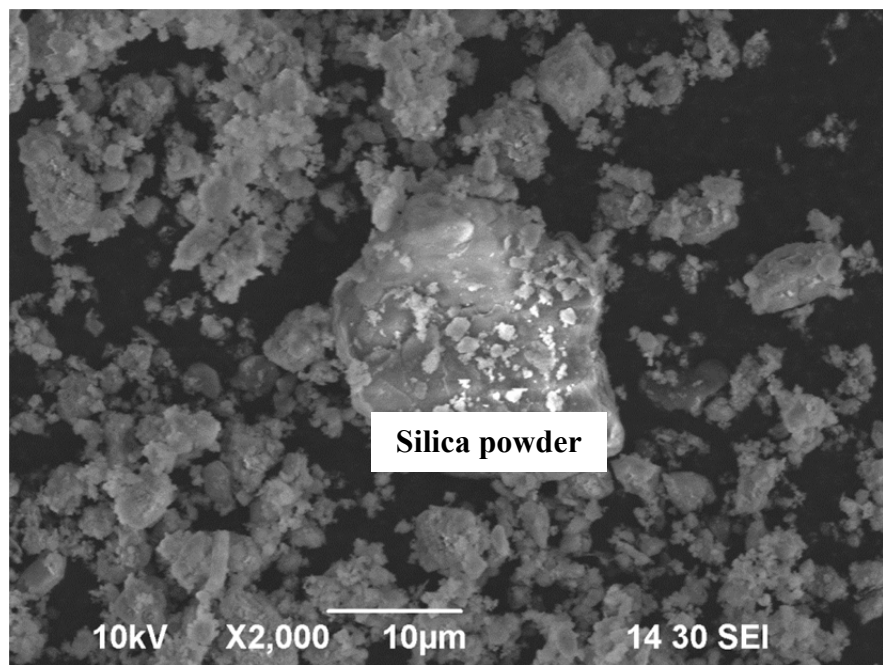
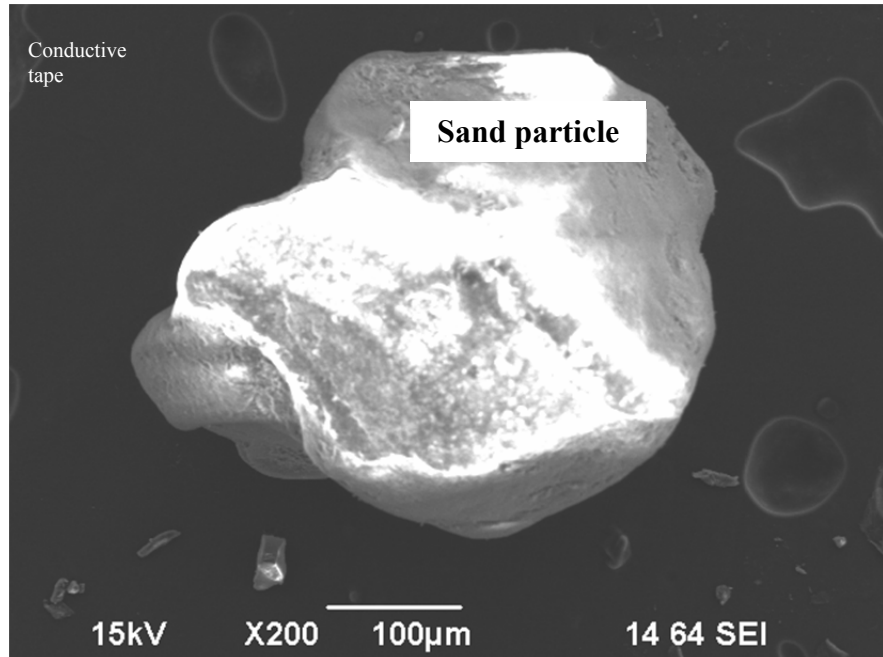


Figure 4.4 SEM images of inorganic silica sand particles and SiO₂ powder.

4.2.4 Experimental Procedure

All corrosion experiments were performed in a stagnant solution with 1 bar total pressure at a desired temperature, controlled by the heater. The test solution was made by adding 1 wt% of sodium chloride (NaCl) to two liters of de-ionized (DI) water. The test solution was heated up to desired temperature and at the same time was deoxygenated by continuously sparging with CO₂ gas for at least 1 hour. Then the pH of the test solution was adjusted to a designated value by adding OH⁻ or H⁺ in the form of de-oxygenated 1 molar sodium bicarbonate (NaHCO₃) or diluted hydrochloric acid (HCl) respectively. Once the test solution was prepared, the API 5L X65 specimen was polished with 200, 400 and 600 grit wet sand paper sequentially. Isopropyl alcohol was used to rinse the specimen to remove the heat generated during the polishing procedure. Once the polishing was done, the specimen was mounted onto the sample holder and immersed into the prepared test solution and experiment was started.

The specimen was firstly corroded for 24 hours without a deposit covering it, when the open circuit potential (OCP) and the uniform corrosion rate of the working electrode were recorded using linear polarization resistance (LPR) technique. Electrochemical impedance spectroscopy (EIS) measurements were also performed to determine the solution resistance in order to compensate the IR drop in the solution when processing of the data. Potentiodynamic Sweep (PDS) measurements were conducted at the end of experiment. The electrochemical response of the bare steel was taken as a reference behavior for later evaluation of the sand deposit effects. In each under deposit corrosion experiment, the specimen was first corroded without any deposit for an hour

(pre-corrosion). The experiment would then proceed to the under deposit stage only when the initial bare steel corrosion process was repeatable and reasonable. OCP, corrosion rate and solution resistance of the working electrode were monitored using LPR and EIS throughout the experiment. When the corrosion rate did not change, a PDS measurement was conducted at the end of the experiment by sweeping first from the OCP in the cathodic direction. When the OCP recovered, the sweep was done from OCP in the anodic direction. The test specimen was then taken out of the solution and rinsed with isopropyl alcohol, dried and stored properly for surface analysis.

4.2.5 Test Matrix

The test conditions for experiments looking into the effect of sand deposits on CO₂ corrosion of mild steel in inhibitor-free environment is shown in Table 4.3. Different sets of experiments were conducted in order to investigate the effect of environmental factors on the under deposit corrosion process. The test matrix for each set of experiment is shown in Table 4.4 - Table 4.7.

Table 4.3 Test conditions.

Material	API 5L X65 mild steel
Deposit type	Silica sand particles, SiO_2 powder
Test solution	1 wt% NaCl, stagnant
LPR	± 5 mV vs. E_{oc} (sweep rate: 0.125 mV/s)
EIS	± 5 mV vs. E_{oc} (frequency range: 10 kHz – 1 mHz)
PDS	Cathodic: from E_{oc} to $E_{\text{oc}} - 0.3$ V Anodic: from E_{oc} to $E_{\text{oc}} + 0.2$ V (sweep rate: 0.125 mV/s)

Table 4.4 Test matrix for the experiments looking into the effect of deposit porosity.

Material	API 5L X65 mild steel
Deposit porosity (porosity)	Silica sand (39%), SiO_2 powder (75%)
Test solution	1 wt% NaCl
CO_2 partial pressure (temperature)	0.96 bar (25°C)
Solution pH	5.0

Table 4.5 Test matrix for the experiments looking into the effect of deposit depth.

Material	API 5L X65 mild steel
Deposit type	Silica sand particles
Deposit depth	2 mm, 5 mm and 10 mm
Test solution	1 wt% NaCl
CO ₂ partial pressure (temperature)	0.96 bar (25°C)
Solution pH	5.0

Table 4.6 Test matrix for the experiments looking into the effect of temperature.

Material	API 5L X65 mild steel
Deposit type	SiO ₂ powder
Deposit depth	5 mm
Test solution	1 wt% NaCl
Temperature (CO ₂ partial pressure)	25°C (P _{CO2} = 0.96 bar), 80°C (P _{CO2} = 0.53 bar)
Solution pH	5.0

Table 4.7 Test matrix for the experiments looking into the effect of solution pH.

Material	API 5L X65 mild steel
Deposit type	Silica sand particle
Deposit depth	10 mm
Test solution	1 wt% NaCl
Temperature (CO ₂ partial pressure)	25°C (P _{CO2} = 0.96 bar)
Solution pH	4.0, 5.0 and 6.0

4.3 Results and Discussion

4.3.1 Effect of Deposit Porosity

In CO₂ corrosion of mild steel, whenever the steel surface is covered by a solid deposit, part of the surface area for corrosion becomes unavailable due to the coverage. The solid deposit layers can also be a diffusion barrier for mass transfer of corrosive species. Silica sand particles with different grain sizes will result in different deposit porosities when they are packed and layered. The effect of surface coverage in terms of deposit porosity on the corrosion process of mild steel in saturated CO₂ solution was therefore tested first.

Figure 4.5 shows the variation of uniform corrosion rate of API 5L X65 steel with time (as measured by LPR) for the two types of deposit: silica powder and silica sand, and compared to the bare steel corrosion rate. The uniform corrosion rate for bare surface specimen was 1.2 ± 0.1 mm/yr, which was calculated by adopting the Stern-Gearay coefficient B of 26 mV (Johns, 1995), and stable within 24 hours. The first data in each set of measurement on specimens with deposit was the corrosion rate before the deposit was added. It indicated the consistency of test specimen preparation and demonstrated the repeatability of the experiments. As observed in Figure 4.5, after the deposit was added the corrosion rates quickly dropped and became stable (± 0.05 mm/yr). The observation of the drop in corrosion rate suggests that the addition of a deposit significantly slowed down the corrosion process, revealing that a direct relationship between the measured corrosion rate and deposit porosity may be defined. The more porous the deposit was, the less the steel surface was covered, and therefore the corrosion process was less

retarded. The corresponding change in corrosion potential after the addition of the inert deposit is shown in Figure 4.5. The corrosion potential increased by about 20 mV after deposit was added. No significant difference in corrosion potential variation between the two deposits was observed.

EIS is a transient electrochemical technique and can be used to measure and correct the solution resistance which is incorporated as a parasitic resistance into the corrosion resistance measured by LPR for more accurate estimation of corrosion rate (Mansfield, 1990; Cao, 1996). It also provides information about the kinetics of the corrosion system under examination (Keddam, 1981; Mansfield, 1991; Baril, 2007). Figure 4.6 shows the Nyquist diagrams obtained from EIS measurements relative to deposit porosity effect. An increase of solution resistance can be observed when the deposit porosity was decreased (bare steel surface has a porosity of 100%). Solution resistance increased from 8.5 ohm in bare steel corrosion to 11.5 ohm in the case with silica powder deposit and 17 ohm with the less porous sand deposit.

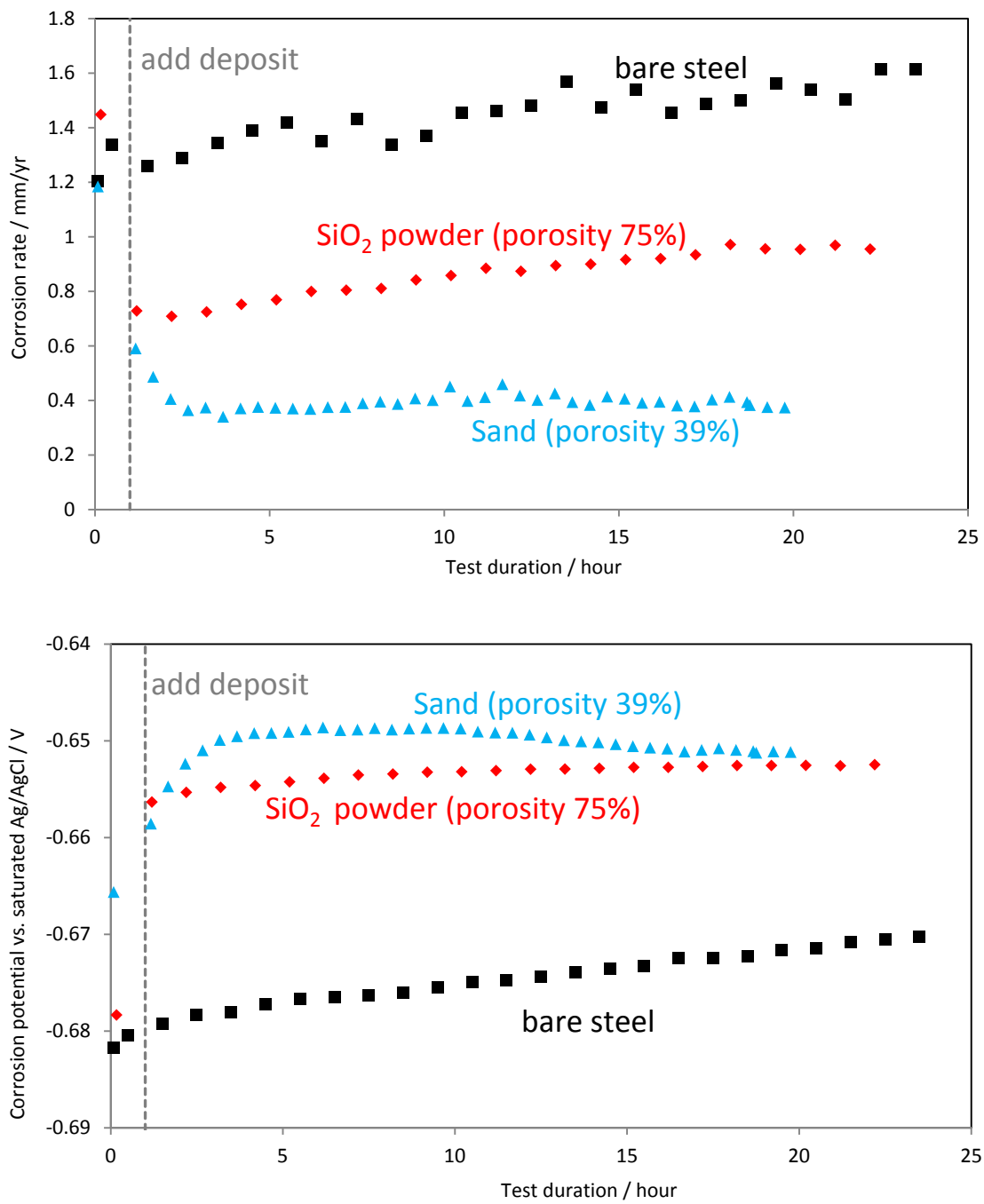


Figure 4.5 LPR corrosion rate and corrosion potential over time at test conditions T = 25°C, 1 wt% NaCl solution, pH = 5.0, 2 mm deposit.

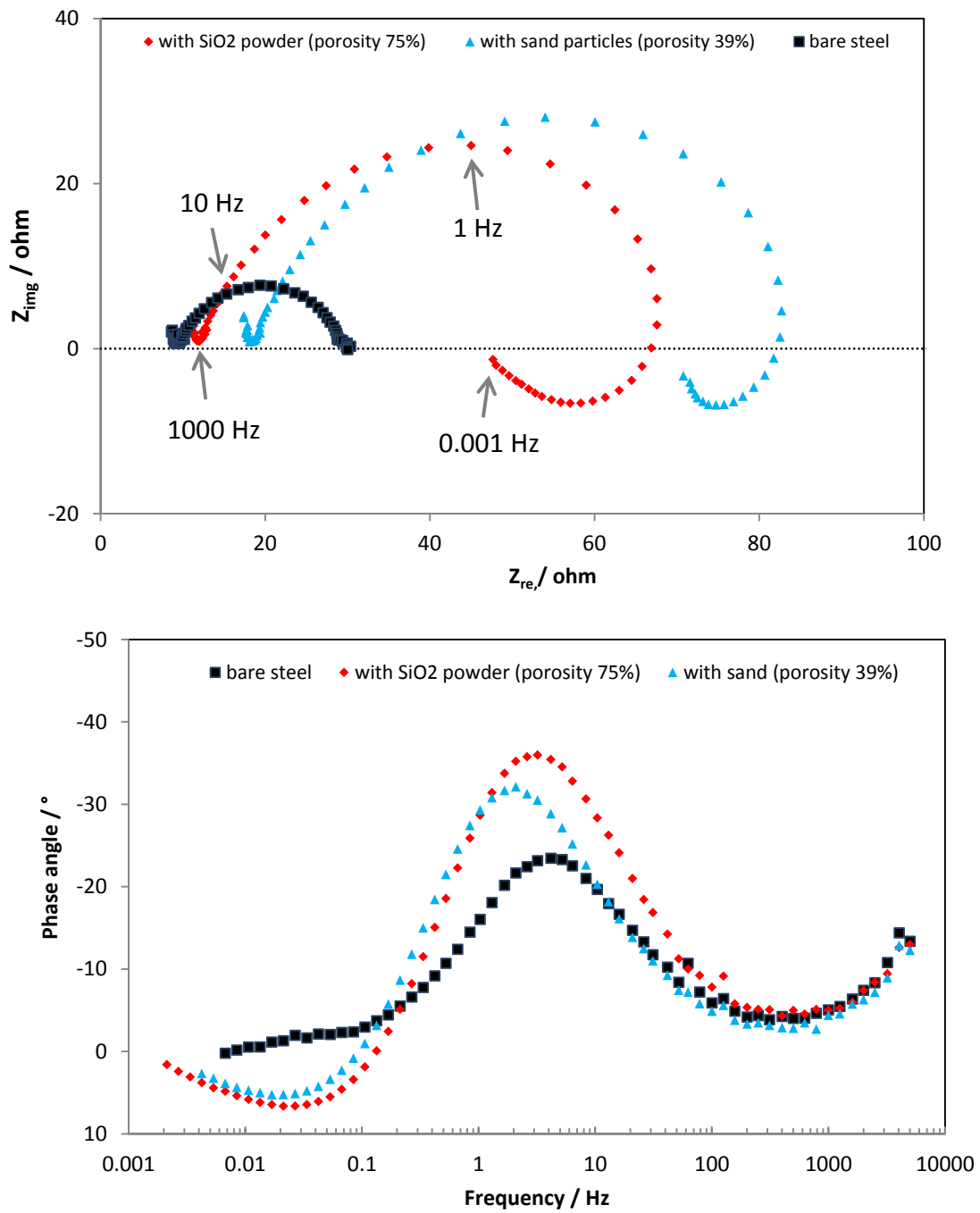


Figure 4.6 EIS Nyquist plots and Bode plots at test conditions 25°C, 1 wt% NaCl solution, pH = 5.0, 2 mm deposit, 20 hours exposure.

In EIS, different processes involved in corrosion (electrochemical reactions, adsorption processes, double layer charge and discharge processes, diffusion, etc.) can be “excited” by potential perturbation at specific frequency ranges. EIS technique therefore measures a corrosion system’s responses to the applied potential perturbation at different frequencies, which enable different processes involved in corrosion to be identified (Epelboin, 1970, 1972; Orazem, 2008). By interpreting EIS measurement data, represented by impedance plane (Nyquist plots) or frequency plane (Bode plots), the corrosion processes can be verified.

As can be seen in the Nyquist graphs shown in Figure 4.6, firstly, the diameter of the loop formed at high (1000 Hz) to intermediate (1 Hz) frequency regions increased when deposit was added. The loop forms at frequency region 1000 – 1 Hz having positive imaginary impedance values is named the capacitive loop and is commonly accepted to be an indication of a charge transfer process during aqueous corrosion of mild steel at the steel/electrolyte double layer (Mansfield, 1990; Silverman, 1990). The increment in the diameter of this capacitive loop manifested a slower corrosion process when deposit was present. The spectra at different deposits porosities are very similar except for the magnitude of the diameter of the loops. The increment in the magnitudes of the impedance values as a function of the deposit porosity revealed that the corrosion process was more retarded by less porous deposit barriers. Secondly, a change of Nyquist plot shape can be noticed which indicates a change of electrochemical response of mild steel corrosion under deposit from bare steel corrosion. A formation of inductive loop (where the imaginary impedance values become negative) at low frequency region (1 – 0.001 Hz

) can be observed in the cases with both silica sand and silica powder deposit, while for the bare steel corrosion case, being much less pronounced. It was suggested that this inductive response can be associated to a surface adsorption process (Chen, 1994; Tan, 1996; Dawson, 1993; Bisquert, 2001).

The same sets of data are also presented in Bode plots. When there was a deposit, the two crests (one at 1000 – 1 Hz region and the other at 0.1 – 0.001 Hz region) can be recognized on Bode plots, which correspond to the two loops appearing on Nyquist plots. While for bare steel corrosion, only one crest was visible in the high frequency region. The number of “loops” in Nyquist plot or crests in Bode plots is an indication of the number of controlling electrochemical kinetic processes on the electrode surface (Orazem, 2008).

Potentiodynamic sweep measurements were conducted at the end of each experiment, as described in the experimental procedure part. As shown in Figure 4.7, both anodic and cathodic reactions were retarded by the presence of a solid deposit. The less porous the deposit was, the more corrosion was affected.

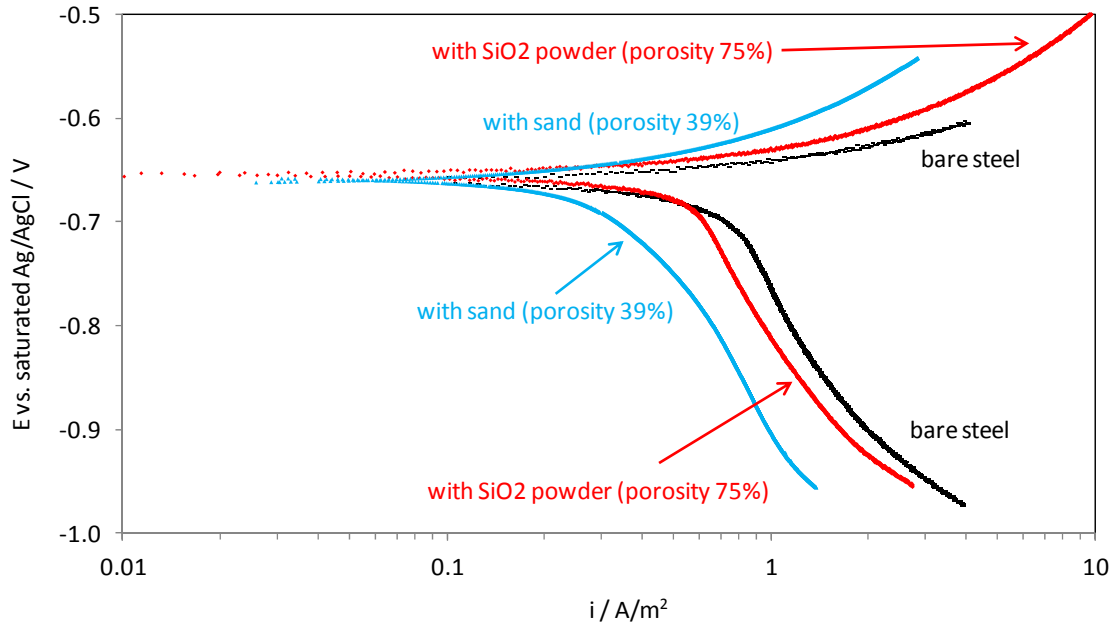


Figure 4.7 Potentiodynamic sweeps at test conditions 25°C, 1 wt% NaCl solution, pH = 5.0, 2 mm deposit, in the 24th hour of exposure.

The test specimens were analyzed by SEM and EDX after each experiment. The SEM images show that a homogeneous surface with some polishing scratches can be seen on the specimen surface (Figure 4.8). A rougher surface was visualized on the specimen under silica powder deposit than the one under silica sand particles, which can be associated with the larger corrosion rate of the former. The change in surface roughness showed consistency with LPR results (Figure 4.5). No localized corrosion at the steel surface was observed in these short term experiments in the presence of solid deposits.

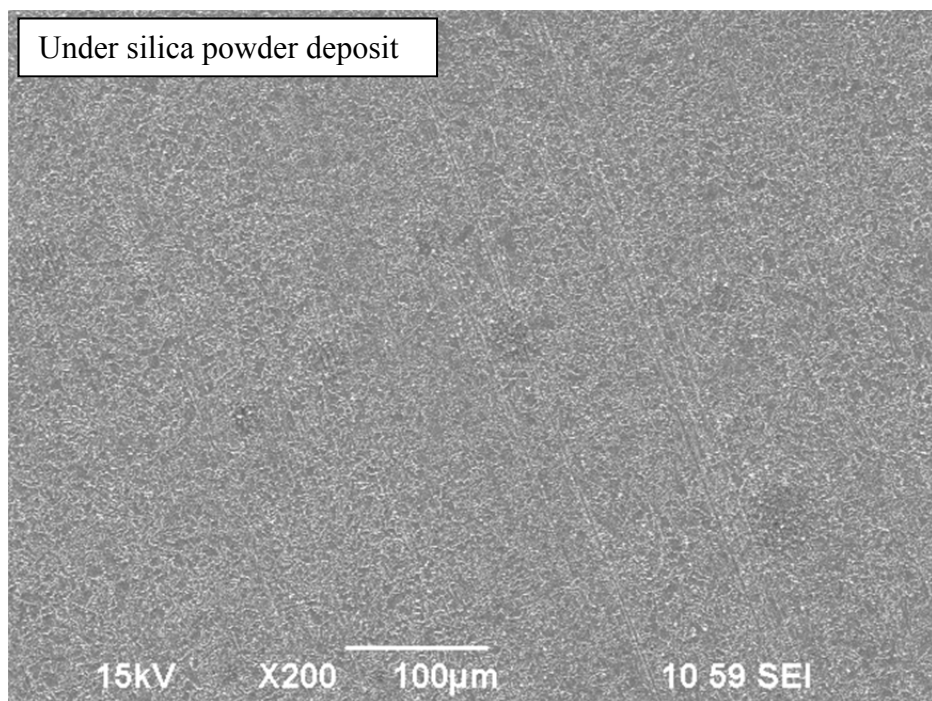
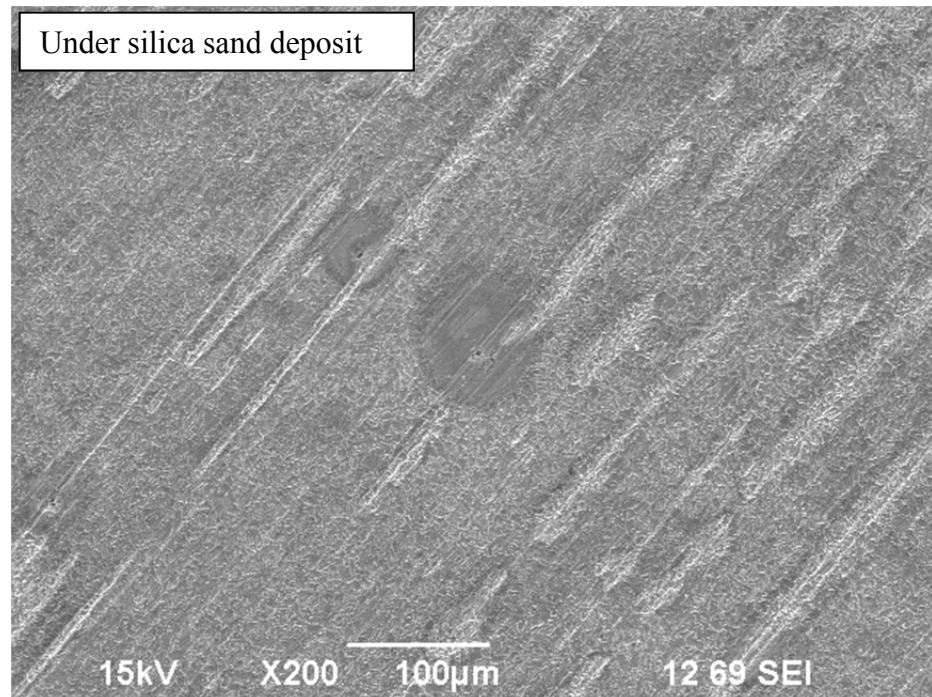


Figure 4.8 SEM images of the steel surface exposed for 24 hours at conditions 25°C, 1 wt% NaCl solution, pH = 5.0, with 2 mm deposit.

4.3.2 Effect of Deposit Depth

As mentioned earlier, the solid deposit creates a tortuous path for corrosive species to diffuse through. This set of experiments was therefore performed to investigate how increasing deposit thickness would affect the corrosion rate of mild steel in CO₂ environment.

Figure 4.9 shows the comparison of general LPR corrosion rate obtained with different thickness of the sand deposit having a uniform porosity 39%. Firstly, it can be seen that at 25°C, solution pH 5.0, the uniform corrosion rate for bare surface X65 specimen was consistent, and that it significantly decreased as the sand deposit was added. The corrosion rate of the steel decreased to a relatively low value (less than 0.4 mm/yr) in a short amount of time (about 5 hours) and then remained stable. The thicker the deposit, the lower the stabilized corrosion rate was. A 20 mV of potential increase was observed after adding 2 mm sand deposit. Increasing the depth of deposit didn't further increase the potential.

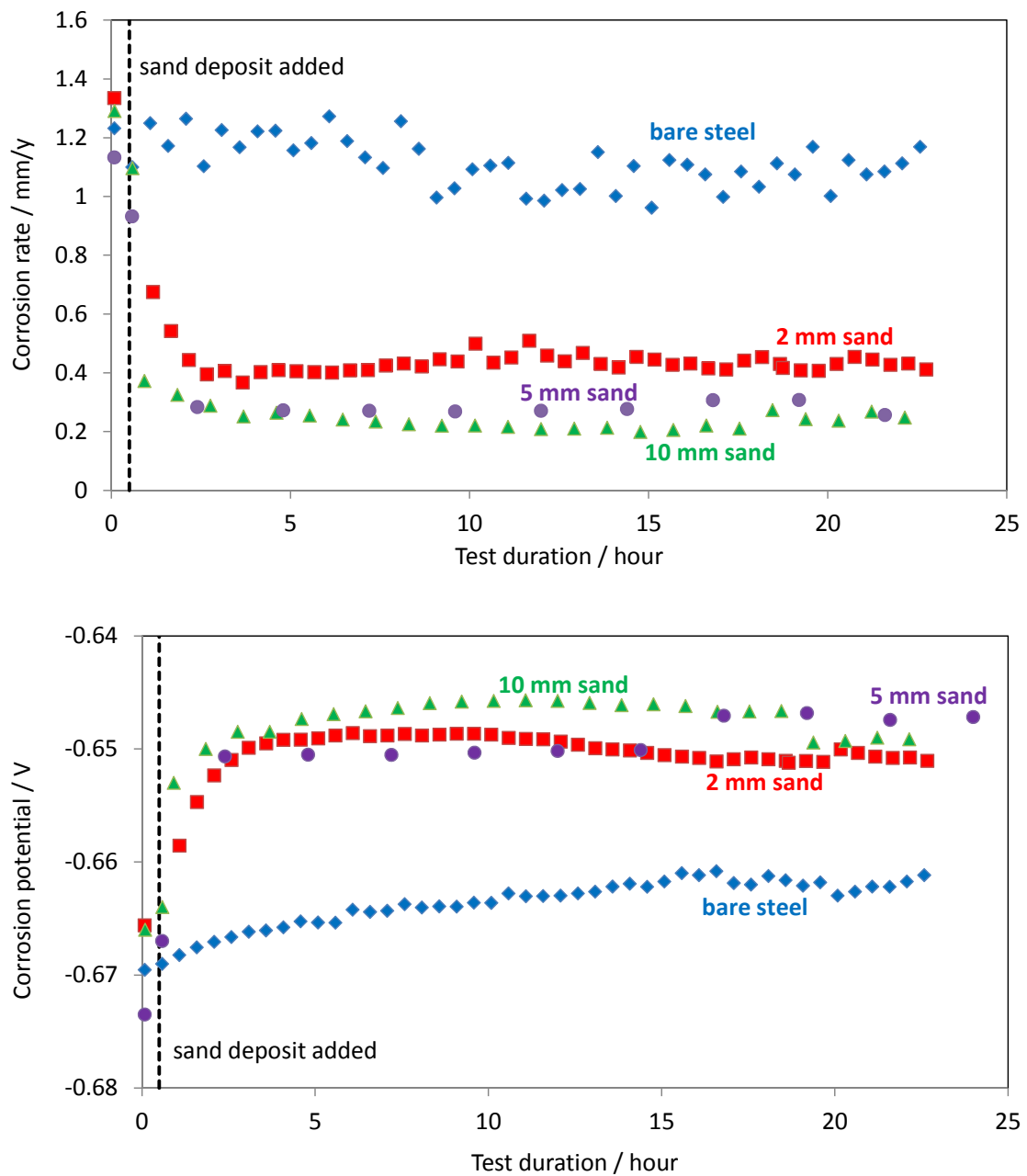


Figure 4.9 LPR corrosion rate and corrosion potential over time under sand deposit at test conditions T = 25°C, 1 wt% NaCl solution, pH = 5.0, 2 mm deposit.

The effect of deposit thickness on corrosion of API 5L X65 was also studied by impedance measurement. Solution resistance increased with increasing deposit thickness, as seen in Figure 4.10. The spectra at different deposit thickness were very similar, as shown in the Nyquist plots. All Nyquist plots showed an inductive behavior at low frequency regions (0.1 – 0.001 Hz). The increment in magnitude of the impedance as a function of the deposit thickness was also observed revealing that the corrosion process was more retarded by thicker deposit barriers.

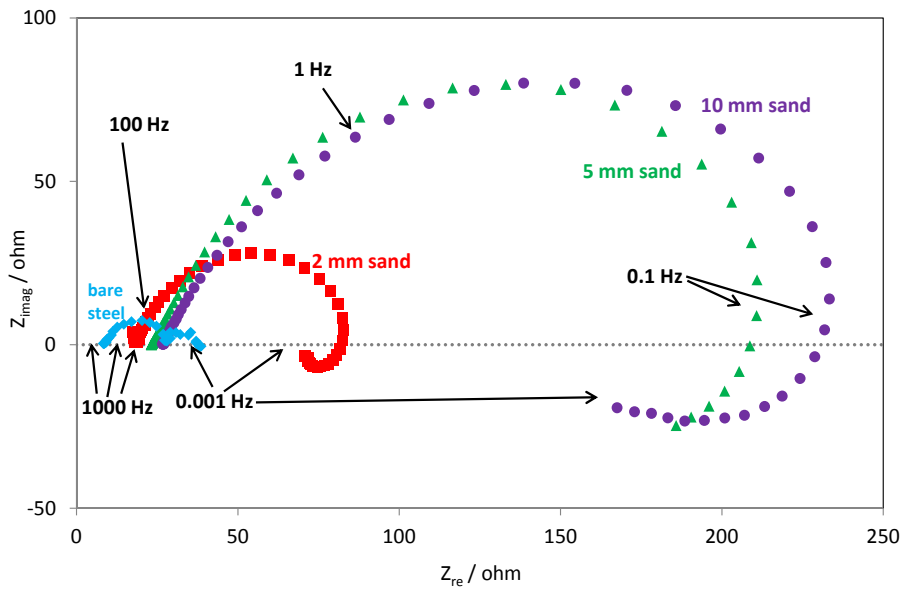


Figure 4.10 EIS Nyquist plots at test conditions 25°C, 1 wt% NaCl solution, pH = 5.0, 20 hours exposure, under sand deposit.

The potentiodynamic sweeps are shown in Figure 4.11. Both anodic and cathodic reactions were retarded by the presence of a sand deposit. The thicker the sand deposit, the more the electrochemical processes underlying corrosion were retarded.

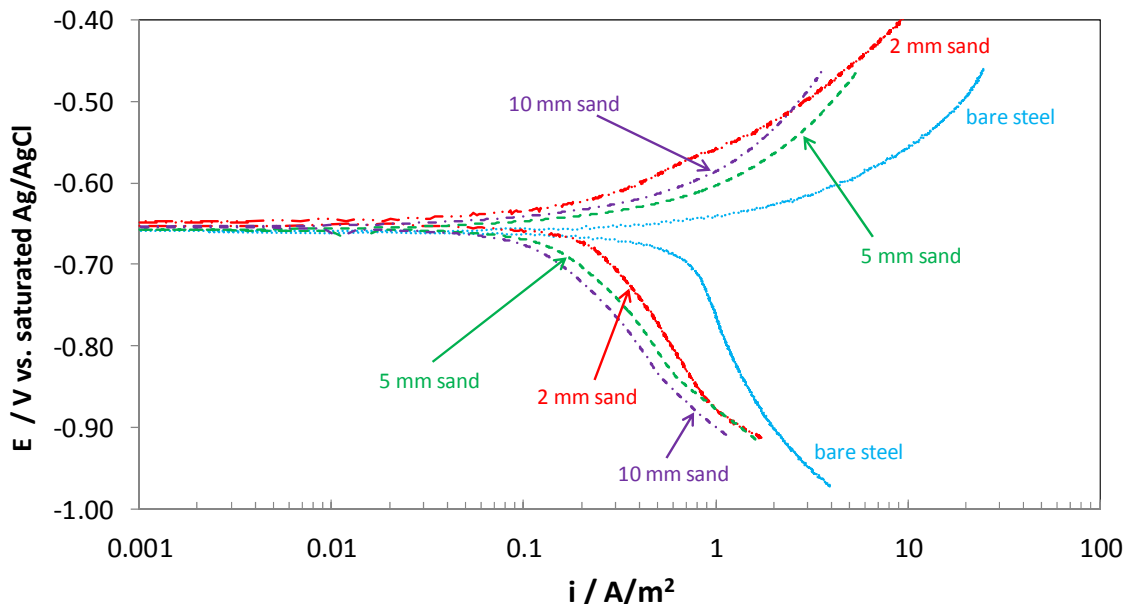


Figure 4.11 Potentiodynamic sweeps at test conditions 25°C, 1 wt% NaCl solution, pH 5.0, in the 24th hours exposure, under sand deposit.

The above observations indicate that a decrease in deposit porosity and/or an increase in deposit thickness are accompanied by an increase in diffusion path length and tortuosity which both slowed down the diffusion of cathodic reactants through the solid deposit barrier. However, the resulting lower corrosion rate seem to be affected just as much by the blockage effect as the overall mechanism of corrosion did not change

significantly (as indicated by the semicircular shape seen in all the EIS plots) and with both the anodic and cathodic reactions being retarded (as indicated by the PDS plots).

4.3.3 Effect of Temperature

Figure 4.12 shows the corrosion rate of X65 mild steel under 5 mm SiO₂ powder deposit with 75% porosity, at 25°C and 80°C in a 1 wt% NaCl solution of pH 5.0 over a 24 hour period. The corrosion rate decreased after the addition of deposits at both temperatures and the stabilized corrosion rate at the end of the experiments were at the same level for both temperatures.

Figure 4.13 shows the SEM images of the steel surface with corrosion product layers. No significant difference can be identified for the two different temperatures.

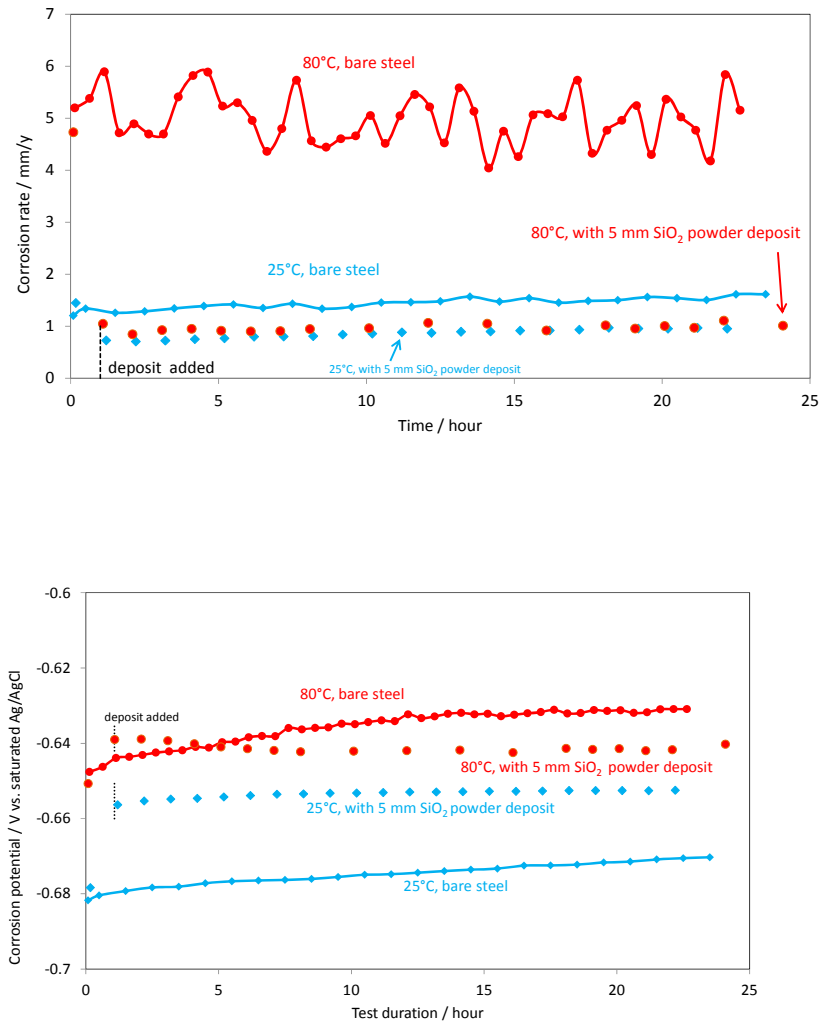


Figure 4.12 LPR corrosion rate and corrosion potential over time at test conditions 1 wt% NaCl solution, pH = 5.0, under 5 mm SiO₂ powder deposit at different temperatures.

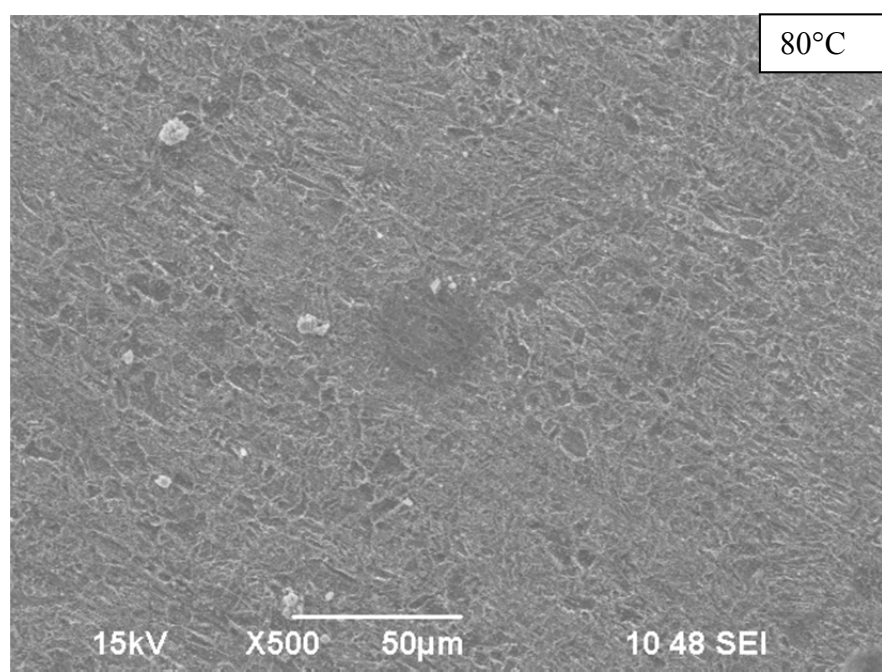
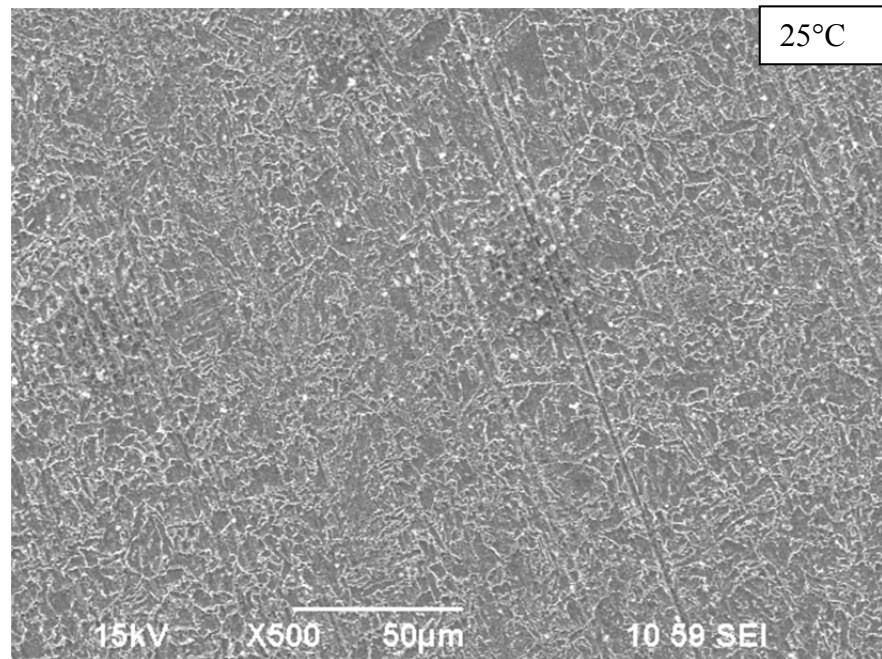


Figure 4.13 SEM images of the steel surface exposed for 24 hours at conditions 1 wt% NaCl solution, pH 5.0, with 5 mm SiO₂ deposit.

4.3.4 Influence of Solution pH

In this section, the effect of bulk solution pH on the corrosion of API 5L X65 under the sand deposit was investigated. The effect of pH has been extensively studied in the mild steel corrosion in aqueous CO₂ solution (Schmitt, 1983; Nešić, 1996) and it is well understood that water chemistry in terms of solution pH is an important factor that would affect the corrosion process in aqueous CO₂ solution.

Figure 4.14 shows the comparison of uniform corrosion rate of mild steel in the presence of a 10 mm silica sand deposit at 25°C at different solution bulk pH. As the experimental results show, no significant differences in corrosion rate can be identified at different bulk solution pH, where in the case of bare steel CO₂ corrosion, the corrosion rate would be largely affected by the solution pH (Nešić, 1996).

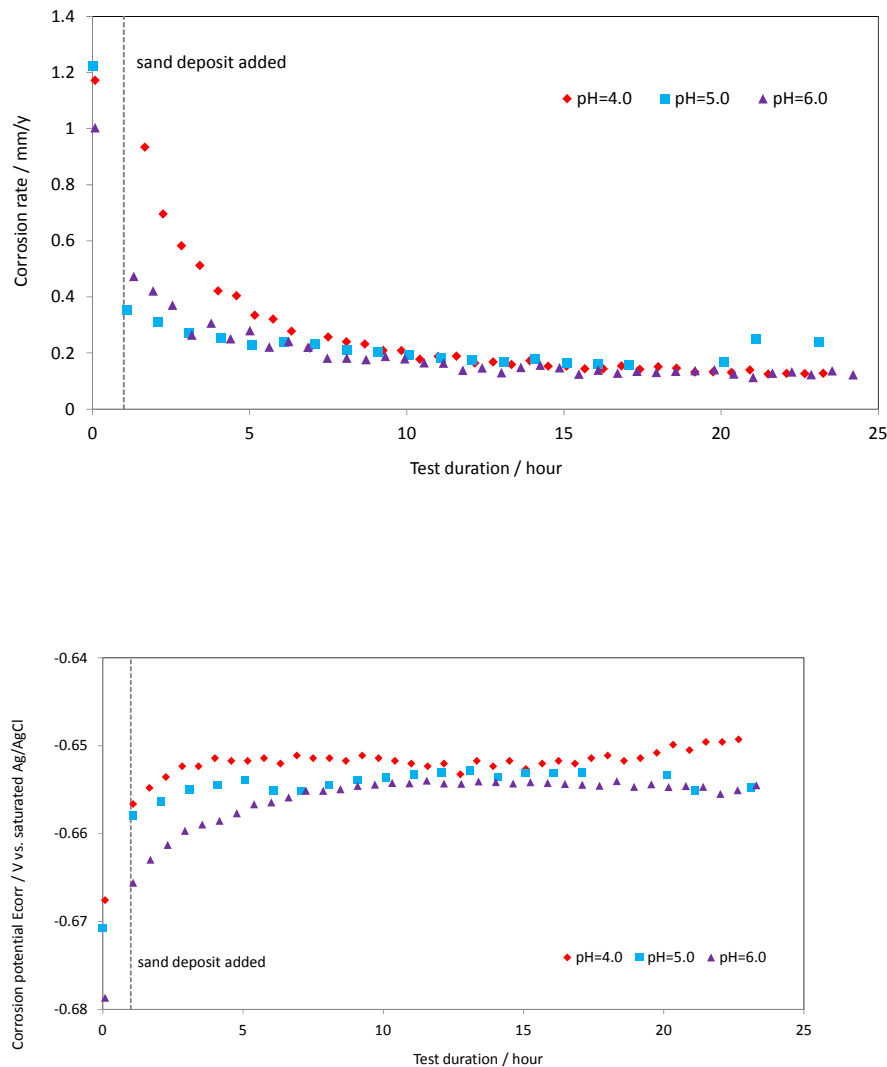


Figure 4.14 LPR corrosion rate and corrosion potential over time at test conditions T = 25°C, 1 wt% NaCl solution, with 10 mm sand deposit at different bulk solution pH.

The water chemistry underneath the deposit is different from the bulk solution above it. From the above discussion, it was found that there is no effect of bulk solution pH in under deposit corrosion. Therefore, the surface pH underneath the solid deposit was likely similar and was investigated.

The measurement of surface pH was achieved by using a unique pH probe design developed in Institute for Corrosion and Multiphase Technologies by Han (2009). The pH probe used in the measurement is sketched in Figure 4.15. The surface pH kit consists a hollow compression fitting and its cap, a mesh made of stainless steel and a commercial flat pH probe. During the surface pH measurement, the solid deposit was filled in a cap where the stainless steel mesh was placed at the bottom to hold the deposit and a mild steel mesh (Figure 4.16) was placed at the top of the deposit. The cap filled with deposit and two pieces of mesh was then mounted into the flat pH probe. The whole piece was immersed into the test solution so that the pH can be recorded. The reading from the flat pH probe was considered as the pH underneath the deposit and was monitored once every few hours until stable.

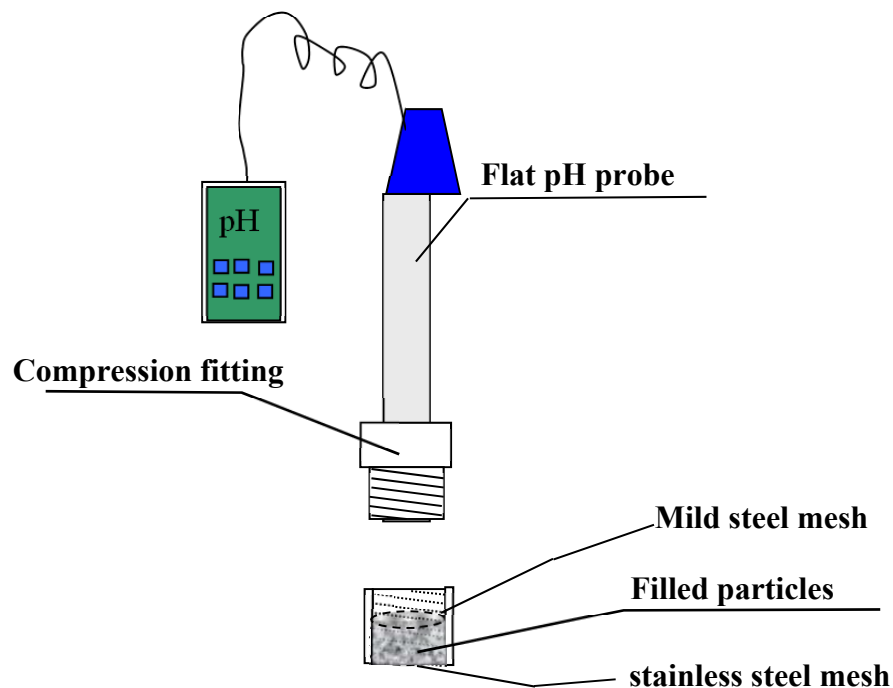


Figure 4.15 Surface pH probe design (Han, 2009).

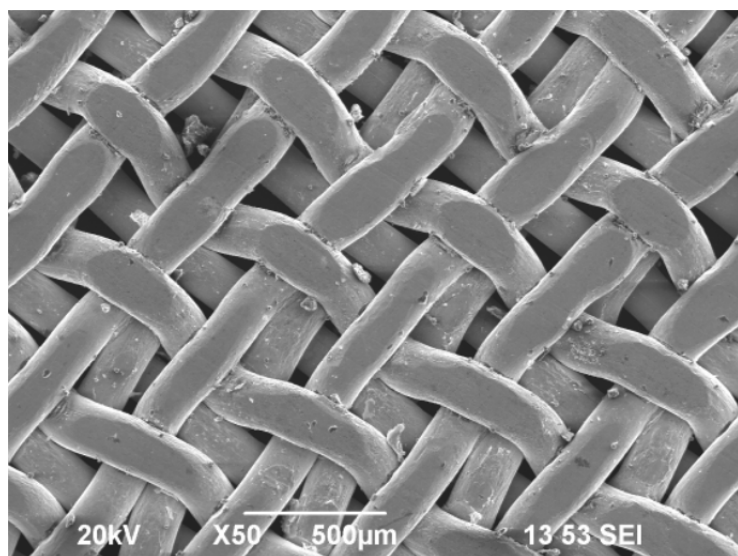


Figure 4.16 SEM image of compressed mesh used for the surface pH probe. (Han, 2009)

All surface pH measurement experiments were conducted in a 1wt% NaCl solution saturated by CO₂. Figure 4.17 shows the measured pH underneath a silica powder deposit with 75% porosity at different temperatures. Figure 4.18 shows the results of pH measured underneath a silica sand deposit with 39% porosity at different temperatures. Figure 4.19 and Figure 4.20 are surface pH measured at different bulk pH with sand deposit. It can be seen that irrespective of what porosity the deposit was and at what bulk pH, or at what temperature, the pH measured underneath the deposit was always between 6 and 6.5, which was 1 to 2 units higher than the bulk pH. Therefore, it is not surprising that the corrosion rate measured at different bulk pH or different temperature was the same. The direct surface pH measurement results also confirmed that the presence of the sand deposit does result in a difference in water chemistry at the steel surface underneath it. The increased pH is a result of a diffusion barrier for corrosive species, particularly the hydrogen ions.

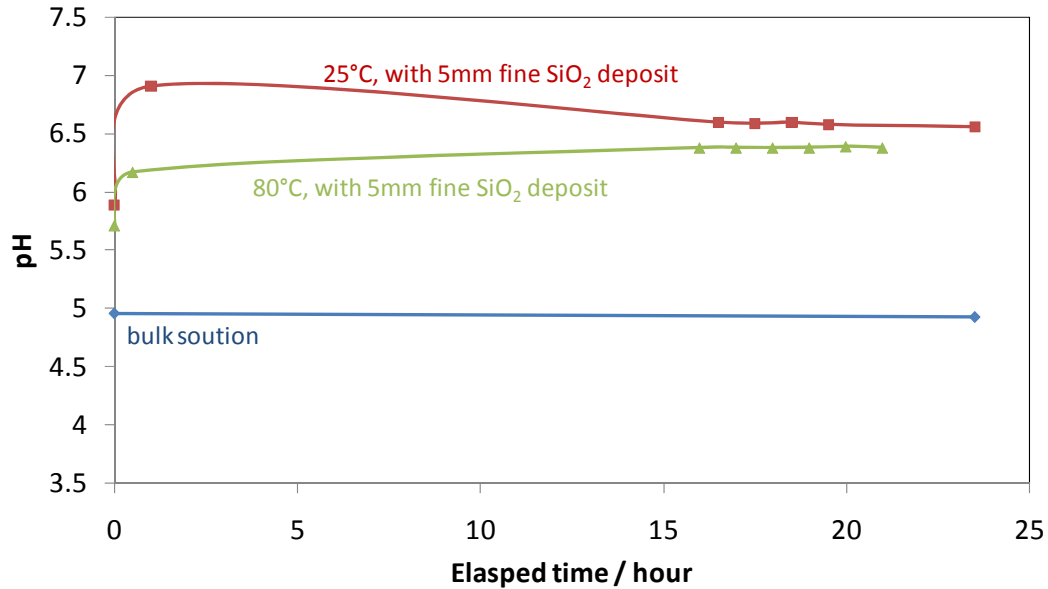


Figure 4.17 Surface pH measured at different temperature at conditions 1 wt% NaCl solution, pH 5.0, with 5 mm SiO₂ powder deposit, 24 hours exposure.

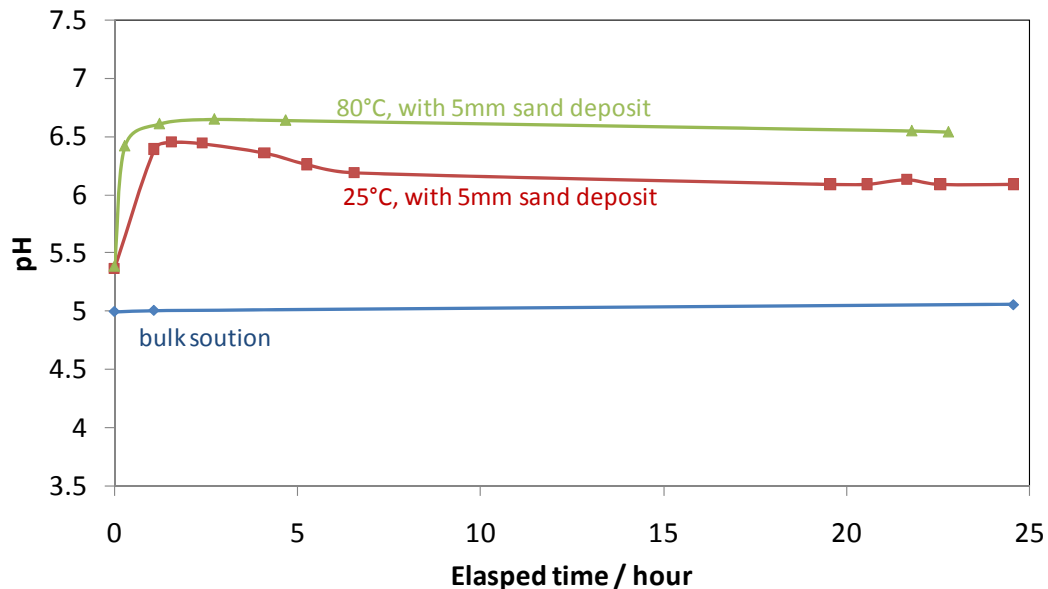


Figure 4.18 Surface pH measured at different temperature at conditions 1 wt% NaCl solutions, pH 5.0, with 5 mm sand deposit, 24 hours exposure.

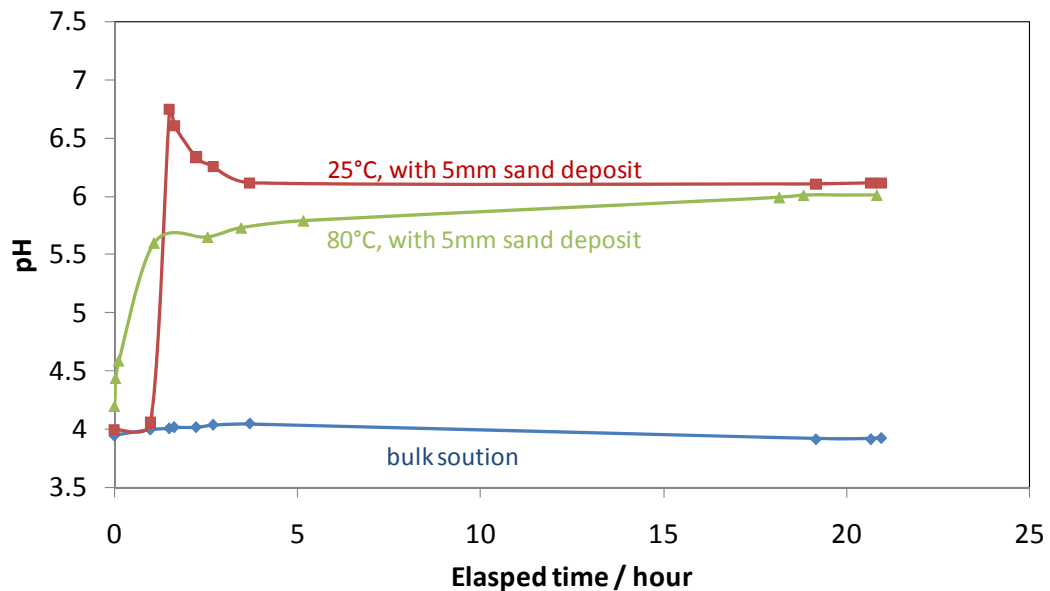


Figure 4.19 Surface pH measured at different temperature at conditions 1 wt% NaCl solution, pH 4.0, with 5 mm sand deposit, 24 hours exposure.

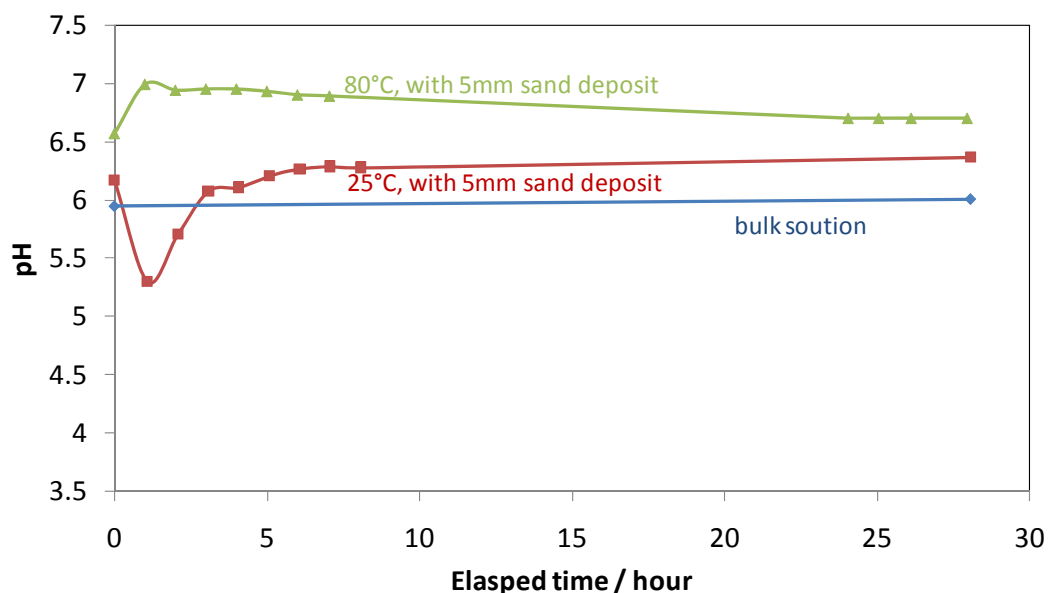


Figure 4.20 Surface pH measured at different temperature at conditions 1 wt% NaCl solution, pH 6.0, with 5 mm sand deposit, 24 hours exposure.

4.3.5 Longer Experiment Duration

As it was confirmed that the surface pH was different from bulk solution pH when a silica deposit was present, the question arose about how would this difference in water chemistry affect the corrosion process in the long run? In this section, results from longer exposure experiments will be discussed.

Figure 4.21 shows the variation of corrosion rate and corrosion potential with time measured from LPR at 80°C with 5 mm silica sand deposit. It clearly shows that the corrosion rate immediately decreased from 3.5 mm/yr to 1.5 mm/yr when the sand deposit was added, and then gradually decreased further as time went by. The corresponding corrosion potential increased went up immediately by 20 mV as the deposit was added and then kept increasing as experiment proceeded.

Impedance data are shown in Figure 4.22. Firstly, an immediate shift in solution resistance can be noted after the deposit was added. Secondly, as time went by, a gradually change of the shape of Nyquist plots was observed. The inductive loop appeared at low frequency regions eventually faded and developed to a tail analogous to a Warburg curve (Epelboin, 1970), which is a suggestion of an involvement of a diffusion resistance.

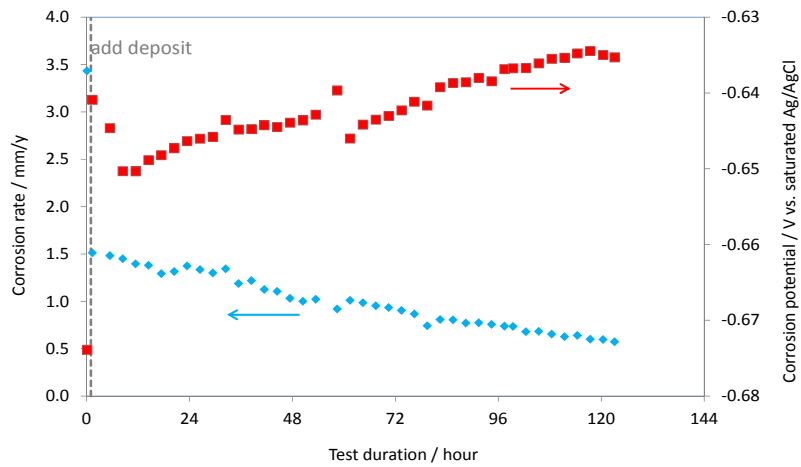


Figure 4.21 LPR corrosion rate and corrosion potential over time at test conditions $T = 80^\circ\text{C}$, 1 wt% NaCl solution, pH = 4.0, 5 mm sand deposit.

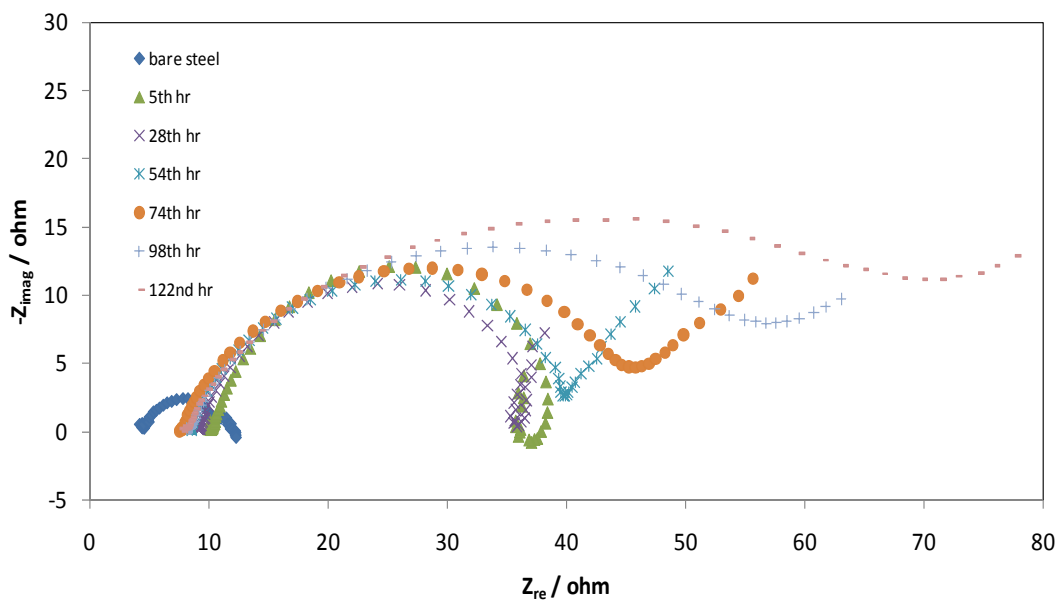


Figure 4.22 EIS Nyquist plots at test conditions 80°C , 1 wt% NaCl solution, pH = 4.0, with 5 mm sand deposit, 5 days exposure.

The steel surface morphology was analyzed by SEM (Figure 4.23). A loose iron carbonate scale was observed as shown in the SEM images. Some sand particles were “stuck” on the metal surface and could not be removed by rinsing with isopropyl.

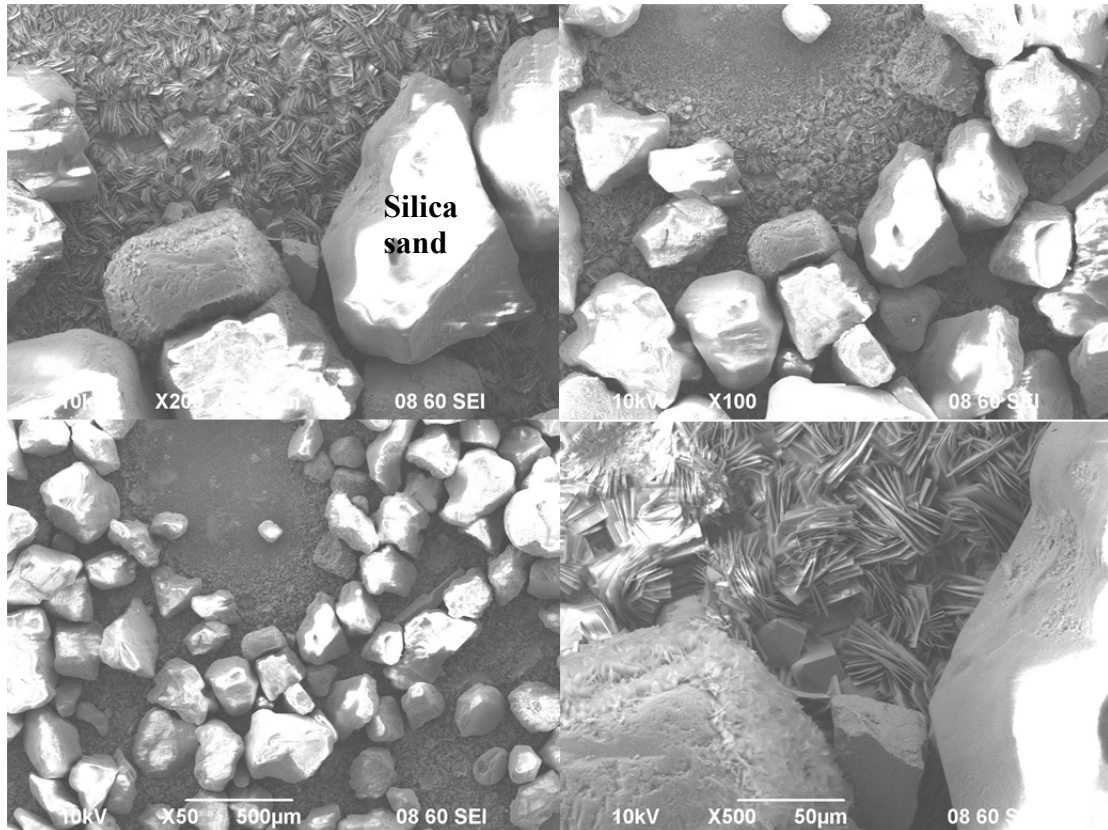


Figure 4.23 SEM images of the steel surface after 5 days exposure under 5mm silica sand deposit at 80°C, bulk solution pH 4.0, 1 wt% NaCl solution.

The steel surface was then cleaned by using Clarke solution⁴ so that both the stuck sand particles and corrosion product layer were able removed. The metal surface was analyzed again by SEM, as seen in Figure 4.24, with further analysis by a infinite focusing microscopy. As shown in Figure 4.24, the circular area indicated in the SEM image was thought to be the location where the sand particle stood because the metal surface corroded much less there than the area around it. For those areas not directly covered by the sand particle but next to it, iron carbonate formed due to increasing concentrations of ferrous ions and carbonate ions reacting within the pores of the deposit. The areas, where the metal was not protected by sand particles or iron carbonate, showed more active corrosion.

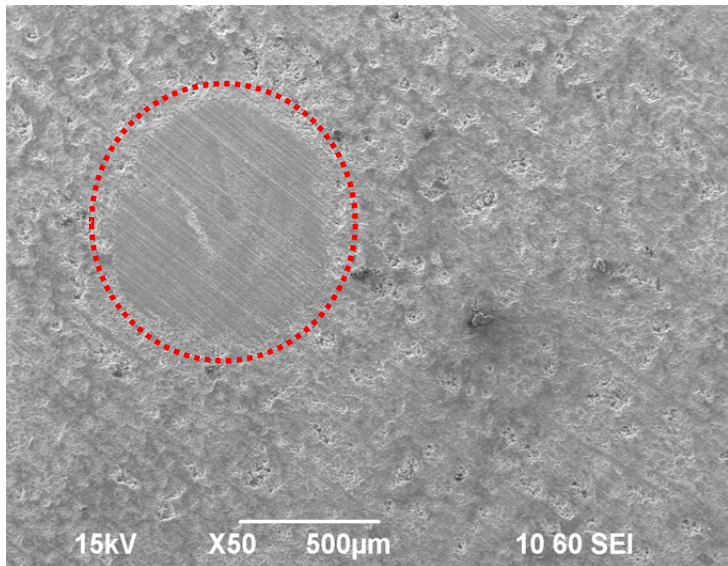


Figure 4.24 SEM image of mild steel after 5 days exposure in 1 wt% NaCl solution, pH 4.0 at 80 °C under 5 mm sand deposit (after surface scale removed)

⁴ Clarke solution is: 1000ml hydrochloric acid solution (HCl, specific gravity [sp.gr.] = 1.19) + 20 g antimony trioxide (Sb_2O_3) + 50g stannous chloride ($SnCl_2$), recommended by ASTM G1 standard.

A typical image of steel surface after corrosion product removal scanned by a infinite focusing microscopy is shown in Figure 4.25. It clearly shows that the areas not covered by silica sand corroded more, as indicated by about 28 μm depth developed due to corrosion.

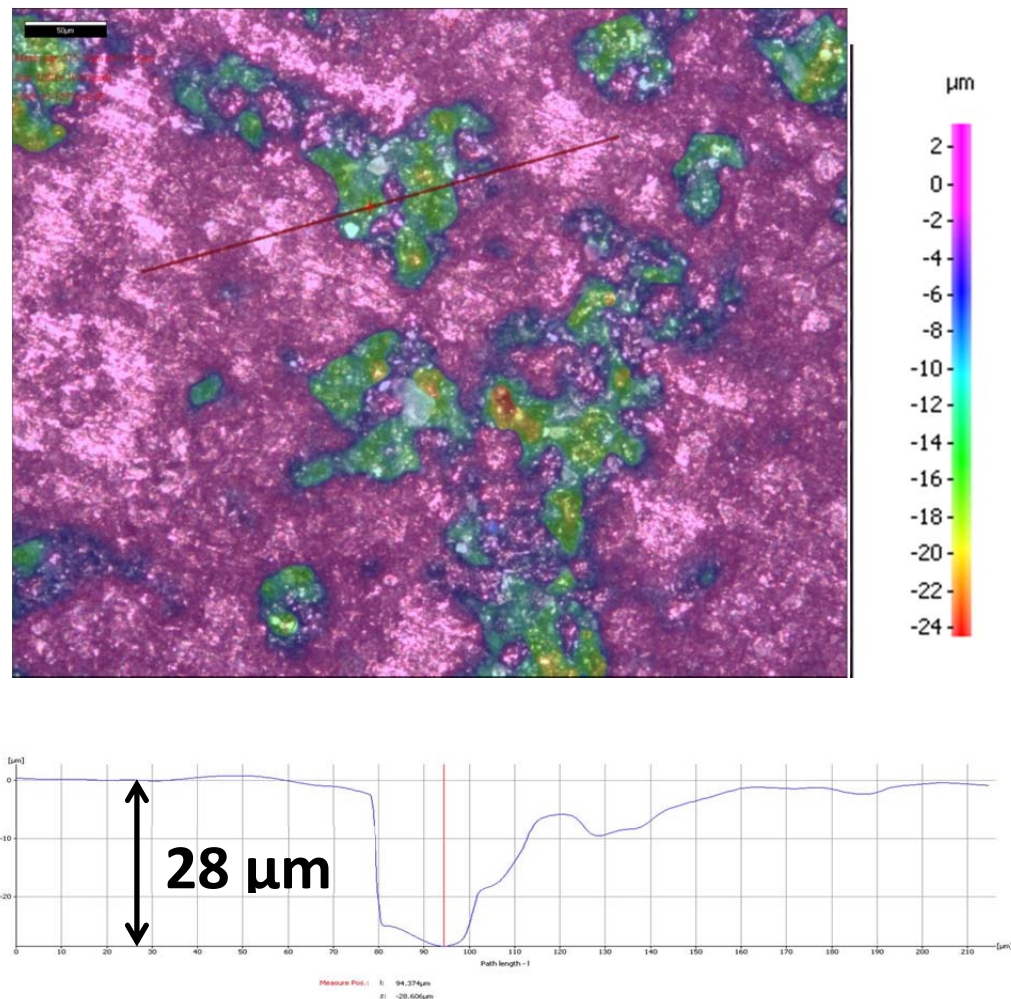


Figure 4.25 An image of infinite focusing microscopy scanning of the steel surface after 5 days exposure in 1 wt% NaCl solution, pH 4.0, at 80°C under 5 mm sand deposit (after surface scale was removed)

The above surface morphology analysis suggested that locations where the metal surface was fully blocked by sand particles could have acted as cathodes while more open areas within the pores of the deposit or nearby were more active and acted as anodes. Although the anode/cathode relationship would suggest local galvanic cells existed, no localized corrosion problem was expected to happen, because the sand covered areas were cathodically protected and had a smaller area than the surrounding areas which were corroding more actively. So the galvanic cell had a small cathode/large anode configuration, where localized corrosion wouldn't be expected.

The surface analysis show that locations where the sand particles were in direct contact with the metal surface corrode less than the areas around them. The deepest areas of metal loss found on the sample surface from Infinite focusing microscopy scanning have an average depth of 28 μm which corresponds to an average corrosion rate of 1.7 mm/yr for this 5 days' experiment. However, as shown in

Figure 4.21, the average corrosion rate calculated from LPR was about 0.6 mm/yr. These two corrosion rates seem very different, but can be justified as explained below. The corrosion rate calculated from LPR measurements takes into account the whole metal surface as if it is corroding uniformly, but when silica sand deposit was present, the steel surface was not homogeneously corroding, with some parts being more active while other become less active. A very simple method to relate the LPR measurement to the observed metal loss was to assume (confirmed from visual observation) that corrosion only occurred between the sand particles. This area can be directly related to the porosity. Therefore:

$$\text{Effective corroding surface} = \text{total area} \times \text{deposit porosity} = 8 \text{ cm}^2 \times 39\%$$

So the corrosion rate calculated from LPR could be corrected to:

$$0.66 \text{ mm/yr} / 39\% = 1.54 \text{ mm/yr}$$

This value is more consistent with corrosion rate obtained from the Infinite focusing microscopy scanning (1.7 mm/yr). Even though there are several embedded assumptions in this calculation, the corrosion observed “around” the sand particles was of the same order of magnitude as the electrochemically measured value and should not be considered as “accelerated localized” corrosion around the sand particles.

A similar experiment was conducted following the same experimental procedure but lasted up to 10 days. The corrosion rate decreased from around 3.7mm/yr for bare steel to about 0.5mm/yr after the sand deposit was introduced (see Figure 4.26). EIS measurements (Figure 4.27) further confirmed that a mass transfer effect appeared and strengthened over time as the characteristic frequency for the mass transfer effect was shifting with time to lower frequency range (0.01 – 0.001 Hz). SEM analysis indicate that after 10 days’ corrosion, there was a layer of iron carbonate scale formed on metal surface (see Figure 4.28), and the scale looked denser than what was observed in 5 days experiment (Figure 4.23). Comparing the data for the first 5 days verifies the repeatability of the experiments.

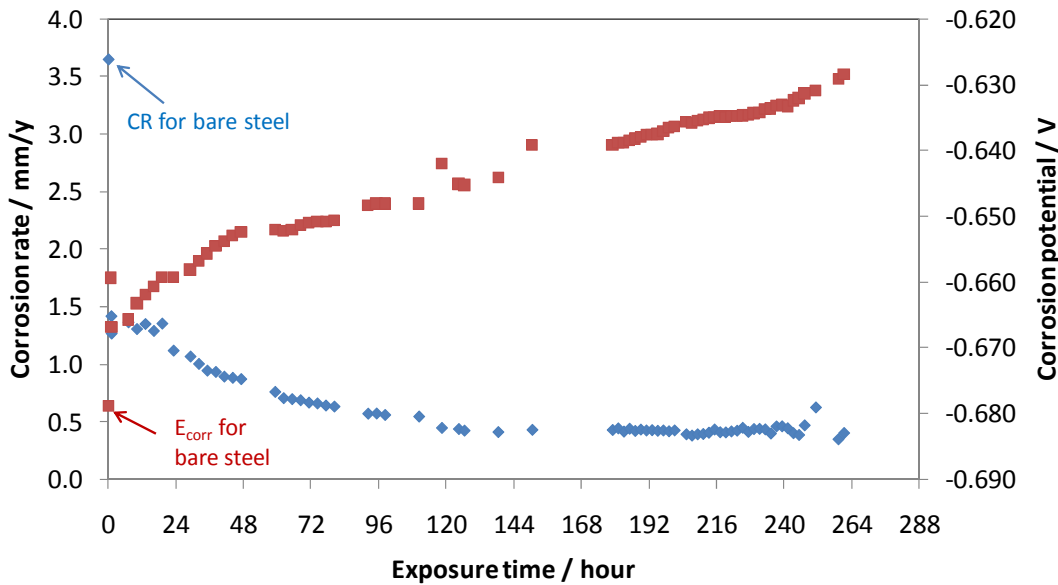


Figure 4.26 LPR corrosion rate and corrosion potential over time at test conditions 80°C,
1 wt% NaCl, pH 5.0, 5 mm silica sand deposit.

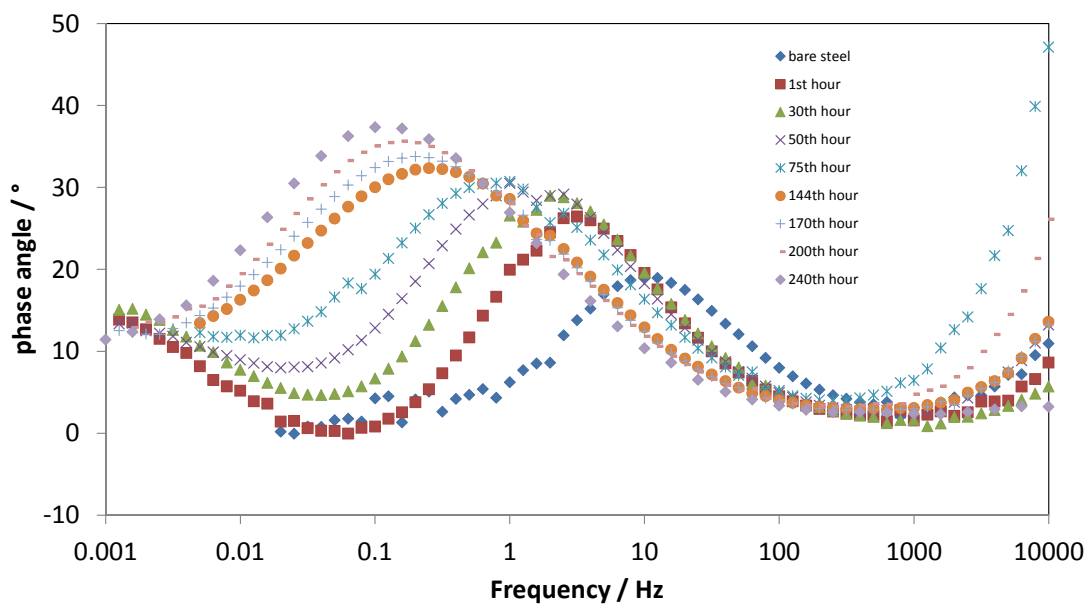


Figure 4.27 EIS Nyquist plots at different exposure time at test conditions 80°C, 1 wt%
NaCl solution, pH = 5.0, 5 mm silica sand deposit.

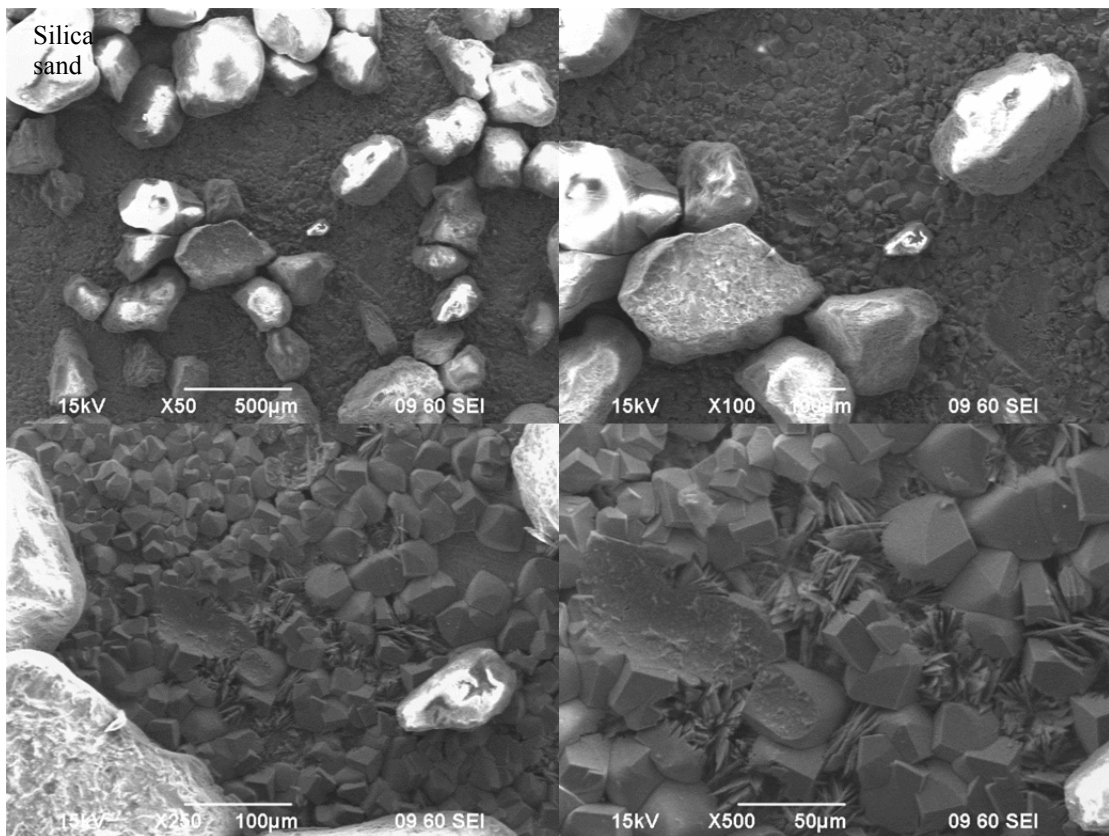


Figure 4.28 SEM image of steel surface after 10 days exposure at test conditions 80°C, 1 wt% NaCl solution, pH 5.0, 5 mm silica sand deposit.

4.4 Electrochemical Modeling

4.4.1 Summary of Experimental Observations

- Both anodic and cathodic current were reduced after solid deposit were added onto metal surface.
- No bulk pH dependency was observed.
- No temperature dependency was found.

- Iron carbonate crystals were observed on metal surface at test conditions where no iron carbonate layers were able to form without deposits.
- No accelerated localized corrosion problem for the system under study.

4.4.2 Corrosion Rate Prediction

Main reactions considered in the model

CO_2 is hydrated to form carbonic acid in water:



which dissociates:



The hydrogen ion is then reduced to hydrogen:



In CO_2 corrosion, at pH range 4 to 6, the presence of CO_2 leads to a much higher corrosion rate than would be found in a solution of a strong acid at the same pH. This is because the presences of carbonic acid, whose dissociation is an additional source of hydrogen ions. In addition, the direct reduction of carbonic acid is another important cathodic reaction and makes the CO_2 environment more corrosive (Nešić, 1996):



Water reduction is considered as one of the cathodic reactions in the present model as well:



Cathodic reaction

H^+ reduction

Current from this reaction is calculated by the equation (Nešić, 1996):

$$\frac{1}{i_{(H^+)}^d} = \frac{1}{i_{\alpha(H^+)}^d} + \frac{1}{i_{\lim(H^+)}^d} \quad (4.7)$$

$$i_{(H^+)}^d = i_{0(H^+)} \times \left\{ \frac{[H^+]_s}{[H^+]_b} \cdot \exp\left(-\frac{\alpha_c F}{RT} \eta\right) \right\} \quad (4.8)$$

where,

$$i_{\alpha(H^+)}^d = \varepsilon \cdot i_{0(H^+)} \times 10^{-\frac{\eta}{b_c}} \quad (4.9)$$

is the charge transfer current density. ε is deposit porosity.

$$i_{\lim(H^+)}^d = k_{m,eff} F [H^+]_b \quad (4.10)$$

is the limiting current density.

The parameters in the above equations are:

Tafel slope at 25°C (Bockris, 1961):

$$b_c = \frac{2.303RT}{\alpha_c F} \quad (4.11)$$

$$\alpha_c = 0.5 \quad (4.12)$$

gives:

$$b_c = 0.118V \quad (4.13)$$

Exchange current density (Bockris, 1961):

$$\frac{\partial \log i_{0(H^+)}^-}{\partial pH} = -0.5 \quad (4.14)$$

Reversible potential:

$$E_{rev(H^+)} = -\frac{2.303RT}{F} pH - \frac{2.303RT}{2F} \log p_{H_2} \quad (4.15)$$

Mass-transfer coefficient k_m :

k_m is calculated in Nešić's model (1996) by taking account of the flow effect.

However, in this work, all experiments were conducted in a stagnant solution with inert inorganic silica deposit. Therefore, in the first approximation, the permeability (κ) of surface layers for transport of species was considered to be dependent on the amount of pores in the layers, expressed as superficial porosity ε_s and the shape and connections between the pores, expressed as the tortuosity ψ :

$$\kappa = \psi \varepsilon_s \quad (4.16)$$

It was found that the superficial porosity is approximately equal to volumetric porosity and the tortuosity is related to porosity and deposit layer thickness:

$$k_{m,eff} = \frac{D_{H^+} \cdot \varepsilon^{1.3}}{L} \quad (4.17)$$

where L is deposit thickness.

H_2CO_3 reduction

The current density contributed by H_2CO_3 reduction is derived in a similar way as H^+ reduction discussed above:

$$\frac{1}{i_{(H_2CO_3)}} = \frac{1}{i_{\alpha(H_2CO_3)}} + \frac{1}{i_{lim(H_2CO_3)}^r} \quad (4.18)$$

At stagnant conditions, the chemical reaction limiting current density $i_{\text{lim}(H_2CO_3)}^r$ is found as:

$$i_{\text{lim}(H_2CO_3)}^r = F \cdot C_{CO_2} \cdot (L^{-1} D_{\text{eff}})^{0.5} \quad (4.19)$$

The effect of deposit is expressed in the effective diffusion coefficient as:

$$D_{\text{eff}} = D \cdot \varepsilon^{1.3} \quad (4.20)$$

and

$$C_{CO_2,b} = k_{CO_2}^d \times p_{CO_2} \quad (4.21)$$

Where $k_{CO_2}^d$ is Henry's constant and is a function of temperature (Nešić, 1996):

$$k_{CO_2}^d = 0.0454(1.6616 - 5.736 \times 10^{-2}t + 1.031 \times 10^{-3}t^2 - 9.68 \times 10^{-6}t^3 + 4.471 \times 10^{-8}t^4 - 7.912 \times 10^{-11}t^5) \quad (4.22)$$

H₂O reduction

Water is present in unlimited quantities at the metal surface. It is then proposed that water reduction is a charge-transfer process. *Tafel* behavior is followed:

$$i_{H_2O} = i_{0,H_2O} \times 10^{\frac{-\eta}{b_c}} \quad (4.23)$$

It was determined experimentally (Nešić, 1996) that the exchange current density for water reduction is:

$$i_{0,H_2O} \approx 3 \times 10^{-5} \text{ A/m}^2 \quad (4.24)$$

Anodic reactions

Iron dissolution in water is the only reaction considered in anodic part:



From the experimental observation, the iron dissolution is under charge transfer control:

$$i_{Fe} = i_{0,Fe} \times 10^{\frac{\eta}{b_a}} \quad (4.26)$$

where according to Bockris (1961)

$$b_a = 40 \text{ mv} \quad (4.27)$$

4.4.3 Model Verification

4.4.3.1 Bare Steel Corrosion Rate Prediction

For under deposit CO₂ corrosion of mild steel, surface coverage effect and mass transfer effect of the silica deposit was considered. The surface coverage effect accounts for the part of the metal surface which is blocked by the deposited particles so that both anodic and cathodic reactions are retarded, and the charge transfer current density is therefore proportional to the available metal surface which is proportional to deposit porosity. To account for the mass transfer effect, the presence of deposit creates an additional mass transfer barrier for corrosive species.

The predicting under deposit CO₂ model can only be reasonable if it works also for bare steel condition. Figure 4.29 is the comparison of the potentiodynamic sweeps predicted from the present model with experiment data. It can be seen that the potentiodynamic sweeps capture the corrosion processes very well and the prediction is in good agreement with experiments.

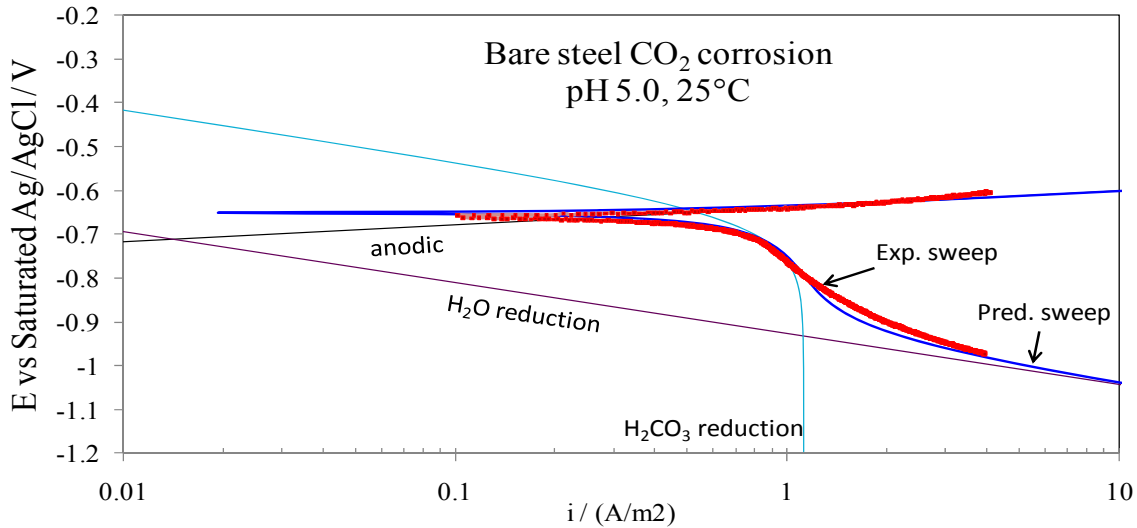


Figure 4.29 Potentiodynamic sweeps of CO_2 corrosion of bare X65 steel at pH 5, 25°C , 1

wt% NaCl solution, $p_{\text{CO}_2} = 0.96 \text{ bar}$.

4.4.3.2 Effect of Deposit Porosity

In Figure 4.30, potentiodynamic sweeps are compared for two different deposit porosities with bare steel at bulk solution pH 5.0 at 25°C . Experiment results are in reasonable agreement with the predictions of individual reactions generated with the present model. The anodic currents in the experiment with silica deposit are smaller than the one on bare steel, and the less porous the deposit is, the smaller the effective anodic current produces, because of the less available metal surface (since the current density is always calculated based on the total surface area). Also, the cathodic current in the case with the deposit layer is smaller than on bare steel, due to the retarded diffusion of corrosive species involved in cathodic reactions.

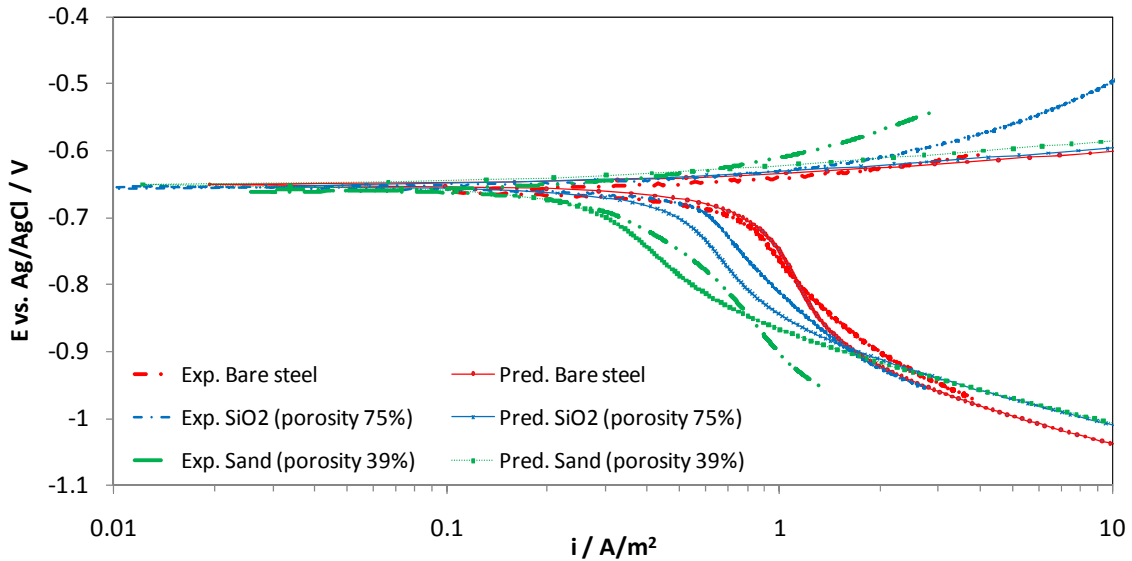


Figure 4.30 Potentiodynamic sweeps of CO_2 corrosion of X65 steel under different deposit at bulk solution pH 5, 25 °C, 1 wt% NaCl, $p_{\text{CO}_2} = 0.96$ bar, 2 mm deposit.

4.4.3.3 Effect of Deposit Thickness

In Figure 4.31, increasing the deposit thickness, the anodic current is not changed, because it only affects the mass transfer of corrosive species for cathodic reactions. The measured potentiodynamic sweeps are in good agreements with the prediction. The thicker the deposit, the more tortuous the diffusion of species therefore results in a smaller cathodic current.

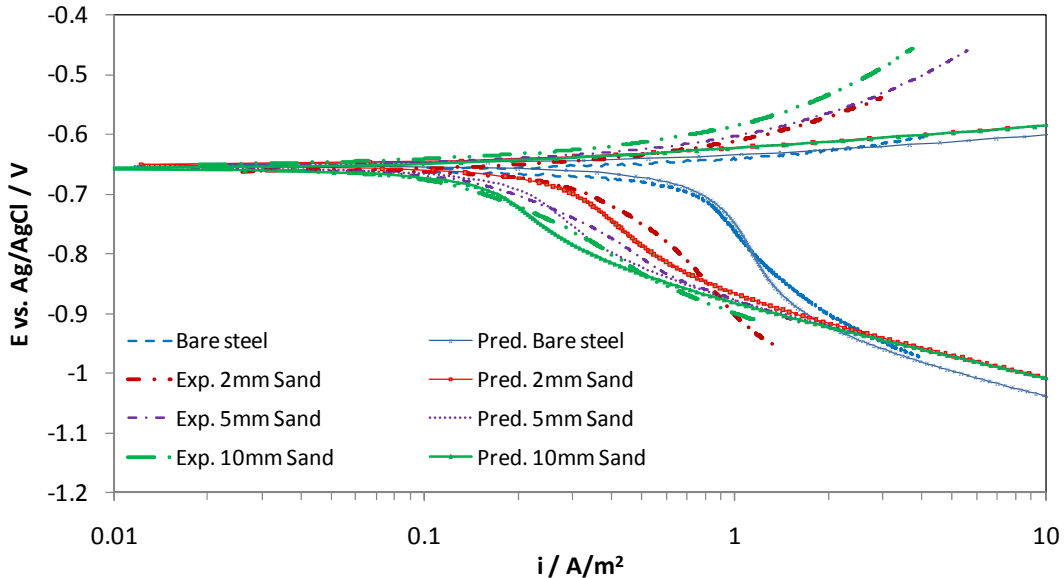


Figure 4.31 Potentiodynamic sweeps of CO_2 corrosion of X65 steel under silica sand deposit with different depth at bulk solution pH 5, 25°C , 1 wt% NaCl, $p_{\text{CO}_2} = 0.96$ bar, silica sand deposit porosity 39%/
silica sand deposit porosity 39%

4.4.3.4 Temperature Dependency

From experiment results, it was found that the corrosion rate of mild steel under deposit did not increase with elevated temperature which would be expected to happen in bare steel corrosion (Figure 4.32). Iron carbonate crystals were also observed on the metal surface under the deposit at test conditions where they are not expected to form given the bare steel corrosion. It is proposed that the iron carbonate layer formed because of one more mass transfer barrier being added for the diffusion of corrosive species including the hydrogen ions. By considering the additional mass transfer barrier effect,

the potentiodynamic sweeps predicted by the present model are in agreement with experimental results.

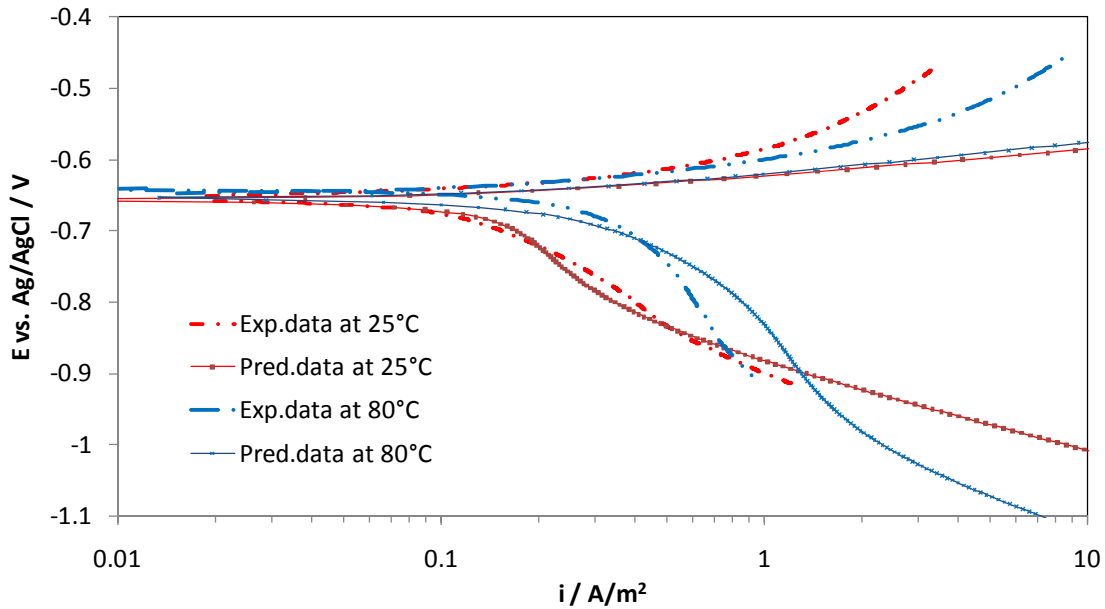


Figure 4.32 Potentiodynamic sweeps of CO_2 corrosion of X65 steel under 10 mm silica sand deposit at different temperature effect at bulk solution pH 5, 1 wt% NaCl, silica sand deposit porosity = 39%.

4.4.3.5 Under Deposit Corrosion Rate Prediction

The uniform corrosion rate predicted by the present model is compared with experimental measurement from LPR. Figure 4.33 compares the corrosion rate for different porosity, and Figure 4.34 is for different deposit thickness. The effect of temperature predicted by the model also agrees with experiments well, as shown in Figure 4.35. The B value used in calculating corrosion rate from LPR data is $B = 26 \text{ mV}$. The prediction of corrosion rate is in good agreements with experimental findings, except

for high temperature. At high temperature iron carbonate formed but was not considered in the present model.

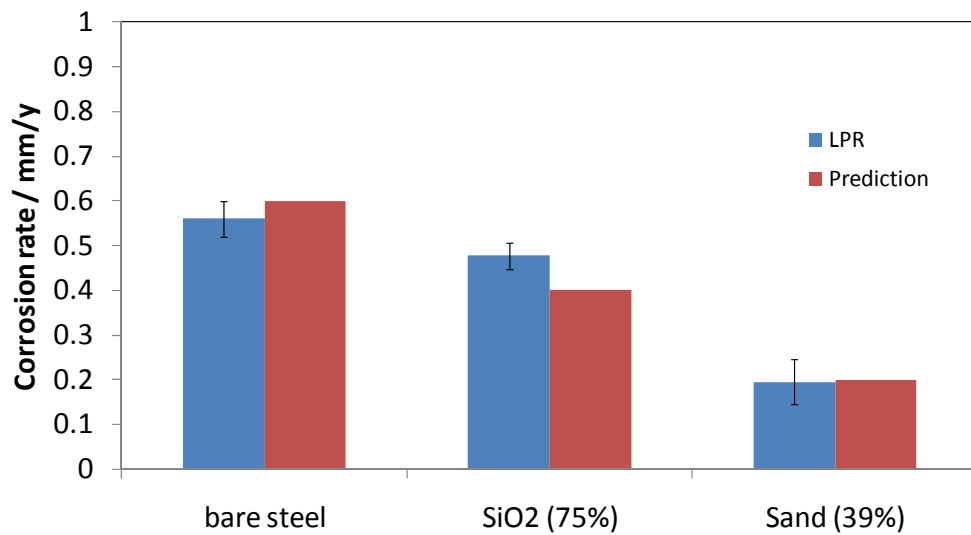


Figure 4.33 Comparison of predicted experimental measured under deposit corrosion rate; at bulk solution pH 5, 25 °C, 1 wt% NaCl solution, $p_{CO_2} = 0.96$ bar, 2 mm deposit.

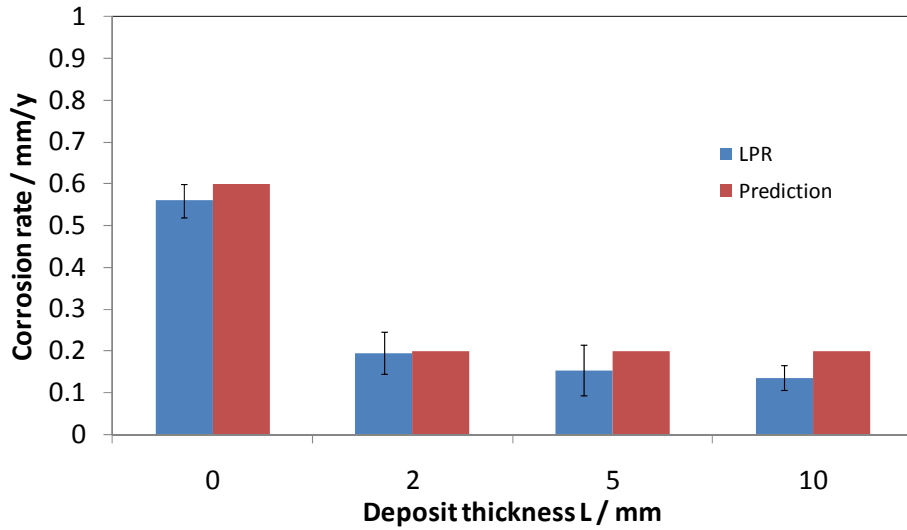


Figure 4.34 Comparison of predicted experimental measured corrosion rate under different depth of deposit; at bulk solution pH 5, 25 °C, 1 wt% NaCl, $p_{CO_2} = 0.96$ bar, silica sand deposit porosity = 39%.

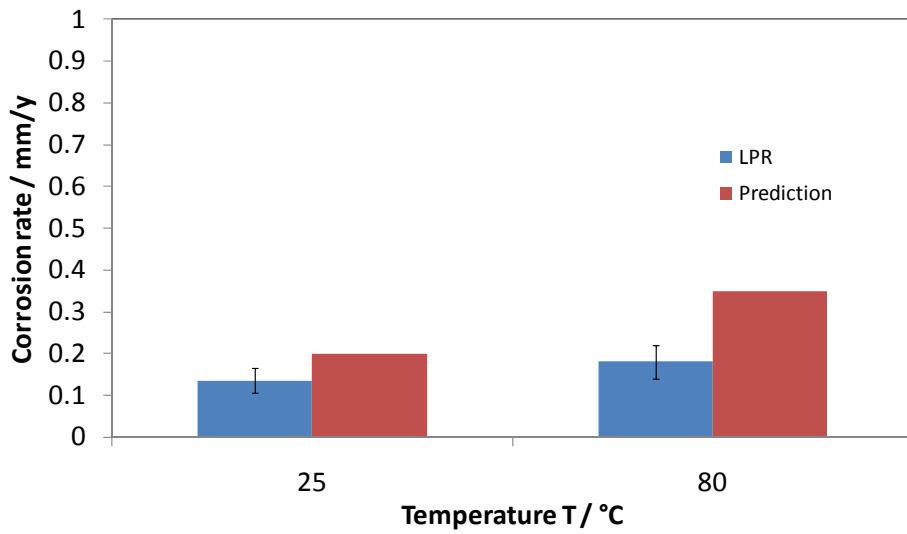


Figure 4.35 Comparison of predicted and measured corrosion rate under 10 mm silica sand deposit at different temperature; at bulk solution pH 5, 1 wt% NaCl, silica sand deposit porosity = 39%.

4.5 Summary

From all the experimental observations, it is verified that in CO₂ corrosion of mild steel in the presence of inorganic silica deposits, both the anodic and the cathodic reactions are retarded by the deposit due to the blocking of the corroding surface. The presence of deposit also causes a water chemistry difference between deposit covered areas and adjacent uncovered areas. This water chemistry difference results in a higher solution pH (1 – 2 units higher than bulk) on steel surface and promotes iron carbonate formation, which acts as a further mass transfer barrier for diffusion. The difference in water chemistry also can lead to a formation of a galvanic cell, which however, in this case, doesn't cause accelerated localized corrosion problem. The results and discussion presented in this section demonstrate that the well-established mechanistic electrochemical model, when corrected for the effects of surface coverage and diffusion, captures the characteristic features of the under deposit corrosion of mild steel in aqueous CO₂ corrosion and is capable of predicting the under deposit corrosion rate.

CHAPTER 5. INHIBITION OF CO₂ CORROSION OF MILD STEEL UNDER SILICA SAND DEPOSITS

5.1 Introduction

Real scenarios for under deposit CO₂ corrosion found in oil/gas pipelines are almost always associated with the use of corrosion inhibitors. The presence of solids, especially in the form of deposits, impacts inhibitor performance. Many studies have been conducted focusing on the effects of solid deposits on inhibitor performance and selection. Contradictory observations have been reported regarding inhibitor's performance when solid settled (Pederson, 2008; de Reus 2005; Turnbull 2009). Consensus has not yet been reached on whether unintended adsorption of corrosion inhibitors on solid deposit surface is the cause of poor corrosion inhibitor performance. In this chapter, generic corrosion inhibitors with only a single active component were chosen for under deposit corrosion experiments. The effect of environment factors such as pH, temperature as well as deposit characteristics on inhibition of corrosion will also be discussed. The inhibition mechanisms of different types of corrosion inhibitors under silica sand deposit will be proposed and evaluated.

5.2 Experimental Method

5.2.1 *Experimental Setup*

Experiments were conducted at atmospheric pressure in the same three-electrode glass cell setup, as shown in Chapter 4. A concentric ring made from platinum wire was used as the counter electrode (CE). A KCl saturated silver-silver chloride (Ag/AgCl) electrode was chosen as the external reference electrode (RE) and was connected to the

test solution *via* a Luggin capillary. The working electrode (WE) specimen was a cylindrical mild steel disc. A temperature probe was connected to a heater to control the test solution temperature. A glass pH probe was also immersed in the solution to monitor the bulk pH during the experiment. CO₂ gas was purged into the test solution before and during each experiment to maintain a de-oxygenated and a CO₂ saturated environment. The test solution was: two liters of DI water with 1 wt% sodium chloride (NaCl). The WE was mounted onto a holder which was connected with CE and RE to a potentiostat for electrochemical measurements during the experiment. The uniform corrosion process was monitored using electrochemical techniques including linear polarization resistance (LPR) and electrochemical impedance spectroscopy (EIS). After the experiments, the specimen surface morphology was analyzed by using a scanning electron microscope (SEM) and the localized corrosion was investigated using a infinite focusing microscopy.

5.2.2 Deposit

For silica deposit, two different particle sizes were chosen: 750 µm and 250 µm. SEM images of these particles are shown in Figure 5.1. Unless specified otherwise, deposits were cleaned with DI water and were stored in test solution saturated by CO₂ prior to experiment. A pipette was used to transfer the deposit material onto the corroding specimen for each experiment.

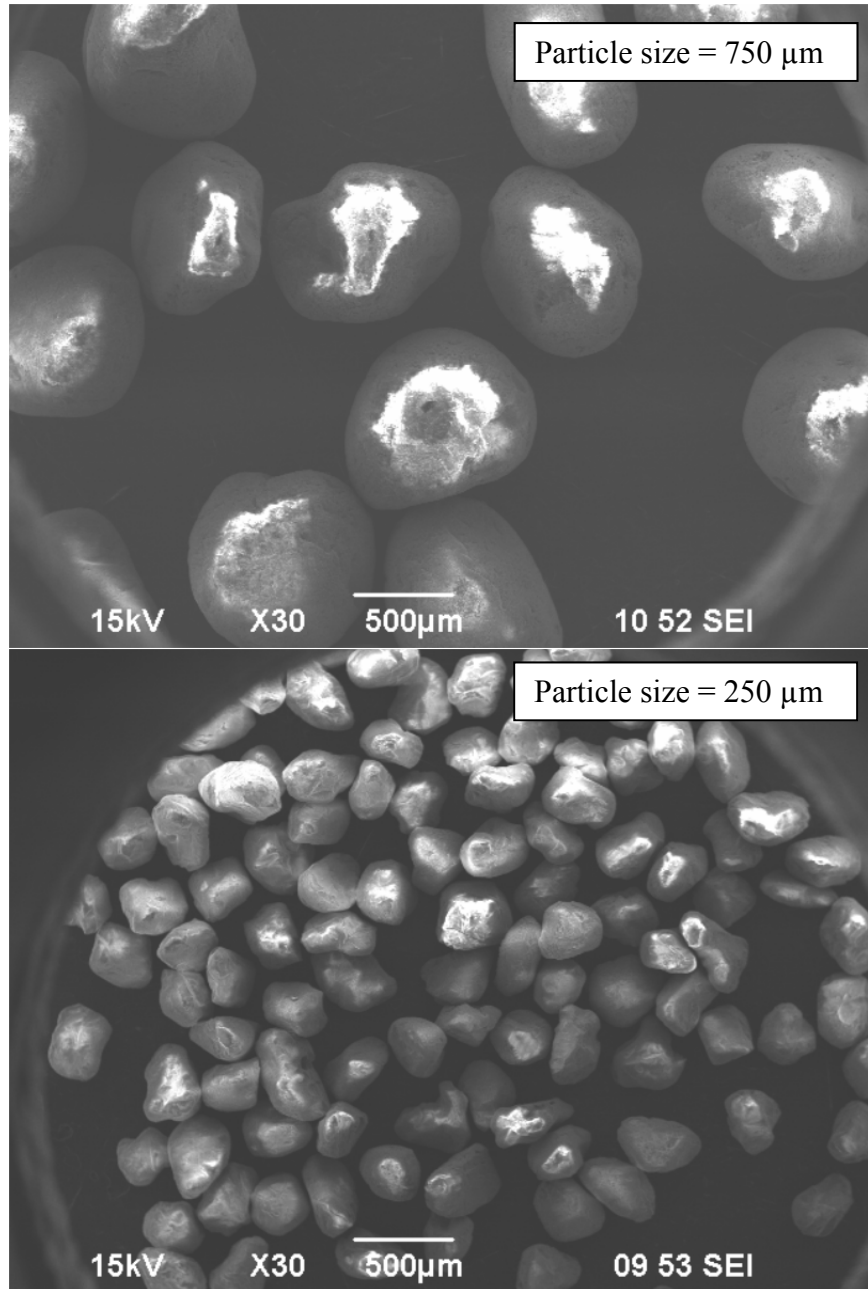


Figure 5.1 SEM images of silica particles of different sizes.

5.3 Inhibitor

Four different generic corrosion inhibitor packages designated in-house as “K1” to “K4” were used in this work. The active components are imidazoline in K1, quaternary amine in K2, and thiosulfate in K3, respectively, while K4 is a blend of K1 and K3.

Generic imidazoline inhibitor and quaternary amine inhibitors were proven to inhibit mild steel CO₂ corrosion by physically adsorbing on the steel surface and thereby impeding the migration of water and electrons to the steel surface (Alsabagh, 2006; Zhang, 2001). Thiosulfate is believed to be able to reduce corrosion by reacting with iron and forming a chemical bond with the steel surface. However, how exactly thiosulfate protects the steel from corrosion is still under debate (Yao, 2012). The formulation of each corrosion inhibitor used in this study is shown in Table 5.1.

Table 5.1 Inhibitors used for present work.

Product	Description	Active ingredient	Components	Concentration used in the experiments
K1	Generic	TOFA/DETA imidazoline	10% CH_3COOH 13% $\text{C}_4\text{H}_9\text{OCH}_2\text{CH}_2\text{OH}$ 24% TOFA/DETA imidazoline Balance water	70 ppm
K2	Generic	Alkylbenzyl dimethyl ammonium chloride	48% Alkylbenzyl dimethyl ammonium chloride Balance water	220 ppm
K3	Generic	Sodium thiosulfate	37.66% $\text{Na}_2\text{S}_2\text{O}_3 \cdot 5\text{H}_2\text{O}$ Balance water	30 ppm
K4	Blends	TOFA/DETA imidazoline + sodium thiosulfate	10% CH_3COOH 13% $\text{C}_4\text{H}_9\text{OCH}_2\text{CH}_2\text{OH}$ 20% TOFA/DETA imidazoline 6.28% $\text{Na}_2\text{S}_2\text{O}_3 \cdot 5\text{H}_2\text{O}$ Balance water	430 ppm

5.2.4 Experimental Procedure

The experimental procedure for experiments conducted in inhibited environment was similar to the one described in Chapter 4, except for the addition of inhibitors. The test solution was heated to the desired temperature and at the same time deoxygenated by continuously purging with CO₂ gas for at least 1 hour. Once the test solution was saturated with CO₂, the pH of the solution was adjusted to the designated value by adding either a deoxygenated sodium bicarbonate (NaHCO₃) or a de-oxygenated hydrochloric acid (HCl) solution. The pH was monitored and recorded regularly. After the test solution was prepared, the API 5L X65 specimen was polished with 200, 400 and 600 grit sand paper sequentially under a continuous rinse by isopropyl alcohol and air dried. The specimen was then mounted onto the specimen holder and immersed into the prepared test solution, and the experiment was started.

Initially, the API 5L X65 specimen was corroded for 24 hours without a deposit, while the open circuit potential and the uniform corrosion rate (as measured by LPR) were monitored. Electrochemical impedance spectroscopy (EIS) measurements were also conducted to determine the solution resistance in order to compensate the polarization resistance for the IR drop in the solution (this was done manually during post-processing of the data). This electrochemical response of the bare steel was taken as a reference behavior for later evaluation of the deposit effects. In each under deposit corrosion experiment, the specimen was first corroded without a deposit for an hour (pre-corrosion), while the open circuit potential, corrosion rate (LPR) and solution resistance (EIS) was recorded. The experiment proceeded to the under deposit stage only when the

initial bare steel corrosion process was in the expected range. After the deposit was added, the open circuit potential, corrosion rate (LPR) and solution resistance (EIS) was monitored once every two hours until the end of the experiment. At the end of the experiment, the specimen was taken out of the solution, rinsed (dehydrated) with isopropyl alcohol, dried with cool air, and stored in a desiccator for surface analysis (SEM and EDX). Then the corrosion product scales were also removed for localized corrosion analysis.

During the LPR measurements, the WE was polarized ± 5 mV from the open circuit potential (E_{oc}) at a scan rate of 0.125 mV/s to obtain the polarization resistance (R_p), which was then used to calculate the uniform corrosion rate of the steel. For the EIS measurement, a sinusoidal potential signal ± 5 mV peak-to-peak around E_{oc} was applied to the working electrode with scanning frequencies from 5 kHz to 1 mHz. Experimental conditions are summarized in Table 5.2.

Table 5.2 Experiment conditions.

Parameter	Conditions
Material	API 5L X65 mild steel
Test solution	DI water + 1wt% NaCl
Temperature	25°C & 80°C
CO ₂ partial pressure	0.96 bar & 0.54 bar, respectively, with temperature
Solution pH	5
Deposit	Silica sand
Sweep rate	0.125 mV/s
Polarization resistance	From -5 mV to 5 mV vs. E_{oc}
AC impedance	±5 mV vs. E_{oc} from 5 kHz to 1 mHz

5.4 Results and Discussion

5.4.1 K1 (Imidazoline) Performance Under Sand Deposit

Imidazoline has been known as an effective inhibitor for CO₂ corrosion of mild steel. To compare the effect of sand deposit on K1's performance, the inhibitor efficiency of K1 on bare steel was first tested. Figure 5.2 shows the variation of uniform corrosion rate with time obtained from LPR measurements. It can be seen that the corrosion rate dropped dramatically after the addition of 70 ppm K1. The presence of K1 induced a 50 mV increase in corrosion potential while the corrosion rate decreased to about 0.15 mm/y after 25 hours achieving 90% inhibitor efficiency. The results of inhibition performance

on bare steel were consistent with previous work, which shows the appropriateness of the inhibitor K1 (imidazoline) used for the current study.

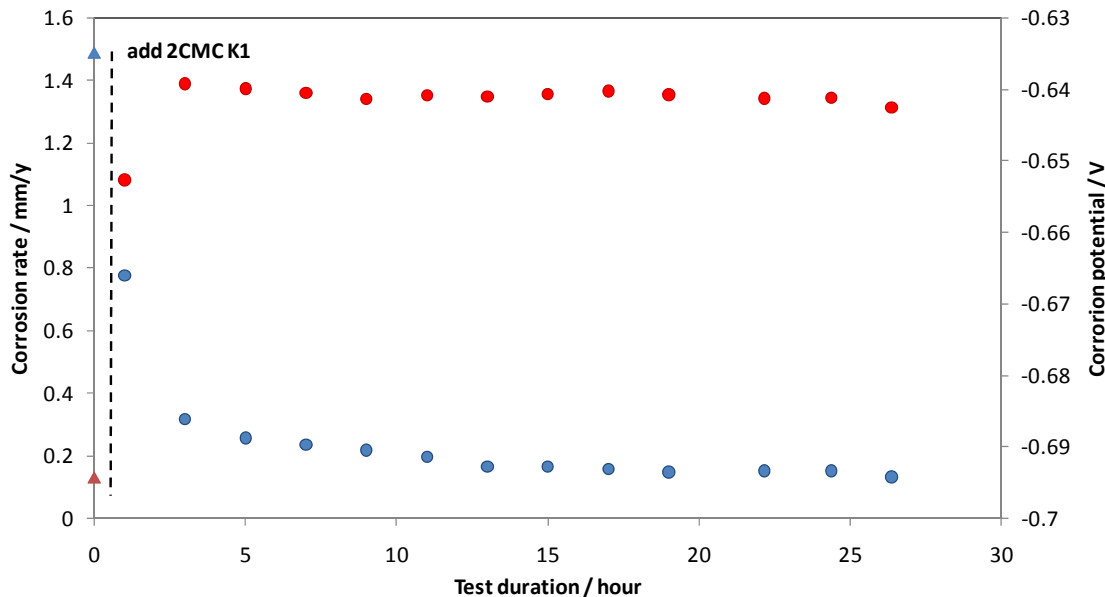


Figure 5.2 LPR corrosion rate and corrosion potential over time at test conditions T = 25°C, 1 wt% NaCl, pH 5.0, 70 ppm K1 added on a bare steel surface.

The performance of K1 on mild steel in the presence of 2 mm silica sand deposit was then studied and compared to the same experiment done with bare steel. The variation of uniform LPR corrosion rate under conditions with sand deposit is shown in Figure 5.3. It can be seen that the sand deposit had a significant effect on K1's performance. In the presence of this sand deposit, the addition of K1 didn't reduce the uniform corrosion rate of mild steel as it did on the bare steel surface (final corrosion rate: 0.45 mm/y vs. 0.15 mm/y).

EIS measurement (

Figure 5.4) further confirmed the observation that addition of K1 did not change the uniform corrosion rate of mild steel in the presence of a 2 mm sand deposit. After sand deposit was added, the shape of Nyquist plots changed and one inductive loop appeared which has been previously discussed in Chapter 4. After K1 was added, no significant change in Nyquist plots can be noticed.

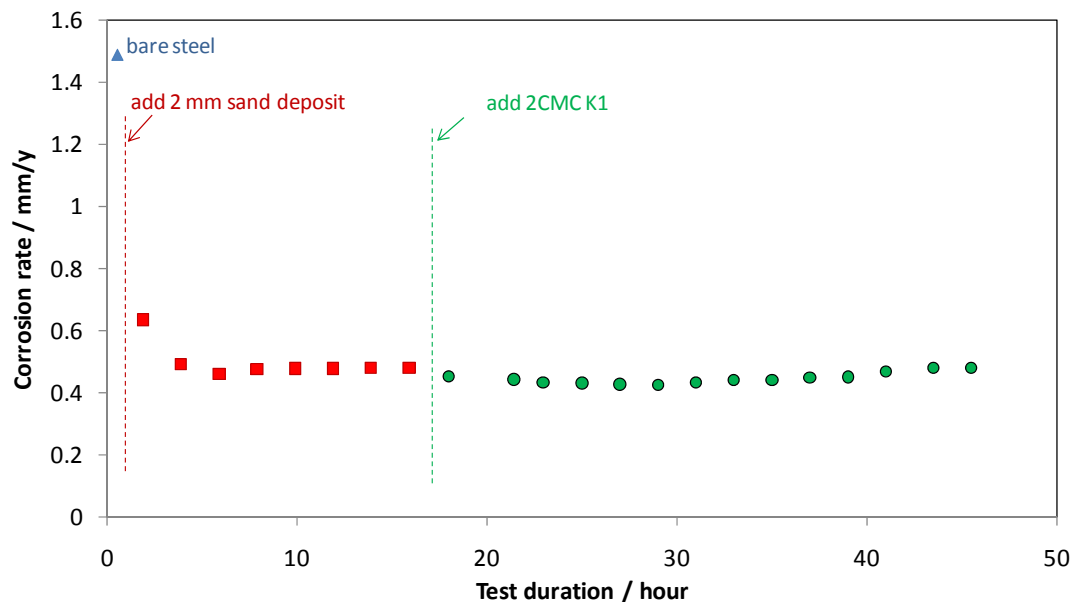


Figure 5.3 LPR corrosion rate over time at test conditions T = 25°C, 1 wt% NaCl, pH 5.0, 2 mm sand deposit presented prior to 70 ppm K1 (imidazoline) addition.

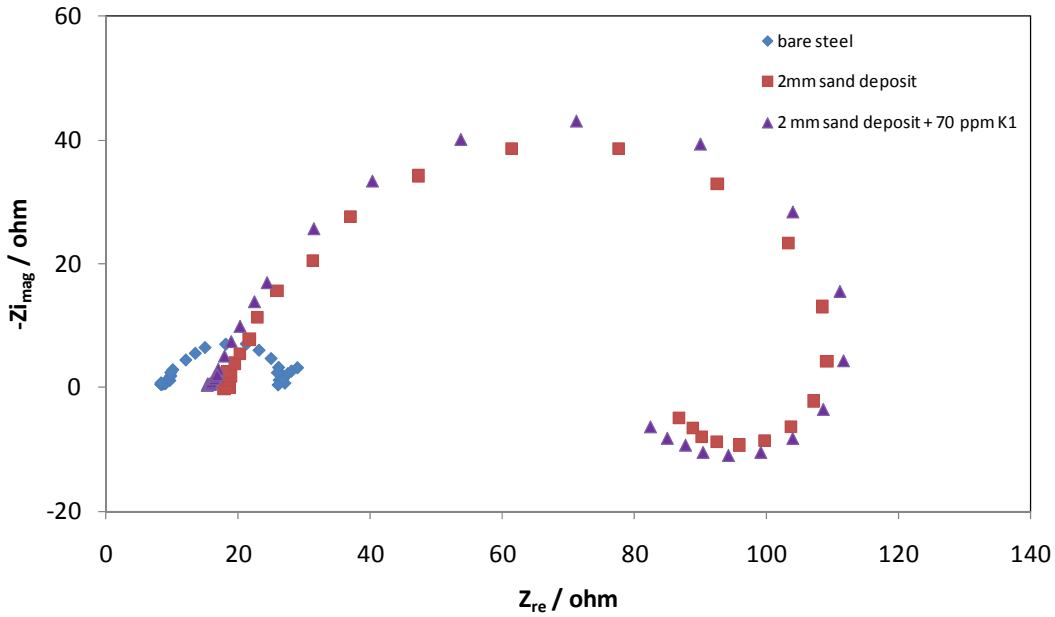


Figure 5.4 EIS Nyquist plots at 24 hours exposure at test conditions 25°C, 1 wt% NaCl, pH 5.0, 2 mm sand deposit presented prior to 70 ppm K1 (imidazoline) addition.

5.4.2 K2 (Ammonium Chloride) Performance

Figure 5.5 shows the change of corrosion rate after 220 ppm K2 (ammonium chloride) was added on bare steel. General LPR corrosion rate the X65 steel decreased immediately after and 95% corrosion inhibition was achieved in 8 hours. When a 2 mm silica deposit was present on the steel surface before the addition of K2, however, no effect of the K2 in further reducing the general LPR corrosion rate can be observed, similar to what has been seen in the case with K1. The measurements by LPR and EIS are shown in Figure 5.6 and Figure 5.7 respectively.

Both K1 and K2 are surfactant inhibitors, their inhibition mechanisms are believed to be dependent on forming a very thin film on the steel surface so as to impede the adsorption and reaction of corrosive species. The results indicate a similar behavior of K1 and K2, i.e., they both did not change the uniform corrosion rate of mild steel under the silica deposit.

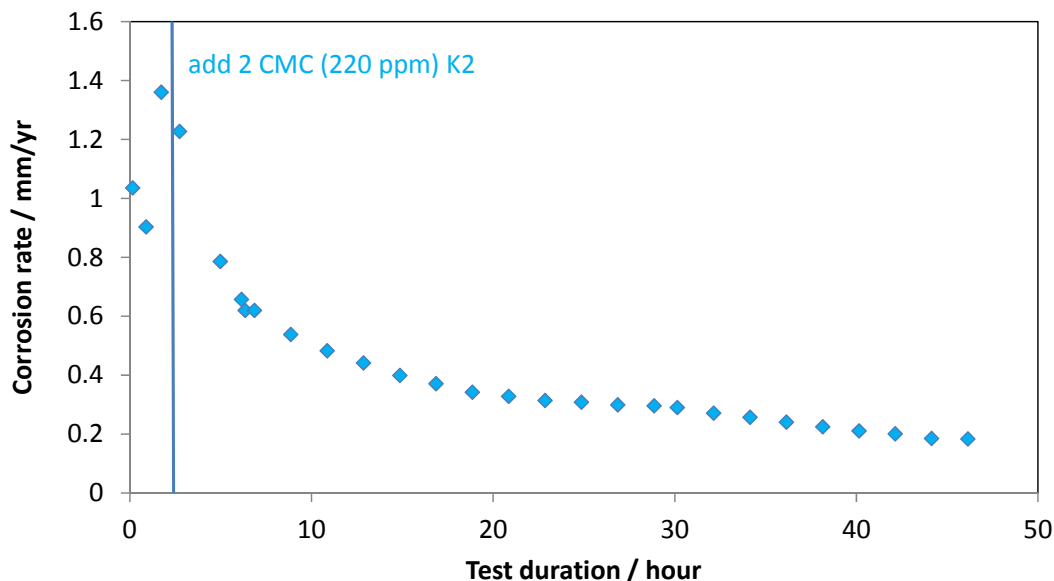


Figure 5.5 LPR corrosion rate over time at test conditions T = 25°C, 1 wt% NaCl, pH 5.0, 220 ppm K2 (ammonium chloride) added on a bare steel surface.

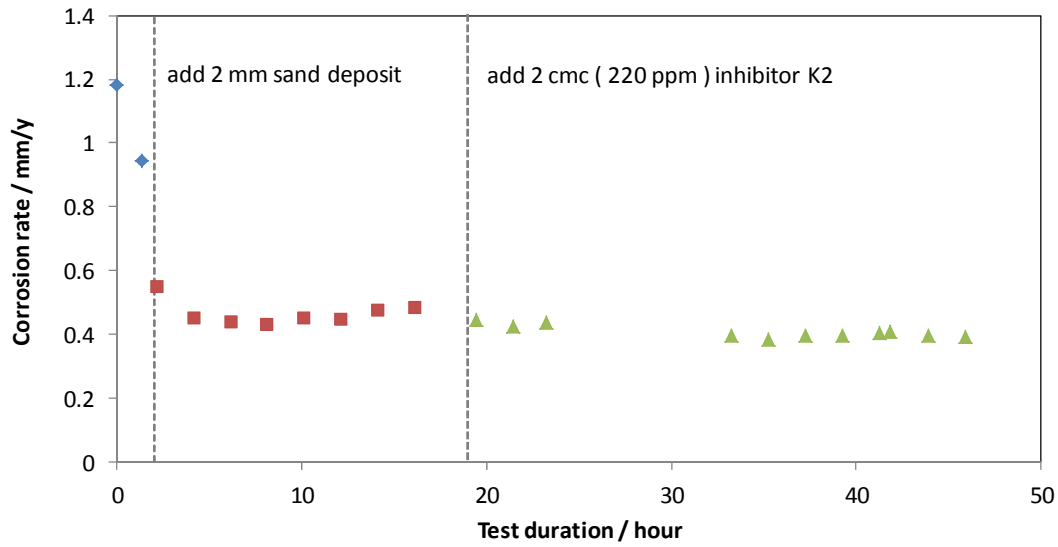


Figure 5.6 LPR corrosion rate over time at test conditions $T = 25^\circ\text{C}$, 1 wt% NaCl, pH 5.0, 2 mm sand deposit presented prior to 220 ppm K2 (ammonium chloride) addition.

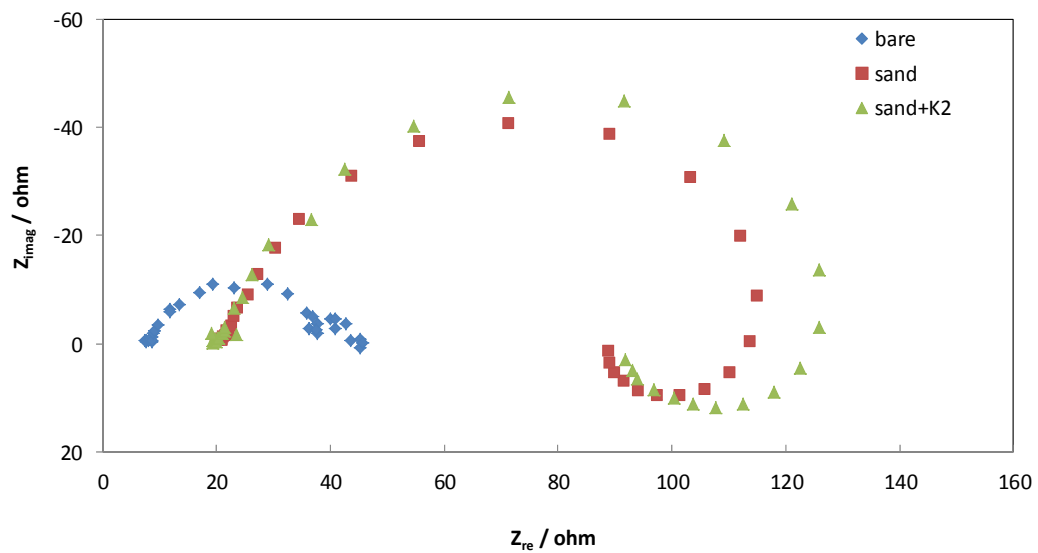


Figure 5.7 EIS Nyquist plots at 24 hours exposure at test conditions 25°C , 1 wt% NaCl, pH 5.0, 2 mm sand deposit presented prior to 220 ppm (ammonium chloride) K2 addition.

5.4.3 K3 (Thiosulfate) Performance

K3 (thiosulfate) is not a surfactant, but is rather expected to undergo a chemical bonding to iron surface (Nyborg, 2000). The amount of K3 added was determined by corrosion experiments, where the minimum amount of K3 needed to reach a 95% inhibition efficiency was designed (Canto, 2011). Followed by a similar procedure, K3's inhibition efficiency on bare steel was firstly tested and then compared when added in the presence of a silica deposit. Figure 5.8 shows that K3 was able to decrease the uniform corrosion rate of a bare steel surface from 1.6 mm/y to about 0.25 mm/y, reaching an efficiency of 95% in 5 hours.

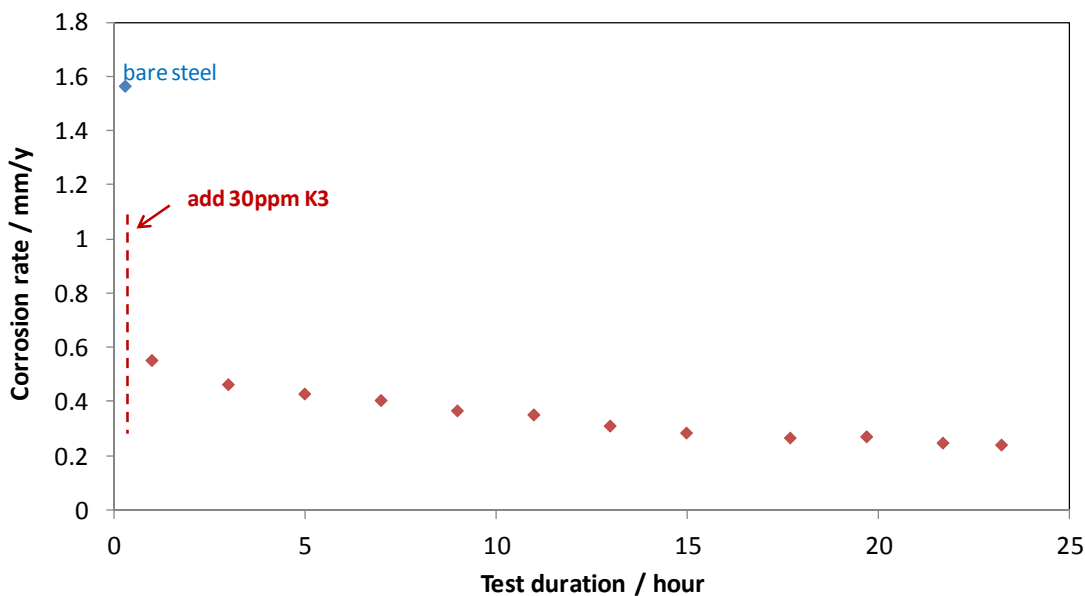


Figure 5.8 LPR corrosion rate over time at test conditions T = 25°C, 1 wt% NaCl, pH 5.0, 30 ppm K3 (thiosulfate) added on a bare steel surface.

With 2 mm silica sand deposit present, K3 was still able to further retard the corrosion rate of the steel by 95%, as can be seen in Figure 5.9. The corrosion rate before K3 addition was about 0.4 mm/yr. Then the corrosion rate decreased to 0.1 mm/yr by 30 ppm K3. The EIS measurements also show the good inhibition of K3 on the sand deposit (Figure 5.10). The presence of silica deposit did not affect K3's performance, which was contrary to the cases with K1 and K2. From EIS measurement, it can also be noticed that the inductive loop that always showed up when sand deposit was present, disappeared after K3's addition, which also indicates that a change of corrosion mechanism was found with addition of K3.

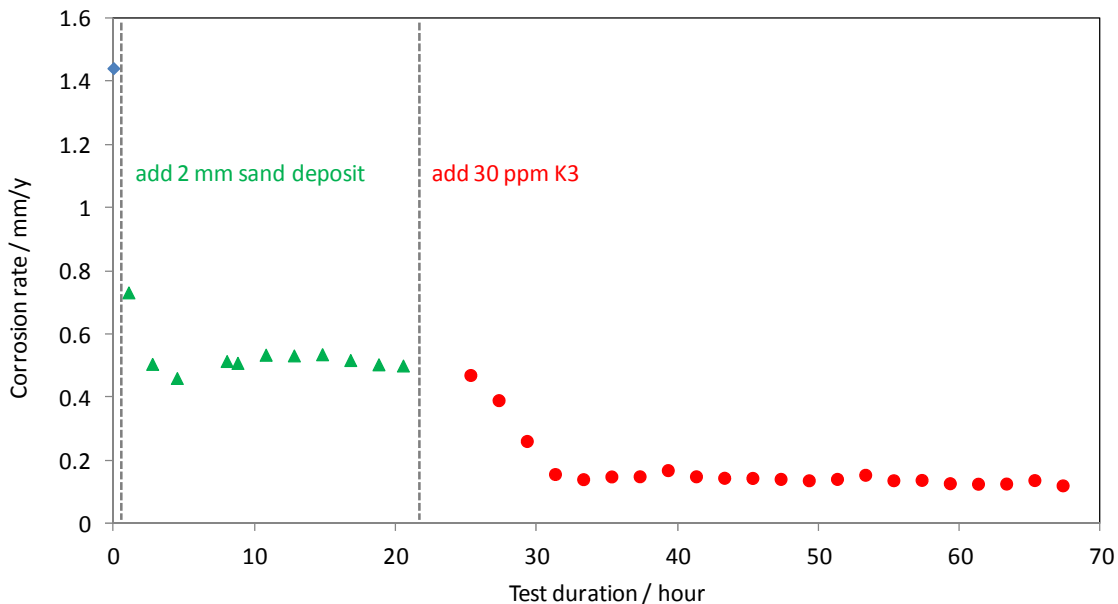


Figure 5.9 LPR corrosion rate over time at test conditions T = 25°C, 1 wt% NaCl, pH 5.0, 2 mm sand deposit presented prior to 30 ppm K3 (thiosulfate) addition.

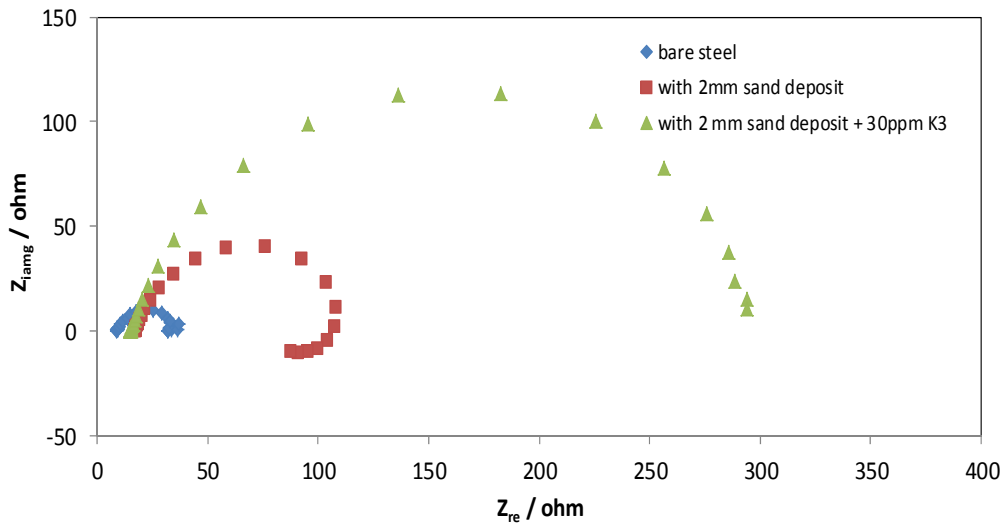


Figure 5.10 EIS Nyquist plots at 25 hours exposure at test conditions 25°C, 1 wt% NaCl, pH 5.0, 2 mm sand deposit presented prior to 30 ppm K3 (thiosulfate) addition.

5.4.4 K4 Performance

Since silica deposit had opposing effects on the performance of surfactant inhibitor (K1 (imidazoline) or K2 (ammonium chloride)) compared to the non-surfactant inhibitor K3 (thiosulfate). Therefore it was decided to test K4 which is a blend of both types. Figure 5.11 shows the inhibition of K4 on bare steel. Corrosion rate was reduced by 95% by 430 ppm K4 in 5 hours. When a 2 mm silica deposit was present, the efficiency of K4 wasn't affected. The uniform corrosion rate was decreased by K4 from 0.6 mm/y to 0.1 mm/y on top of the deposit. As can be seen from EIS measurements (Figure 5.13), inhibitor K4 showed similar behavior as inhibitor K3 when sand deposit was present.

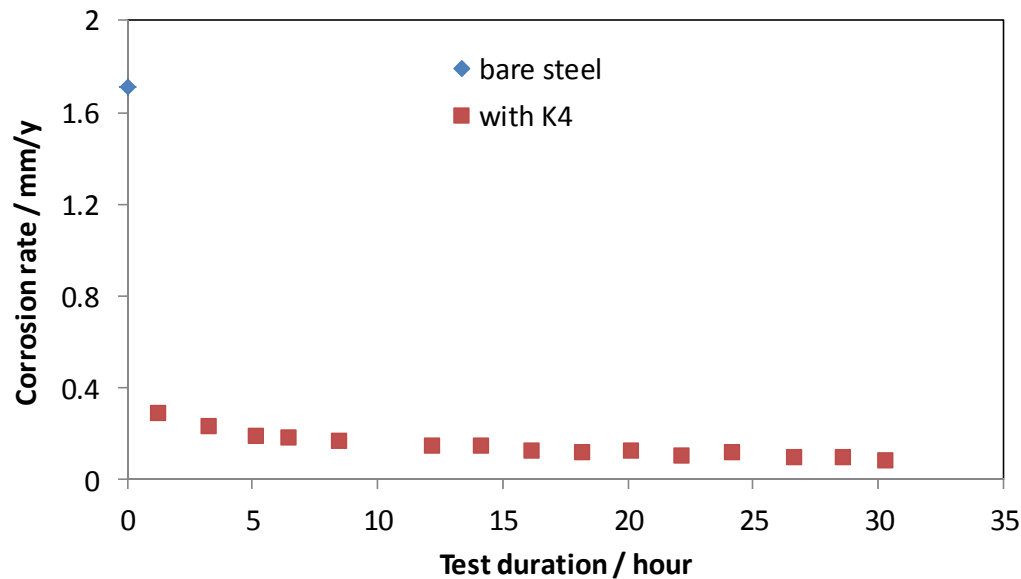


Figure 5.11 LPR corrosion rate over time at test conditions T = 25°C, 1 wt% NaCl, pH 5.0, 430 ppm K4 (imidazoline + thiosulfate) added on a bare steel.

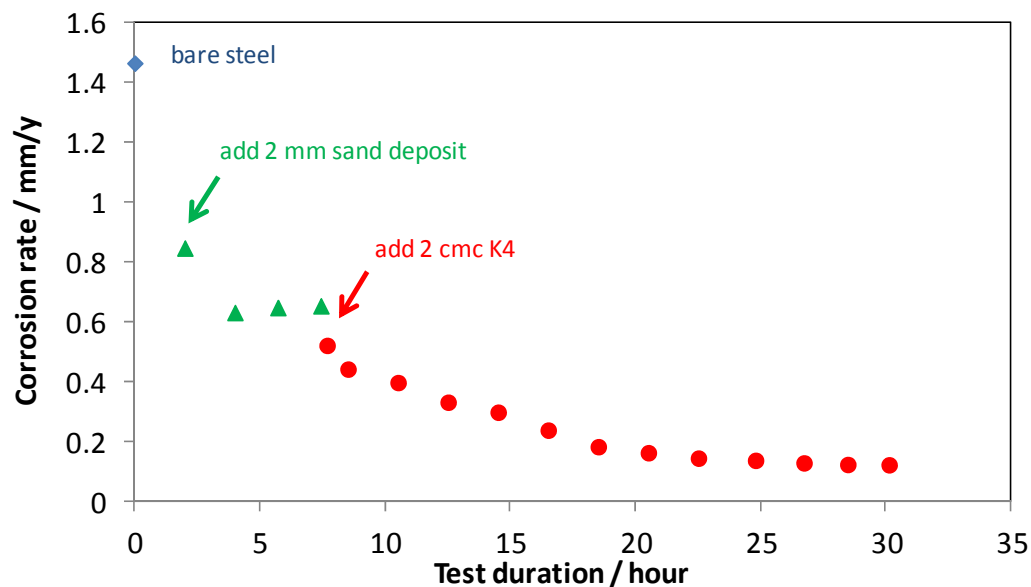


Figure 5.12 LPR corrosion rate over time at test conditions T = 25°C, 1 wt% NaCl, pH 5.0, 2 mm deposit presented prior to 430 ppm K4 (imidazoline + thiosulfate) addition.

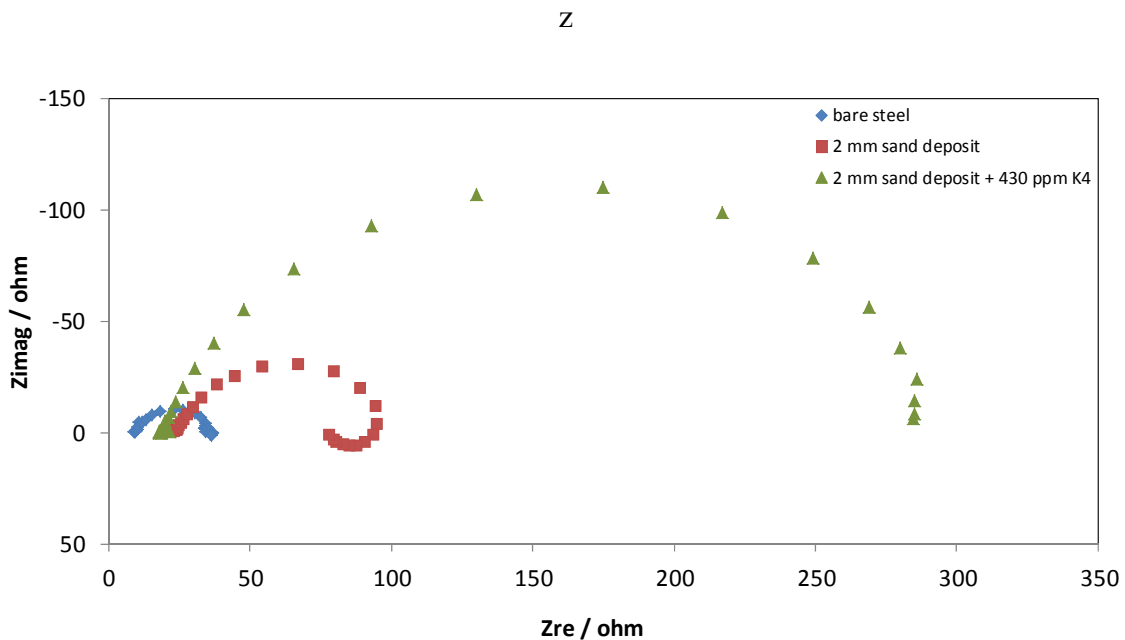


Figure 5.13 EIS Nyquist plots at 25°C, 1 wt% NaCl, pH = 5.0, 2 mm sand deposit presented prior to 430 ppm K4 (imidazoline + thiosulfate) addition.

The results for K1, K2, K3 and K4 are summarized in Figure 5.14 for easier comparison. The blue bar in the figure was the corrosion rate for bare steel surface, the red one was the corrosion rate of mild steel with 2 mm silica deposit. The purple one was the corrosion rate after inhibitor was added. It can be clearly seen that:

- 1) the presence of a silica deposit resulted in a decrease in uniform corrosion rate of mild steel.
- 2) the addition of surfactant inhibitor K1 or K2 was not able to further decrease the uniform corrosion rate in the presence of the deposit.
- 3) the inhibition efficiency of non-surfactant inhibitor K3 was not affected by the deposit.

- 4) the inhibition efficiency K4 which has a thiosulfate component was not affected by the silica deposit either.

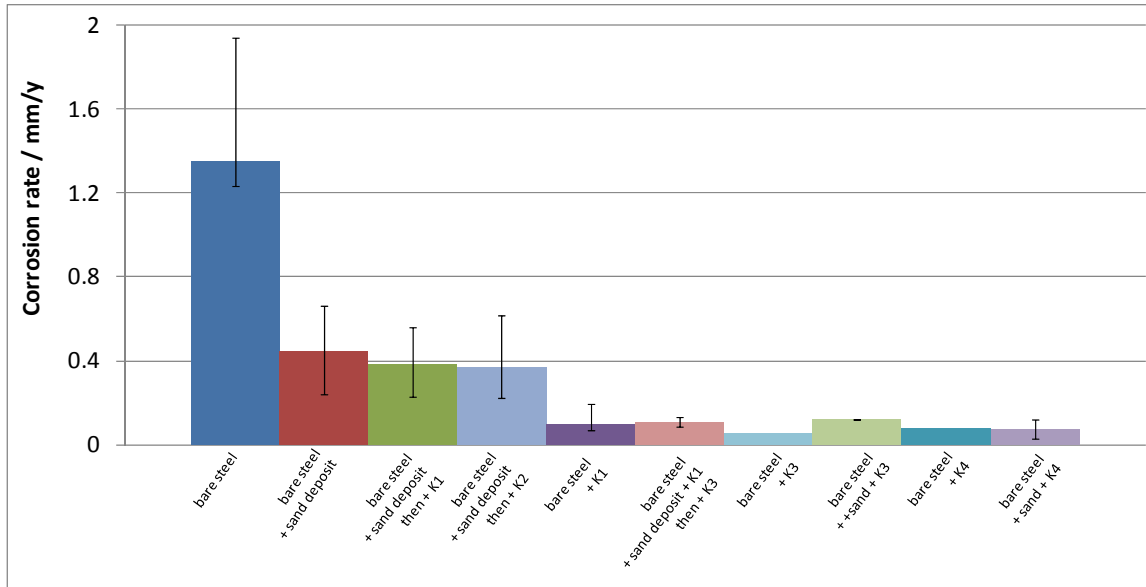


Figure 5.14 Comparison of the effect of sand deposit on different inhibitors at test conditions 25°C, 1 wt% NaCl solution, pH 5.0. 2 mm sand deposit present prior to inhibitor addition.

5.4.5 Al_2O_3 Deposit

Given that there was a significant effect of the deposit layer on the performance of surfactant based corrosion inhibitors, the question was if this happened because of the physical presence of the deposit or due to nature of the silica surface. Silica sand is often seen as the threat for corrosion inhibitor performance as apparently a large amount of corrosion inhibitors can be adsorbed on silica surface (Horsup, 2007). To find out if it was the nature of the silica surface that causes the problem, a deposit made from Al_2O_3

powder was tested to see how the same inhibitors respond to a different type of surface. The SEM image of this powder is shown in Figure 5.15. The SEM image of the silica sand is put in the same figure for comparison. It can be seen that the Al_2O_3 particle has similar size as silica sand particle. However, the porosity measured is larger than silica sand.

Figure 5.16 shows the variation of uniform corrosion rate with time in the presence of the Al_2O_3 deposit in conjunction with an inhibitor K1 (imidazoline). K1's performance in the presence of Al_2O_3 deposit can be clearly seen. K1's ability to reduce the uniform corrosion rate of mild steel was not affected. In the presence of this Al_2O_3 deposit, the corrosion rate was still inhibited by 90%. The EIS measurement also confirmed that the Al_2O_3 deposit had no effect in deteriorating K1's performance (Figure 5.17). The shape of Nyquist plot after K1's addition in the presence of an Al_2O_3 deposit looks similar to the one where no deposit was present.

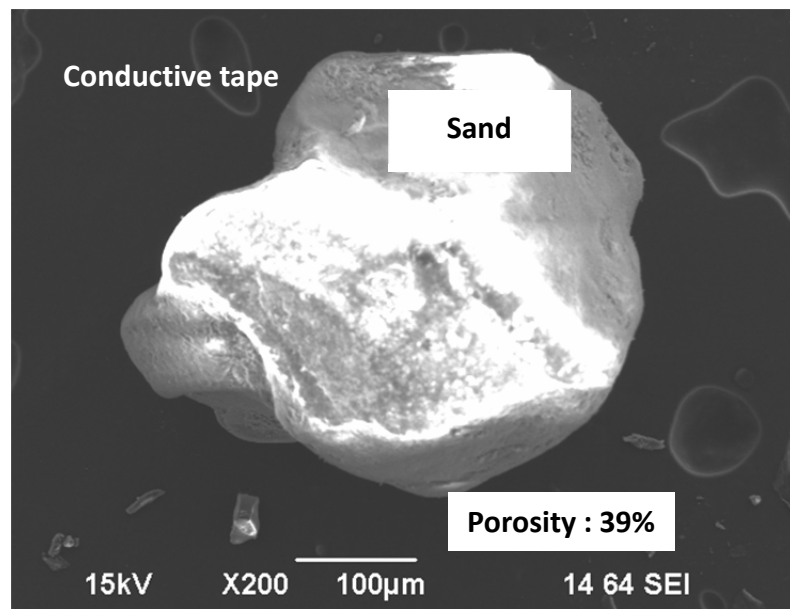
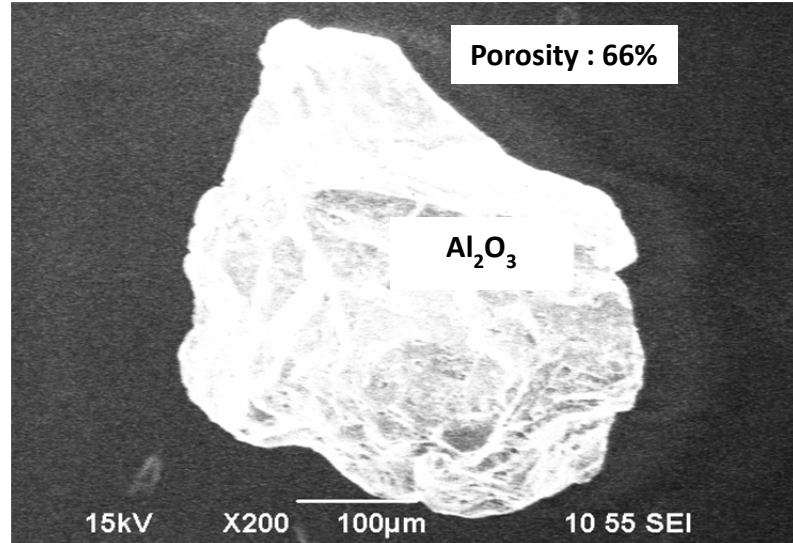


Figure 5.15 SEM images of Al_2O_3 particle and silica sand particle.

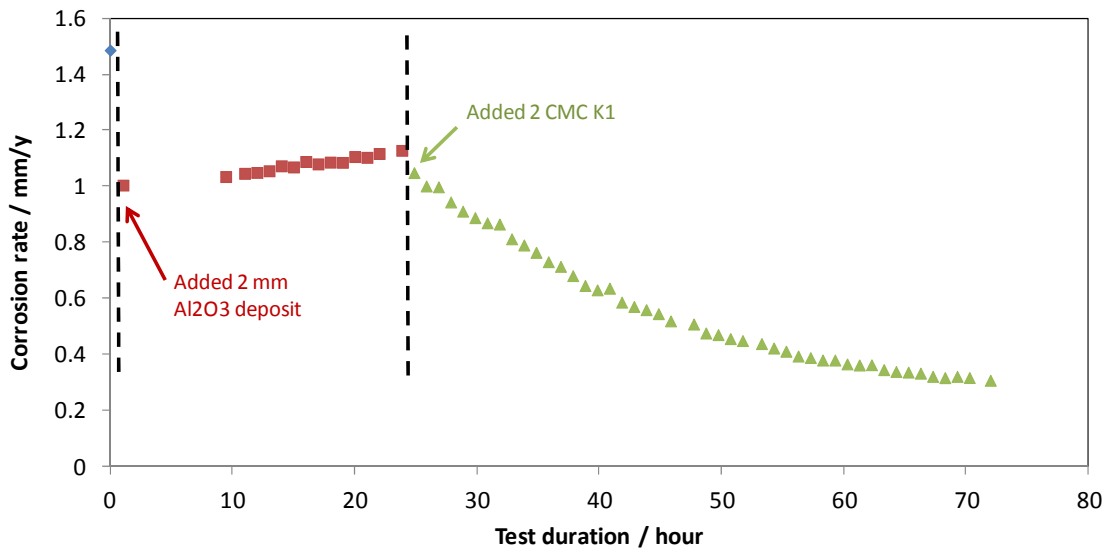


Figure 5.16 LPR corrosion rate over time at test conditions $T = 25^\circ\text{C}$, 1 wt% NaCl solution, pH 5.0, 2 mm Al₂O₃ deposit presented prior to 70 ppm K1 (imidazoline) addition.

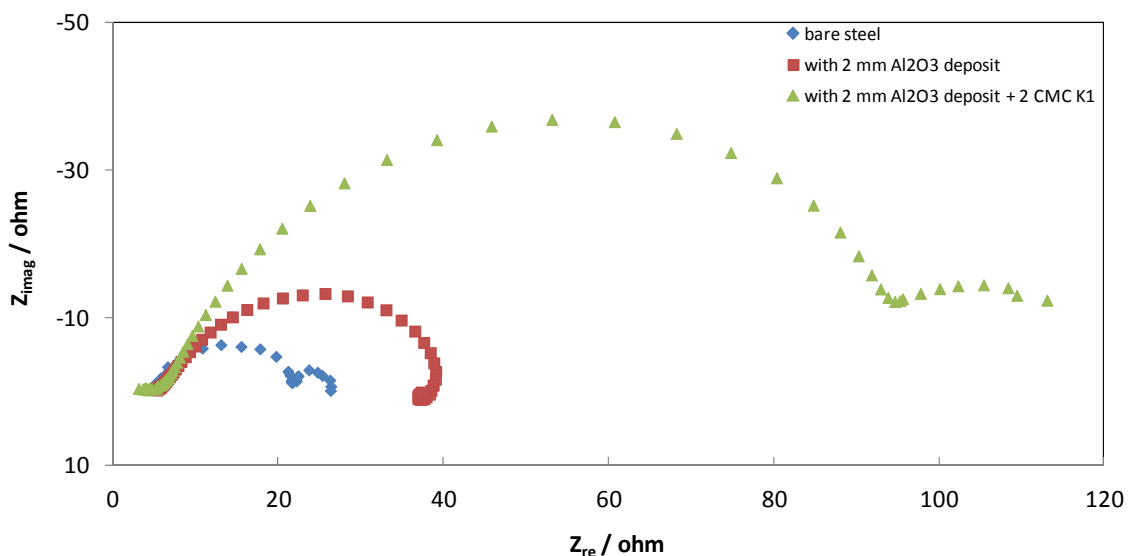


Figure 5.17 EIS Nyquist plots at 25°C , 1 wt% NaCl, pH = 5.0, 2 mm Al₂O₃ deposit presented prior to 70 ppm K1 (imidazoline) addition.

5.4.6 Inhibition Failure Mechanisms for Surfactant Corrosion Inhibitors on Silica Sand

The observation that the imidazoline based inhibitor K1 and the amine based inhibitor K2 had no effect on the uniform corrosion rate of mild steel in the presence of a sand deposit is in general agreement with other reported work (de Reus, 2005; Pederson, 2008). Place (2009). However, it has been reported elsewhere that, even with a solid deposit present, some inhibitors still worked very well (Turnbull, 2009). For the cases when the inhibitors did not function well in the presence of sand deposits, it is commonly believed that the large surface area of the deposit generally depletes the inhibitor, therefore making it unavailable to adsorb onto the steel surface underneath the deposit. This hypothesis was tested first:

5.4.6.1 Hypothesis A: Adsorption of Inhibitor on The Sand Surface Caused a General Depletion of The Inhibitor and Resulted in A Failure to Inhibit.

To test this hypothesis, the following experiments were conducted: the experiment was repeated as described above and then the sand deposit was removed from the steel surface at the end of the experiment. In this case, it was expected that, if Hypothesis A was true, that the inhibitor should still not perform well, as it was already consumed by adsorption onto the sand. Figure 5.18 shows the variation of corrosion rate of mild steel with time. After one hour of bare steel pre-corrosion, only one layer of sand was added and then 70 ppm of inhibitor K1 was added after another 24 hours. At the end of the experiment the sand was removed. The LPR corrosion rate data, noted by black dots, were for an API 5L X65 steel sample inhibited by 70 ppm K1 but without sand deposit. It can be seen that without a sand deposit, this 70 ppm K1 inhibited the corrosion

rate from 1.5 ± 0.1 mm/y to 0.1 ± 0.01 mm/y. When there was a sand deposit, the corrosion was firstly retarded by the sand deposit from 1.2 ± 0.1 mm/y to 0.55 ± 0.1 mm/y, but only a little further decrease in corrosion rate (from 0.55 mm/y to 0.45 mm/y in about 3 days) after K1 was added. Then the sand deposit was lifted off the steel surface, it can be seen that the corrosion rate decreased immediately from 0.45 mm/y to 0.2 mm/y in 24 hours. The LPR corrosion rate data suggest that once the sand was gone from the steel surface, good inhibition was obtained as would be obtained on a bare steel surface. This experiment has proven that the K1 inhibitor was not depleted by adsorption onto the sand, and that this mechanism cannot be used to explain K1's failure to reduce the corrosion rate of steel covered by sand.

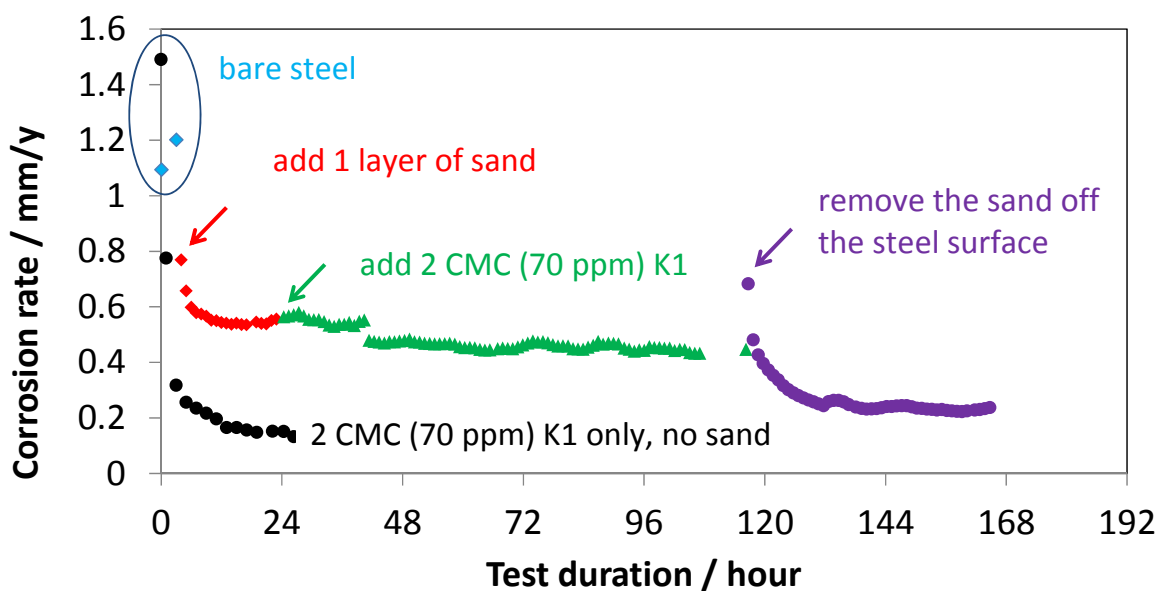


Figure 5.18 LPR corrosion rate over time at test conditions 25°C, 1 wt% NaCl solution, pH 5.0, under various amount of sand deposit which was present prior to 70 ppm K1 (imidazoline) addition.

The silica sand surface is normally more negatively charged (Ho, 1967), thereby attracting the more positively charged parts of the inhibitor molecule to adsorb onto it. It was thought that if the surface charge is altered the amount of inhibitor adsorbed onto the silica sand would change. The silica sand was therefore washed by different solutions in order to change the surface charge and change the adsorption of the inhibitor molecules. Dichlorodimethylsilane is believed to have the ability to change the silica surface charge from negative to neutral (Herzberg, 1970). Figure 5.19 shows the variation of corrosion rate of mild steel with time under various sand deposits which were pretreated differently. All deposits were added after one hour of bare steel corrosion. The short vertical lines shown indicate the moment when inhibitor K1 was added. The LPR corrosion rate data indicate no effect on corrosion rate by inhibitor K1 in the presence of the sand deposit, no matter how the deposit surface was pre-treated. The differences between the pre-treated sand deposits are summarized in Figure 5.20. The results from these two experimental series clearly disproved the Hypothesis A that: "adsorption of inhibitor on the sand surface causes general depletion of the inhibitor and failure to inhibit." Other possibilities had to be explored.

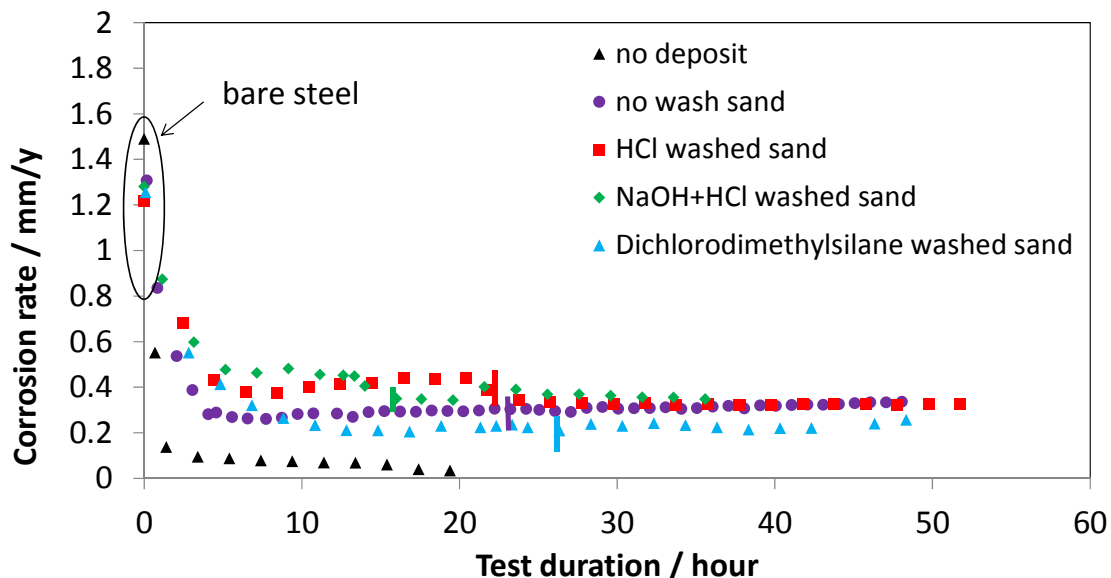


Figure 5.19 LPR corrosion rate over time at test conditions 1 wt% NaCl solution, pH 5 and 25°C, under different pre-treated silica sand deposits. Deposit present prior to 70 ppm K1 (imidazoline) addition.

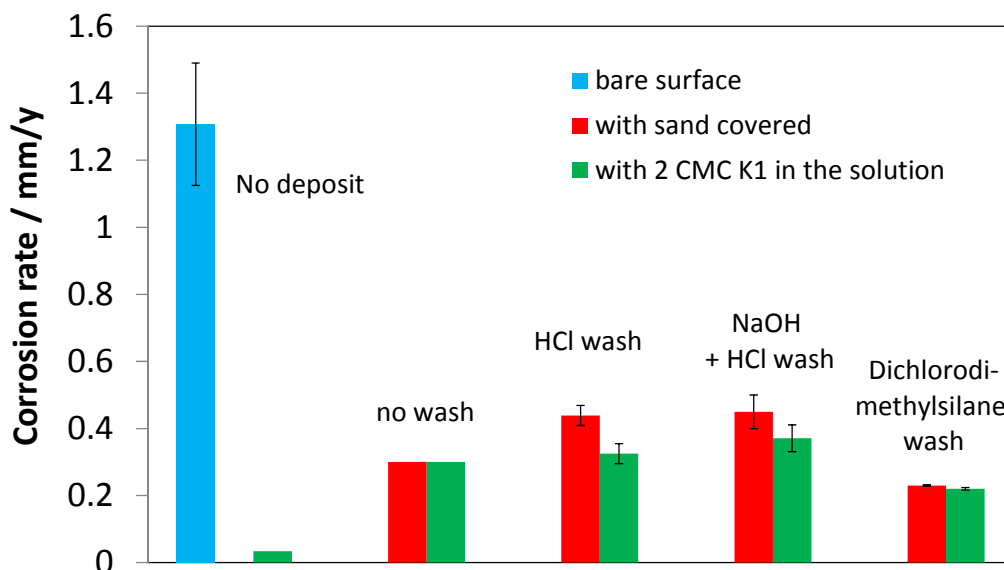


Figure 5.20 Comparison of general LPR corrosion rate under different pre-treated sand deposits at test condition 1 wt% NaCl solution, pH 5 and 25°C.

5.4.6.2 Hypothesis B: Slow Diffusion of Inhibitor Through The Sand Deposit is The Limiting Factor That Causes Inhibitor Failure.

The other popular belief is that the poor efficiency of the inhibitor in the presence of sand deposits is due to slow diffusion of the inhibitor through a porous deposit layer. One can simply express diffusion though a porous layer by using on Fick's law:

$$N = -D_{eff} \frac{\Delta C}{\Delta x}$$

Therefore, if Hypothesis B is correct, increasing the rate of diffusion through the sand deposit (N) should result in better inhibition. This can be easily accomplished by increasing the effective diffusivity (D_{eff}), by increasing the inhibitor concentration gradient across the sand deposit (ΔC), or by decreasing the depth of the porous sand deposit (Δx). Three series of experiments were conducted at conditions designed to accelerate the inhibitor diffusion process.

The diffusion coefficient D_{eff} was increased. This was achieved by:

- (a) Using larger sand particles for the deposit, having larger porosity and tortuosity (i.e. larger open spaces between sand particles for inhibitor to diffuse).
- (b) Conducting experiments at a higher temperature, i.e. 80°C.

Figure 5.21 shows the variation of corrosion rate with time for two layers made up of very different particle sizes. No difference was observed in terms of uniform corrosion rate obtained by LPR - in both cases the sand deposit layer prevented inhibition by K1 (imidazoline) in a similar way.

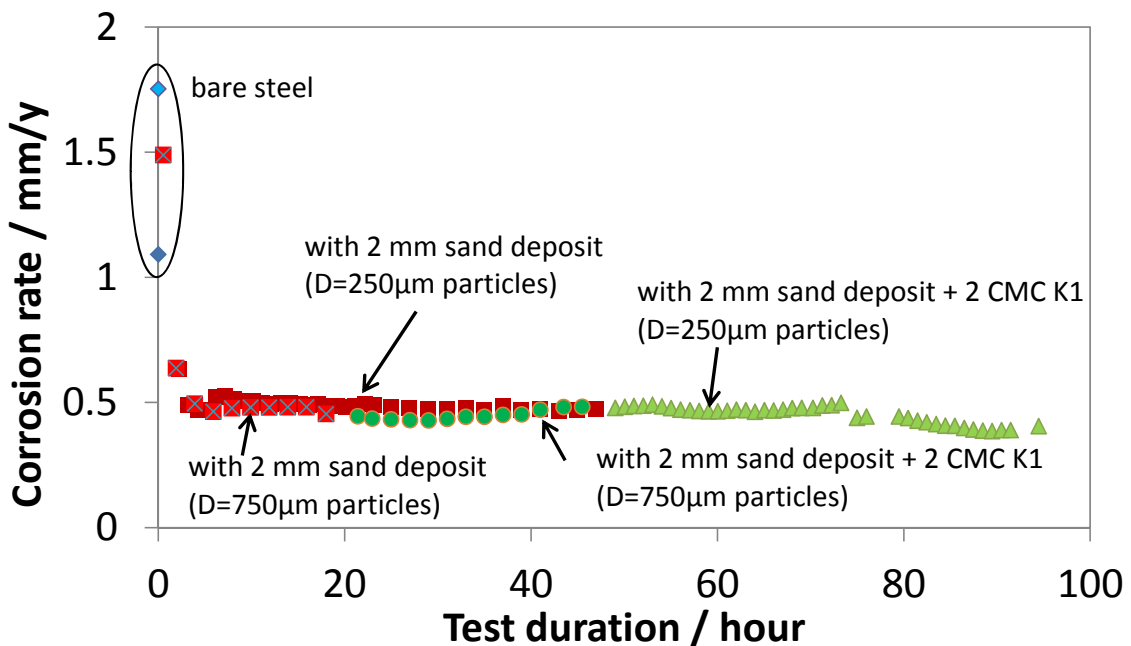


Figure 5.21 LPR corrosion rate over time at conditions 1 wt% NaCl solution, pH 5.0, 25°C at two different sizes of sand particles.

The diffusion coefficient in liquids can be estimated by using the Stokes-Einstein equation:

$$D = \frac{kT}{3\pi\mu d} \quad (5.1)$$

where k is the Boltzmann constant, T is the absolute temperature, d is the diameter of the inhibitor molecule, and μ is the viscosity of the liquid; indicating that an increase in temperature will increase the diffusion coefficient. A new series of experiments were performed at 80°C. The variation of corrosion rate with time measured from LPR is shown in Figure 5.22. Little effect of inhibitor was observed in the presence of the sand deposit even at this high temperature.

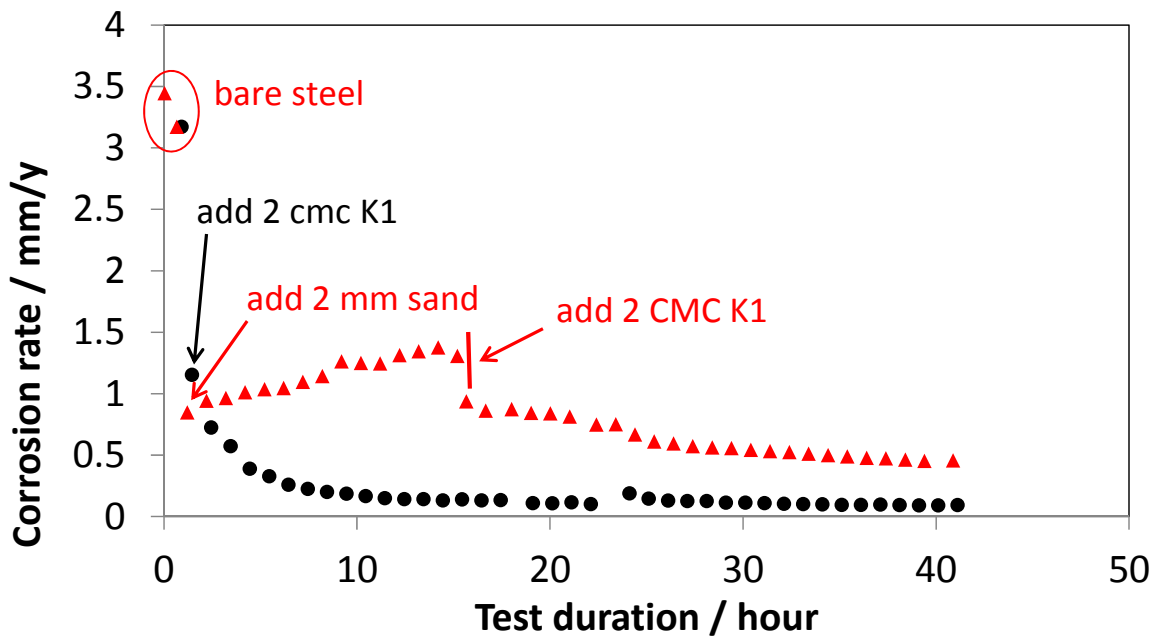


Figure 5.22 LPR corrosion rate at test conditions 1 wt% NaCl solution, pH 5.0, 80°C. 2 mm sand deposit present prior to 70 ppm K1 (imidazoline) addition.

The driving force ΔC for diffusion was increased by increasing the bulk concentration of inhibitor. In previous experiments, 70 ppm K1 was used. In the new experiments, 1800 ppm K1 was used in order to have an extreme driving force for inhibitor diffusion assuming that this was the limiting factor. Figure 5.23 shows the variation of corrosion rate with time in the presence of 2 mm sand deposits and with 1800 ppm K1 added. The behavior was similar as before - poor inhibition was achieved.

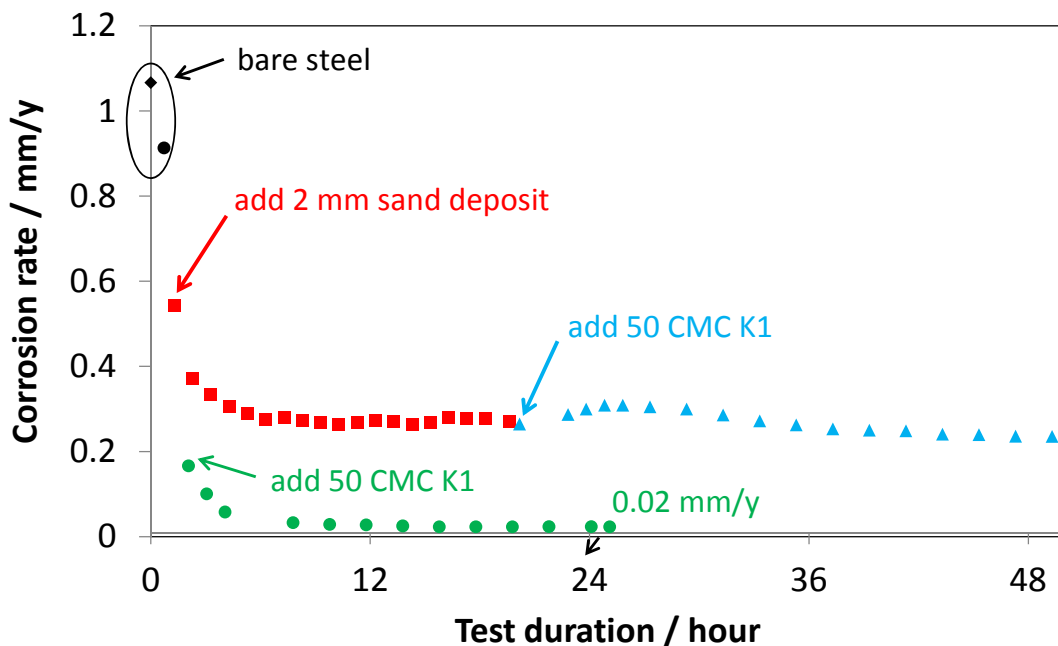


Figure 5.23 LPR corrosion rate over time at test conditions 1 wt% NaCl solution, bulk pH 5.0, 25°C, 2 mm sand deposit present prior to 1800 ppm K1 (imidazoline) addition.

The diffusion path Δx for diffusion was decreased. This was achieved by using less sand. A 2 mm sand deposit consisting of sand particles with average size of 250 μm is roughly 8 layers of sand. The 70% coverage was achieved with the sand particles scattered on the steel surface with approximately 30% of the steel surface area directly exposed to the test solution. The variation of corrosion rates with time for these different cases is shown in

Figure 5.24. It shows that one layer of sand was as detrimental for the performance of the inhibitor as were the 10 layers of sand. Furthermore it appears that as long as there was any sand on the steel surface, the inhibitor efficiency was affected. The final stable corrosion rate measured from LPR is also summarized in Figure 5.25. From

the different series of experiments described above, *Hypothesis B* could also be rejected and it was confirmed that diffusion of inhibitor through a sand deposit towards the steel surface is not the limiting factor. It came as surprise though, that even partial (70%) coverage with a single layer of sand lead to poor inhibition. This was followed up on by surface analysis and pits were found on the steel surface. Actually pits were present in several cases described above. Therefore, the emphasis in this work shifted to localized corrosion.

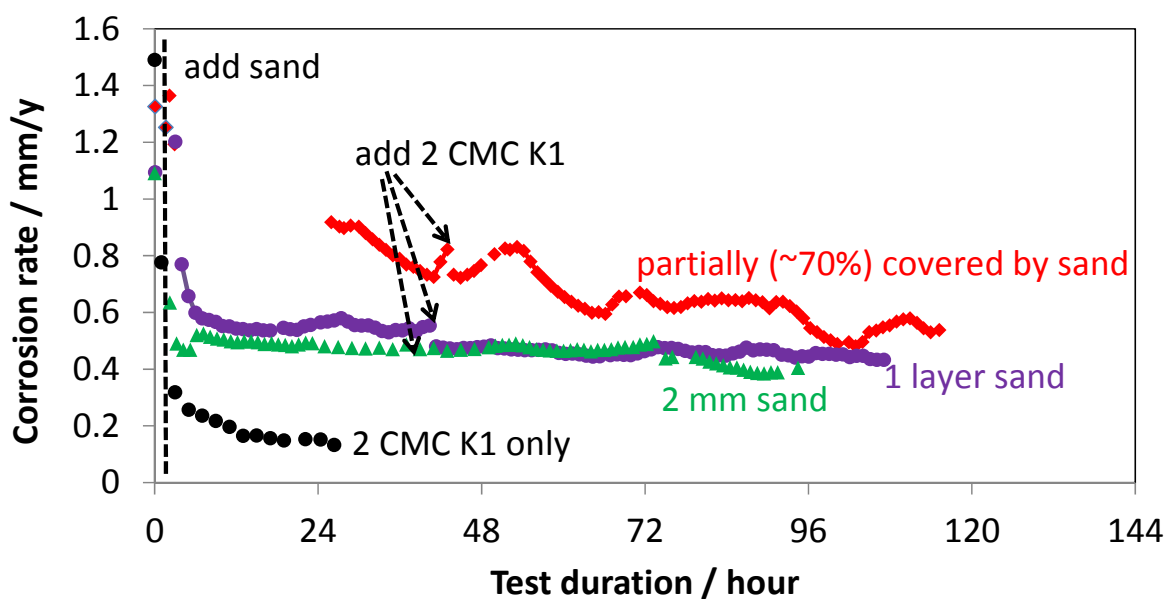


Figure 5.24 LPR corrosion rate over time at test conditions 25°C, 1 wt% NaCl solution, pH 5, sand deposit present prior to 70 ppm K1 (imidazoline) addition.

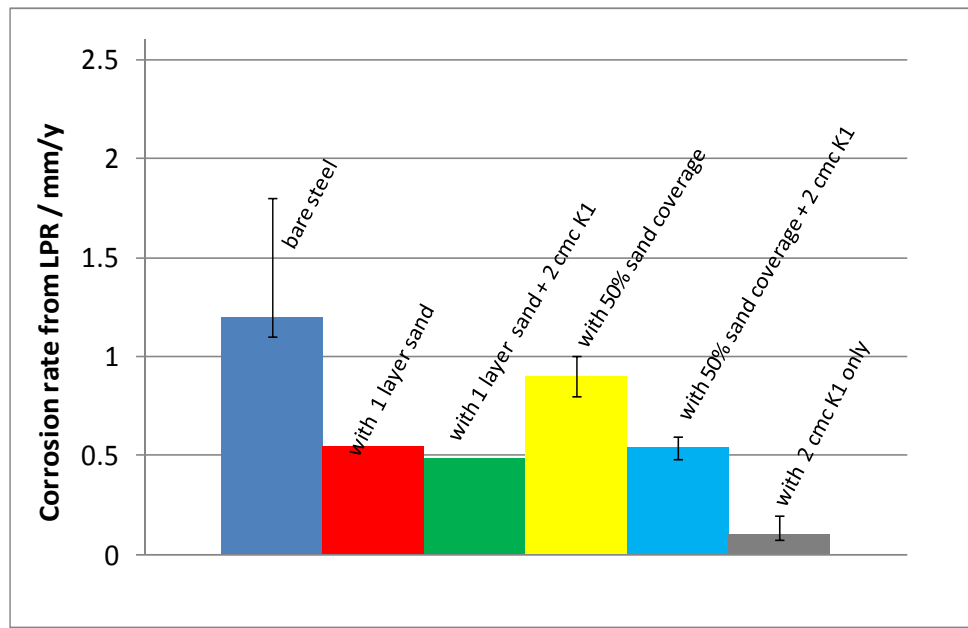


Figure 5.25 Comparison of stable corrosion rate after 70 ppm of K1 inhibitor added after different amount of sand deposit, at test conditions: 25°C, pH 5, 1 wt% NaCl solutions.

5.4.7 Localized Corrosion

A number of different experiments were organized in this part of the study focusing on localized corrosion.

CASE 1: One layer of sand used, full surface coverage, 70 ppm K1 (imidazoline) added after the sand.

This case is represented by the LPR data in Figure 5.18. A single layer of sand was added after one hour of bare steel corrosion, followed by 70 ppm K1 added 24 hours after the sand deposit, and then the deposit was removed after approximately 90 hours, followed by another 24 hours without the sand layer. The SEM image of steel surface after corrosion is shown in Figure 5.26. Pits can be found at many locations across the specimen surface. From infinite focusing microscopy scanning (Figure 5.27), the average

pit depth was found to be 35 μm , which is equal to a corrosion rate of 2.0 mm/y. This pit penetration rate is 10 times greater than the uniform corrosion rate calculated from LPR (Figure 5.18).

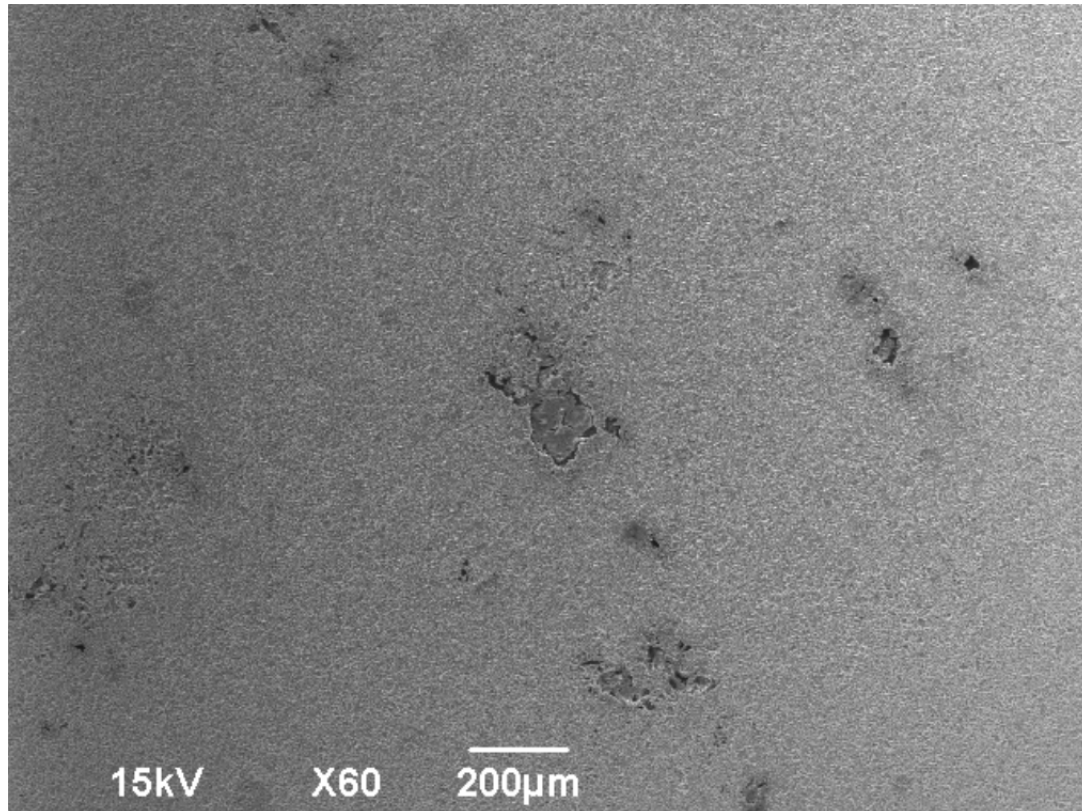


Figure 5.26 SEM of steel surface after 5 days exposure at test conditions 25°C, 1 wt% NaCl solution, pH 5.0, 1 layer sand deposit present prior to 70 ppm K1 (imidazoline) addition, corrosion product removed.

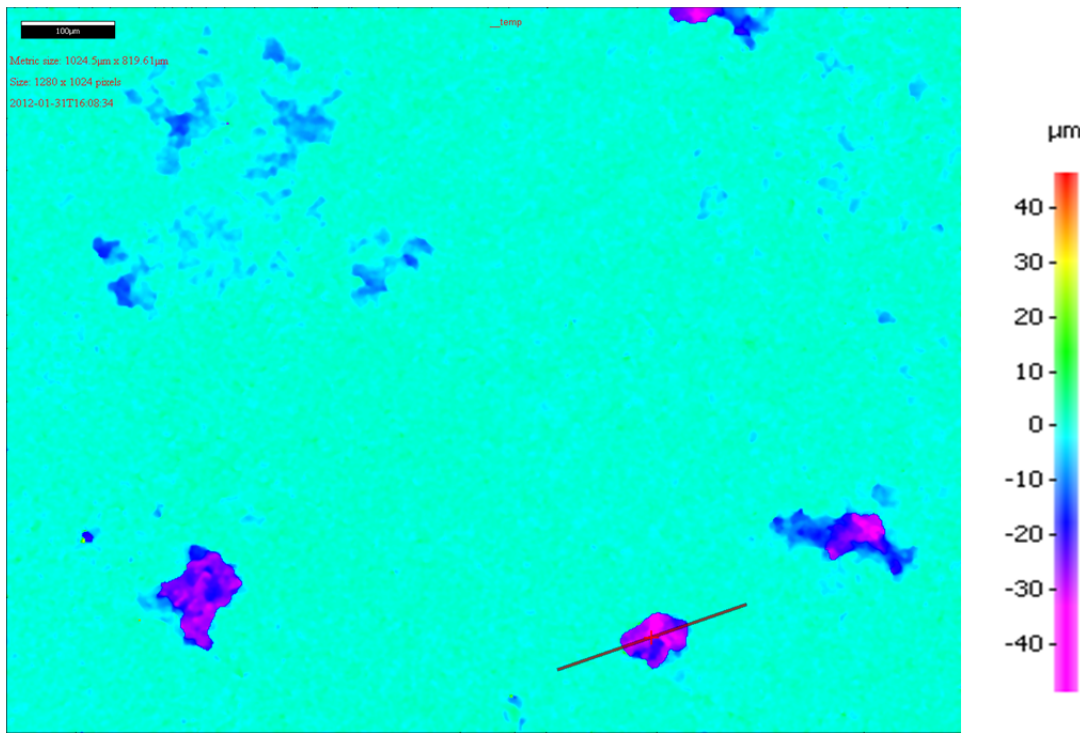


Figure 5.27 A image from infinite focusing microscopy scanning of pits on steel surface after 5 days exposure, at test conditions 25°C, 1 wt% NaCl solution, pH 5.0, 1 layer sand deposit present prior to 70 ppm K1 (imidazoline) addition.

CASE 2: One layer of sand used, scatter sand particles (about 70% coverage), 70 ppm K1 (imidazoline) added after sand.

In this case, less sand was added on the steel surface so that only about 70% of the steel surface was covered by sand particles, the rest was bare steel exposed directly to the electrolyte. The LPR data for this experiment are shown in Figure 5.28. After one hour of pre-corrosion, the sand was added on the surface, and after 24 hours 70 ppm K1 was added, and the corrosion rate observed for 72 more hours before removal of the sand and observation for another 48 hours. Specimen surface analysis shows that pits were found

underneath the sand particles. Figure 5.29 is the SEM image of steel surface before corrosion product removal. The pit penetration rate was calculated from infinite focusing microscopy scanning (Figure 5.30) to be 2.0 mm/y as most of pits have a depth of 40 μm . This is about 6 times of LPR uniform corrosion rate 0.3 mm/y during the last 48 hours of the experiment time.

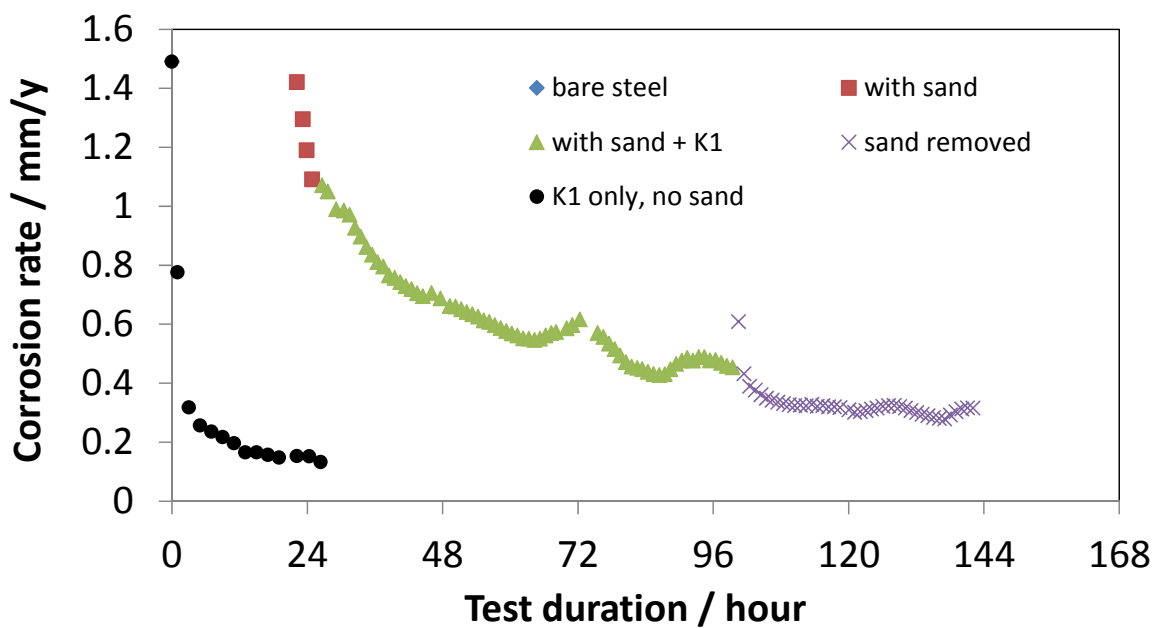


Figure 5.28 LPR corrosion rate over time at test conditions 25°C, 1 wt% NaCl solution, pH 5.0, steel surface is partially covered by sand particles.

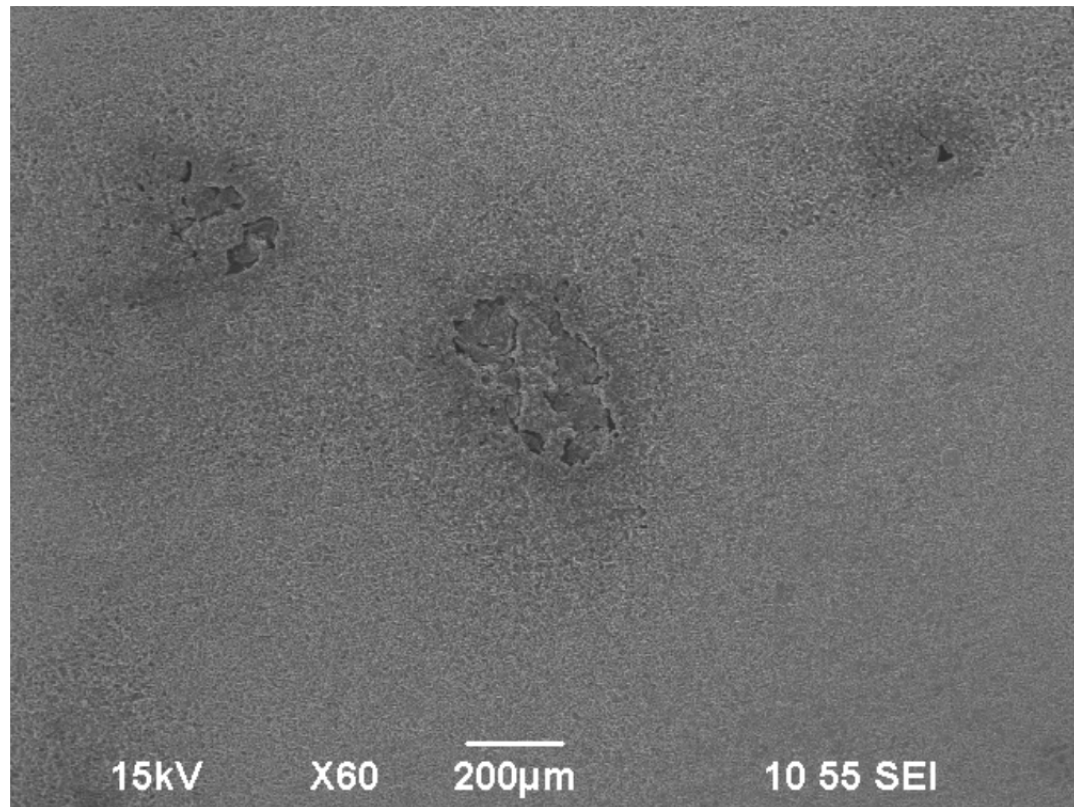


Figure 5.29 SEM of steel surface after 144 hours exposure at test conditions 25°C, 1 wt% NaCl solution, pH 5.0, steel surface is partially covered by sand particles, corrosion product removed.

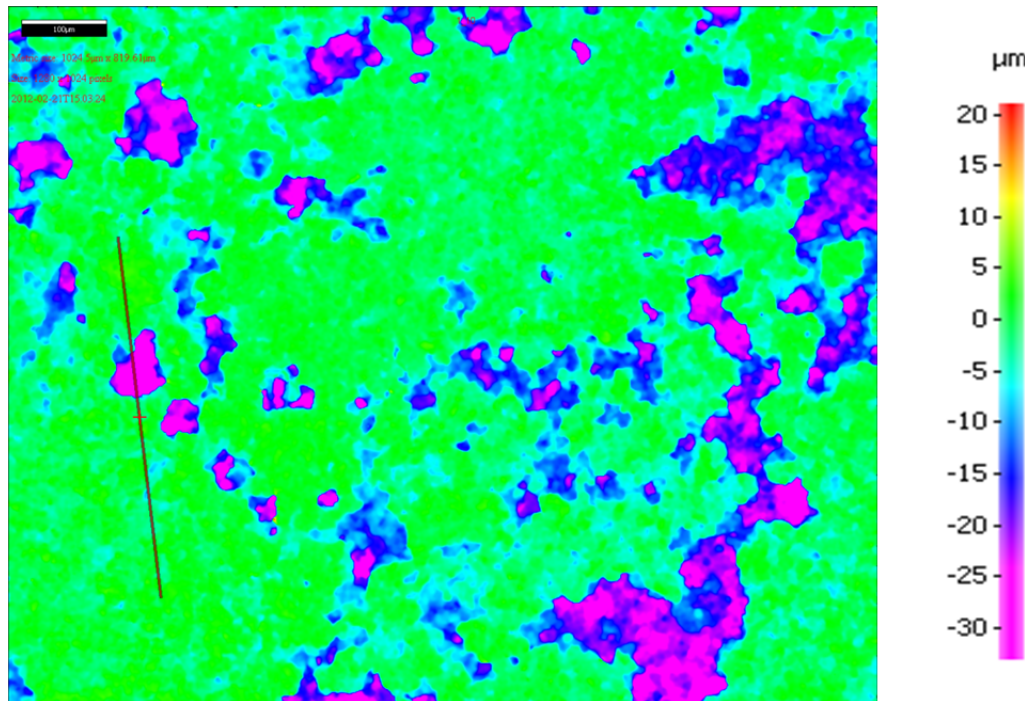


Figure 5.30 Infinite focusing microscopy scanning of steel surface after 144 hours exposure at test conditions 25°C, 1 wt% NaCl solution, pH 5.0, steel surface is partially covered by sand particles and corrosion product removed.

CASE 3: Multiple layers of silica sand used (2 mm), full coverage, 70 ppm K1 added before sand.

In this case, the steel surface was fully covered with 2 mm deposit. But the 70 ppm K1 was added before the sand deposit was present. The sand deposit was lifted off the steel surface and the corrosion process proceeded for another 20 hours before experiment ended. Surprisingly, lots of pits were found by SEM analysis (Figure 5.31). The maximum pit depth was measured to be was 45 μm from Infinite focusing

microscopy scanning (Figure 5.32). The whole steel surface was also scanned and 90% of pits were found to be having a depth of 40 µm equal to a corrosion rate of 2.2 mm/y. This pit penetration rate is about 30 times greater than the LPR measured uniform corrosion rate (Figure 5.33).

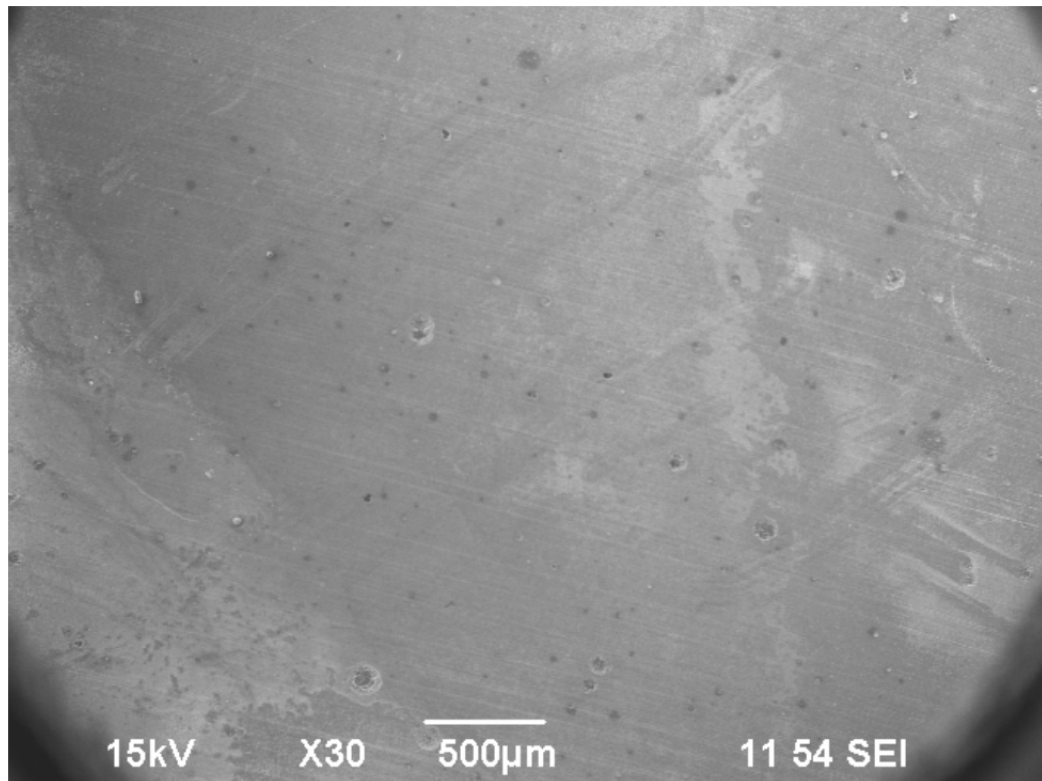


Figure 5.31 SEM image of the steel surface after 160 hours exposure at test conditions 25°C, 1 wt% NaCl solution, 5.0, 2 mm sand deposit present after 70 ppm K1 addition.

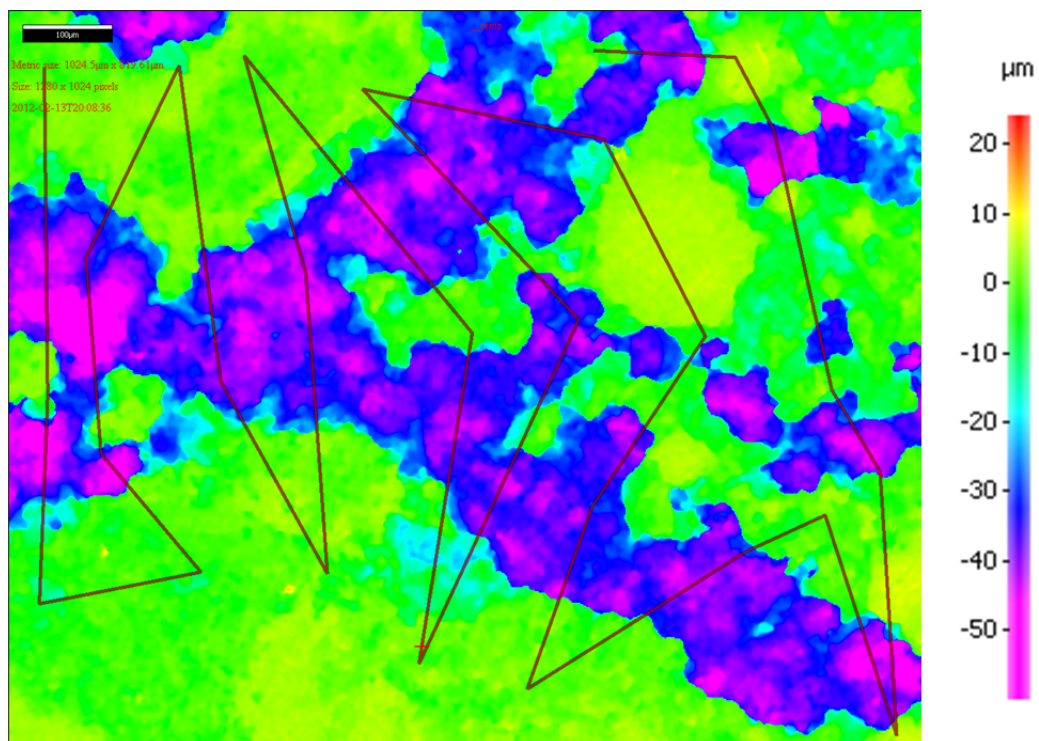


Figure 5.32 IFM scanning of the steel surface after 160 hours exposure at conditions 25°C, 1 wt% NaCl solution, pH 5.0, 2 mm sand deposit present after 70 ppm K1 addition.

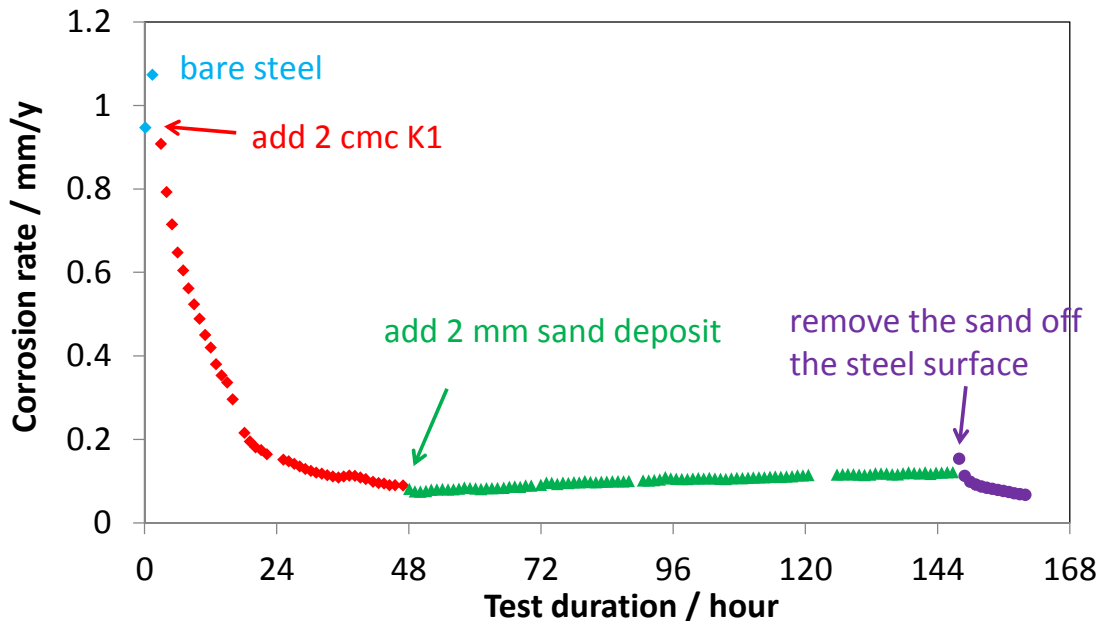


Figure 5.33 LPR corrosion rate over time at test conditions 25°C, 1 wt% NaCl solution, pH 5.0, 2 mm sand deposit present after 70 ppm K1 addition.

In summary, the cases where pits were found are listed in Table 5.3. The pit penetration rate and corresponding uniform corrosion rate measured from LPR are compared. It can be seen that it did not matter whether the steel surface was inhibited before the addition of the deposit, and it did not matter if the steel surface was fully covered by sand particles or not – in all cases pitting corrosion was found. And those pits were all found underneath individual sand particles. Based on all experimental observations, a localized corrosion mechanism based on a failure to inhibit underneath each individual sand particle could be proposed. It appears that in the crevices formed between the sand particles and the steel, the inhibitor molecules failed to adsorb and

protect the steel surface, while other more open access areas were inhibited. This lack of inhibition was compounded by formation of galvanic cells which lead to even higher localized corrosion rates underneath each sand particle. Indeed the large numbers of small pits developing underneath each sand particle eventually merge into one large rapidly corroding area underneath the whole sand deposit. This mechanism can help explain why no change in corrosion rate was measured by LPR when the inhibitor was added. One needs to recall that the corrosion rate calculated from LPR measurement is an average corrosion rate across the whole steel specimen surface. The calculation is based on the assumption that the steel surface corrosion is uniform. However, when a sand deposit is present, the steel surface is not uniform corroded, because of the high pit penetration rate underneath each sand particle. This localized high corrosion rate is roughly balanced with the low (inhibited) corrosion rate of the adjacent more exposed area, which resulted in the observation of little change in measured LPR uniform corrosion rate. This also leads to the conclusion that LPR is not a suitable method to monitor corrosion in an under deposit corrosion study.

Table 5.3 Summary of cases where pits were found.

Case		Pit penetration rate (IFM)	Uniform corrosion rate (LPR)	Note
Partially covered surface	70%	2.0 mm/y	0.3 mm/y	Inhibitor K1 (imidazoline) added after sand
Fully covered surface	1 layer (~ 0.75 mm)	2.0 mm/y	0.2 mm/y	Inhibitor K1 (imidazoline) added before sand
	2 mm	2.5 mm/y	0.08 mm/y	

5.5 Summary

In this chapter, the effects of deposit on three generic inhibitors' performances were investigated in different experiment configurations using electrochemical techniques. In the majority of the experiments, a solid deposit was present before inhibitor's addition (although when it was added after the inhibitor the same behavior was observed). From electrochemical measurement, no inhibition of the corrosion rate by surfactant inhibitor K1 (imidazoline) or K2 (ammonium chloride) was observed in the

presence of the silica deposit. But the inhibition by K1 and K2 was not affected by the Al₂O₃ deposit. Hypotheses were defined to explain why surfactant inhibitors K1 or K2 were not able to reduce the corrosion rate when silica deposit was present. Experimental results proved that the retarded diffusion and adsorption mechanisms proposed previously cannot explain the low inhibitor efficiency in the case of under deposit corrosion. Steel surface analysis showed that pits were formed under sand particles, which provided clues for the investigation of under deposit mechanisms in inhibited environment. The observation of pits also helped understand results obtained by the LPR technique, which is powerful in uniform corrosion studies but is not suitable for the under deposit corrosion study discussed here. Therefore, infinite focusing microscopy analysis was used for the investigation of localized corrosion mechanisms in under deposit corrosion which will be discussed in next Chapter. Based on the results discussed in this chapter, the following conclusions can be made:

- I. A simple and reliable method for testing of localized under deposit corrosion was developed and verified.
- II. Mechanisms for localized corrosion in the presence of solid deposits were identified.
 - a. General depletion of the surfactant inhibitor (imidazoline based) by adsorption on silica sand surface was proven not to be the critical factor that causes inhibition failure in under deposit CO₂ corrosion.
 - b. Slow diffusion of inhibitor molecules through the porous sand deposit layer is also not the limiting factor in cases where inhibition failed.

- c. Pits found in under deposit corrosion are related to the inability of the inhibitor to protect the steel surface in the crevices immediately underneath each individual sand particle. These pits propagated very fast due to galvanic effects, eventually merging and causing a high rate of "general" attack underneath sand deposits.

CHAPTER 6. LOCALIZED CORROSION OF MILD STEEL UNDER SILICA SAND DEPOSIT IN INHIBITED ENVIRONMENTS

6.1 Introduction

In this chapter, work is described which has been focusing on investigating the mechanisms of localized corrosion in under deposit CO₂ corrosion of mild steel. In order to better understand the galvanic corrosion process and the location of localized corrosion, both the single electrode specimen (as described previously) and a coupled two-electrode specimen were designed for corrosion experiments. The use of a coupled two-electrode set up was aimed at understanding the driving force for the formation of a galvanic cell due to the presence of silica sand and inhibitor, as well as quantitatively determining the galvanic current generated in under deposit corrosion process. The single electrode experiments were designed to verify the occurrence of localized corrosion and to investigate the propagation of localized corrosion. The steel surface was either fully or partially covered by silica sand particles. Electrochemical techniques including LPR and weight loss method were used to monitor the uniform corrosion rate. Galvanic current measurements were conducted for experiments with coupled electrodes to determine the galvanic effect. A infinite focusing microscopy was used to measure the localized corrosion rate of the cleaned mild steel surface after each experiment. In this Chapter, *intrinsic* corrosion rate is defined as the corrosion rate of the mild steel without any galvanic effects. It is used to describe the corrosion process of the mild steel sample when it is not galvanically connected to another steel sample.

6.2 Experimental Method

6.2.1 Experiment Setup and Procedure

A standard three electrode glass cell described in Chapter 4 was used for the present work as well. All corrosion experiments were conducted at ambient temperature in a glass cell filled with 2 liter of the test solution, which was a 1 wt% sodium chloride DI water solution saturated with CO₂ at 1 bar total pressure. The test solution was deoxygenated by continuously sparging with CO₂ gas for at least 1 hour. Then the pH of the test solution was adjusted to designated value by adding OH⁻ or H⁺ in the form of de-oxidized 1 molar sodium bicarbonate (NaHCO₃) or diluted hydrochloric acid (HCl). The pH change was monitored and recorded regularly during the experiment. Once the test solution was prepared, the specimen was polished with 200, 400 and 600 grit sand paper sequentially, then dried and inserted to the solution, experiment started. For experiments with no electrochemical measurements, the specimen was weighed for later calculation of uniform corrosion rate using weight loss method before inserting into the solution.

Notwithstanding their limitations, the surface area averaged corrosion “uniform” rate was monitored using LPR, weight loss method and dissolved ferrous ion, Fe²⁺ measurement. The measurement procedure for experiments using LPR technique was the same as described in Chapter 5. In the experiments where no electrochemical measurements were conducted, Fe²⁺ concentration measurement and weight loss method were used to determine the time-averaged uniform corrosion rate. After one hour of exposure, a 5 ml test solution sample was taken and the Fe²⁺ concentration was measured using a spectrophotometer. The surface averaged corrosion rate for the bare steel

corrosion at test conditions without inhibition was 1.0 ± 0.3 mm/yr. For each experiment with silica sand and/or inhibitor added, sand particles were added on the specimen surface once bare steel corrosion rate was obtained to be in the same range as expected. A solution sample was taken once every few hours throughout the whole process for obtaining the time-averaged uniform corrosion rate measurement. When the experiment was finished, the specimen was taken out of the solution and rinsed with isopropyl alcohol, dried and stored properly for surface analysis using SEM and EDX. The specimen was also cleaned by the Clarke solution as outlined in ASTM G1 to remove corrosion product layers for pit analysis using the infinite focusing microscopy. Experimental conditions are summarized in Table 6.1.

Table 6.1 Experimental conditions.

Parameter	Conditions
Material	API 5L X65 mild steel
Test solution	DI water + 1 wt% NaCl
Temperature	25 °C
CO ₂ partial pressure	0.96 bar
Solution pH	5.0
Deposit	Silica sand particles, silica crystal
Inhibitor type	K1 (imidazoline), K3 (thiosulfate)
Inhibitor concentration	70 ppm (K1), 30 ppm (K3)

6.2.2 Deposit and Inhibitor

Silica sand particles and very large silica crystals were used as solid deposit in this series of experiments. The images of the silica particles and silica crystal are shown in Figure 6.1. The silica particles have a diameter of 750 µm. The silica crystal has an irregular shape and is about 5 - 10 mm in length. Both particles were cleaned with DI water and were stored in a 1 wt% NaCl solution the same as test solution sparged by CO₂. A pipette was used to transfer sand particles onto corroding specimen as the experimental procedure required.

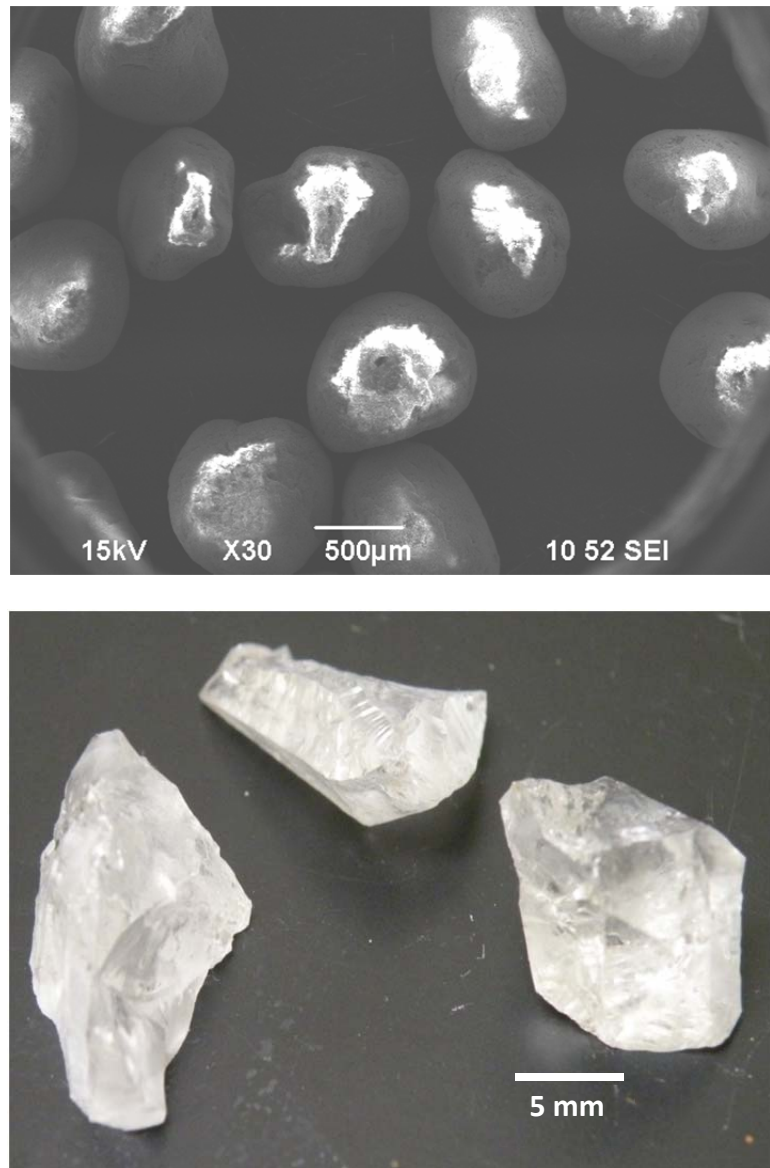


Figure 6.1 Deposit used for localized corrosion experiments: silica sand particles (750 μm), silica crystals (5 mm).

Surfactant inhibitor K1 (imidazoline) and non-surfactant inhibitor K3 (thiosulfate) were used. Description of the two inhibitors is listed in Table 6.2.

Table 6.2 Inhibitors used in present work.

Inhibitor	Description	Active ingredient	Concentration used in experiments
K1	Generic	TOFA/DETA Imidazoline	70 ppm
<hr/>			
K3	Generic	Sodium Thiosulfate	30 ppm

6.3 Results and Discussion

6.3.1 Establishment of a Galvanic Cell between Silica Sand Covered Electrode and Exposed Electrode

In order to study the localized corrosion process, a coupled two-electrode specimen coupon set was designed to study if and how a galvanic cell would be established in under deposit CO₂ corrosion.

The working electrode consisted of two separate parts, a small cylinder disc and a big cylinder disc ring. Both electrodes were machined from C1018 mild steel. The chemical composition of the C1018 steel is listed in Table 6.3.

Table 6.3 Chemical composition of C1018 mild steel (mass % balance is Fe).

Al	As	Zn	C	Zr	Co	Cr	Mn	Mo	Ni	Nb
0.022	0.006	0.002	0.2	0.003	0.003	0.1	0.87	0.024	0.071	0.001
P	S	Sb	Si	Sn	Ta	Ti	V	W	Cu	Fe
0.009	0.012	0.011	0.25	0.007	0.029	0.001	0.003	0.02	0.083	Balance

In the experiment, the small disc was placed in the center and surrounded by the big cylinder ring so as to obtain an evenly distributed galvanic current between them. There were electrical connections extended from the back of both electrodes. After the electrical components were attached, both electrodes were coated with a Teflon coating⁵ and then only the front face of the disc was polished and exposed to corrosion. The different views of the electrode couple is shown in Figure 6.2. The insulated parts assembled on the electrodes were used to physically support the electrodes in the glass cell. It can also be seen that the central small electrode was placed lower than the surrounding electrode, so the sand deposit could be added on top and the amount of deposit could be controlled.

⁵ Xylan 1014 (blue) from Whitford Corporation (www.whitfordww.com).

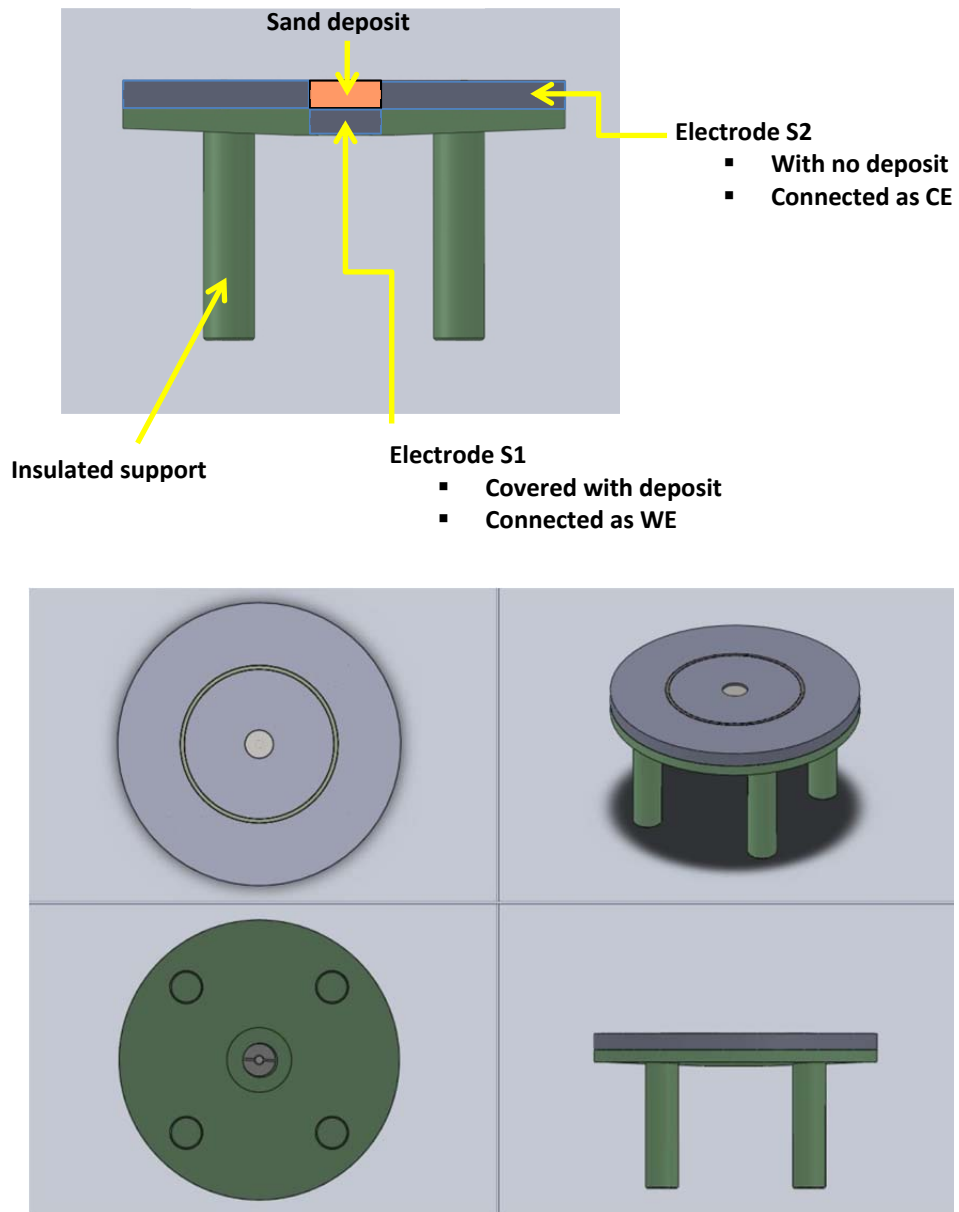


Figure 6.2 Galvanic-couple working electrode. The surface area ratio of the surrounding ring electrode to the central disc electrode is 60:1.

The set of experiments using this coupled two-electrode system was designed to investigate if a galvanic cell would be formed and function due to the presence of the sand deposit and addition of inhibitor. Experiments were conducted following this procedure:

- 1) Pre-corrosion: at the beginning, the two electrodes S1 and S2 were not connected and both were bare (no deposit). LPR and EIS measurements were conducted on both S1 and S2 separately to obtain their intrinsic corrosion rate (intrinsic meaning corrosion without any galvanic effect). This pre-corrosion step lasted 1 hour.
- 2) While electrodes S1 and S2 were still both bare, they were connected as an electrode couple through a zero resistance ammeter. Galvanic current was measured between the coupled electrodes for about an hour.
- 3) While electrodes S1 and S2 were still connected, 2 mm sand deposit was added on top of electrode S1, which is the central small electrode. Galvanic current was measured and recorded for a few hours. Then, 70 ppm K1 was added to the glass cell and the galvanic current was recorded until the experiment ended.
- 4) Open circuit potential for S1 was measured before adding sand or adding inhibitor during the experiment. The coupled electrodes, S1 and S2, were disconnected for 10 minutes on a regular basis so that individual intrinsic corrosion rate measurements by LPR could be performed for each electrode separately.

Figure 6.3 shows the variation of intrinsic corrosion rate with time, for both electrodes. It can be seen that at the beginning when there was no sand deposit and no

inhibitor, the central electrode and surrounding electrode had the same corrosion rate as expected (The data points for the central electrode overlap with the ones for the surrounding electrode). Once the sand deposit was added onto the central electrode, the corrosion rate of this electrode decreased from 1.2 ± 0.2 mm/yr to about 0.45 mm/yr, while the corrosion rate of surrounding bare electrode did not change. When 70 ppm of inhibitor K1 was added, the corrosion rate of the surrounding bare electrode decreased dramatically to about 0.02 ± 0.01 mm/yr. But no further decrease in corrosion rate was observed for the central sand covered electrode after an additional 100 hours of experiment, as expected.

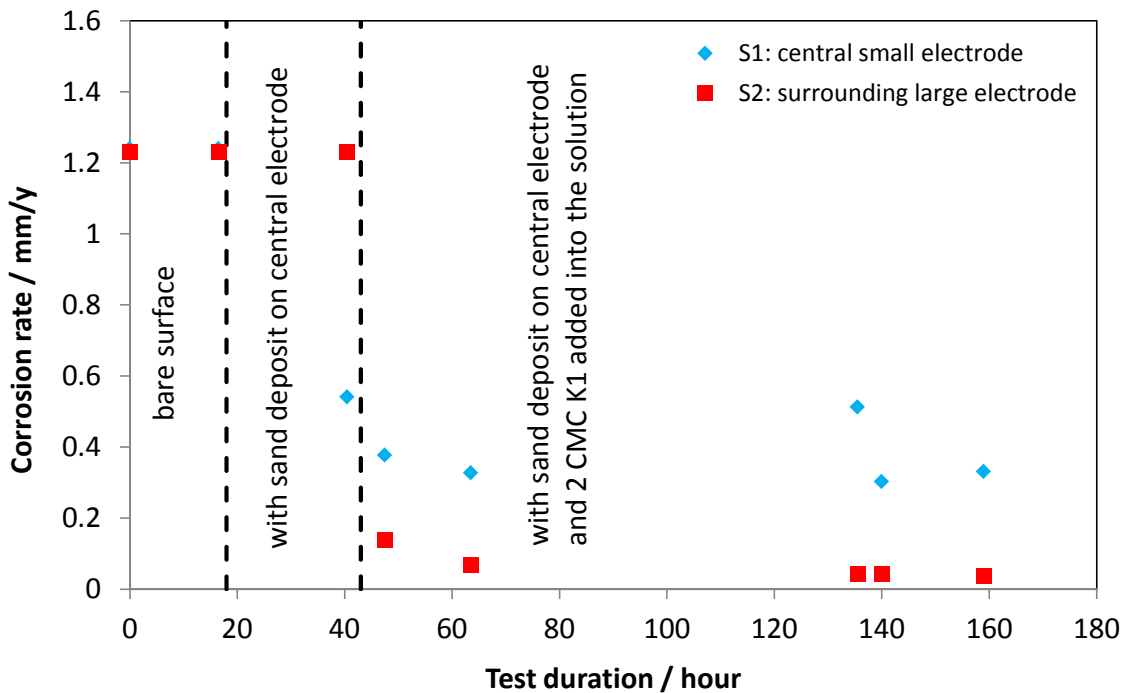


Figure 6.3 LPR corrosion rate (uncoupled) over time at test conditions 25°C, 1 wt% NaCl, pH 5.0. 2 mm sand deposit present only on the central small electrode S1 prior to 70 ppm K1 addition.

Figure 6.4 shows the variation of corrosion potential with time for the same experiment. The open circuit potential was measured independently for each electrode when the two were not coupled together. Along with having the same corrosion rate, the two uncoupled electrodes had same corrosion potential at the beginning of the experiment. (The data points for the central electrode overlap with the ones for the surrounding electrode). The addition of a sand deposit shifted the central electrode by 20 mV to more positive values, while the surrounding electrode had seen little change. Then after adding the inhibitor K1, the surrounding electrode's potential increased by about 80

mV to more positive values, while only 10 mV increase was observed for the central sand covered electrode.

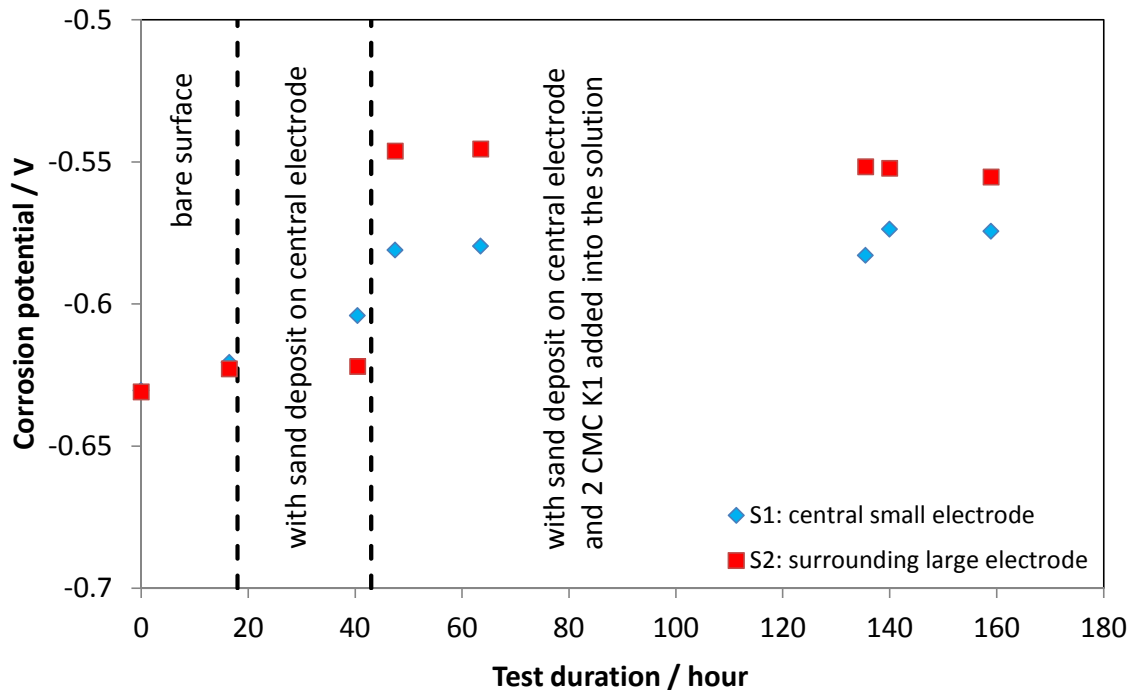


Figure 6.4 Corrosion potential vs. Ag/AgCl reference electrode (uncoupled) over time at test conditions 25°C, 1 wt% NaCl, pH 5.0. 2 mm sand deposit present only on the central small electrode S1 prior to 70 ppm K1 addition.

This corrosion potential difference is what “drives” the galvanic current. The variation with time of the potential difference between the two electrodes is plotted in Figure 6.5. The galvanic current shown in Figure 6.6 is therefore generated due to the “driving force” which is the corrosion potential difference between the two electrodes.

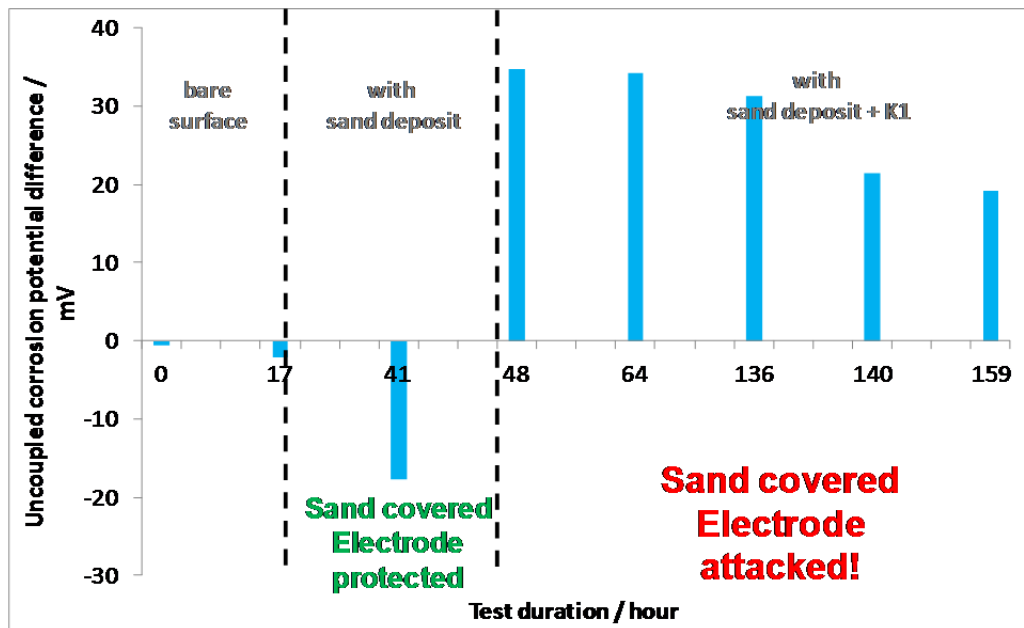


Figure 6.5 LPR corrosion potential (uncoupled) difference between the two electrodes over time at test conditions 25°C, 1 wt% NaCl, pH 5.0. 2 mm sand deposit present only on the central small electrode S1 prior to 70 ppm K1 addition.

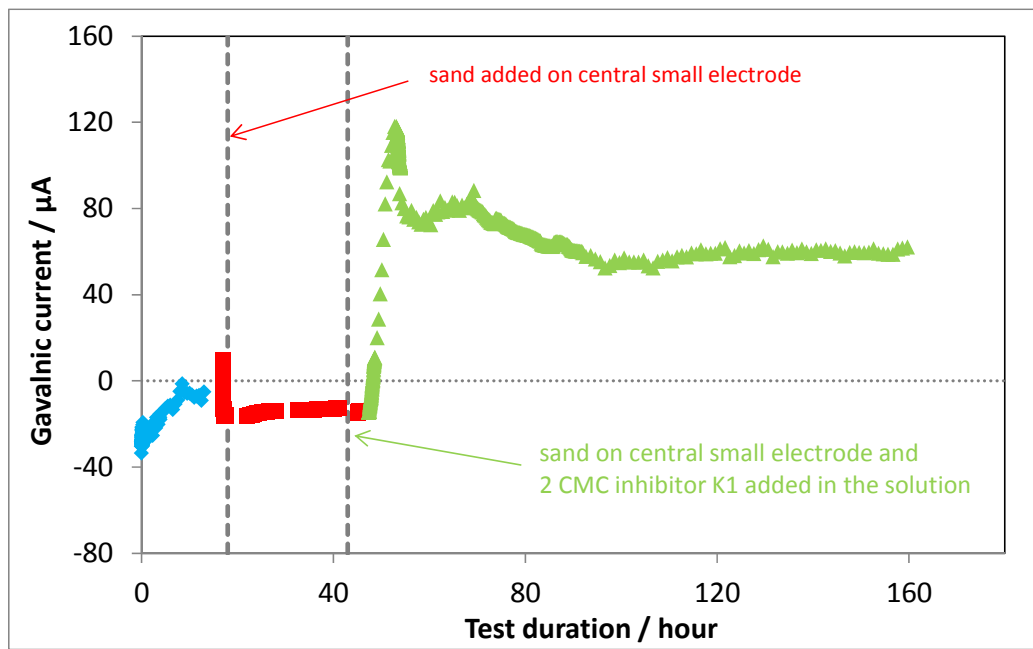


Figure 6.6 Galvanic current between the two electrodes coupled together over time at test conditions 25°C, 1 wt% NaCl, pH 5.0. A 2 mm sand deposit is present only on the central small electrode, S1, prior to 70 ppm K1 addition.

As can be seen from the Figure 6.5 and Figure 6.6, at the beginning, both electrodes S1 and S2 were exposed to the same solution, corroding the same, having the same corrosion rate and potential; the galvanic current density between them was negligible. Then sand deposit was added to the central small electrode S1, free corrosion of electrode S1 was retarded by the sand, having more positive corrosion potential than the surrounding bare surface electrode S2. The potential difference between them was about 8 mv, which resulted in a galvanic current density (with respect to S1) of 0.15 A/m^2 . When these two were connected as a couple, the sand covered S1 electrode became cathodically protected. The galvanic current was flowing from S1 to S2. At this time, the surrounding electrode S2 was acting as an anode. As S2 had a surface area 60 times

larger than S1, the galvanic current density with respect to S2 was small. Then 70 ppm inhibitor K1 was added to the test solution, the anode and cathode between electrodes S1 and S2 switched, because the effect of the inhibitor on the surface of the large electrode was to provide a full surface coverage, which retards the anodic reaction and increases the corrosion potential of the covered surface. Therefore a positive galvanic current was observed. The change in galvanic current was due to the addition of inhibitor, which protected the surrounding bigger bare electrode S2, but was not able to inhibit the sand covered electrode S1. Because of the inhibitor, the open circuit (uncoupled) potential of the bare surface electrode S2 was raised by 20 mV more positive than the central sand covered electrode S1, therefore, when these two electrodes were coupled together, a galvanic current density of 0.3 A/m^2 with respect to S1 was generated. Before the addition of inhibitor, the sand covered electrode S1 was protected by sand and also its potential was raised to be a more positive value so it acted as the cathode. With the inhibitor present, the S1 corrosion increased due to the galvanic effect.

It is known that inhibitor K1 primarily retards the anodic reaction, which results in the increase of the surface potential of the bare electrode S2, which is much more than the sand covered steel electrode S1. Figure 6.7 shows the effect of galvanic current on the corrosion rate of the sand covered electrode S1. Before adding inhibitor, the intrinsic corrosion rate of S1 was decreased by about 20% by the addition of the silica sand deposit. When the inhibitor was added, S1 corroded many times (almost 90 times) faster than the S2 and almost as fast as uninhibited bare steel corrosion rate.

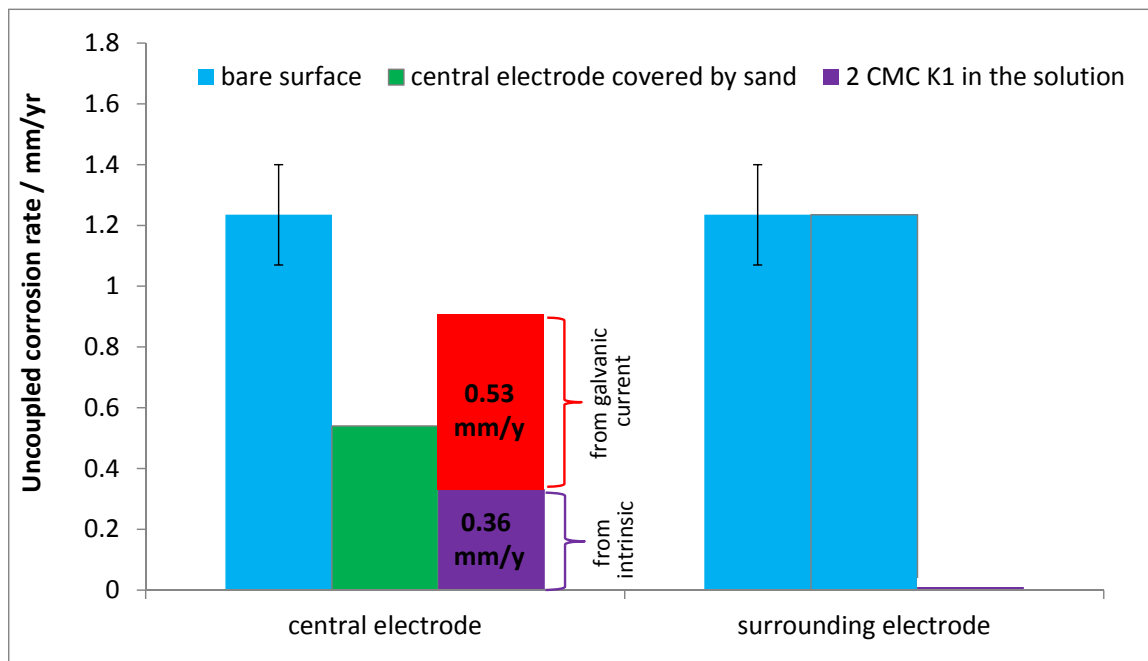


Figure 6.7 Galvanic effect on corrosion rate at test conditions 25°C, 1 wt% NaCl, pH 5.0.

2 mm sand deposit present only on the central small electrode S1 prior to 70 ppm K1 addition.

From discussion above, it can be stated that the presence of a silica sand deposit would lead to formation of a galvanic cell between the sand covered area and surrounding bare steel surface area. For a sand deposit layer, there is a void between each sand particle. The above experiment setup can be considered as a system consisted of many couples of single sand particle covered area and its adjacent bare surface areas. By studying the individual galvanic cell formation and propagation, the mechanisms of localized corrosion in under deposit CO₂ corrosion of mild steel can be understood.

6.3.2 Location and Propagation of Localized Under Deposit Corrosion

Using the coupled electrode specimen, it was confirmed that a galvanic cell formed when a silica sand deposit and imidazoline-based inhibitor were both present. Experimental results of single electrode experiments discussed in Chapter 5 also showed that pits were observed under individual silica sand particles at conditions where no localized corrosion normally occurred if silica sand and imidazoline based inhibitor were not present. Therefore, questions were raised on what mechanisms or physical attributes provide the environment to form a galvanic cell on mild steel when both silica sand and imidazoline inhibitor are present. Experiments were then designed to answer those questions.

The single electrode methodology was used in this part of the work, where individual silica sand particles were placed on the electrode surface during the experiment. The purpose of using only a few individual silica sand particles was to investigate the occurrence of localized corrosion in a more precise way and on a smaller scale, i.e., to study if and how a galvanic cell would form between the area right under a single silica sand particle and the surrounding more exposed area on the steel surface. The electrode was made of the same X65 steel material as described in Chapter 4.

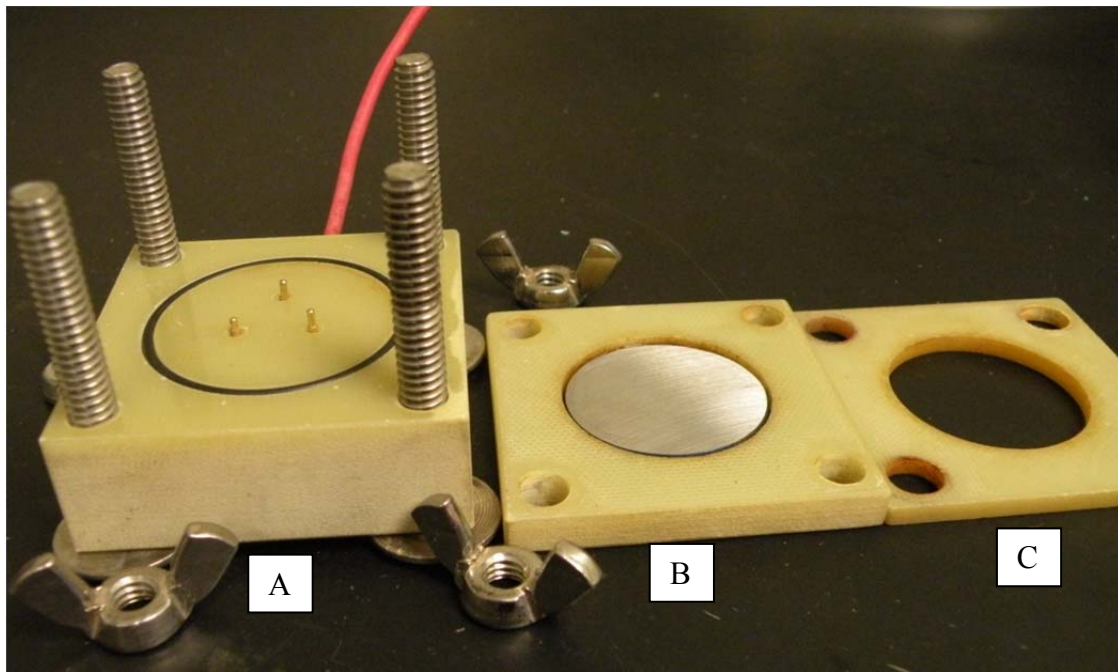


Figure 6.8 API 5L X65 mild steel specimen holder: (A) base, with three gold contacts to connect the steel specimen and wire for electrochemical measurement; (B) steel sample holder, where steel specimen is installed; (C) sand holder, fill up to 2 mm sand deposit.

Single electrode was used in order to investigate the propagation of localized corrosion. The steel surface was designed to be either fully or partially covered by silica sand particles..

1. Multiple Small Grains of Sand

The experiment was conducted at 25°C, in a 1 wt% NaCl solution with inhibitor added after pre-corrosion and addition of sand particles. Figure 6.9 shows the trend of uniform corrosion rate from electrochemical measurements for linear polarization resistance (LPR). After two hours bare steel corrosion, a few grains of 750 µm sand

particles were added on the steel surface, and then after another 24 hours, 70 ppm K1 inhibitor was added to the solution. The efficiency of inhibitor K1 was about 86% as the uniform corrosion rate decreased from 1.1 mm/yr to about 0.15 mm/yr after inhibitor's addition. The "uniform" LPR corrosion rate is calculated based on the whole steel surface as it assumes the whole steel surface had uniform corrosion even when a silica sand deposit was present, which obviously was not the case.

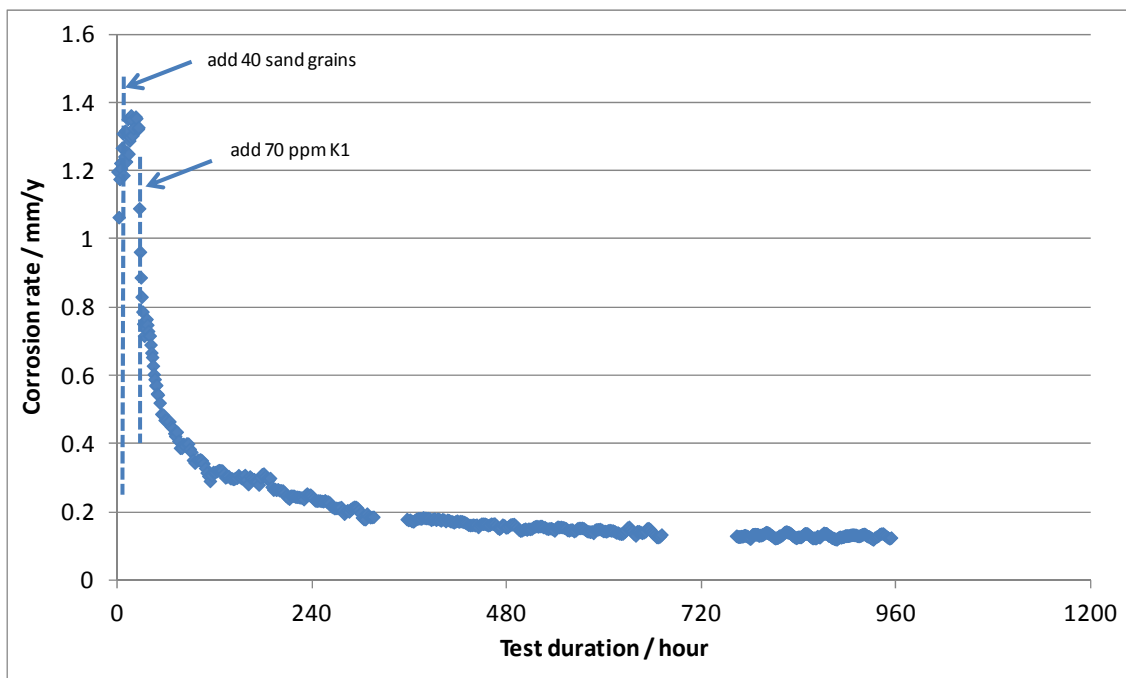


Figure 6.9 LPR corrosion rate over time at test conditions 25°C, pH 5, 1 wt% NaCl solution saturated with CO₂. About 40 grains of sand particles present prior to 70 ppm K1 addition.

Figure 6.10 is the picture of the steel surface taken after experiment finished. A lot of pits can be seen on the steel surface. Figure 6.11 shows the SEM images of the corrosion product where a grain of sand was located. It clearly shows the localized corrosion developed underneath each sand particle. The shape of pit area is similar in shape and size of the sand particles. No iron carbonate was observed.



Figure 6.10 View of the steel surface showing a lot of pits after 40 days exposure at conditions 25°C, pH 5, 1 wt% NaCl solution saturated with CO₂.

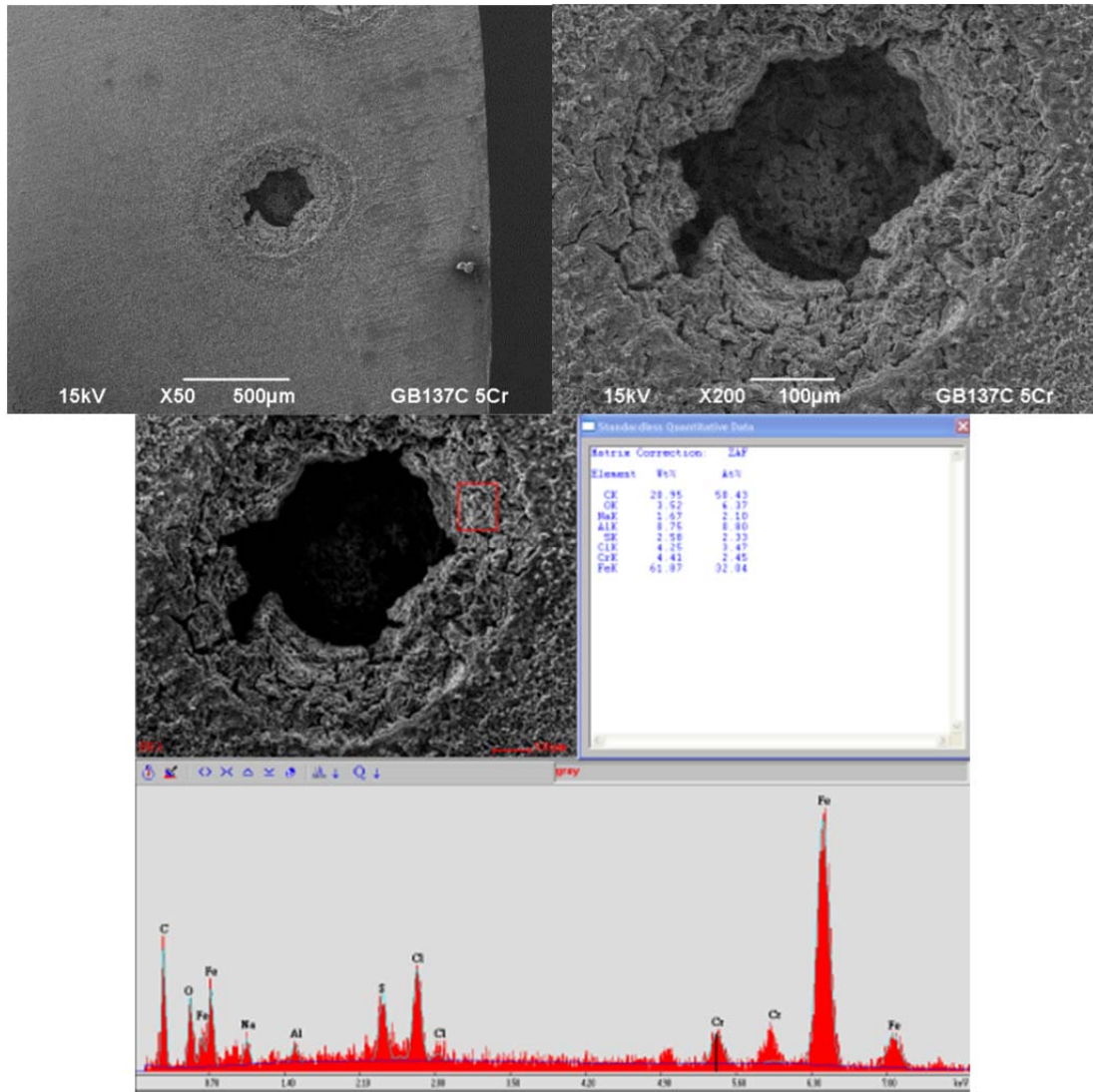


Figure 6.11 SEM and EDS images of the steel surface with corrosion product layers after 40 days exposure at conditions 25°C, pH 5, 1 wt% NaCl solution saturated with CO₂.

After SEM analysis, the specimen was cleaned to remove the corrosion product to measure the depth with a infinite focusing microscopy. A infinite focusing microscopy image with depth indicated by color is shown in Figure 6.12. The pit penetrated 250 μm

in about 40 days, which is equal to a pitting rate of 2.3 mm/yr. Compared to the final uniform corrosion rate measured from LPR which was 0.15 mm/yr, this localized corrosion rate is 15 times greater and is considered to be very significant, as can be seen in the comparison shown in Figure 6.13.

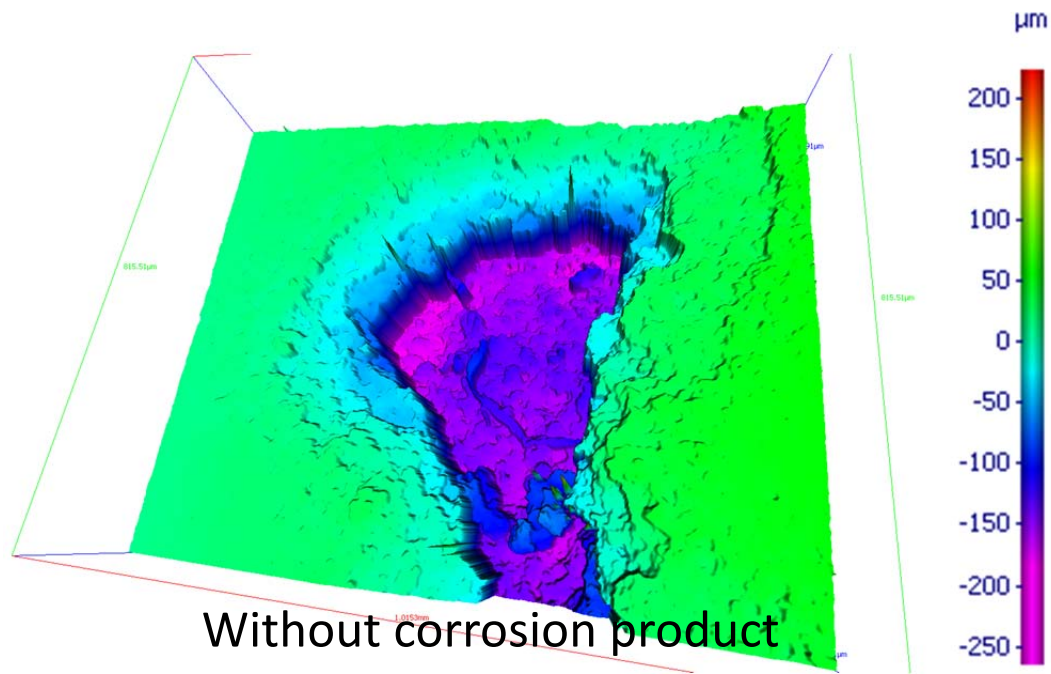


Figure 6.12 Prolifometer image of one of the pits found on the steel surface after 40 days exposure at conditions 25°C, pH 5, 1 wt% NaCl solution saturated with CO₂.

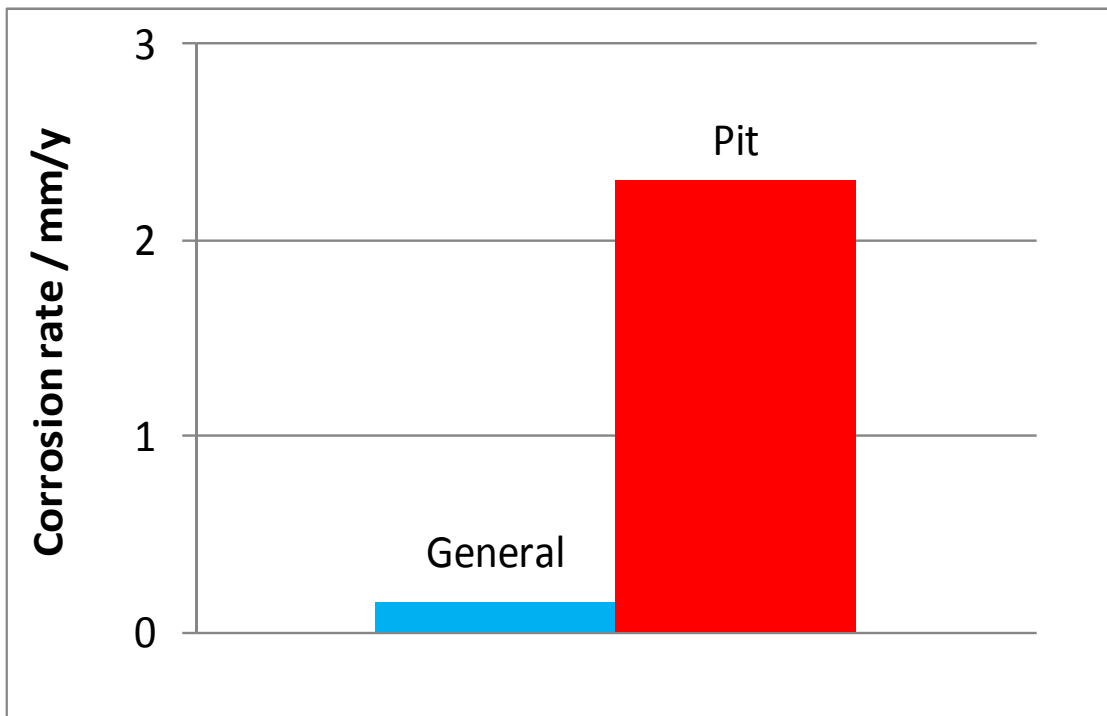


Figure 6.13 Comparison of pitting rate and surface averaged corrosion rate obtained from LPR after 40 days exposure at conditions 25°C, pH 5, 1 wt% NaCl solution saturated with CO₂.

2. Single Large Silica Crystal

Another experiment with only one big silica crystal on the steel surface was also conducted (equivalent to a “very large grain of sand”). Imidazoline based inhibitor K1 was added after the silica particle, following the same procedure as described above. Figure 6.14 shows how the experiment specimen looked during the experiment with this big crystal on the steel surface.

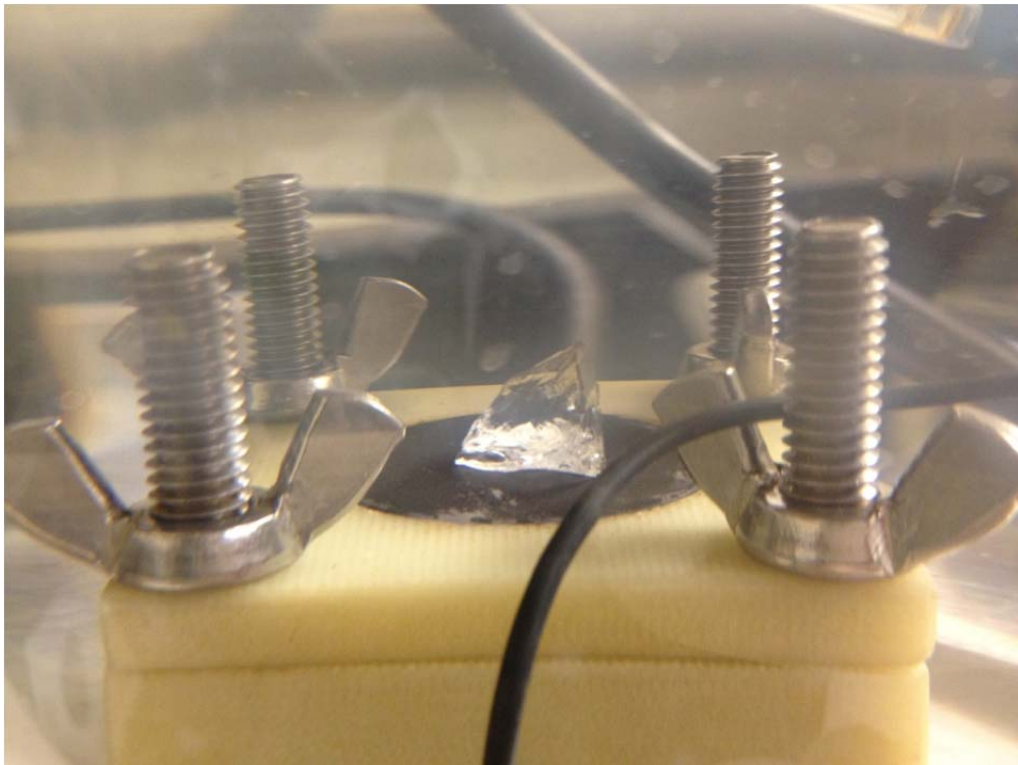


Figure 6.14 View of one big crystal sitting on the steel surface at test conditions 25°C,
pH 5, 1 wt% NaCl solution saturated with CO₂.

Figure 6.15 shows how the steel surface looked after corrosion. The shape of the silica crystal can be clearly recognized imprinted on the steel surface by corrosion.

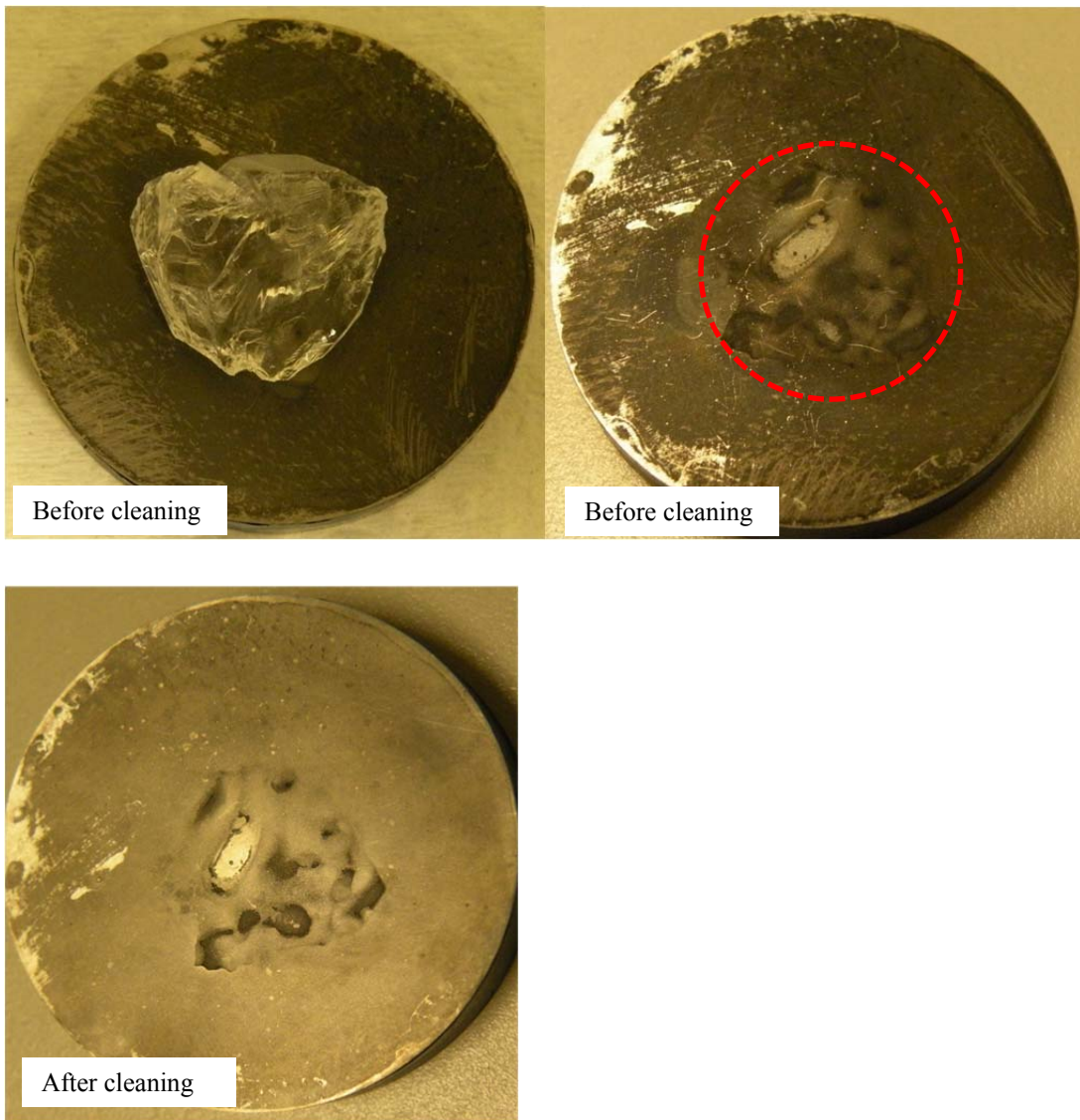


Figure 6.15 View of the steel surface after 9 days exposure at test conditions 25°C, pH 5,

1 wt% NaCl solution saturated with CO₂.

Before the corrosion product layer was removed, the steel surface was scanned by SEM. Iron carbonate was found at those pitting areas, see Figure 6.16. The crystal has an irregular shape and only part of the bottom of the grain was in touch with the steel. In

those confined area covered by the crystal, Fe^{2+} and CO_3^{2-} became saturated due to large pitting rate and retarded diffusion, therefore, iron carbonate could easily form.

The whole steel surface was then scanned by the infinite focusing microscopy, and the deepest area was found to be $70 \mu\text{m}$ (Figure 6.17), which equals to a penetration rate of 2.8 mm/yr - average for 9 days corrosion. Comparing to the uniform corrosion rate 0.1 mm/yr calculated from LPR measurement, the localized corrosion was significant (Figure 6.18).

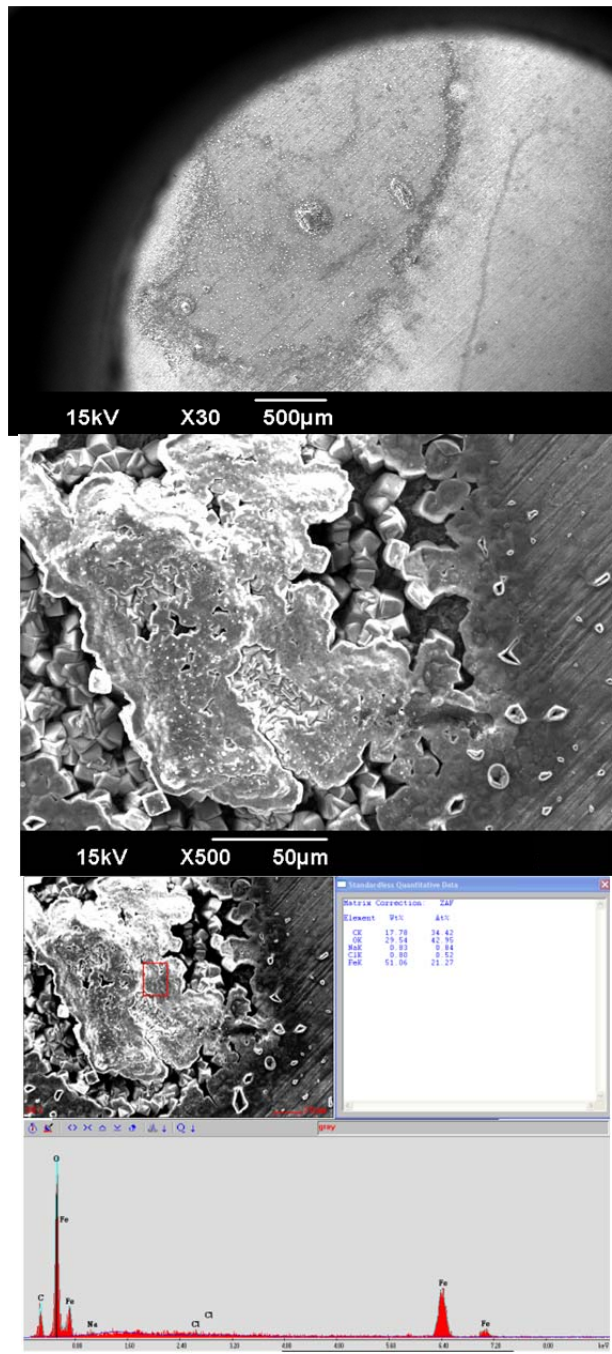


Figure 6.16 SEM and EDX images of the steel surface with corrosion product layers after 9 days exposure at test conditions 25°C, pH 5, 1 wt% NaCl solution saturated with CO₂.

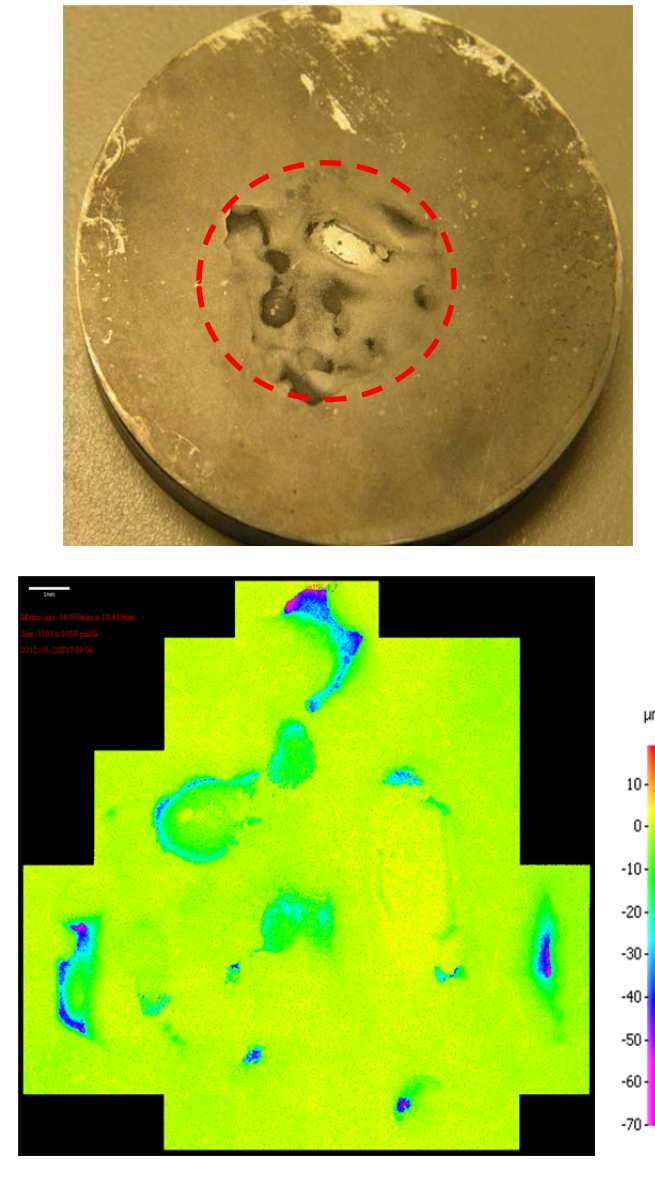


Figure 6.17 Infinite focusing microscopy Image of the steel surface after 9 days exposure and corrosion product layer removed at test conditions: 25°C, pH 5, 1 wt% NaCl solution saturated with CO₂.

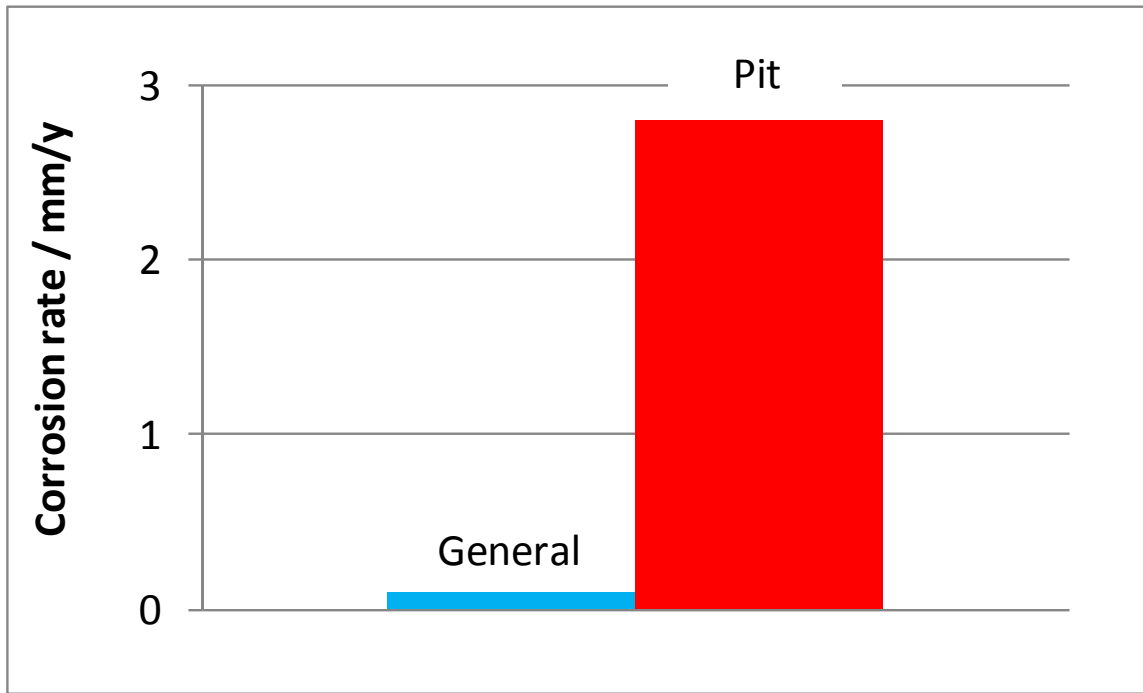


Figure 6.18 Comparison of the pitting rate and surface averaged corrosion rate obtained from weight loss after 9 days exposure at test conditions 25°C, pH 5, 1 wt% NaCl solution saturated with CO₂.

3. Pit propagation

The experiment above clearly shows that in the presence of silica sand particles an imidazoline-only inhibitor K1 promoted the occurrence of localized corrosion underneath the silica particles. Pitting occurred in this environment for a stable, non-moving set of sand particles, but, if the sand particles were to be moved (e.g. from increased flow in a pipeline), would the localized corrosion continue? To verify if pit propagation would stop, experiments were designed where sand particles were removed

from the steel surface after the localized corrosion had begun, but the steel remained in the inhibited environment for another period of time.

The test procedure for this set was the same as in the above experiment, except that there were two specimens in the same cell at the beginning. Then, at the same time, specimen #1 was taken out for analysis and the sand particles were removed from specimen #2's surface and it was left in the solution for another 9 days.

Figure 6.19 shows the view of specimen #1 after 25 day's corrosion with sand particles and inhibitor K1 (imidazoline). Deep pits can be seen on the steel surface. SEM image of the steel surface with corrosion product layer is shown in Figure 6.20. No iron carbonate was observed. After corrosion product layer was removed, the pit depth was measured using a infinite focusing microscopy. All the pits were developed under each single sand grain and had a depth of $220 \mu\text{m} \pm 40 \mu\text{m}$ (Figure 6.21), which is equal to a $3.3 \pm 0.5 \text{ mm/yr}$ penetration rate for 25 days' corrosion. The surface averaged corrosion rate was $0.05 \text{ mm/yr} \pm 0.01 \text{ mm/yr}$ (Figure 6.22), as obtained from Fe^{2+} concentration measurement. This pit penetration rate is very large as compared to the uniform corrosion rate (Figure 6.23).



Figure 6.19 View of the experiment sample #1 after 25 days exposure with corrosion product layers and without corrosion product layers at test conditions 25°C, pH 5, 1 wt% NaCl solution saturated with CO₂.

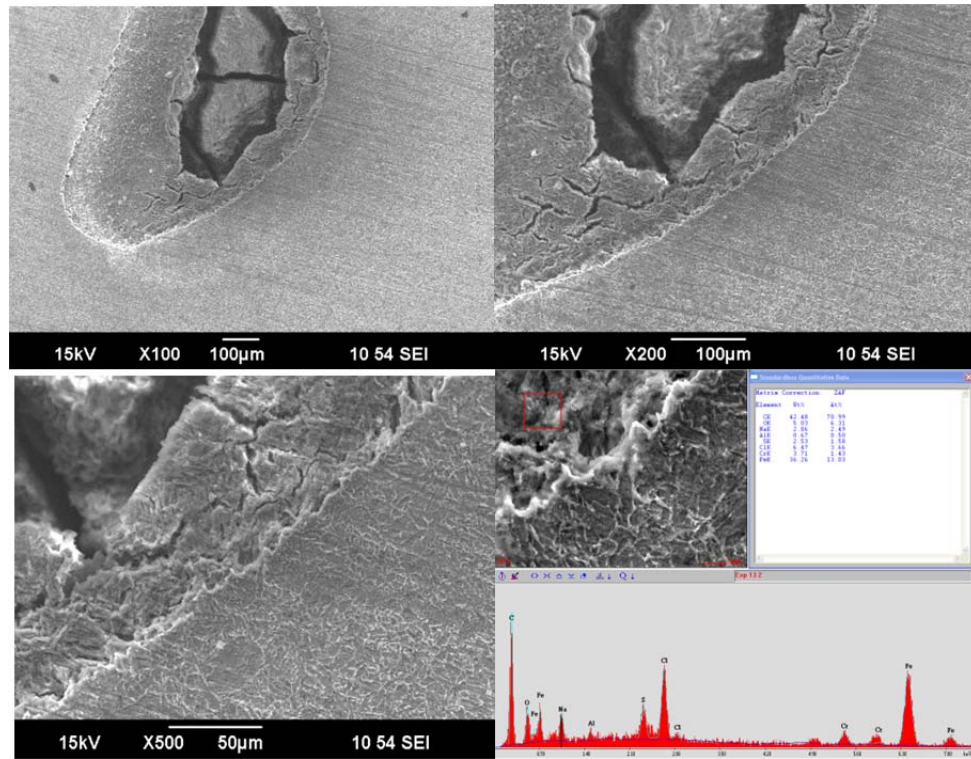


Figure 6.20 SEM and EDS images of the experiment sample #1 with corrosion product layers after 25 days exposure at test conditions 25°C, pH 5, 1 wt% NaCl solution saturated with CO₂.

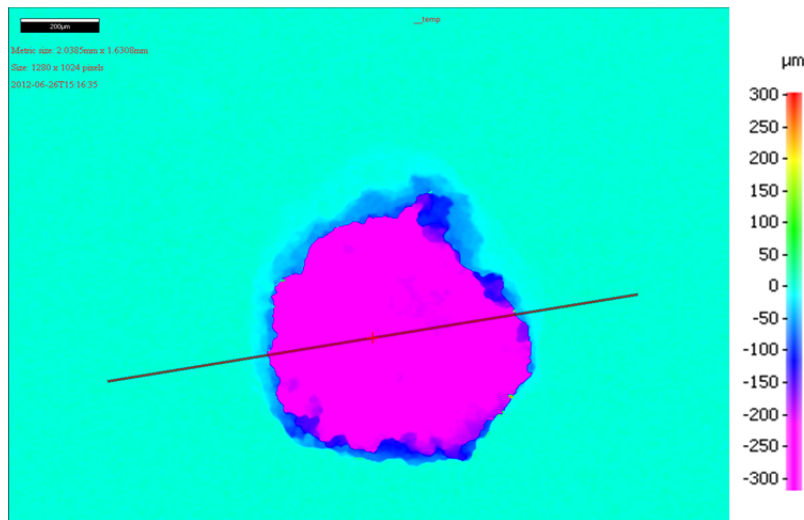


Figure 6.21 An infinite focusing microscopy image of one of the pits found on the steel surface after 25 days exposure at test conditions 25°C, pH 5, 1 wt% NaCl solution saturated with CO₂.

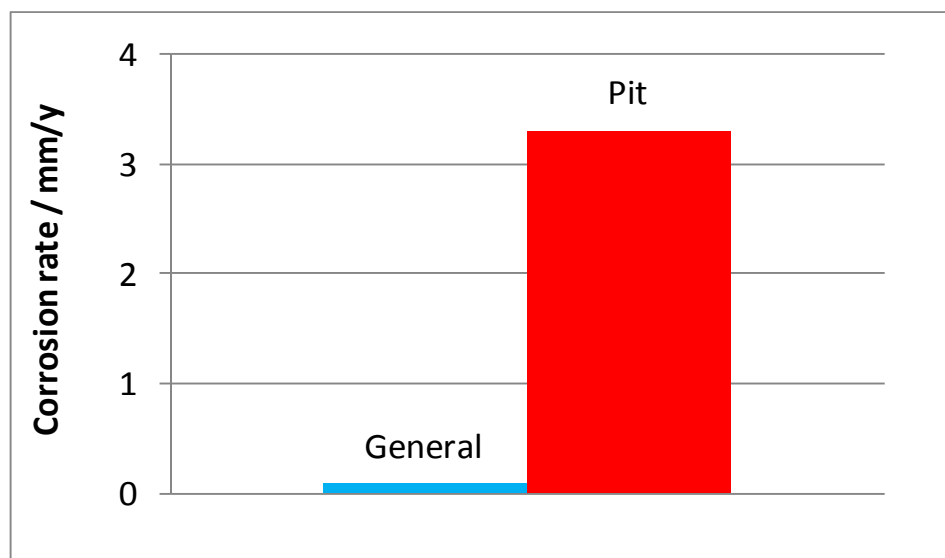


Figure 6.22 Comparison of pitting rate and surface averaged corrosion rate obtained from weight loss method at test conditions 25°C, pH 5, 1 wt% NaCl solution saturated with CO₂.

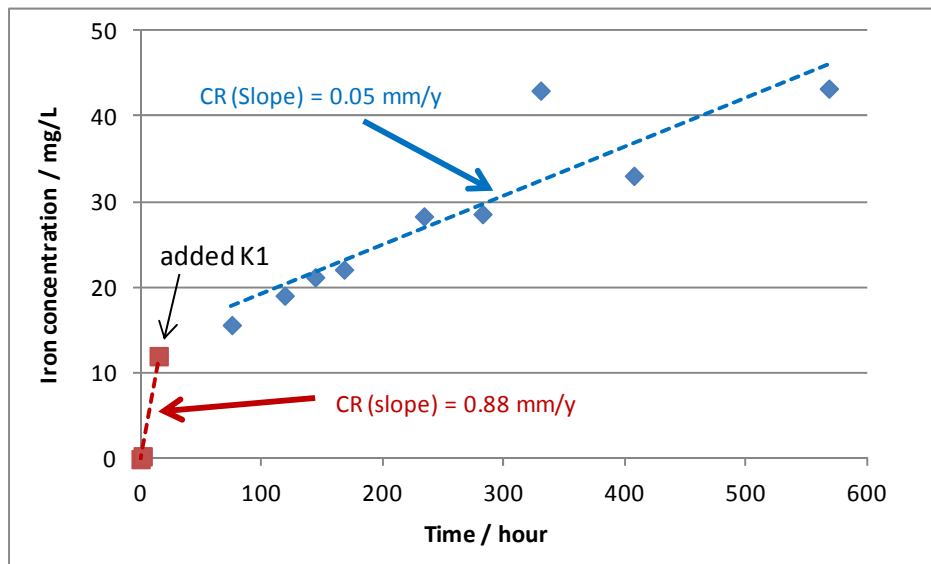


Figure 6.23 Fe^{2+} concentration vs. time at test conditions 25°C , pH 5, 1 wt% NaCl solution saturated with CO_2 .

Figure 6.24 shows the view of specimen #2 which was left in the corrosion cell for 9 more days than specimen #1 with the sand particles removed from it. Pits can also be observed on the steel surface as expected. The SEM image of the pits before corrosion product removal is shown in Figure 6.25. No significant difference of the pit morphology can be distinguished between specimen #1 and #2. The deepest part of the pit was measured at $210 \mu\text{m} \pm 30 \mu\text{m}$ (Figure 6.26), corresponding to a pit penetration rate of $2.3 \pm 0.3 \text{ mm/yr}$. As compared to the uniform corrosion rate of 0.09 mm/yr , the localized corrosion is 25 times greater (Figure 6.27).



Figure 6.24 Views of the experiment sample #2 after 34 days exposure with corrosion product layers (left) and without corrosion product layers (right) at test conditions 25°C, pH 5, 1 wt% NaCl solution saturated with CO₂.

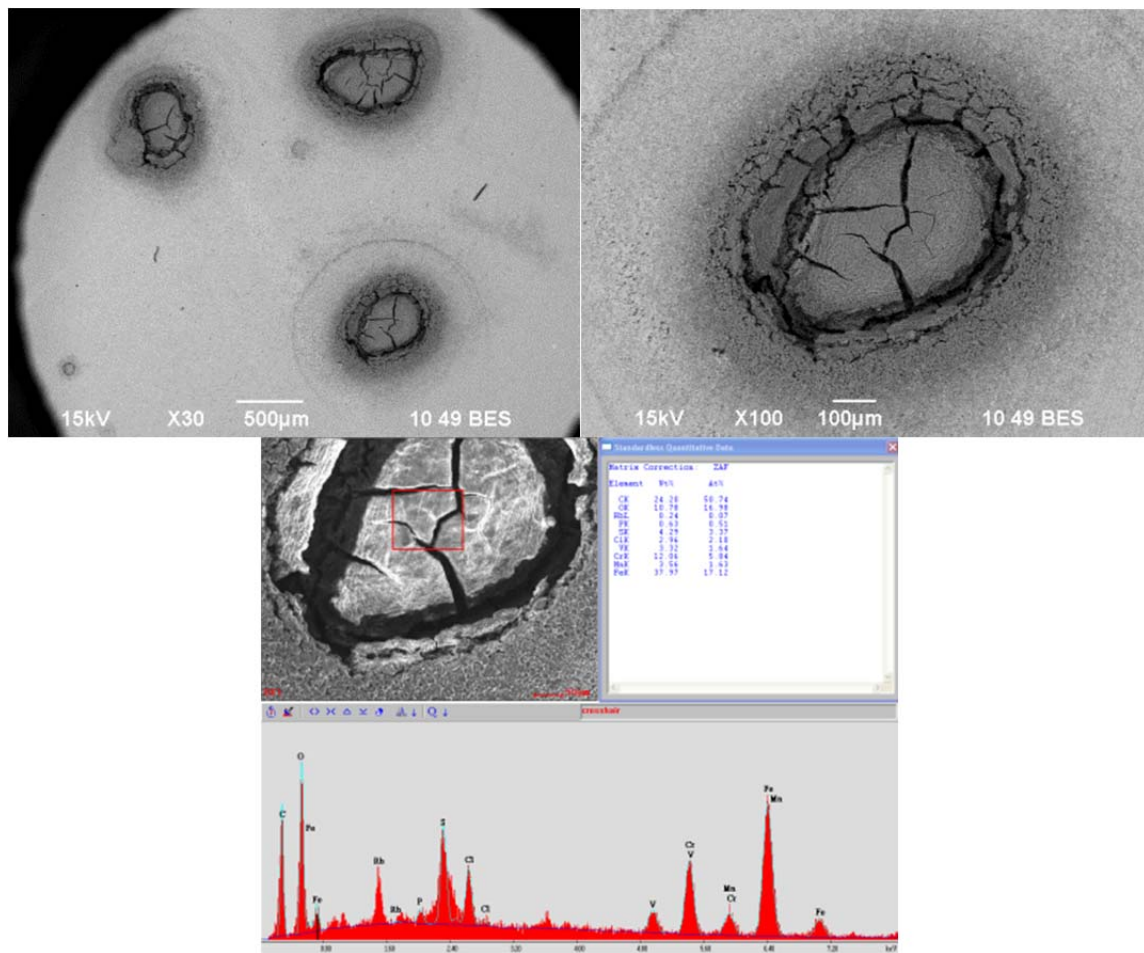


Figure 6.25. SEM and EDS images Pictures of the experiment sample #2 after 34 days exposure with corrosion product layers at test conditions 25°C, pH 5, 1 wt% NaCl solution saturated with CO₂.

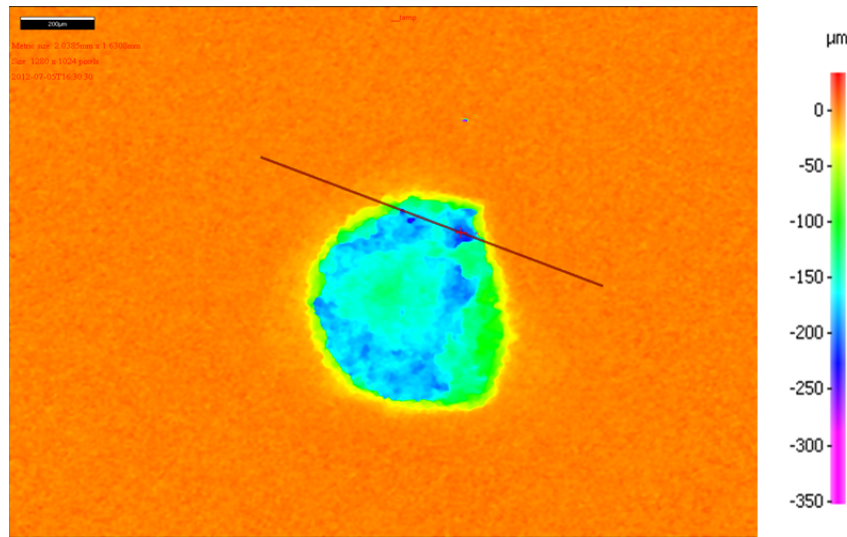


Figure 6.26 An infinite focusing microscopy image one of the pits found on the steel sample #2 surface after 34 days exposure at test conditions 25°C, pH 5, 1 wt% NaCl solution saturated with CO₂.

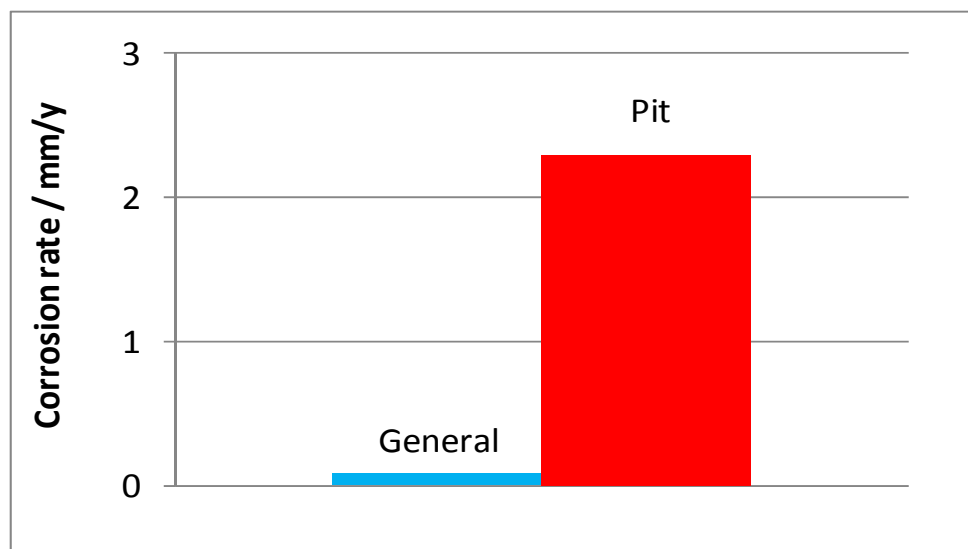


Figure 6.27 Comparison of pitting rate and surface averaged corrosion rate obtained from weight loss method after 34 days exposure at test conditions 25°C, pH 5, 1 wt% NaCl solution saturated with CO₂.

The comparison of pit depth between specimen #1 and #2 is shown in Figure 6.28. It can be seen that even with 9 more days' corrosion, the pit on specimen #2 had not grown deeper. It indicates that once the sand particles were removed and the steel surface was exposed to the test solution, the inhibitor K1 was able to protect the steel again and prevent the pit from penetrating further.

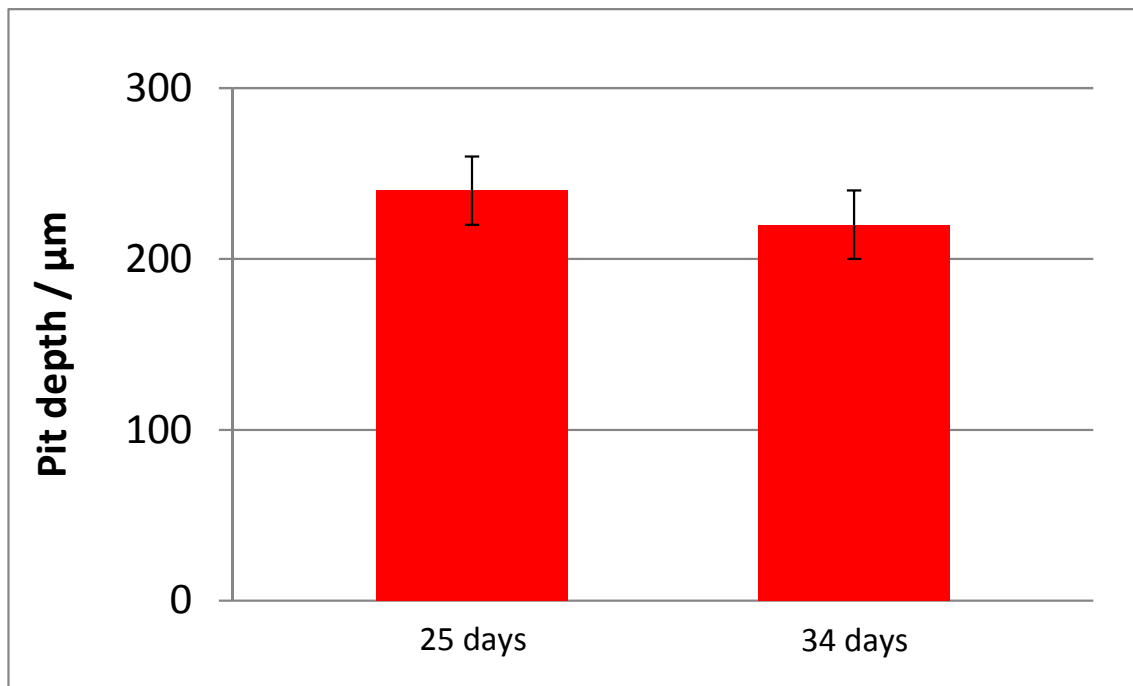


Figure 6.28 Comparison of the pit depth of sample #1 and #2. Test conditions are as described in 6.23, except that for sample #2 it corroded 9 more days with sand particles removed.

4. Experiments with silica crystal

Another experiment with only one silica crystal was conducted as well, following the same procedure, i.e., two samples in the same test solution and by the time the sample

#1 was taken out, the crystal on the sample #2 was taken away and sample #2 continued corroding for more days.

Figure 6.29 shows the image of sample #1 after 17 days' corrosion. The shape of the bottom of the crystal can be configured on the steel surface. Before corrosion product removal, the steel surface was analyzed by SEM. The bottom of the crystal is not flat, so the areas underneath the crystal were confined where the edges of the crystal had direct contact with the metal surface and iron carbonate was found at those confined areas. Different areas of the metal surface were scanned and iron carbonates with different morphologies were observed, see in Figure 6.30. Some of the iron carbonate crystals were well developed while others were not. The formation of iron carbonate was due to the high pitting rate in the small areas underneath the silica and retarded diffusion by the crystal, therefore, saturated Fe^{2+} and CO_3^{2-} concentrations can be easily reached. The corrosion product was removed by using Clark solution. Figure 6.31 shows the images of experiment sample scanned after product scale removal from IFM, where the whole areas of the steel surface was scanned and the deepest area was found to be 160 μm (Figure 6.31), which corresponds to a penetration rate of 3.5 mm/yr for a 17 days' corrosion. Most of the areas where crystal was in touch with the steel, the penetration depth was 100 μm , equivalent to a penetration rate of 2.2 mm/yr. The surface averaged uniform corrosion rate from Fe^{2+} concentration and weight loss measurement was 0.16 mm/yr (Figure 6.32). The pitting rate is very high as compared to the uniform corrosion rate (Figure 6.32).

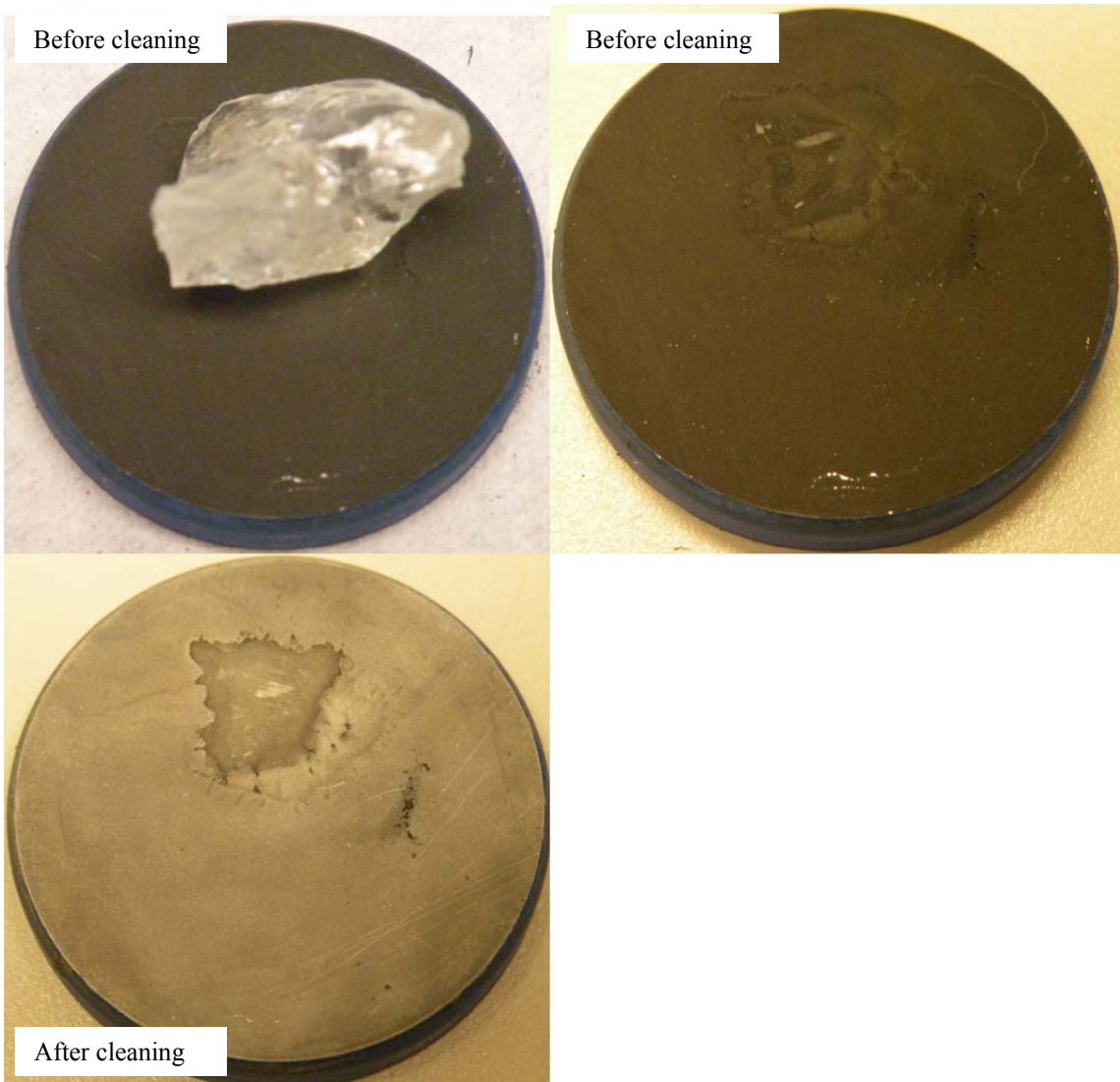


Figure 6.29 Views of the experiment sample #1 after 17 days exposure at test conditions

25°C, pH 5, 1 wt% NaCl solution saturated with CO₂.

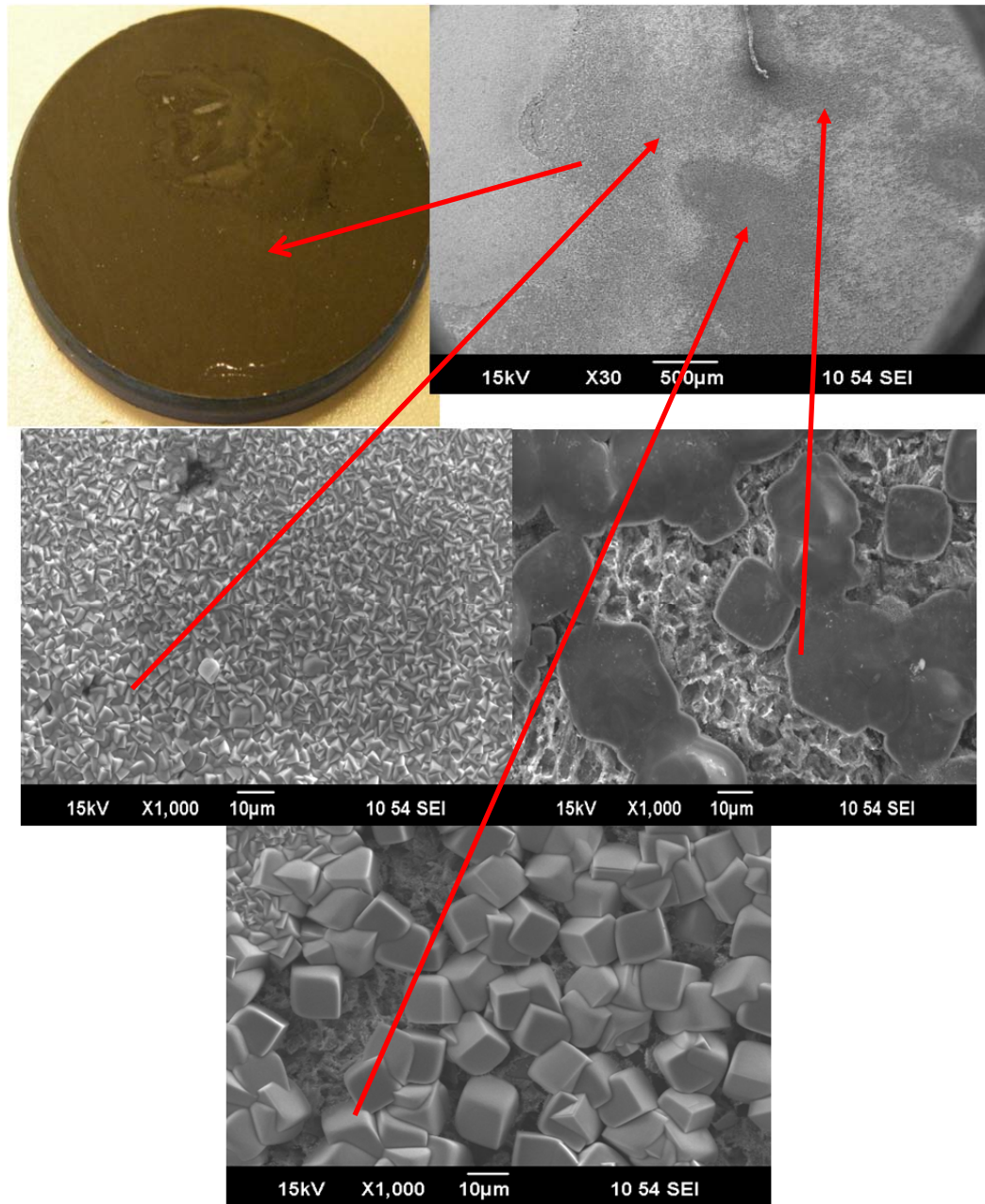


Figure 6.30 SEM images of the experiment sample #1 with corrosion product layers after 17 days exposure at test conditions 25°C, pH 5, 1 wt% NaCl solution saturated with CO₂.

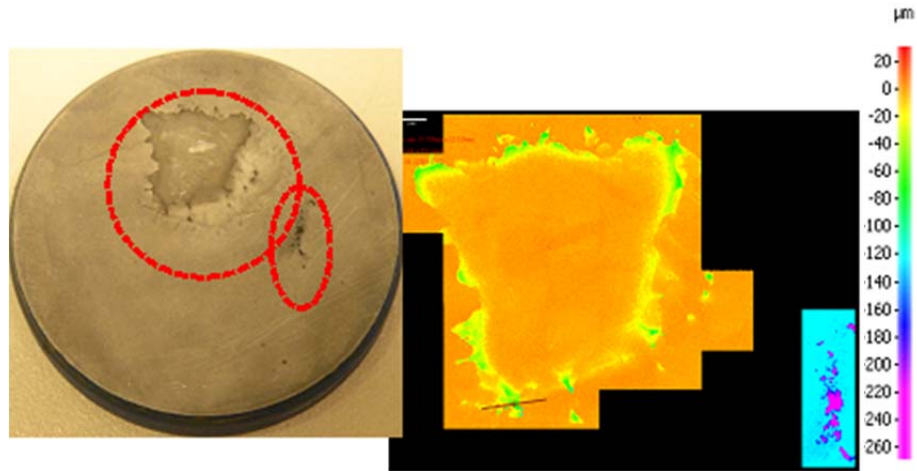


Figure 6.31 Infinite focusing microscopy images of the steel surface after corrosion product layer was removed at test conditions 25°C, pH 5, 1 wt% NaCl solution saturated with CO₂.

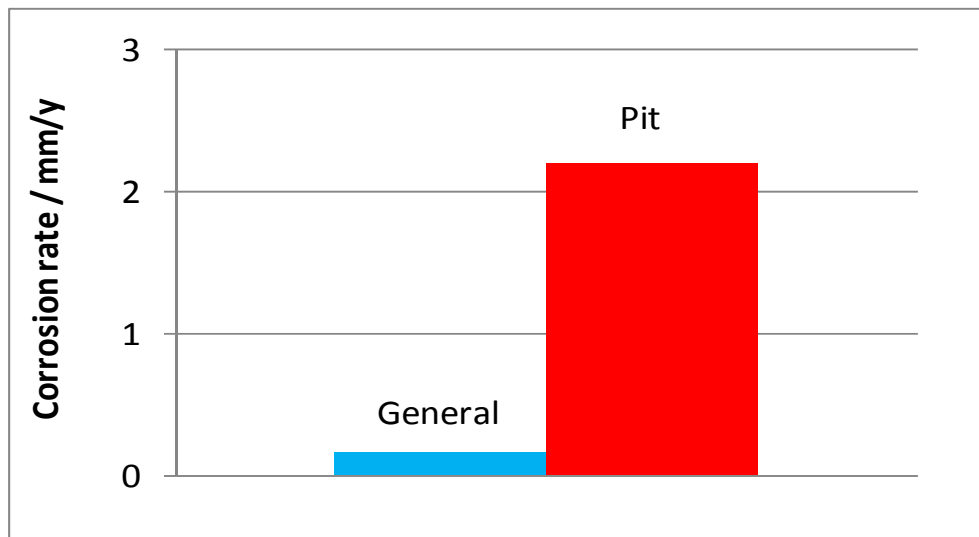


Figure 6.32 Comparison of pitting rate and surface averaged corrosion rate obtained from weight loss method at test conditions 25°C, pH 5, 1 wt% NaCl solution saturated with CO₂.

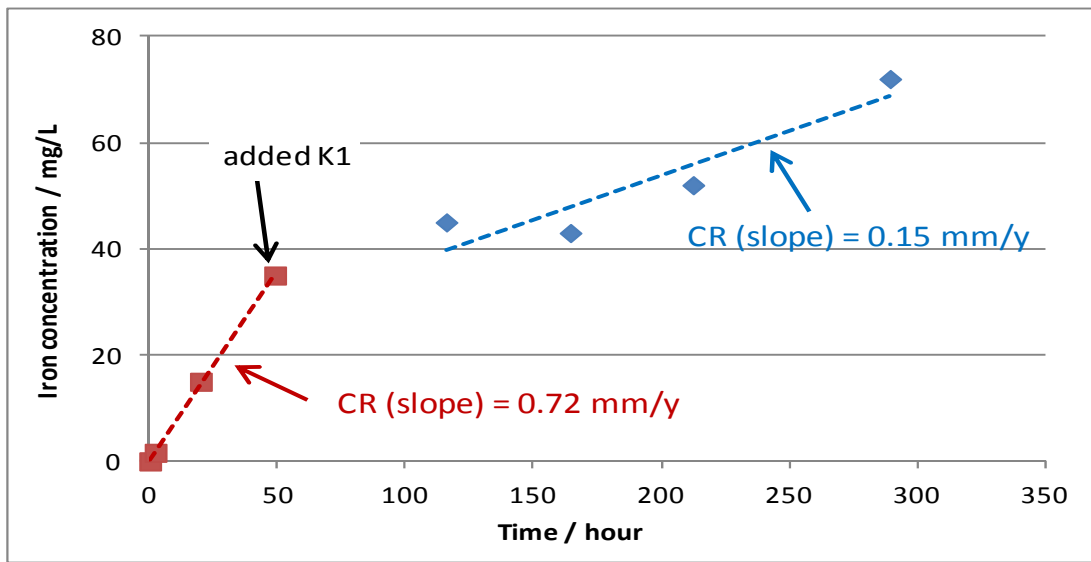


Figure 6.33 Fe^{2+} concentration variation over time at test conditions 25°C , pH 5, 1 wt%

NaCl solution saturated with CO_2 ..

By the time sample #1 finished corroding, the crystal on sample #2 was taken out, and sample #2 remained in the test solution for 9 more days. Figure 6.34 shows the image of the sample before and after corrosion product removal.

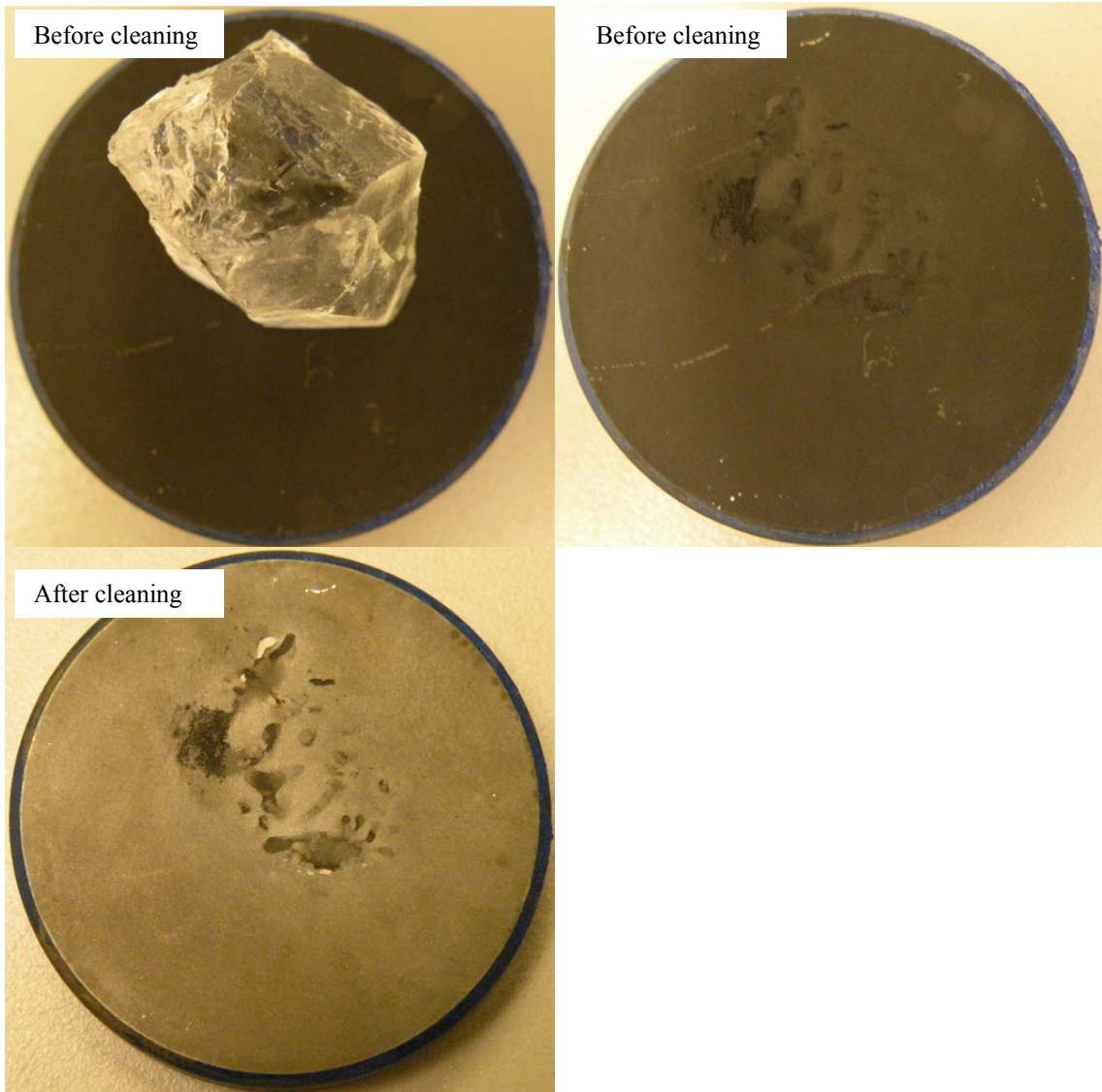


Figure 6.34 Views of the experiment sample #2 after 26 days exposure. For this sample, the first 17 days, it was under exactly the same condition as sample #1 as described in Figure 29, but the last 9 days, the sand particles were removed from the steel surface.

The steel surface morphology before corrosion product removal was analyzed using SEM. No iron carbonate was found at the areas where the silica crystal was present for this specimen (Figure 6.35). it was because once crystal was removed from the surface, the surface was exposed to bulk solution and Fe^{2+} and CO_3^{2-} concentration became under-saturated, and iron carbonate dissolved away.

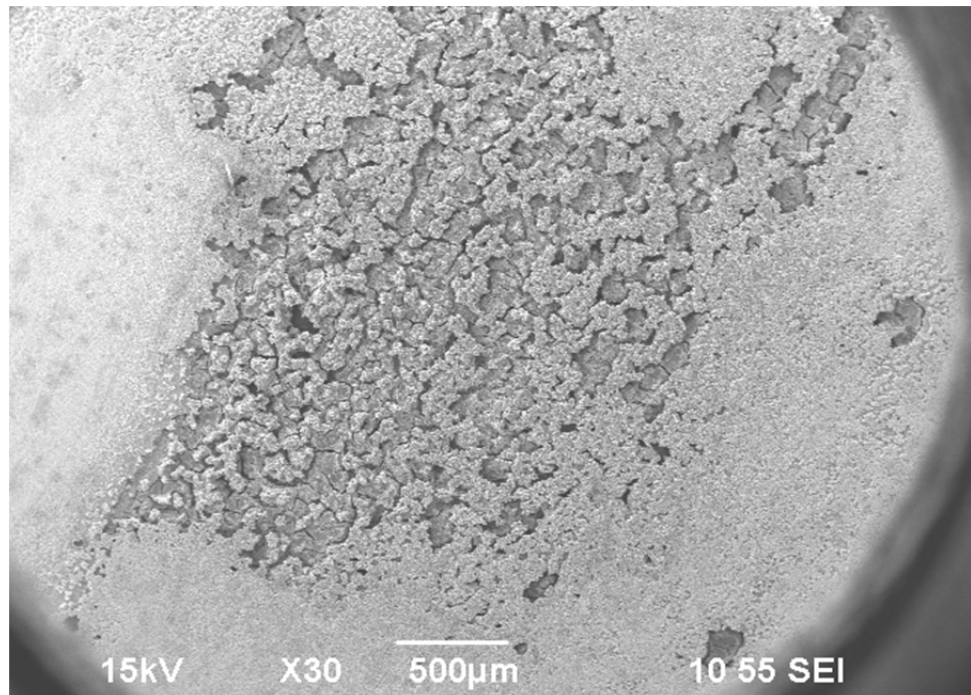


Figure 6.35 SEM images of the experiment sample #2 with corrosion product layers at test conditions 25°C, pH 5, 1 wt% NaCl solution saturated with CO_2 .

After SEM scanning, the corrosion product on the steel surface was removed carefully, and localized corrosion was analyzed by a infinite focusing microscopy. Deepest depth of localized corrosion was found to be 155 μm , where most of the accelerated corrosion areas had a depth of 80 μm (Figure 6.36). For a total 26 days'

corrosion, this depth of penetration equals to a penetration rate of 1.8 mm/yr, which is very large as compared to uniform corrosion rate based on surface averaged calculation (Figure 6.37).

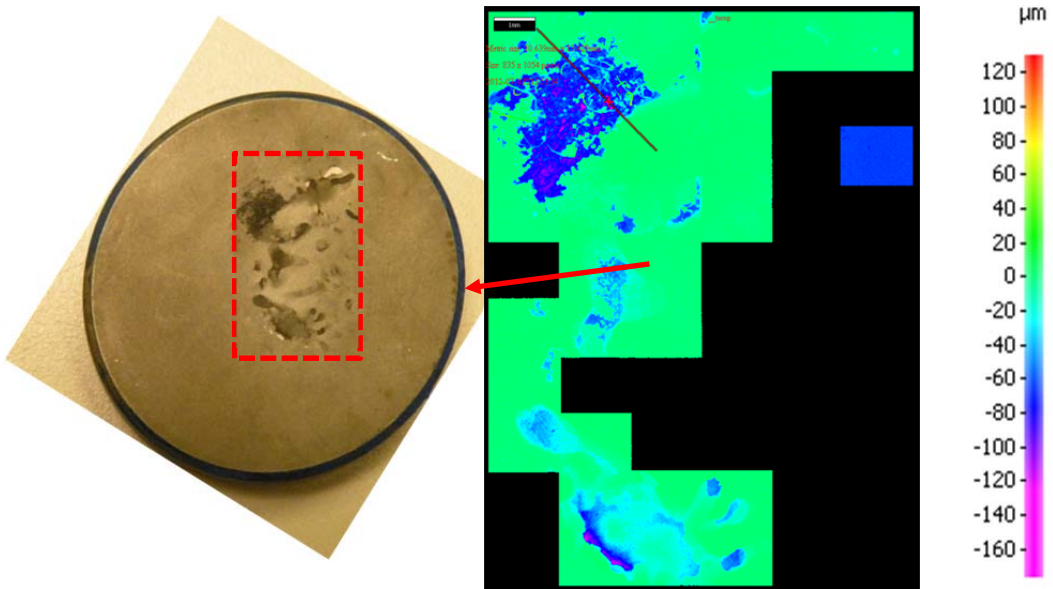


Figure 6.36 Profilometer Image of the steel surface of sample #2 after corrosion product layer was removed at test conditions 25°C, pH 5, 1 wt% NaCl solution saturated with CO₂.

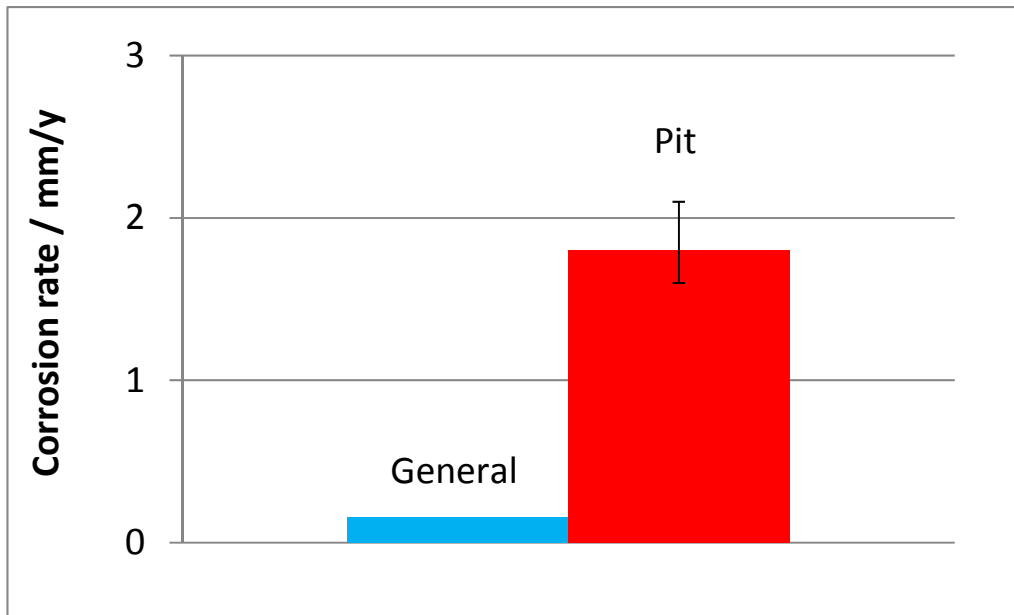


Figure 6.37 Comparison of pitting rate and surface averaged corrosion rate obtained from weight loss method at test conditions 25°C, pH 5, 1 wt% NaCl solution saturated with CO₂.

The comparison of pit depth between sample #1 and #2 is shown in Figure 6.38, it shows that, the same as in experiment with a few sand particles, with 9 more days' corrosion, the pits one sample #2 did not grow deeper. It confirms that the pit stopped growing after the big crystal was removed. Once the steel surface was exposed to the test solution, the inhibitor K1 was able to protect the steel again and prevent the pit from penetrating further.

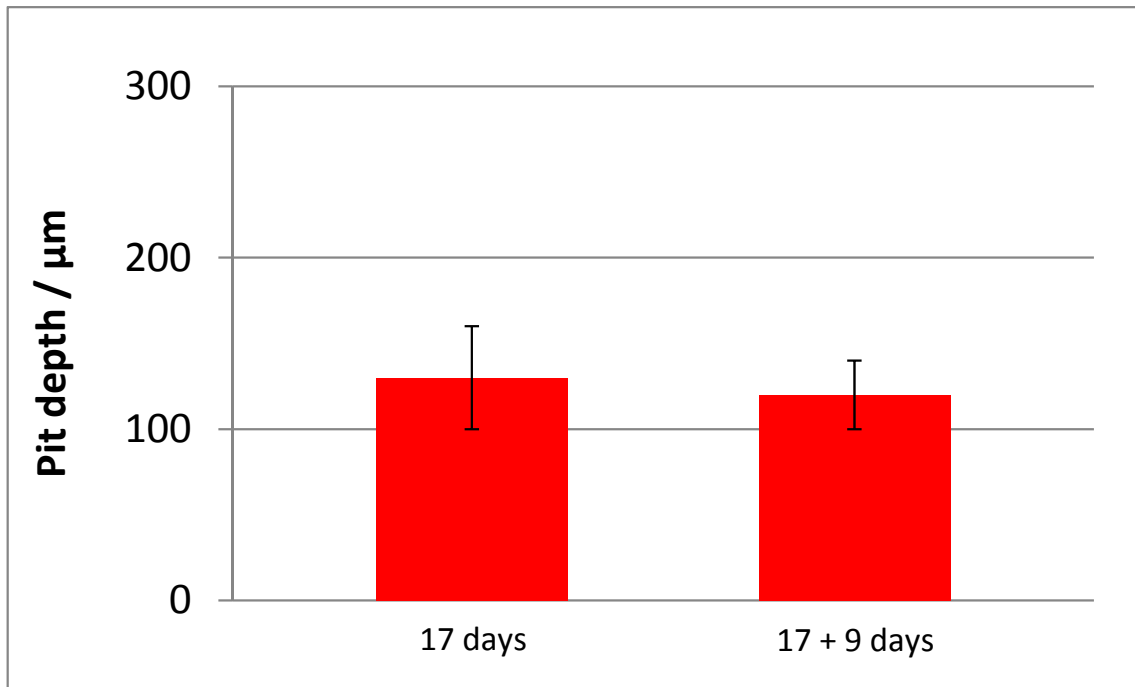


Figure 6.38 Comparison of the pit depth of sample #1 and #2 at test conditions 25°C, pH 5, 1 wt% NaCl solution saturated with CO₂.

5. Summary – inhibition after sand addition

As discussed above, the pitting corrosion was significant, even though environmental conditions (pH 5.0, T = 25 C, pCO₂ = 0.97 bar) including a corrosion inhibitor would not be expected to lead to serious corrosion. At those conditions, if there were no sand particles or corrosion inhibitor, the bare steel corrosion rate was about 1.0 mm/yr. If there was only a generic imidazoline corrosion inhibitor K1, the steel would be protected well having a corrosion rate below 0.1 mm/yr. However, when sand particles and corrosion inhibitor K1 were present together, very serious localized corrosion in the form of pitting occurred. At the same time the pits were developing, the surface averaged

corrosion rate was still low as the inhibitor was effective across the remaining steel surface. Figure 6.39 shows how the corrosion rate would be in different scenarios. The dashed line at 0.1 mm/yr (bottom) is the inhibited surface averaged corrosion rate whether sand particles were present or not. The dashed line at 1 mm/yr (middle) is what the corrosion rate would be if there were no sand nor corrosion inhibitor. The red dashed line (top) is the average pitting corrosion rate found on the steel surface when both sand particles and imidazoline corrosion inhibitor were present. The data points represent pitting rate measured from repeated experiments, but with different exposure times.

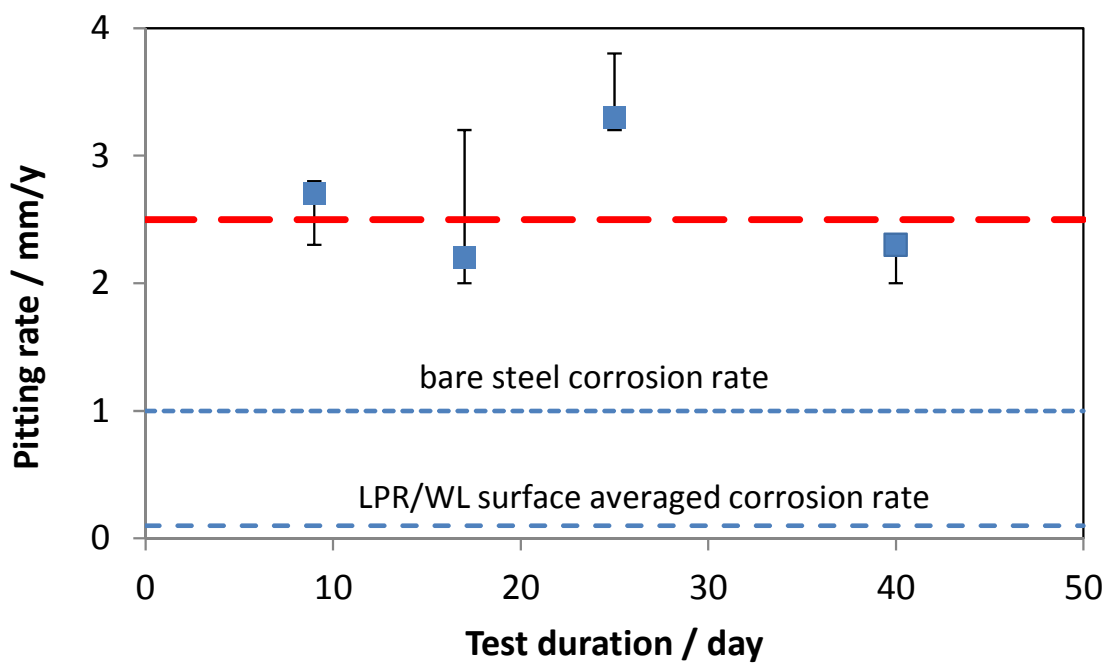


Figure 6.39 Comparison of pitting rate with bare steel corrosion rate and surface averaged corrosion rate from LPR/WL at test conditions 25°C, pH 5, 1 wt% NaCl solution saturated with CO₂.

Figure 6.40 also shows that, after the silica sand or crystal was removed, even with longer corrosion, the pit propagation stopped. Once the steel surface was exposed to the solution again, it was protected by inhibitor and further corrosion could be prevented.

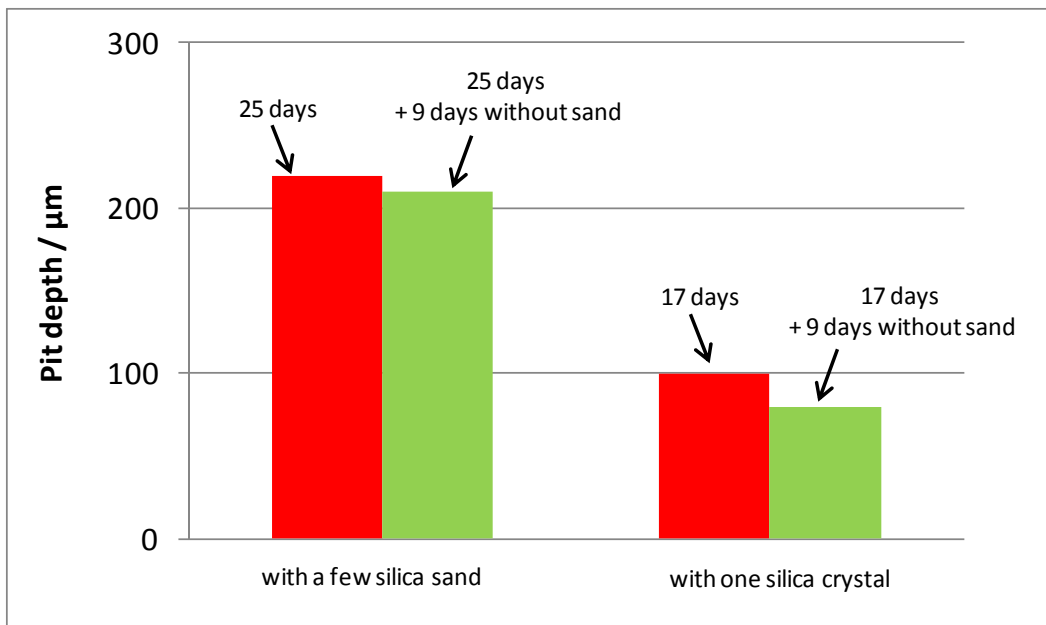


Figure 6.40 Change of pitting depth after silica sand or silica crystal was removed from the steel surface for experiments conducted at 25°C, pH 5, in a 1 wt% NaCl solution saturated with CO₂.

6. Inhibition before sand addition

Another set of experiments were conducted where generic imidazoline inhibitor K1 was added before sand particle addition to verify if the inhibitor has a preference to being adsorbed on the sand surface. Two specimens were placed in a same test solution and corroded under same conditions for 28 days to get duplicate results. After an hour's bare steel corrosion, 70 ppm K1 was added to the solution and the experiment continued

for another 24 hours. Then sand particles were added to the specimens. The ferrous ion (Fe^{2+}) concentration was measured and recorded during the experiment for the average corrosion rate. Figure 6.41 shows the view of one of the specimens after removal from the glass cell, before and after removing the corrosion product. The trace of sand particles can still be seen on the sample surface. SEM scanning indicated local corrosion occurred only at the sand particle locations (Figure 6.42). After the corrosion product was removed, the steel surface was analyzed by infinite focusing microscopy which clearly shows that there were pits formed underneath the sand particles. The depths of those pits were $15 \pm 3 \mu\text{m}$ (Figure 6.43), which corresponded to a pit penetration rate of 0.2 mm/yr. This penetration rate value seems low, but it is 15 times greater than the 0.013 mm/yr uniform corrosion rate measured from weight loss, therefore it is still considered as localized corrosion.



Figure 6.41 View of the experiment specimen after 14 days exposure at test conditions:
 25°C , pH 5, 1 wt% NaCl solution saturated with CO_2 .

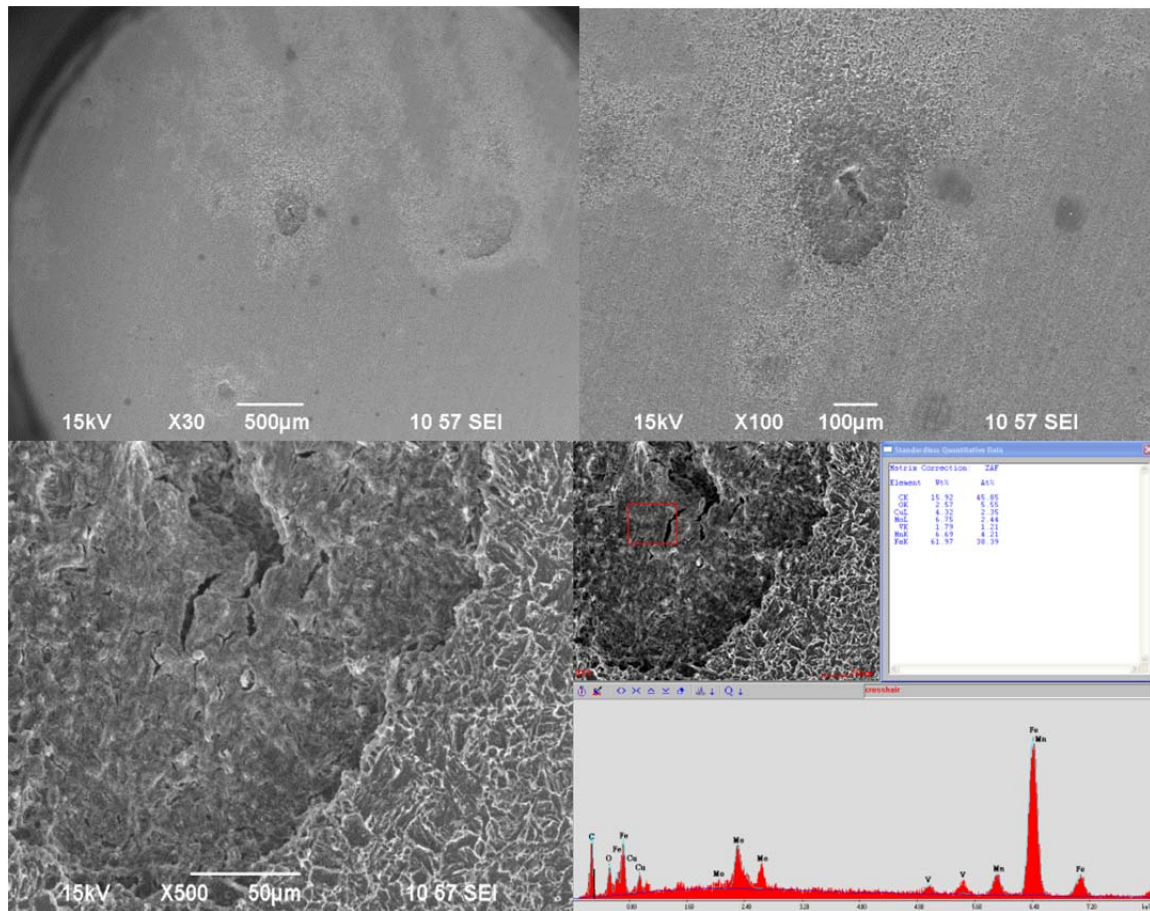


Figure 6.42 SEM and EDX images of the experiment sample #1 with corrosion product layers. Test conditions: 25°C, pH 5, 1 wt% NaCl solution saturated with CO₂.

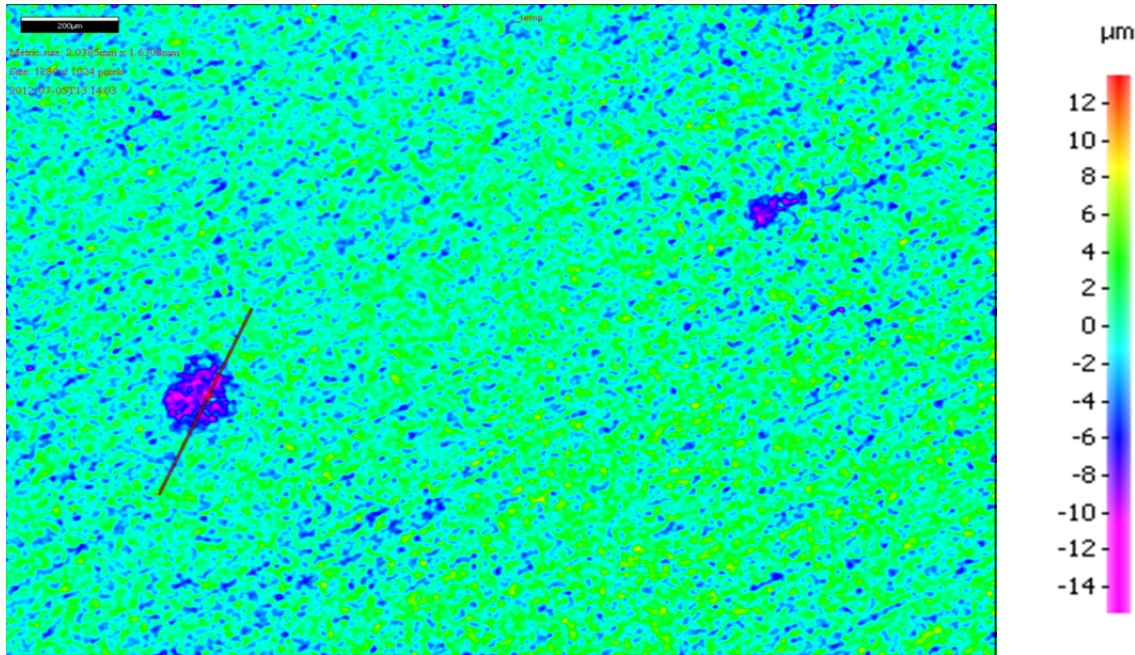


Figure 6.43 A infinite focusing microscopy image of the experiment sample #1 without corrosion product layers. Test conditions: 25°C, pH 5, 1 wt% NaCl solution saturated with CO₂.

For specimen #2, similar results were obtained. Steel surface showed similar morphology as specimen #1 did, see Figure 6.44 and Figure 6.45. Some pits were found on the surface underneath sand particles, having depth of $11 \pm 2 \mu\text{m}$ (Figure 6.46), which equals to penetration rate of 0.14 mm/yr. even though this value is considered low in terms of corrosion, it is still 10 times bigger than uniform corrosion rate calculated from weight loss, which is 0.013 mm/yr. Therefore, it is considered as localized corrosion. These two specimens were corroded under same conditions, so the results obtained are considered to be consistent and repeatable. The comparison of pit penetration rate and

uniform corrosion rate is shown in Figure 6.47. In this set of experiment, imidazoline inhibitor K1 was added before sand particles, i.e., the steel surface was already inhibited before silica's present. Localized corrosion was still observed, which indicates that the inhibitor K1 did have preference on being absorbed by silica surface and the mechanism proposed here was confirmed.

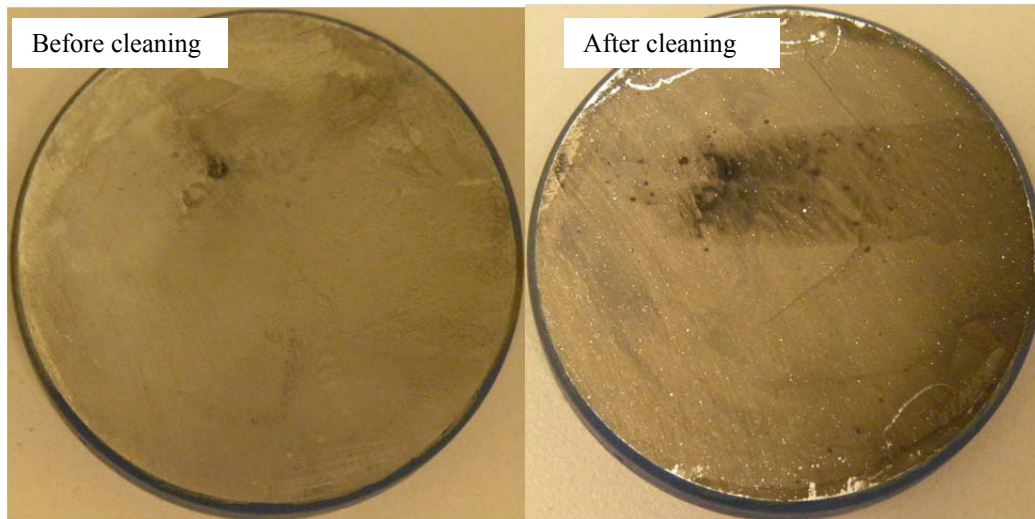


Figure 6.44 View of the experiment specimen after 14 days exposure at test conditions:

25°C, pH 5, 1 wt% NaCl solution saturated with CO₂.

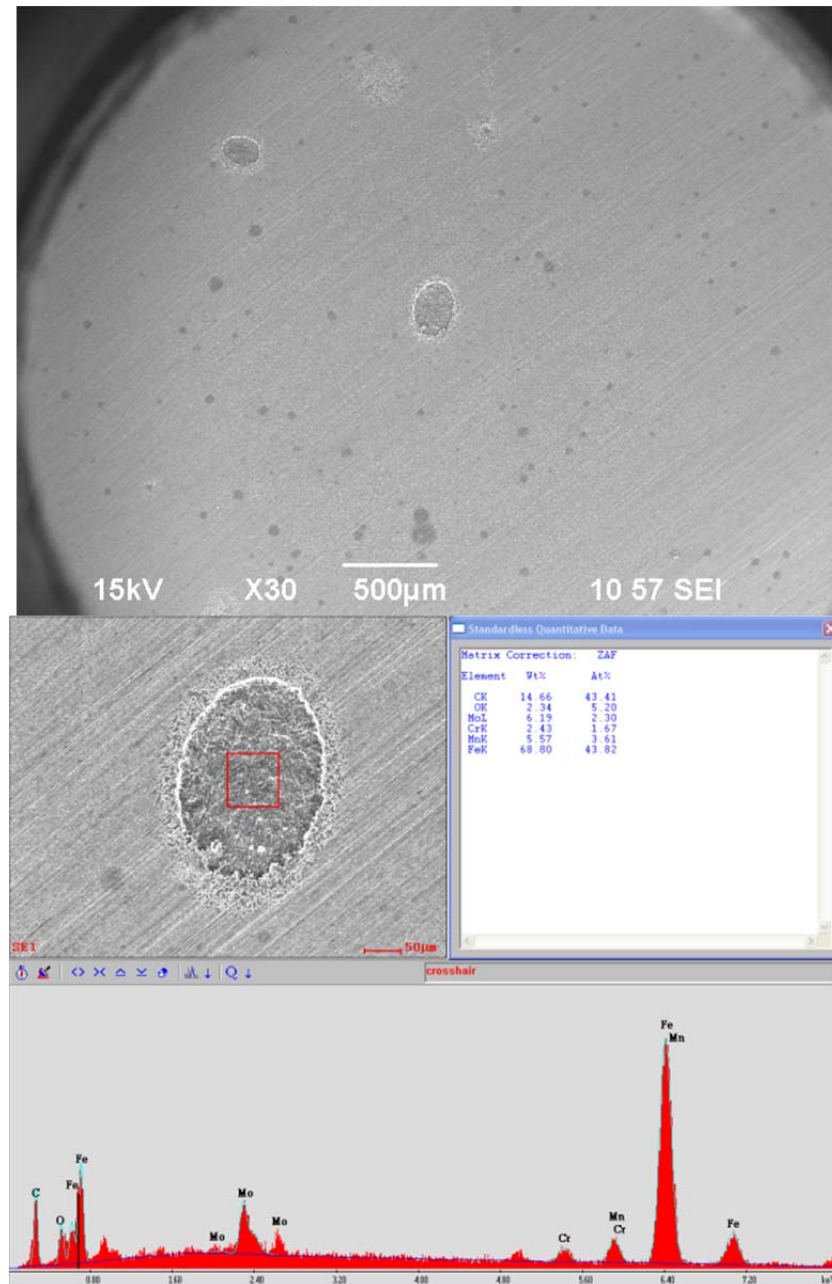


Figure 6.45 SEM and EDS images of the experiment sample #2 with corrosion product layers. Test conditions: 25°C, pH 5, 1 wt% NaCl solution saturated with CO₂.

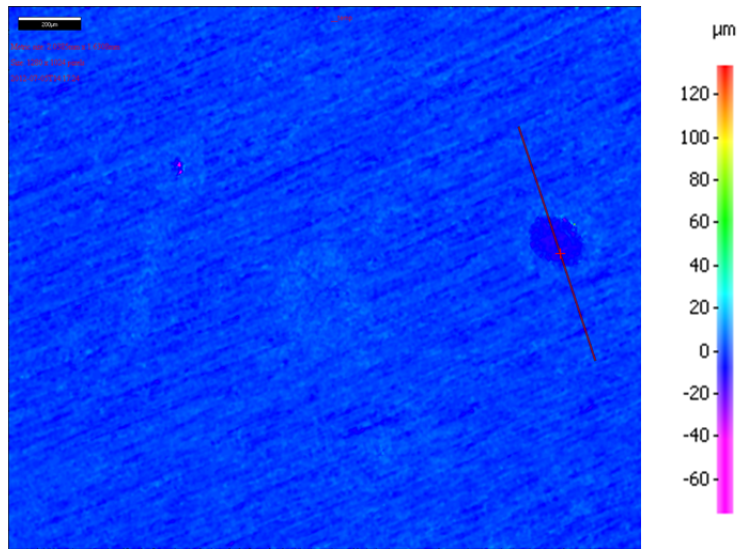


Figure 6.46 A infinite focusing microscopy image of the experiment sample #2 without corrosion product layers. Test conditions: 25°C, pH 5, 1 wt% NaCl solution saturated with CO₂.

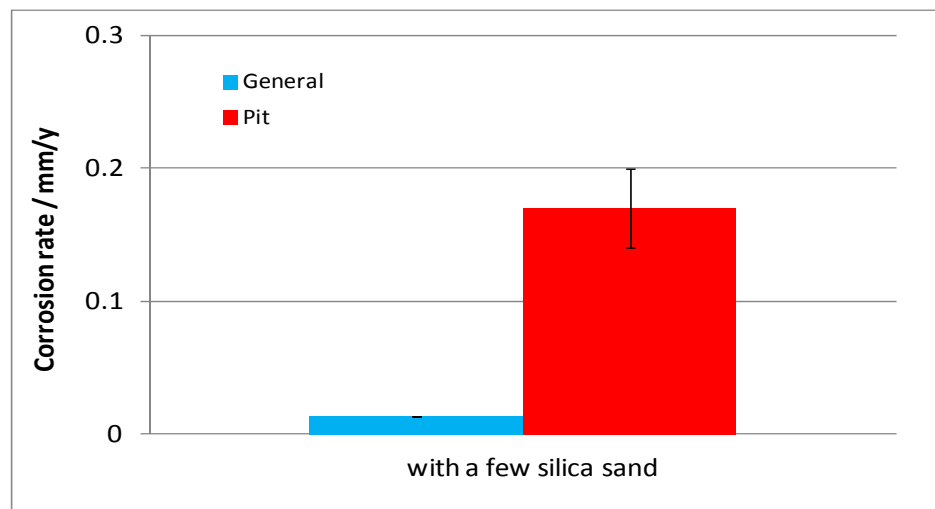


Figure 6.47 Comparison of the maximum corrosion rate from IFM scanning with surface averaged corrosion rate obtained from weight loss method. Test conditions: 25°C, pH 5, 1 wt% NaCl solution saturated with CO₂.

7. Conclusion –imidazoline inhibitor

So far two scenarios were tested, one was inhibitor K1 added after sand deposit and the other was vice versa. Localized corrosion in the form of pitting was found in both cases. However, by comparing the pitting depth from both experiments, the localized corrosion rate would be much more significant if the corrosion inhibitor K1 was added after sand addition (Figure 6.48).

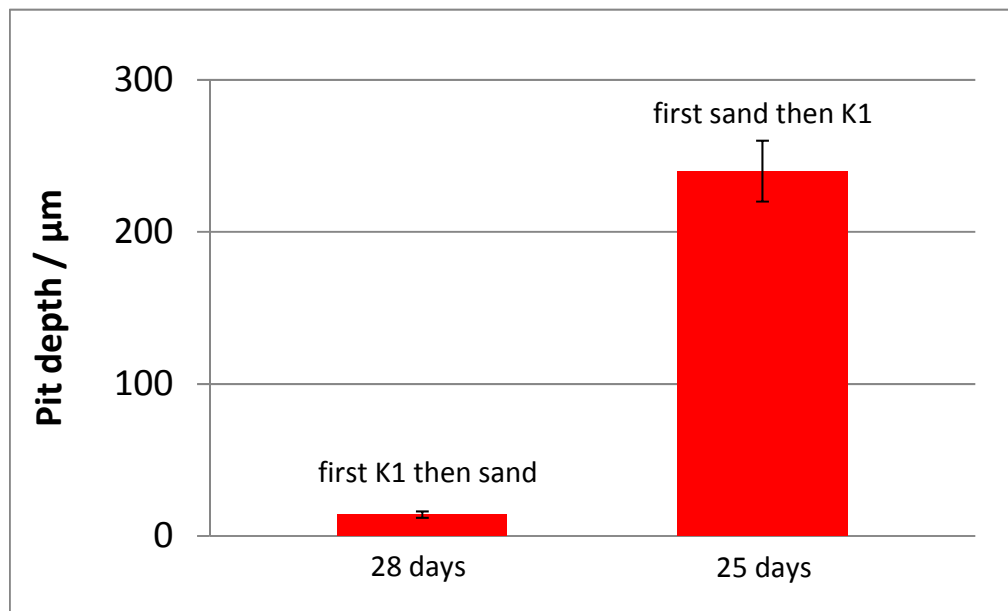


Figure 6.48 Comparison of pitting rate in two scenarios. Test conditions are 25°C, pH 5, in 1 wt% NaCl solution saturated with CO₂.

8. Experiment of thiosulfate inhibitor

To verify if non-surfactant inhibitor K3 (thiosulfate) would have the same effect as the surfactant inhibitor K1 (imidazoline), Experiments were conducted with inhibitor K3 following the same procedure as with K1.

Sand particles were added after 2 hour's bare steel corrosion and then 30 ppm K3 was added in the solution. Two samples were tested at the same time so the results can be considered as duplicate. In this case, the 30 ppm of K3 is equivalent to 70 ppm of K1 where both have an inhibition efficiency of 95%.

Figure 6.49 shows how the #1 sample looked after 14 days corrosion. SEM shows no iron carbonate corrosion product was formed, and some indication of sand particles can be observed (Figure 6.50). However, after the corrosion product layer was removed, areas following sand particle shapes can be observed on the steel surface. Infinite focusing microscopy measurement shows an average of depth $12 \pm 2 \mu\text{m}$ for those areas, see in Figure 6.51. This depth developed in 14 days is equivalent to a corrosion rate of 0.3 mm/yr. As compared to the uniform corrosion rate measured from weight loss, which is 0.17 mm/yr, this penetration rate is not considered as localized corrosion.



Figure 6.49 View of the experiment specimen #1 after 14 days exposure at test condition:
25°C, pH 5, 1 wt% NaCl solution saturated with CO₂.

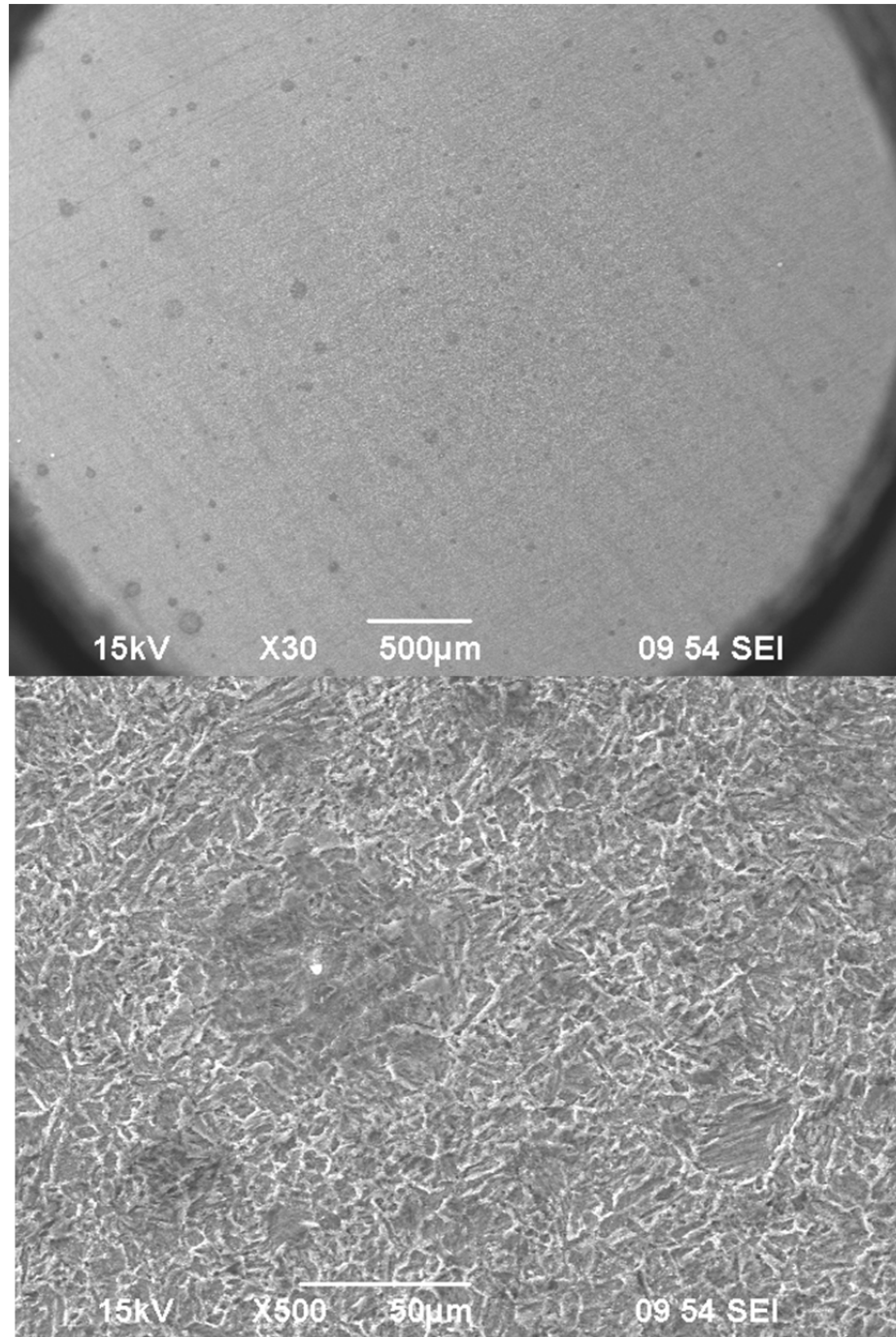


Figure 6.50 SEM images of the experiment sample #1 with corrosion product layers at test condition: 25°C, pH 5, 1 wt% NaCl solution saturated with CO₂.

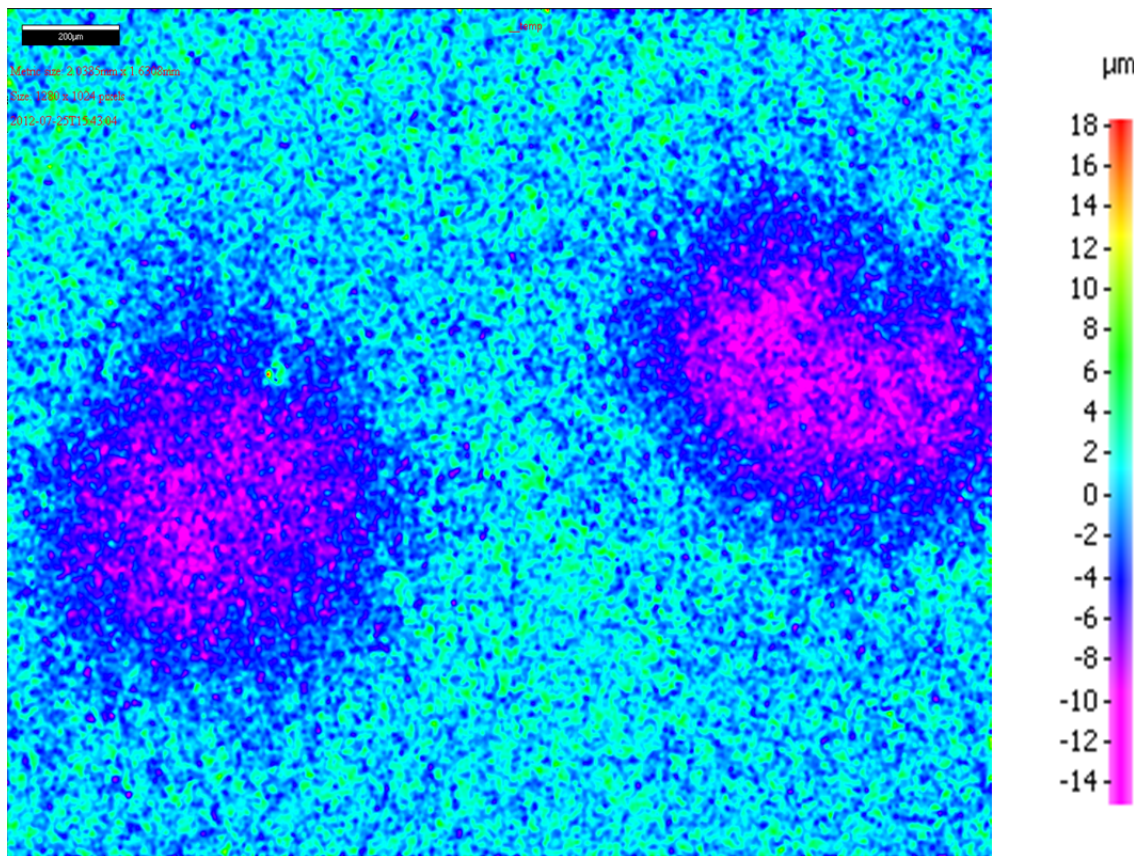


Figure 6.51 A infinite focusing microscopy image of experiment sample #1 after 14 days

exposure at test condition: 25°C, pH 5, 1 wt% NaCl solution saturated with CO₂.

The #2 sample showed the same results. As shown in Figure 6.52. SEM also indicates some effect of sand particles (Figure 6.53), however those areas underneath the sand, corrosion rate was not significant larger than surface averaged uniform corrosion rate, see infinite focusing microscopy scanning results shown in Figure 6.54.

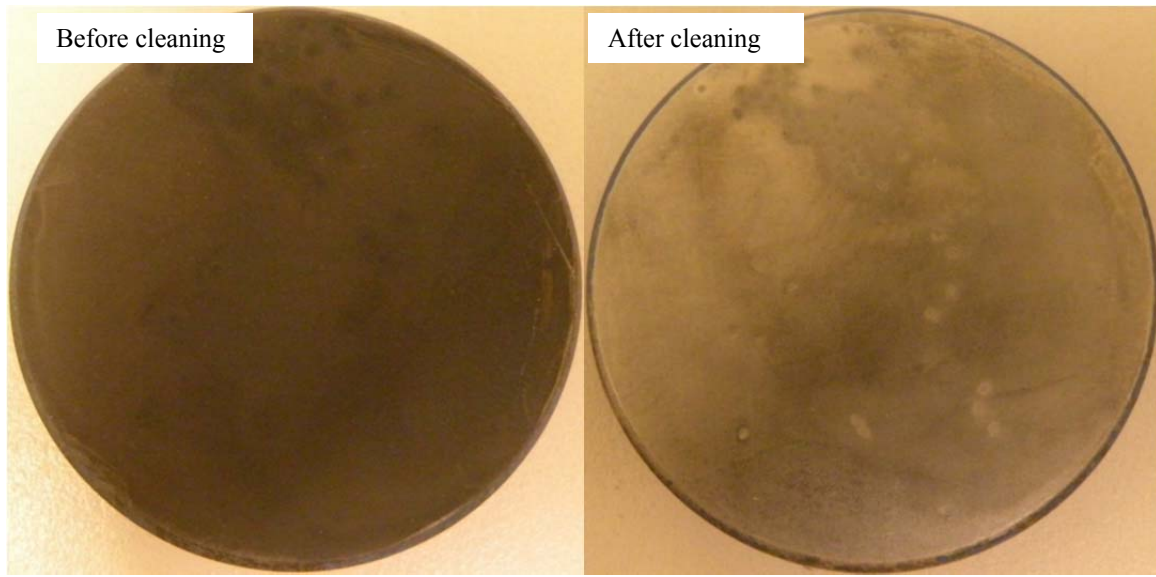


Figure 6.52 View of the experiment specimen #2 after 14 days exposure at test condition:
 25°C , pH 5, 1 wt% NaCl solution saturated with CO₂.

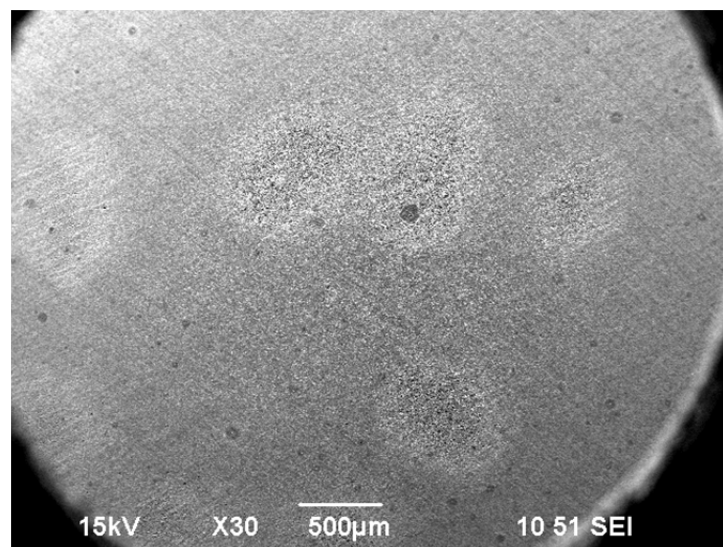


Figure 6.53 SEM images of the experiment sample #1 with corrosion product layers after
14 days exposure at test condition: 25°C , pH 5, 1 wt% NaCl solution saturated with CO₂.

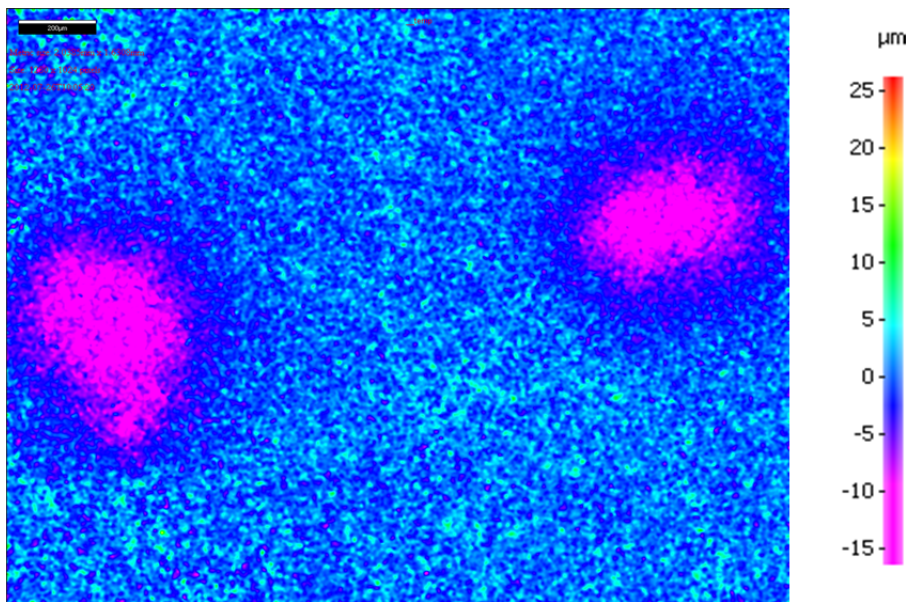


Figure 6.54 A infinite focusing microscopy image of experiment sample #1 after 14 days exposure at test condition: 25°C, pH 5, 1 wt% NaCl solution saturated with CO₂.

The comparison of the effect of K1 (imidazoline) and K3 (thiosulfate) is shown in Figure 6.55. For the same experimental conditions, the addition of K1 after sand particles are present led to a serious localized corrosion with a pitting rate as high as 2.5 mm/yr. With inhibitor K3, no localized corrosion was detected.

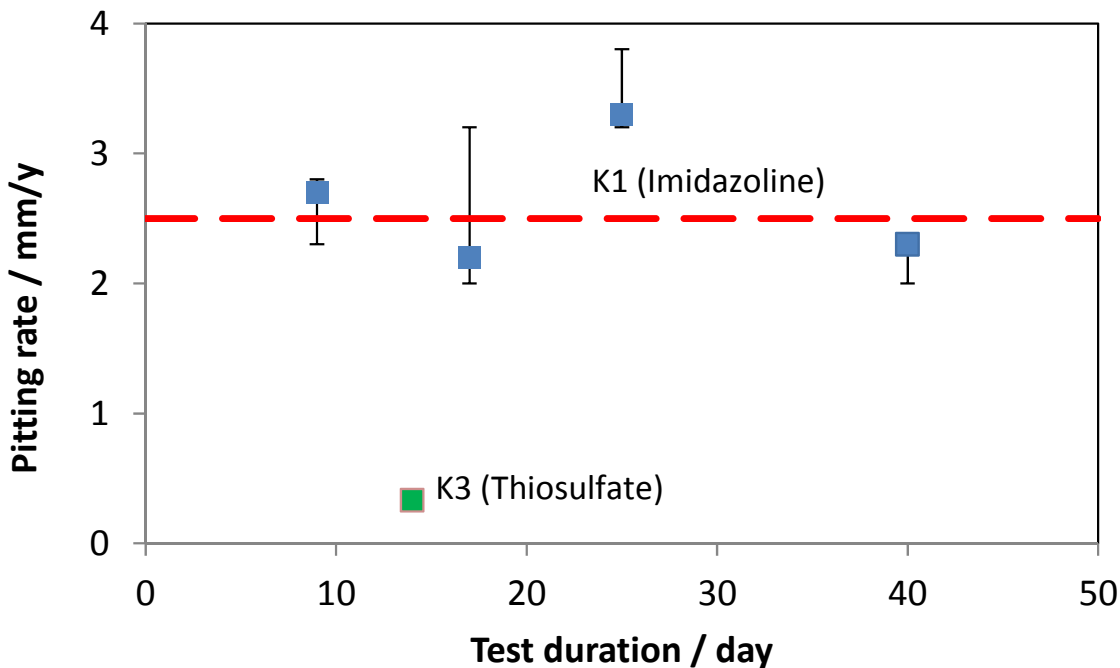


Figure 6.55 Comparison of the pitting rate found in the cases with inhibitor K1 (imidazoline) with the maximum corrosion rate found in the cases with inhibitor K3 (thiosulfate) at same test conditions, i.e., 25°C, pH 5, 1 wt% NaCl solutions saturated with CO₂.

6.4 Proposed Mechanisms of Localized Corrosion in Under Deposit Corrosion of Mild Steel

It was shown that when inhibitor K1 was present in addition to the sand deposit, pitting corrosion occurred. Based on all the experimental observations, pits were all found underneath each sand particle grain. It was observed that a steel surface fully covered by the sand deposit (with many layers or only one) experienced the same localized corrosion process as a steel surface with a partial sand deposit coverage, i.e.,

localized corrosion initiated and propagated under each sand particle irrespectively (Figure 6.56).

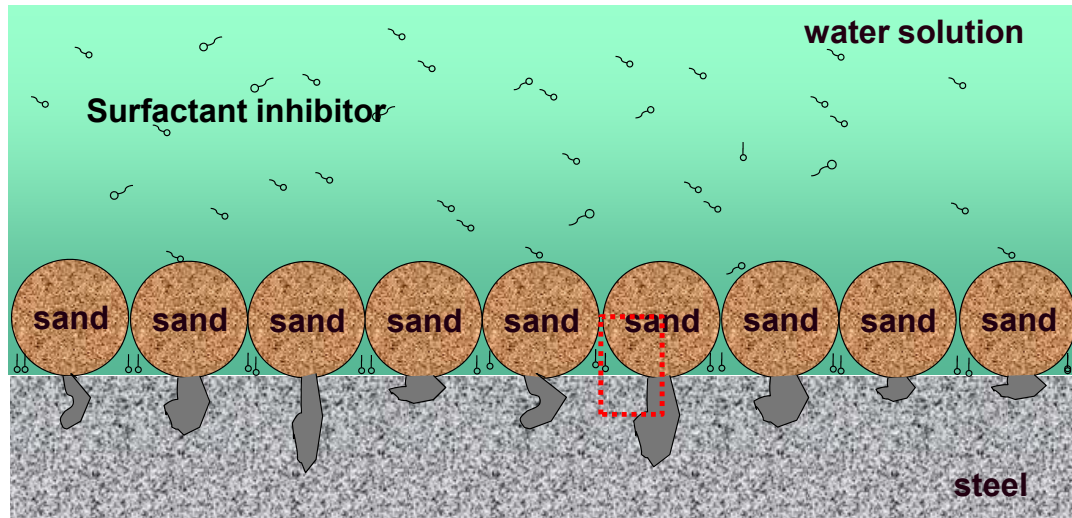


Figure 6.56 Description of the appearance of localized corrosion in under deposit corrosion in inhibited environment.

Therefore, a localized corrosion mechanism based on a single sand particle on steel surface is proposed:

Before inhibition (Figure 6.57):

- Due to diffusion limitation and coverage effect, the sand covered areas have low corrosion rate.

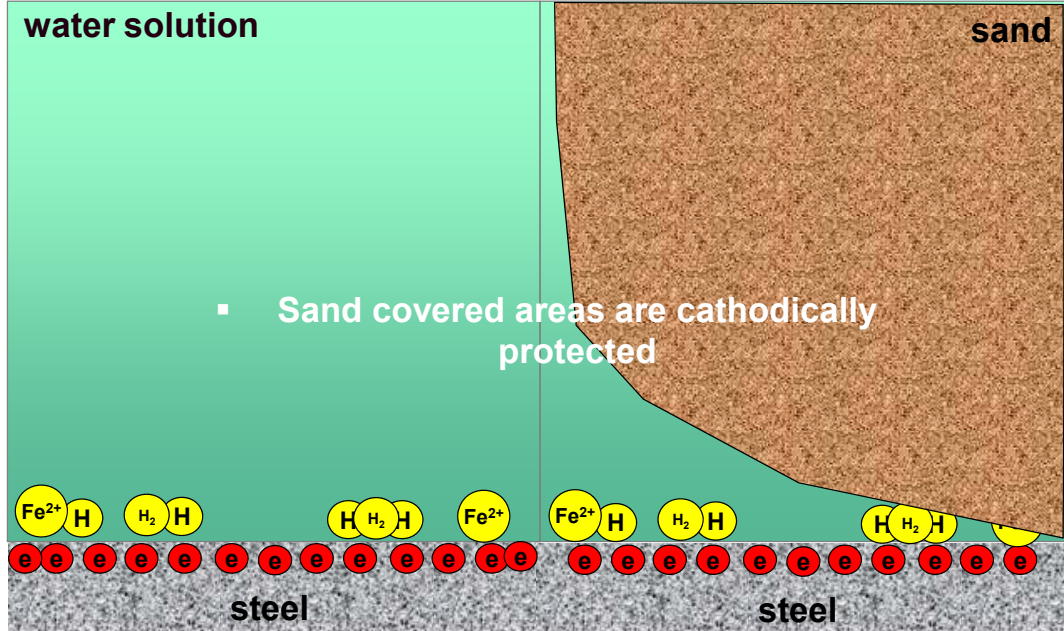


Figure 6.57 Description of the corrosion process in under deposit corrosion in inhibitor-free environment. (Sketches are not drawn to scale)

After inhibitor K1 was added (Figure 6.58):

- The steel surface area adjacent to each sand particle covered area is inhibited and has a very low corrosion rate and a more positive corrosion potential. Therefore, a galvanic cell is formed between that area and sand particle covered area on the metal surface. The sand covered area has a more negative potential so it acts as the anode, while adjacent areas have more positive potential acting as the cathode. This is the mechanism that initiates localized corrosion in the sand covered area. Furthermore, when the sand covered area is small as compared to the adjacent exposed area

(individual particles instead of a sand bed), there is a smaller anodic surface area with a larger cathodic surface area and the pit penetration rate may be accelerated.

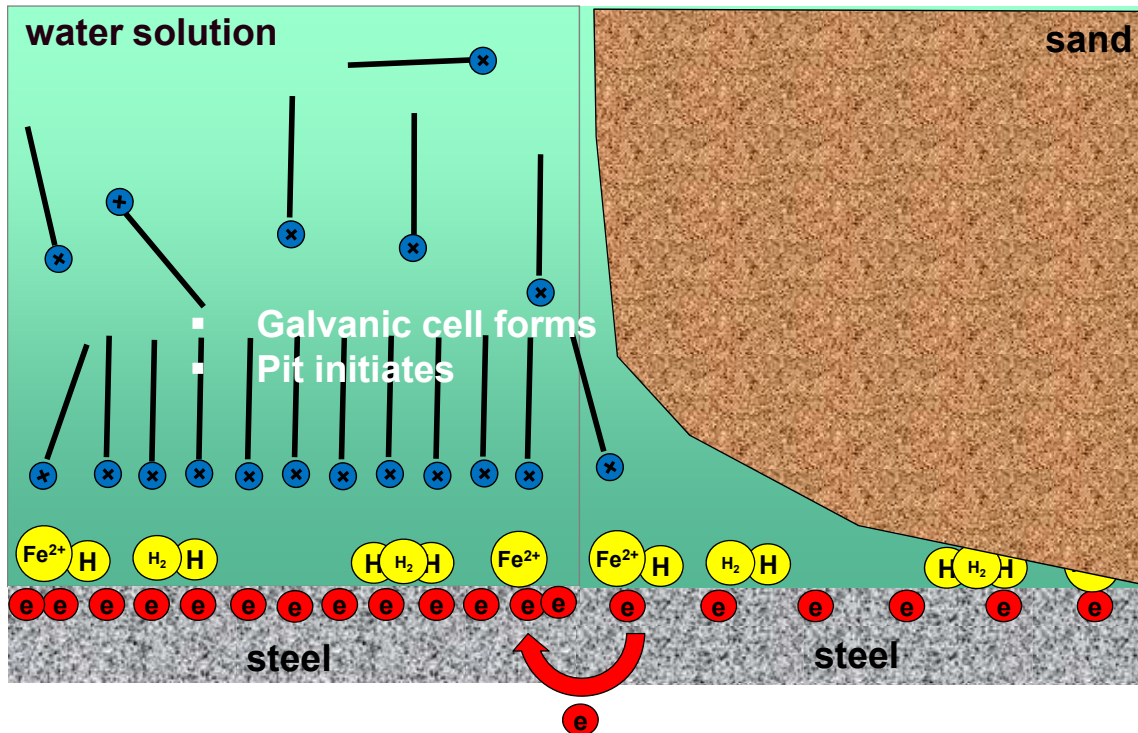


Figure 6.58 Description of the mechanism of localized corrosion in under deposit corrosion in inhibited environment. (Sketches are not drawn to scale)

It was asked what if the silica sand deposit was saturated with corrosion inhibitors, would localized corrosion still happen? As observed from present work, with an 1800 ppm inhibitor K1, the decay in uniform corrosion rate still was not obtained. Similar results were found in Turnbull's work, where replenished inhibitor (as named inhibitor "B" but unknown composition) up to 1000 ppm was injected into the under deposit corrosion system but no decrease in LPR calculated corrosion rate was observed

for up to 30 days. In truth, the replenishment or over dosage of the corrosion inhibitor provides a more severe condition for inhibitor performance because the inhibitor is more readily available to the external bare electrode so the polarization between it and the sand covered electrode is easier which makes the localized corrosion initiation easier.

Another issue to consider is what if the sand deposit was saturated with corrosion inhibitor, would localized corrosion still happen? By measuring the residue inhibitor concentration in the test solutions, Turnbull (2009), Pedersen (2008) both found that localized corrosion still occurred after the sand deposit was saturated by corrosion inhibitor (composition confidential for both work). Being consistent with what's believed in this dissertation, Turnbull also discarded the adsorption of inhibitor on silica sand surface caused the inhibition failure which is believed by other researchers (Horsup, 2007, Pandarinathan, 2013). Turnbull did suspect that the sluggish inhibition in his work was due to transport limitations with the pre-corroded regions adding an additional tortuous corrosion path. However, as tested in this dissertation, even with partially covered steel surface, the inhibition of imidazoline was still not evenly effective over the whole steel surface but induced localized corrosion. It was also suggested that when localized corrosion initiates, un-corroded areas of the steel surface or those areas with smaller corrosion rate becomes inhibited preferentially, turning into cathodes as time progresses.

Since both the hypothesis of bulk depletion of corrosion inhibitor and diffusion limitation have been disapproved as discussed in this dissertation, new hypothesis are needed to understand the inhibition mechanisms and localized corrosion mechanisms

encountered in under deposit corrosion. The interactions between the inhibitors, metal surfaces and silica sand need to be studied and can be a future direction for extending the current under deposit corrosion work. As Zhang et al. (2010) pointed out, imidazoline corrosion inhibitor molecules' reactivity on steel surface is not evenly distributed but has local preferences. By using molecular dynamics simulation and molecular mechanics, Zhang also found that the interaction of imidazoline ring on FeCO₃ is different from on Fe surface, which affects the inhibitor performances. In a recent work conducted by Hassani et al. (2013), very fine small silica particles (less than 44 µm) were found to be posing a less severe localized corrosion risk in under deposit corrosion. In the future, parameters like the adsorption oriental angle, adsorption energy and adsorption coverage ratio etc for interactions in between inhibitor molecules, silica sand and metal surface, as well as corrosion product surface can be studied at molecular level to better understand the corrosion and inhibition mechanisms in under deposit corrosion processes.

6.5 Summary

In this chapter, the localized corrosion in the presence of a deposit and generic corrosion inhibitors was investigated. A galvanic cell setup was built for localized corrosion study. Reliable procedures were developed for corrosion experiments. It is confirmed that localized corrosion occurs exactly underneath each individual silica sand particle in the form of pitting irrespective whether inhibition was added prior to sand or after sand. However, the pitting rate was much higher in the cases where the corrosion inhibitor was added after sand deposition.

Localized corrosion is induced by the presence of the solid deposits when a surfactant inhibitor is added. The driving force for the localized corrosion is the potential difference underneath the sand and its adjacent inhibited steel surface. A 20 – 40 mV potential differences can be expected with silica sand deposit and imidazoline based inhibitor. This localized corrosion would stop once the solid particle or deposit is removed from the steel surface. It is also found that iron thiosulfate inhibitor K3 does not lead to a localized corrosion as the imidazoline based surfactant inhibitor K1 does.

CHAPTER 7. CONCLUSIONS AND RECOMMENDATIONS FOR FUTURE WORK

7.1 Conclusions

Inhibitor – free environment:

- No localized corrosion problem would occur when an inert inorganic solid deposit is present on a mild steel surface. The deposit retards the uniform corrosion of mild steel by blocking part of the corroding steel surface as well as by slowing down the mass transfer of corrosive species to and from the steel surface from the bulk solution.
- Bulk solution pH and temperature do not affect the corrosion rate of mild steel beneath a sand deposit in the same way they would affect the corrosion of a bare steel surface.
- The surface pH measured underneath a sand deposit may be 1 to 2 pH units higher than in the bulk solution pH.
- Long term experiments shows that the presence of a sand deposit promotes iron carbonate formation, which would not be expected at bare steel corrosion conditions.

Inhibited environment:

- A simple and reliable method for testing of localized under-deposit corrosion was developed and verified.
- Mechanisms for localized corrosion in the presence of solids were identified and explained.

- a) General depletion of surfactant inhibitor (imidazoline based) by adsorption on silica sand surface is not the critical factor that causes inhibition failure in under-deposit CO₂ corrosion.
 - b) Slow diffusion of inhibitor through the porous sand deposit layer is also not the limiting factor in cases where inhibition failed.
 - c) Pits were found in under deposit corrosion and related to the inability of the corrosion inhibitor to protect the steel surface in the crevices immediately underneath each individual sand particle. These pits propagated very fast due to galvanic effects, eventually merging and causing a high rate of attack underneath the entire sand deposits.
- The localized corrosion is induced by the presence of the solid deposit, at a scale of a single sand grain. The driving force for the localized corrosion is the potential difference underneath the sand and its adjacent inhibited steel surface. 20 – 40 mV potential differences can be expected with silica sand deposit and imidazoline based inhibitor.
 - Iron thiosulfate inhibitor does not lead to localized corrosion probably due to the reaction mechanism of the thiosulfate salt and the steel surface and the lack of its interaction with silica sand.

7.2 Recommendations for Future Work

- Investigate the effect of silica deposits using mild steels with different microstructure which may affect inhibitor adsorption.

- Perform experiments at elevated temperature where FeCO_3 can be formed and study the effect of the corrosion product layer in under deposit corrosion and inhibition.
- Conduct experiments using very fine silica particles (e.g. $< 50 \mu\text{m}$) in under deposit corrosion to see if localized corrosion and inhibitor performance would be the same as using large particles.
- Study the under deposit corrosion using other types of deposit such as corrosion product and precipitates (e.g.: FeCO_3 , Fe_3C), or scales such as CaCO_3 , BaSO_4 , etc, as well as organic deposit such as wax and asphaltene.
- Investigate the possible effect of pre-corrosion on localized corrosion and inhibition in under deposit corrosion.
- Apply the test methodology and techniques developed in this dissertation to H_2S system.
- Study the interaction mechanisms in between inhibitor molecules, silica sand and metal surface, as well as corrosion product surfaces using advanced computational modeling at molecular level.

REFERENCES

- Abass, H. H., Nar-Ei-Din, H. A. & BaTaweeel, M. H. (2002). Sand control: sand characterization, failure mechanisms, and completion methods. Paper presented at the society for petroleum engineers (SPE) paper no. 77686.
- Abduh, M. (2008). The 50 Major Engineering Failures, access on: <http://abduh137.wordpress.com/2008/04/25/the-50-major-engineering-failures-1977-2007-part-1/>
- Achour, M., Kolts, J., Humble, P. & Hudgins, R. (2008). Experimental evaluation of corrosion inhibitor performance in presence of iron sulfide in CO₂/H₂S environment. Paper presented at the NACE Corrosion/08, paper no. 08344.
- Alsabagh, A. M., Migahed, M. A. & Awad, H. S. (2006). Reactivity of polyester aliphatic amine surfactants as corrosion inhibitors for msteel in formation water (deep well water). Corrosion Science 48, 813-828.
- Armstrong, R. D., Peggs, L. & Walsh, A. (1994). Behaviour of sodium silicate and sodium phosphate (tribasic) as corrosion inhibitors for iron. Journal of Applied Electrochemistry 24, 1244-1248.
- ASTM Standard G1, 2003, Standard Practice for Preparing, Cleaning, and Evaluating Corrosion Test Specimens, ASTM International, West Conshohocken, PA, 2003, DOI: 10.1520/G0001-03, www.astm.org
- Atkin, R., Craig, V. S. J., Wanless, E. J. & Biggs, S. (2003). Mechanism of cationic surfactant adsorption at the solid-aqueous interface. Advances in Colloid and Interface Science, 103, 219-304.

- Baril, G., Galicia, G., Deslouis, C., Pébère, N., Tribollet, B & Vivier, V. (2007). An impedance investigation of the mechanism of pure magnesium corrosion in sodium sulfate solutions. *Journal of the Electrochemical Society*, 154, C108-C113.
- Juan Bisquert, J. & Compte, A. (2001). Theory of the electrochemical impedance of anomalous diffusion. *Journal of the Electrochemical Chemistry*, 499, 112-120.
- Brady, P. V., & Walther, J. V. (1989). Controls on silicate dissolution rate in neutral and basic pH solutions at 25°C. *Geochimica et Cosmochimica Acta*, 53, 2823-2830.
- Bockris, J. O. M., Drazic, D. & Despic, A. R. (1961). The electrode kinetics of the deposition and dissolution of iron, *Electrochimica Acta*, 4, 325.
- Bonis, M. R. & Crolet, J. L. (1989). Basics of the Prediction of the Risks of CO₂ Corrosion in Oil and Gas Wells, paper presented at the NACE Corrosion/89. Paper presented at the NACE Corrosion/89, paper no. 89466.
- Canto, C., Brown, B. & Nešić, S. (2011). Integrity of corrosion inhibitor films in multiphase flow. Paper presented at the NACE Corrosion/11, paper no. 238.
- Cao, C. (1996). On electrochemical techniques for interface inhibitor research, *Corrosion Science*, 38 (12), 2073-2082.
- Chen, H. J. (1994) Evaluation of Oilfield Corrosion Inhibitors by EIS. Paper presented at the NACE Corrosion/94, paper no. 92.
- Chokshi, K., Sun, W. & Nešić, S. (2005). Iron carbonate film growth and the effect of inhibition in CO₂ corrosion of mild steel. Paper presented at the NACE Corrosion/05, Paper presented at the NACE Corrosion/05, paper no. 05285.

- Cotton, J. J. (2001). Reduction of deposition and corrosion in cooling systems. *Materials Performance*, 40(9), 50-51.
- Crolet, J. L., Thevenot, N. & Nešić, S. (1998). Role of conductive corrosion products in the protectiveness of corrosion layers. *Corrosion*, 54 (3), 197-203.
- Dawson, J. L. (1993). Electrochemical Measurements for Inhibitor Assessments. Paper presented at the NACE Corrosion/93, paper no. 108.
- de Reus, J. A. M. & Simon Thomas M. J. J. (2002). Corrosion inhibitor selection and field verification in oil and gas production. Paper presented at the NACE Corrosion/02, paper no. 279.
- de Reus, J. A. Hendriksen, E. L. J. A., Wilms, M. E., Al-Habsi, Y. N., Durnie, W. H. & Gough, M. A. (2005). Test methodologies and field verification of corrosion inhibitors to address under deposit corrosion in oil and gas production systems, Paper presented at the NACE Corrosion/05, paper no. 288.
- de Waard, C. & Lotz, U. (1993). Prediction of CO₂ Corrosion of Carbon Steel. Paper presented at the NACE Corrosion/93, paper no. 069.
- de Waard, C. & Milliams, D. E. (1975a). Carbonic acid corrosion of steel, *Corrosion*, 31, 177-181.
- Dugstad, A. (2006). Fundamental aspects of CO₂ metal loss corrosion - Part I: Mechanism, Paper presented at the NACE Corrosion/06, paper no. 111.
- Durnie, W., Gough, M. & de Reus, H. (2005). Development of corrosion inhibitors to address under deposit corrosion in oil and gas production systems, Paper presented at the NACE Corrosion/05, paper no. 290.

- Epelboin, I. & Keddam, M. (1970). Faradaic impedances: diffusion impedance and reaction impedance. *Journal of the Electrochemical Society*, 117, 1052-1056.
- Epelboin, I., Keddam, M & Takenouti, H. (1972). Use of impedance measurements for the determination of the instant rate of metal corrosion. *Journal of Applied Electrochemistry*, 2, 71-79.
- Espan, T., Kapusta, S. D. & Simon Thomas, M. J. J. (2001), Case study: extreme corrosion of a 20" oil pipeline in the niger delta region. Paper presented at the NACE Corrosion/01, paper no. 629.
- Foss, M., Gulbrandsen, E. & Sjoblom, J. (2008). Interaction of carbon dioxide corrosion inhibitors with corrosion products deposit, paper presented at the NACE Corrosion/08, paper no. 343.
- Gray, L. G. S., Anderson, B. G., Danysh, M. J. & Tremaine, P. R. (1990). Effect of pH and temperature on the mechanism of carbon steel corrosion by aqueous carbon dioxide. Paper presented at the NACE Corrosion/90, paper no. 040.
- Gu, T., Zhao, K & Nešić, S. (2009). A New Mechanistic Model for MIC Based on a Biocatalytic Cathodic Sulfata Reduction Theory. Paper presented at the NACE Corrosion/09, paper no. 390.
- Gulbrandsen, E. & Pedersen, A. (2007). Alteration of sand wettability by corrosion inhibitors and its effect on formation of sand deposits, SPE International Symposium on Oilfield Corrosion, 106492.
- Hackerman, N. & Snavely, E. E. (1984). Inhibitors, in Brasunas, A. de S. (ed.), *Corrosion Basics*, Houston, TX, NACE International, 1984, page 127.

- Han, J. (2009). Galvanic mechanism of localized corrosion for mild steel in carbon dioxide environments, Doctoral Dissertation, Ohio University.
- Han, J., Nešić, S., Yang, Y & Brown, B. (2011). Spontaneous passivation observations during scale formation on mild steel in CO₂ brines. *Electrochimica Acta*, 56(15), 5396-5404.
- Hassani, S. (2013). Personal communication.
- Herzberg, W. J. & Erwin, W. R. (1970). Gas-chromatographic study of the reaction of glass surfaces with dichlorodimethylsilane and chlorotrimethylsilane, *Journal of Colloid and Interface Sciences*, 83, 1.
- Hinds, G. & Turnbull, A. (2010). Novel multi-electrode test method for evaluating inhibition of underdeposit corrosion. Part 1: Sweet conditions. *Corrosion*, 66, 046001-1.
- Horsup, D. I. (2007). I put it in, but where does it go?- the fate of corrosion inhibitors in multiphase systems. Paper presented at the NACE Corrosion/07, paper no. 07617.
- Huang, J., Brown, B. Jiang, X., Kinsella, B. & Nešić, S. (2010). Internal CO₂ Corrosion of Mild Steel Pipelines under Inert Solid Deposits. Paper presented at the NACE Corrosion/10, paper no. 379.
- Huang, J., Brown, B. Choi, Y. S. & Nešić, S. (2011). Prediction of Uniform CO₂ corrosion of Mild Steel under Inert Solid Deposits. Paper presented at the NACE Corrosion/11, paper no. 260.

- Huang, J., Brown, B. & Nešić, S. (2013). Localized Corrosion of Mild Steel under Silica Deposits in Inhibited Aqueous CO₂ solutions, paper to be presented at the NACE Corrosion/13.
- Hurlen, T., Gunvaldsen, S., Tunold, R., Blaker, F. & Lunde, P. G. (1984). Effects of carbon dioxide on reactions at iron electrodes in aqueous salt solutions, Journal of Electroanalytical Chemistry, 180, 511-526.
- Ismail Abdelrhman Aiad, Hafiz, A. A., El-Awady, M. Y. & Habib, A. O. (2010) Some Imidazoline Derivatives as Corrosion Inhibitors, Journal of Surfactant Detergent, 13:247-254.
- Jackson, J. E. (2011). Cost of corrosion, <http://www.g2mtlabs.com/cost-of-corrosion/>
- Johns, D. A. (1995). Principles and Prevention of Corrosion, 2nd Ed., Prentice Hall.
- Johnson, M. L. & Tomson, M. (1991). Ferrous carbonate precipitation kinetics and its impact on CO₂ corrosion. Paper presented at the NACE Corrosion/91, paper no. 2689.
- Kang, C., More, P. P., Vera, J., Ferreira, P. A., Bastos, E. C. & Araujo, M. (2008). Effect of flow on corrosion and its inhibition in riser pipelines. Paper presented at the NACE Corrosion/08, paper no. 562.
- Keddam, M., Mattos, O. R. & Takenouti, H. (1981). Reaction Model for Iron Dissolution Studied by Electrode Impedance I . Experimental Results and Reaction Model. Journal of the Electrochemical Society, 6, 257-266.
- Kibala, E. B. & Nugent, M. J. (1999). Naphthenic acid corrosion literature survey. Paper presented at the NACE Corrosion/99, paper no. 378.

- Koch, G. H., Brongers, M. P. H., Thompson, N. G. , Virmani, Y. P., & Payer, J. H. (2002). Corrosion costs and preventive strategies in the United States, FWHA-RD-01-156, U. S. Department of Transportation, Federal Highway Administration.
- Lepkova K. & Gubner, R. (2010). Development of standard test method for investigation of under-deposit corrosion in carbon dioxide environment and its application in oil and gas industry. Paper presented at the NACE Corrosion/10, paper no. 331.
- Li, C. (2009), Effect of Corrosion Inhibitor on Water Wetting and Carbon Dioxide Corrosion In Oil-Water Two-Phase Flow, Doctoral Dissertation, Ohio University.
- Li, J., Webb, C., Pandiella, S. S., Campbell, G. M., Dyakowski, T., Cowell, A. & McGlinchey, D. (2005). Solids deposition in low velocity slug flow pneumatic conveying. *Chemical Engineering and Processing*, 44, 167-173.
- Mansfeld, F. (1990) Electrochemical impedance spectroscopy (EIS) as a new tool for investigating methods of corrosion protection. *Electrochimica Acta*. 35, 10, 1533-1544.
- Mansfeld, F. & Tsai, C.H. (1991). Determination of Coating Delamination with EIS. I. Basic Relationship, *Corrosion* 47, 958.
- Marsh, J., Palmer, J. W. & Newman, R. C. (2002). Evaluation of inhibitor performance for protection against localized corrosion. Paper presented at the NACE Corrosion/02, paper no. 288.
- Mercer, A. D. (1994). Corrosion inhibition: Principles and practice, in L. L. Shreir, R. A. Jarman and G. T. Burstein, eds, corrosion control, Oxford, UK, Butterworths Heinemann, 17:11-17: 39.

- Miksic, B. M., Furman, A. Y. & Kharshan, M. A. (2009). Effectiveness of the corrosion inhibitors for the petroleum industry under various flow conditions, paper presented at the NACE Corrosion/09, paper no. 573.
- Moretti, G., Guidi, F. & Grion, G. (2004). Tryptamine as a green iron corrosion inhibitor in 0.5 M deaerated sulphuric acid. *Corrosion Science* 46, 387-403.
- Morita, N. & Boyd, P. A. (1994). Typical sand production problems: case studies and strategies for sand control. Paper presented at the SPE paper no. 27343.
- Nešić, S., Postlethwaite, J. & Olsen, S. (1996). An Electrochemical Model for Prediction of Corrosion of Mild Steel in Aqueous Carbon Dioxide Solutions. *Corrosion*, 52(4).
- Nešić, S. (2007). Key issues related to modeling of internal corrosion of oil and gas pipelines – A review. *Corrosion Science*, 49, 4308-4338.
- Nešić, S & Lee, J. (2003). A mechanistic model for carbon dioxide corrosion of mild steel in the presence of protective iron carbonate films – Part 3: Film growth model. *Corrosion*, 59(7), 616-628.
- Nyborg, R., Gulbrandsen, E., Loeland, T., & Nisancioglu, K. (2000). Effect of steel microstructure and composition on inhibition of CO₂ corrosion. Paper presented at the NACE Corrosion/00, paper no. 023.
- Oddo, J. E. & Tomson, M. B. (1998). Method predicts well bore scale, corrosion. *Oil and Gas Journal*, 96(23), 107-114.
- Orazem, M. E. & Tribollet, B. (2008). *Electrochemical Impedance Spectroscopy*. Hoboken, New Jersey: John Wiley & Sons.

- Osman, M. M., El-Ghazawy, R. A. & Al-Sabagh, A. M. (2003). Corrosion inhibitor of some surfactants derived from maleic-oleic acid adduct on mild steel in 1 M H₂SO₄. *Material of Chemical Physics*, 80, 55-62.
- Pandarinathan, V., Lepkova, K., Bailey, S. I. & Gubner, R. (2013). Evaluation of corrosion inhibition at sand-deposited carbon steel in CO₂-saturated brine. *Corrosion Science*, 72, 108-117.
- Papavinasam, S. (2007). Empirical equations to predict conditions for solid deposition. *Materials Performance*, 58-61.
- Parfitt, G. D. & Rochester, C. H. (1983). Adsorption from solution at the solid/liquid interface. Academic Press.
- Paria, S. & Khilar, K. C. (2004). A review on experimental studies of surfactant adsorption at the hydrophilic solid-water interface. *Advances in Colloid and Interface Science*, 110, 75-95.
- Pedersen, A., Bilkova, K., Gulbrandsen, E. & Kvarekvål, J. (2008). CO₂ corrosion inhibitor performance in the presence of solids: test method development. Paper presented at the NACE Corrosion/08, paper no. 08632.
- Place, T. D., Holm, M. R., Cathrea, C. & Ignacz, T. (2009). Understanding and mitigating large pipe underdeposit corrosion, *Materials Performance*, Jan. 2009, 54-61.
- Popova, A., Christov, M., Raicheva, S. & Sokolova, E. (2004). Adsorption and inhibitive properties of benzimidazole derivatives in acid mild steel corrosion. *Corrosion Science*, 46, 1333-1350.

- Salama, M. M. (2000). Influence of sand production on design and operations of piping systems. Paper presented at the NACE Corrosion/00, paper no. 80.
- Scamehorn, J. F., Schechter, R. S. & Wade, W. H. (1982). Adsorption of Surfactants on Mineral Oxide Surfaces from Aqueous-Solutions .1. Isomerically Pure Anionic Surfactants. *Journal of Colloid and Interface Science*, 85, 463-478.
- Schmitt, G. (1983). Corrosion of steels: An attempt to range parameters and their effects. Paper presented at the NACE Corrosion/83, paper no. 83023.
- Schmitt, G. & Rothmann, B. (1978a). Studies on the corrosion mechanism of unalloyed steel in oxygen – free carbon dioxide solutions, Part 1: Kinetics of the liberation of hydrogen, *Werkstoffe Und Korrosion*, 28, 154-162.
- Schmitt, G. & Rothmann, B. (1978b). Studies on the corrosion mechanism of unalloyed steel in oxygen – free carbon dioxide solutions, Part 2: Kinetics of iron dissolution. *Werkstoffe Und Korrosion*, 29, 153-166.
- Schmitt, G. (2006). Fundamental aspects of CO₂ metal loss corrosion - Part II: influence of different parameters on CO₂ corrosion mechanisms. Paper presented at the NACE Corrosion/06, paper no.06112.
- Shadley, J. R., Shirazi, S. A., Dayalan, E. & Rybicki, E. F. (1998). Prediction of erosion Corrosion penetration rate in a carbon dioxide environment with sand. *Corrosion*, 54(12), 972-978.
- Shadley, J. R., Shirazi, S. A., Dayalan, E. & Rybicki, E. F.(1996). Velocity Guidelines for Preventing Pitting of Carbon Steel Piping when the Flow Medium Contains CO₂ and Sand. Paper presented at the NACE Corrosion/1996, paper no. 015.

- Shim, S. H., Johnson, D. A. & Moriarty, B. E. (1988). Characterization of Localized and Underdeposit Corrosion in Cooling Water Systems. Paper presented at the NACE Corrosion/88, paper no. 023.
- Silverman, D. C. (1990). Rapid corrosion screening in poorly defined systems by electrochemical impedance technique, Corrosion 6(7), 589.
- Smart, J. S. (2009) Flow velocity required for solid particle movement in oil and gas pipelines, Corrosion/09, paper no. 469.
- Sooknah, R. D., Papavinasam, S. & Revie, R. W. (2007). Monitoring microbiologically influenced corrosion: a review of techniques. Paper presented at the NACE Corrosion/07, paper no. 517.
- Soror, T. Y. & El-Ziady, M. A. (2003). Effect of cetyl trimethyl ammonium bromide on the corrosion of carbon steel in acids. Materials Chemistry and Physics, 77, 697-703.
- Sridhar, N., Dunn, D. S., Anderko, A. M., Lencka, M. M. & Schutt, H. U. (2001). Effect of water and gas compositions on the internal corrosion of gas pipelines – modeling and experimental studies. Corrosion, 57(3), 220-235.
- Sun, W. (2006). Kinetics of iron carbonate and iron sulfide scale formation in CO₂/H₂S corrosion, Doctoral Dissertation, Ohio University.
- Tan, Y. J., Bailey, S. & Kinsella, B. (1996). The monitoring of the formation and destruction of corrosion inhibitor films using electrochemical noise analysis (ENA). Corrosion Science, 38, 1681-1695.

Tanupabrunsgsun, T., (2012). Thermodynamics and Kinetics of Carbon Dioxide Corrosion of Mild Steel at Elevated Temperatures, Doctoral dissertation, Ohio University.

Thomas, J. G. N., The mechanisms of corrosion, in L. L. Shreir, R. A. Jarman and G. T. Burstein, eds, corrosion control, Oxford, UK, Butterworths Heinemann, 1994, 17:40-17: 65.

Turnbull, A., Coleman, D., Griffiths, A. J., Francis, P. E. & Orkney, L. (2003). Effectiveness of corrosion inhibitors in retarding the rate of propagation of localized corrosion. *Corrosion*. 59(3), 250.

Turnbull, A., Hinds, G., Cooling, P & Zhou, S. (2009). A multi-electrode approach to evaluating inhibition of underdeposit corrosion in CO₂ environments, paper presented at the NACE Corrosion/09, paper no. 09445.

Vera, J. R., Daniels, D. & Achour, M. H. (2012). Under deposit corrosion (UDC) in the oil and gas industry: a review of mechanisms, testing and mitigation. Paper presented at the NACE Corrosion/12, paper no. 1379.

Yang, Y., Brown, B., Nešić, S., Gennaro, M. E. & Molinas, B. (2010). Mechanical strength and removal of a protective iron carbonate layer formed on mild steel in CO₂ corrosion. Paper presented at the NACE Corrosion/10, paper no. 383.

Yao, X. (2012). AFM studies of the Metallicity of Single-walled Carbon Nanotubes and Corrosion Inhibitor Adsorption, Doctoral dissertation, Ohio University.

- Yen, A., Yin, Y. R. & Asomaning, S. (2001). Evaluating asphaltene inhibitors: laboratory tests and field studies. Paper presented at the SPE International Symposium on Oilfield Chemistry, 13-16 February 2001, Houston, Texas.
- Zhang, J., Liu, J., Yu, W., Yan, Y., You, L. & Liu, L. (2010). Molecular modeling of the inhibition mechanism of 1-(2-aminoethyl)-2-alkyl-imidazoline. Corrosion Science, 52, 2059-2065.
- Zhang, X., Wang, F., He, Y. & Du, Y. (2001). Study of the inhibition mechanism of imidazoline amide on CO₂ corrosion of Armco iron. Corrosion Science, 43, 1417-1431.
- Zhu, A., Sand, K. W. & Teevens, P. J. (2010). Solids deposition in liquids petroleum (oil) and wet-gas pipelines. Paper presented at the NACE internal corrosion predictive modeling (ICPM), NACE Northern Area Western Conference.



Thesis and Dissertation Services